Polynuclear Dioxolene Complexes with Redox-Active Transition Metals – Novel Synthesis Routes, Characterization and Capabilities

Dissertation

zur Erlangung des Grades

„Doktor der Naturwissenschaften“

im Promotionsfach Chemie

am Fachbereich Chemie, Pharmazie und Geowissenschaften

der

Johannes Gutenberg-Universität Mainz

Marcel Diehl

geboren in Hadamar

Mainz, 2015

Die vorliegende Arbeit wurde unter Betreuung von [redacted] in der Zeit von April 2012 bis Juni 2015 am Institut für Anorganische und Analytische Chemie der Johannes Gutenberg-Universität Mainz angefertigt und wurde durch ein Promotionsstipendium im Rahmen der Graduiertenschule MAINZ (Materials Science in Mainz) gefördert.

Mainz, Juni 2015

Dekan: [redacted]
Erster Berichterstatter: [redacted]
Zweiter Berichterstatter: [redacted]

Tag der mündlichen Prüfung: 20. Juli 2015

D77

Kurzzusammenfassung

Aufgrund ihrer einzigartigen Redoxchemie erweisen sich „nicht-unschuldige“ (non-innocent) Dioxolen-Liganden als beachtenswerte und vielseitige Verbindungen der Koordinationschemie. Komplexe dieser chinoiden Systeme können in bestimmten Fällen unter externen Stimuli intramolekulare Elektronenübertragungsprozesse zwischen Ligand und Metallion aufweisen, die sogenannte Valenztautomerie. Neben ihrer Eignung zur Untersuchung dieser Redoxprozesse können diese schaltbaren Moleküle in vielfältigen Anwendungen genutzt werden, wie etwa im Bereich der Sensorik, Datenspeicherung oder der molekularen Elektronik. Während in der Literatur im Wesentlichen einkernige Dioxolen-Komplexe diskutiert werden, beschäftigt sich die vorliegende Arbeit mit der Synthese und Charakterisierung mehrkerniger Übergangsmetallkomplexe mit redox-aktiven Dioxolen-Liganden. Diese bieten durch ihre Mehrzahl an Redox-Zentren die Möglichkeit zu mehrstufigen valenztautomeren Übergängen und kommen somit als polymodale molekulare Schalter in Frage. Zur Untersuchung des Einflusses von Ligand-Verbrückungsmodi auf die Elektronenkonfiguration der Komplexe wurden unterschiedliche Methoden zur gezielten Synthese mehrkerniger Dioxolen-Komplexe entwickelt: die Selbstorganisation kleiner Bausteine unter geeigneten Bedingungen, der Einsatz von Metallakronen-Fragmenten als strukturgebende, präorganisierende Elemente sowie die Verwendung von starren, bis-chelatisierenden Co-Liganden. Auf Basis dieser Methoden konnten vielfältige mehrkernige Komplexe verschiedener Übergangsmetalle erhalten werden. Die Untersuchungen dieser Verbindungen mittels einkristalldiffraktometrischer Strukturbestimmung sowie spektroskopischer und magnetometrischer Messungen inklusive deren Simulation erlaubten eine exakte Aussage über die vorliegenden Oxidationsstufen von Ligand und Metallionen. Für einige der synthetisierten Kobalt-Verbindungen konnte thermische Valenztautomerie oberhalb von Raumtemperatur ausgemacht werden. Überdies zeigten spektroskopische Studien bei einigen geeigneten Komplexen die katalytische Aktivität bei der Oxidation von Catecholen zu *o*-Chinonen mithilfe von Disauerstoff, deren Kinetik durch die Michaelis–Menten-Theorie beschrieben und ausgewertet werden konnte. Diese mehrkernigen Systeme fungieren somit als Modellkomplexe für die Metalloenzyme Catecholase und Tyrosinase und leisten einen Beitrag zum mechanistischen Verständnis der entsprechenden biologischen Prozesse.

Abstract

Due to their unique redox chemistry, non-innocent dioxolene ligands prove to be valuable and versatile compounds in coordination chemistry. Complexes with this kind of quinoid systems in some cases may exhibit intramolecular electron transfer processes, triggered by external stimuli, the so-called valence tautomerism. Beside their purpose as test-ground for the examination of redox processes, manifold applications for these switchable molecules are found in the fields of sensor devices, data storage or molecular electronics. While previous studies mainly covered mononuclear dioxolene complexes, the present work deals with the synthesis and characterization of polynuclear transition metal complexes with redox-active dioxolene ligands. Due to the presence of multiple redox centers, suchlike complexes offer the possibility for multi-step valence-tautomeric transitions and can therefore be regarded as polymodal molecular switches. In order to examine the ligand bridging mode's influence on the electron configuration, multiple methods for the targeted synthesis of polynuclear dioxolene complexes were developed: the self-organization of small components under appropriate conditions, the utilization of metallacrown fragments as structuring and preorganizing elements and the use of rigid, bis-chelating ancillary ligands. Based on these methods, multifaceted polynuclear complexes were obtained. Single crystal structure determination, spectroscopic and magnetometric measurements on those compounds allowed the exact determination of the possessed oxidation states for dioxolenes and metal ions. For some synthesized cobalt complexes, thermal valence tautomerism above room temperature was observed. Moreover, spectroscopic studies on suitable complexes showed catalytic activity in the oxidation of catechols to *o*-quinones with dioxygen, for which the kinetics could be described by the Michaelis–Menten theory. These polynuclear systems therefore serve as model complexes for the metalloenzymes catecholase and tyrosinase, contributing to the mechanistic understanding of the corresponding biological processes.

für Papa

Contents

List of Figures

List of Tables

Abbreviations

bipy	2,2'-Bipyridine
4,4'-bipy	4,4'-Bipyridine
bispicen	*N*,*N*-Bis(2-pyridylmethyl)-1,2-ethanediamine
bobupimp	2-Benzooxazol-2-yl-4-*tert*-butyl-6-[(2-hydroxy-phenylimino)-methyl]-phenol
cat	Catecholate (general)
$Cr_7NiEtglu$	$[Cr_7NiF_3(Etglu)(piv)_{15}(H_2O)]$
cth	*meso*-5,5,7,12,12,14-Hexamethyl-1,4,8,11-tetraazacyclotetradecane
dabup	4-*tert*-butyl-2,6-bis(((2-hydroxyphenyl)imino)methyl)phenolate
3,5-dbbq	3,5-Di-*tert*-butyl-1,2-benzoquinone
3,5-dbcat	3,5-Di-*tert*-butylcatecholate
3,6-dbcat	3,6-Di-*tert*-butylcatecholate
3,5-dbdiox	3,5-Di-*tert*-butyldioxolene (oxidation state undefined)
dbmpat	4,6-Di-*tert*-butyl-3-(4-methyl-piperidin-1-yl)-catecholate
dbmpsq	4,6-Di-*tert*-butyl-3-(4-methyl-piperidin-1-yl)-1,2-semiquinonate
3,5-dbsq	3,5-Di-*tert*-butylsemiquinonate
3,6-dbsq	3,6-Di-*tert*-butylsemiquinonate
debup	4-*tert*-butyl-2,6-bis(((2-hydroxyethyl)imino)methyl)phenolate
DFT	Density functional theory
dhbq	2,5-Dihydroxy-1,4-benzoquinone
diox	Dioxolene ligand (oxidation state undefined)
DMF	*N*,*N*-Dimethylformamide
EDTA	Ethylenediaminetetraacetic acid
EPR	Electron paramagnetic resonance
ESI	Electrospray ionization
hs	high spin
IR	Infrared (spectroscopy)
LIESST	Light induced excited spin state trapping
LMCT	Ligand-to-metal charge transfer
ls	low spin
4-Mepip	4-Methylpiperidine

MLCT ..... Metal-to-ligand charge transfer
MO ..... Moleculear orbital
MS ..... Mass spectrometry
NIL ..... Non-innocent ligand
NMR ..... Nuclear magnetic resonance (spectroscopy)
o-dppd ..... 1,3-Bis(pyridin-2-yl)propane-1,3-dione
phencat 9,10-phenanthrenediolate
phensq 9,10-phenanthrenesemiquinonate
pip ..... Piperidine
pipycat ..... 3-(4-Piperidino-3-pyridyl)-4,6-di-*tert*-butylcatecholate
piv ..... Pivalate, trimethylacetate
pym ..... Pyrimidine
pyz ..... Pyrazine
QIP ..... Quantum information processing
qubit ..... Quantum bit
shi ..... Salicyl hydroxamate
SMM ..... Single molecule magnet
sol ..... Solvent molecule, solvate
sq ..... Semiquinone (general)
tbcat ..... Tetrabromocatechol
TCNE ..... Tetracyanoethylene
thf ..... Tetrahydrofurane
tmeda ..... Tetramethylethylenediamine
tmmda ..... Tetramethylmethylenediamine
tmpda ..... Tetramethylpropyldiamine
tpa ..... Tris(2-pyridylmethyl)amine
tpbap ..... *N*,*N*,*N*',*N*'-Tetra-2-picolyl-1,4-bis(2-aminoethyl)piperazine
tpom ..... Tetrakis(4-pyridyloxymethylene)methane
VT ..... Valence tautomerism

List of compounds

P1 ..... $[Co_2(OH_2)(piv)_4(Hpiv)_4]$
P2 ..... $[Co(piv)_2]_n$
P3 ..... $[Cu_2(piv)_4(EtOH)_2]$
P4 ..... $[Ni_2(H_2O)(piv)_4(Hpiv)_4]$
P5 ..... $[Ni(piv)_2]_n$
P6 ..... $[Fe_3O(piv)_6(H_2O)_3]piv$
P7 ..... $[Fe_3O(piv)_6(py)_3]$
P8 ..... $[Fe_2CoO(piv)_6(pip)_3]$
L1a ..... Di-*tert*-butylcatechol (3,5-dbcat)
L1b Di-*tert*-butyl-1,2-benzoquinone (3,5-dbbq)
L2 ..... 4-*tert*-Butyl-2,6-diformylphenol
L3 ..... 4-*tert*-butyl-2,6-bis(((2-hydroxyethyl)imino)methyl)phenol (H_3debup)
L4 ..... 4-*tert*-butyl-2,6-bis(((2-hydroxyphenyl)imino)methyl)phenol (H_3dabup)
L5 ..... *N*,*N*'-Bis(cyanomethyl)piperazine
L6 ..... *N*,*N*'-Bis(2-aminoethyl)piperazine
L7 ..... *N*,*N*,*N*',*N*'-Tetra-2-picolyl-1,4-bis(2-aminoethyl)piperazine (tpbap)
L8 ..... 1,3-Bis(pyridine-2-yl)propane-1,3-dione (*o*-dppd)
L9 ..... 3,5-Bis(pyridine-2-yl)pyrazole (Hbpp)
C1 ..... $[Fe_2(H3,5\text{-}dbcat)_2(3,5\text{-}dbsq)_4]$
C2 ..... $[Fe_2(3,5\text{-}dbcat)_2(3,5\text{-}dbsq)_2(py)_2]$
C3 ..... $[Fe_4(OH)_2(3,5\text{-}dbcat)_4(py)_2(piv_2)]$
C4 ..... $[Co(3,5\text{-}dbsq)(3,5\text{-}dbcat)(4\text{-}Mepip)_2]$
C5 ..... $[Co(dbmpsq)(dbmpcat)(4\text{-}Mepip)_2]$
C6 ..... $(Hpip)[Co(tbcat)_2(pip)_2]$
C7a ..... $[Co_3(3,5\text{-}dbsq)_2(piv)_4(NEt_3)_2]$ triclinic, synclinal
C7b ..... $[Co_3(3,5\text{-}dbsq)_2(piv)_4(NEt_3)_2]$ monoclinic, antiperiplanar
C8 ..... $[Co_4(3,5\text{-}dbsq)_4(3,5\text{-}dbcat)(piv)_2(Hpiv)_2]$
C9 ..... $[Co_2(3,5\text{-}dbsq)_2(pipycat)_2(pip)_2]$
C10 ..... $[Cu_6(3,5\text{-}dbsq)4(\ 3,5\text{-}dbcat)_2(piv)_4]$
C11 ..... $[Ni_4(3,5\text{-}dbcat)_2(H3,5\text{-}dbcat)(piv)_2(MeCN)_4]$

C12 ..... $(Hpip)_2[Co_2Fe_2(OH)(3,5\text{-dbcat})_3(piv)_5(pip)]$

C13 ..... $[Co_4(shi)_2(3,5\text{-dbcat})(piv)_2(py)_5]$

C14 ..... $[Co_2^{III}Co_7^{II}(shi)_4(piv)_8(Hpiv)_2(H_2O)_2(py)_4]$

C15 ..... $[Co_2^{III}Co^{II}(sal)_4(py)_4]$

C16 ..... $[Co_6(OH)_2(debup)_2(piv)_8]$

C17 ..... $(HNEt_3)_2[Co_6(CO_3)(dabup)_3(piv)_3]$

C18 ..... $[Co_4(OH)_2(dabup)(bobupimp)(piv)_3]$

C19 ..... $[Cu_4(3,5\text{-dbcat})_2(bobupimp)_2(acetone)_2]$

C20 ..... $[Co_6(CO_3)(bpp)_3(H3,5\text{-dbcat})_4(piv)_3]$

C21a ..... $[Co_2(tpbap)(3,5\text{-dbcat})_2](SO_4)$

C21b ..... $[Co_2(tpbap)(3,5\text{-dbcat})_2](ClO_4)_2$

1 Introduction

> *In fact, it is often stated that of all the theories proposed in this century, the silliest is quantum theory. Some say that the only thing that quantum theory has going for it, in fact, is that it is unquestionably correct.*[1]
>
> — **Michio Kaku**
> *Hyperspace* (1995)

1.1 Quantum Computers

Most of the things of our surrounding we know from childhood can be described by classical physics. When we for example see a ball on the floor, we can exactly state the position and size of the ball. We know how it feels like and we are able to determine the pressure of the air inside. When a ball is tossed, no child is wondering about the parabolic trajectory, simply because everybody is used to this and has experienced this behavior innumerable times before.

Things are different at a nanoscopic scale. Because we cannot see single atomic or subatomic particles or touch them with our hands, quantum mechanical phenomena often seem kind of magical to us. Even notable physicists like Richard Feynman have to confess their lack of knowledge concerning quantum mechanics. ("I think I can safely say that nobody understands quantum mechanics."[2]) Although not quite intuitive, quantum theory is much more fundamental and accurate than classical physics.[1] Since the Copenhagen interpretation from around 1927, quantum mechanics has had enormous success in explaining experimental findings. Not only the behavior of single subatomic or atomic particles is accurately described, but also the assembly of multiple particles to molecules and thus materials is theoretical subject

[1] Indeed, classical physics can be considered as an approximation of quantum physics for large numbers of particles (decoherence).

of quantum chemistry. Quantum effects have significant impact on the invention of modern technology. Notable examples are the laser, the electron microscope, MRI imaging or the transistor, without which all kinds of modern electronics would not exist. However, the mathematical formalism of quantum theory is rarely used during the invention or development and only indirectly applied. To date there are hardly any *direct* applications of quantum mechanics.

One attempt to directly utilize quantum physical states is the development of quantum computers. Such a device is based on the quantum physical phenomena superposition and entanglement, uses quantum bits instead of classical bits and will be able to process certain computations exponentially faster than classical computers. Today, quantum computers are predominantly theoretical devices, only single laboratory experiments have been carried out using a very limited number of qubits as a proof of concept.[3,4] The theoretical investigation of this novel type of computation mainly stems from two recent developments: On one hand, according to Moore's Law, electronic parts are getting smaller every year.[5] If the rate of miniaturization was more or less constant, atomic size could be achieved around the year 2020. The more the size of electronic parts converges to atomic scale, the more important quantum effects become. On the other hand, there is an urgent need for computers that can perform operations which are not accessible to conventional computers. Some of the most important application areas would be the safe encryption of data, teleportation of information, the generation of real random numbers or the decryption of nowadays "safe" encryption methods. The unique capabilities of quantum computers allow for the use of algorithms (e.g. Lov Grover algorithm) which will provide up to exponential speedup for certain operations. Such an increase in calculation power could also significantly enhance database inquiries, route-finding processes or the simulation of quantum many-body systems.[6]

While classical computers take use of bits which can represent either 0 or 1, quantum computers are based on quantum bits (so-called *qubits*). Those qubits can not only represent the states $|0\rangle$ or $|1\rangle$ but also any quantum superposition of these two states.

$$\alpha|0\rangle + \beta|1\rangle \tag{1.1}$$

with

$$|\alpha|^2 + |\beta|^2 = 1 \tag{1.2}$$

A quantum computer with n entangled qubits thus can simultaneously be in any arbitrary superposition of 2^n states. Normal computers with the same number of bits can only possess *one* of these 2^n states at a time. Transformations of qubits are performed with so-called quantum gates. A sequence of certain quantum gates, a quantum algorithm, can perform a calculation on these 2^n states at once, but result in a defined set of n pure $|0\rangle$ and $|1\rangle$ qubits.

For the realization and scalability of quantum computers, possible qubits have to meet certain requirements, the so-called DiVincenzo criteria:[7,8]

1. The qubits need to be well-defined quantum systems with two energetically separated states, e.g. a $S = \frac{1}{2}$ system.
2. The preparation of the initial state needs to be easy and reliable.
3. The system needs to exhibit low decoherence.
4. Quantum gate operations (transformations) may be applied accurately.
5. Single qubits need to allow read-out processes.

In search of possible qubits fulfilling these requirements, various microscopic systems have proven as promising candidates for the use in quantum computers, for example atoms or ions in traps, nuclear spin, photons or spin-based systems like electrons.[9] Latter ones are of particular interest and importance, as an isolated electron is a true two-level system ($m_s = \pm\frac{1}{2}$). Moreover, electrons can easily be "localized" using organic radicals or open-shell metal-containing systems as carriers, such as transition metal complexes. To perform logical operations in the sense of quantum information processing (QIP), one additionally needs to arrange qubits in a certain manner to form quantum gates. For this purpose, the "bottum-up" approach using applied chemistry can be seen as a major chance. Especially coordination chemistry can be very helpful in the design of novel qubits, as the arrangement of unpaired electrons within a molecule is easily controlled by building suitable ligands, using appropriate metal ions or choosing a certain type of bonding. The molecular qubits' properties can thus be tuned very rationally. Furthermore, an upscaling of the desired qubits or quantum gates is very easy as all molecules are perfectly

identical.[10] It has to be noted, that a qubit does not necessarily have to be based on a $S = \frac{1}{2}$ system. When two well separated states are found in a certain energy regime, an *effective* $S = \frac{1}{2}$ system is present, which also may fulfill the DiVincenzo criteria.[10]

1.1.1 Molecular Systems as Qubits

From a chemist's point of view, molecules are ideal candidates for the practical development of qubits. Applying common synthetic procedures in combination with a chemist's skill and creativity, tailor-made molecular architectures can be created to fulfill the qubit's requirements. Among the most promising approaches toward molecule-based qubits are molecular (nano)magnets. While there have been proposals about the use of high-spin single molecule magnets (SMMs) for the implementation of certain quantum algorithms using multiple m_s states,[11] the more common approach includes low-spin magnetic clusters.[12] The increased size of suchlike clusters compared to single ions or isolated electrons makes an individual addressing of single qubits and read-out processes more amenable and practicable. Early examples for magnetic molecules used as prototypical qubits are the Cr_7Ni rings with dominant antiferromagnetic couplings.[12–14] Those clusters were

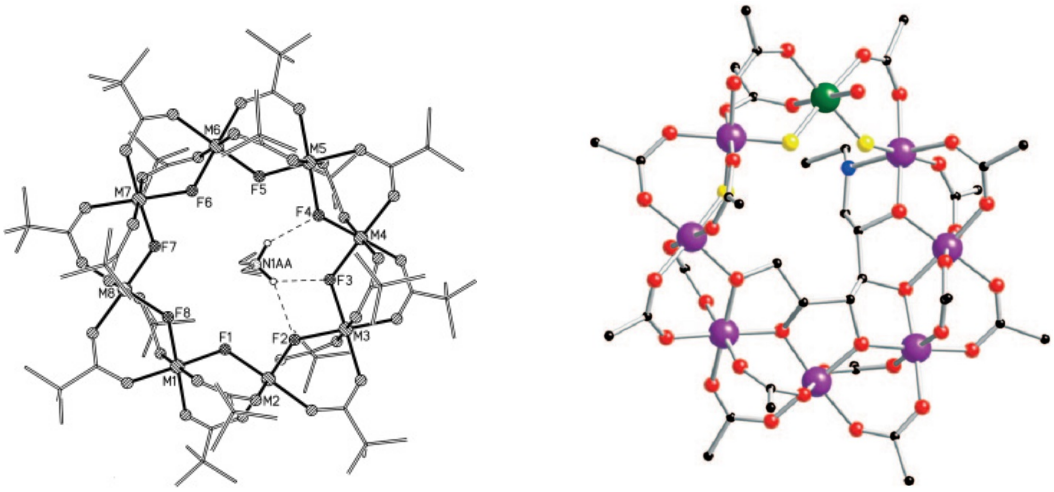

(a) Molecular structure of $[Et_2NH_2Cr_7NiF_8(piv)_{16}]$ (Cr_7Ni)[13]

(b) Molecular structure of $[Cr_7NiF_3(Etglu)(piv)_{15}(H_2O)]$ ($Cr_7NiEtglu$)[14]

Fig. 1.1: Cr_7Ni wheels with isolated $S = \frac{1}{2}$ ground state

found to exhibit an isolated $S = \frac{1}{2}$ ground state, which is accessible for quantum information storage and processing.[12,15] The decoherence times in these systems

are identified to be mainly dependent on hyperfine coupling of the electron spin with nuclear spins.[16] One main strategy to increase decoherence times was thus to decrease the numbers of hydrogen atoms, for example by perdeuteration. For the perdeuterated $[Et_2NH_2Cr_7NiF_8(piv)_{16}]$ for example the decoherence time in the order of microseconds is already sufficient for spin manipulations but still leaves room for further tuning.[17]

To enable the required entanglement the attachment of suitable bridging ligands can provide weak magnetic exchange coupling between the single spin-clusters. For the Cr_7Ni rings, this has been shown for a large variety of different organic and metallorganic bridges with adjustable coupling strength, which linked two or more $S = \frac{1}{2}$ fragments to larger, supramolecular arrangements.[14,17–21]

More recently, Minkin et al. were able to show on the basis of DFT calculations, that also dinuclear cobalt complexes with redox-active bis-dioxolenes may serve as 2-qubit quantum gates.[22] Switching of the qubits is in this case based on valence tautomeric transitions, which can be thermally triggered or controlled by light (see section 1.3). These novel findings enable the expansion of research into a whole

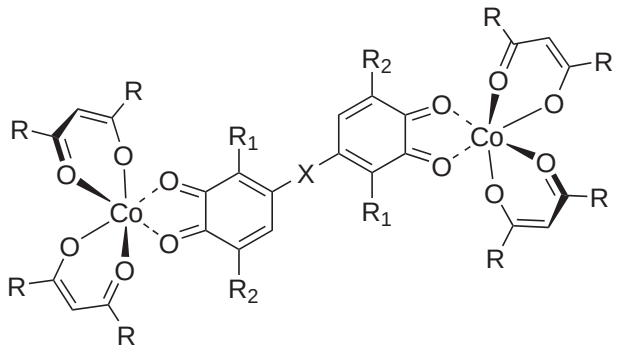

Fig. 1.2: Proposed 2-qubit quantum gates based on valence tautomerism[22] (R = H, CF_3; $R_1 = R_2$ = H, Alk; X = none, HC=CH, H_2C-CH_2, piperazindiyl)

new area. The extensive experiences and knowledge collected for other applications of valence tautomeric complexes can now be used for the targeted design of qubits and quantum gates. However, the predictions made about possible dioxolene based quantum gates are of computational nature and thus need to be considered with care. Experimental confirmations of Minkin's claim are still ongoing and this work represents one contribution to this intention.

1.2 Toward Molecular Switches

After this rather specialized section about quantum computing and suitable molecular materials for this purpose, the following section will give general information about switchable molecules and molecules which are stable in more than one state.

The quest of the scientific community for molecular materials suitable for technological applications has never been more active than today. Molecular systems are particularly attractive due to the feasibility of chemical fine-tuning which allows for tailor-made applications. Chemical ingenuity can offer the rational creation of a manifold of novel materials with uncharted physical properties.[23] An upscaling can simply be achieved by a replication of perfectly identical molecules. Additionally, molecular sizes allow a miniaturization of the resulting technologies. Among many classes of molecular systems, molecules that can exist in two different electronic states depending on external parameters are most interesting for possible technological applications, as they can react on the environment and thus can serve as molecular electronic devices. As outlined in 1.1.1, those switchable molecules can also be considered as building blocks for molecular qubits, permitting the development of a whole new research area. The group of molecules for which these properties are found are called *electronically labile* compounds.[24]

1.2.1 Electronically Labile Molecules

Electronically labile molecules show electronic structures which are very much dependent on external stimuli such as changes in temperature or pressure, (light) irradiation or chemical triggers. The most important examples of suchlike molecules are those that exhibit *mixed-valence*, *spin crossover* or *valence tautomerism*. Those compounds are valuable research objects for the study and understanding of intramolecular electron transfer, conductivity, magnetism or related phenomena.[25] Beside their purpose as test-ground for physical properties, electronically labile materials arouse technological interest for the application as sensors,[26] information storage devices or in the field of molecular electronics.[27–29]

1.2.1.1 Mixed Valence

Mixed valent compounds typically consist of two or more metal ions with different oxidation states bridged by an organic linker, but also organic mixed valent systems have been reported.[30–38] In these mixed valent compounds, an intramolecular, ligand-mediated electron transfer between the redox centers can occur. Depending on the degree of interaction between the metal centers via the bridging ligand(s), mixed valent complexes with two redox centers in an identical coordination environment are divided into three classes (Robin–Day classification scheme, see fig. 1.3).[39] If no interaction of the redox centers is possible (e.g. for long metal-metal

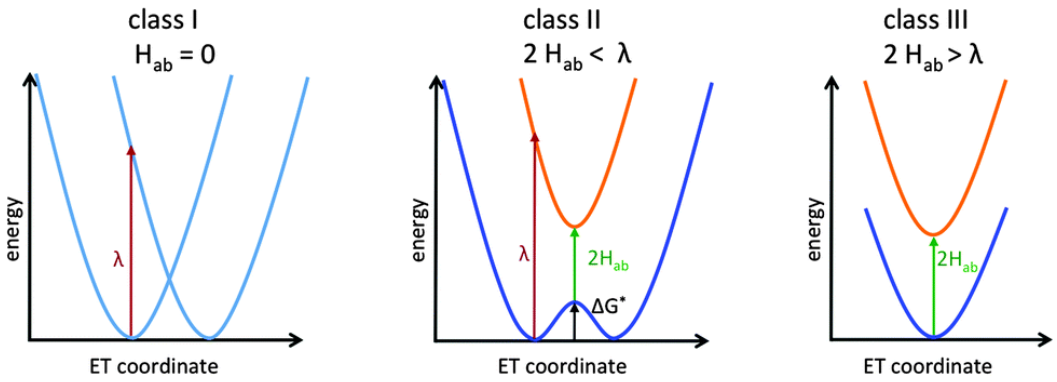

Fig. 1.3: Potential curves for the three Robin–Day classes: class I (left), class II (middle) and class III (right).[40] $2H_{ab}$: electronic coupling; λ: Marcus reorganization energy; ΔG^*: free energy electron transfer barrier.

distances and/or aliphatic ligands), the complex is assigned to **class I**. The valence electrons are completely localized and the assignment of the oxidation states is unambiguous. Such class I complexes only show the properties of their isolated centers. **Class II** mixed valent compounds exhibit weak electronic interactions, leading to a double well ground-state potential curve with a barrier for thermal electron transfer (see fig. 1.3, middle). This coupling has influence on the redox centers' character so that other properties than those of the isolated centers are observed. In this special case, a particular valence state can be trapped and localization occurs if the thermal energy is not sufficient to overcome the barrier ΔG^*. Furthermore, intervalence electronic transitions are spectroscopically observed. **Class III** complexes are completely delocalized due to very strong electronic coupling and the oxidation states are indistinguishable.

1.2.1.2 Spin Crossover

Spin crossover refers to a change of the spin state of transition metal complexes with electron configurations d^4 to d^7 due to external stimuli such as temperature changes, pressure, light irradiation or magnetic fields. Depending on the ligand field

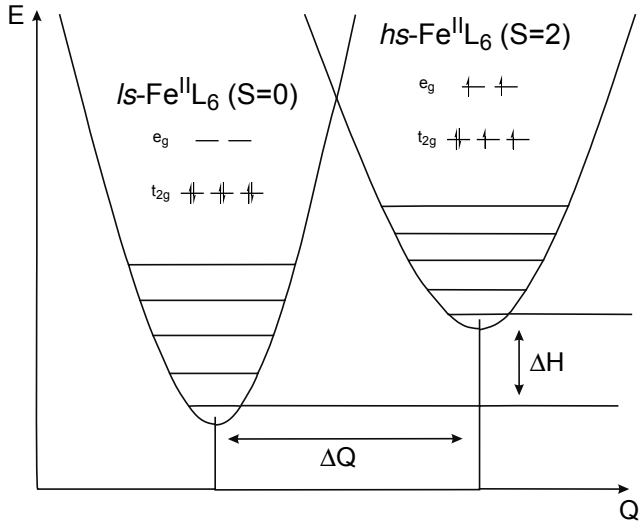

Fig. 1.4: Potential curves for spin crossover transitions[41]

strength, those ions can possess a low spin or a high spin state. If the magnitude of the ligand field splitting is in the order of the spin pairing energy, a transition from *ls* to *hs* or vice versa can be observed. For a thermally induced spin transition, a major requirement is a small change in enthalpy $\Delta H°$ but a large change in entropy $\Delta S°$ of the same sign.[42] For many complexes, this is ensured by large differences in bond lengths for low spin and high spin states. Numerous examples of spin crossover complexes are based on Fe^{II}, which entropically prefer *hs*-Fe^{II} at high temperatures and *ls*-Fe^{II} at low temperatures. Additionally, light induced trapping of metastable excited spin states has been found at low temperature (light induced excited spin state trapping = LIESST).[43] Irradiation into d-d or MLCT absorption bands may lead to a spin allowed transition to an excited state (e.g. $^1A_1 \longrightarrow {}^1T_1$), followed by two successive intersystem crossing processes to reach the $^5T_2$ *high spin* state, which is trapped at low temperatures.[44]

The third type of electronically labile complexes are those which exhibit intramolecular metal-ligand electron transfer combined with spin state transitions. As it is a main part of this dissertation, section 1.3 is dedicated to a complete examination of this phenomenon.

When these types of bistable compounds exhibit thermal hysteresis, non-volatile memories can be realized. This effect, based on cooperative intermolecular interactions, enables the use of electrically labile materials for molecular switching and information storage.

1.3 Valence Tautomerism

1.3.1 General Consideration and Prerequisites

The third reason for electronic lability in metal complexes is valence tautomerism. Valence tautomerism is referred to the phenomenon of temperature induced switching of electronic ground states in molecules of the general type $A-D^+$ (A: acceptor, D: donor).[45] Due to intramolecular electron transfer (combined with the formation or rupture of single and/or double bonds), two or more valence tautomers with different charge distributions can be identified and the following equilibrium is found.

$$A-(D^+) \rightleftharpoons (A^+)-D \tag{1.3}$$

To allow valence tautomeric transitions, several conditions must be met in general.[46] First of all, the involved donor and acceptor orbitals need to be energetically similar. Additionally, the intramolecular electronic coupling needs to be sufficiently strong to allow electron transfer. However, if the coupling is too strong, the discrete electronic structures are lost due to complete delocalization and mixing of orbitals. Similar to spin crossover transitions or other entropy-driven equilibria, the electron transfer needs to be accompanied by structural changes with contributions to ΔH and ΔS of the same sign (see section 1.3.4).

Usually, different valence tautomers can be distinguished easily due to distinct properties. These can be of chemical, spectroscopic, magnetic or physical nature, depending on the character of the different electron distributions.

Very early examples for valence tautomerism include mostly organic molecules. Among the most prominent or at least the oldest ones are the valence tautomeric equilibrium of 1,3,5-cyclooctatriene and bicyclo[4.2.0]octa-2,4-diene[47] (see fig. 1.5) or other cyclic polyenes which can undergo electrocyclic reactions or other types

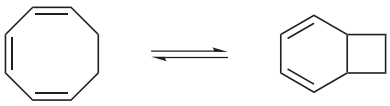

Fig. 1.5: Valence tautomeric equilibrium for 1,3,5-cyclooctatriene and bicyclo[4.2.0]octa-2,4-diene[47]

Fig. 1.6: Bullvalene

of pericyclic rearrangements. A famous example with many degenerate valence tautomers is bullvalene (fig. 1.6).

Since 1980, transition metal complexes which exhibit valence tautomerism came into the focus of research.[48] These complexes are based on redox-active metal ions such as cobalt, manganese or copper coordinated by redox-active or so-called “non-innocent ligands” (short: NIL). In this case of complex-based valence tautomerism eq. (1.3) can be written more precisely.

$$(NIL)^{x}M^{y}L_{n} \rightleftharpoons (NIL)^{x-1}M^{y+1}L_{n} \tag{1.4}$$

1.3.2 Dioxolene Ligands and other Non-innocent Ligands

In the year 1966 Jørgensen coined the term “non-innocent ligands” (or “suspect” ligands) by using the following definition: “Ligands are innocent when they allow oxidation states of the central atoms to be defined.”[49] While some ligands are unequivocally charge-defined (e.g. H_2O, NH_3 or Cl^-), for non-innocent ligands an unambiguous[2] assignment of physical oxidation states of the central ions is not possible.[50] This can be valid for redox-active ligands with frontier orbitals, which are of similar energy as the metal frontier orbitals. Hence, an intramolecular electron transfer from the ligand to the metal ion or vice versa may occur. As this ability strongly depends on an interplay of ligands with the metal ions, non-innocence is not only a property of the ligand, but of the complex as a whole. The wording "non-innocent ligand" is misleading in this respect. The effect of non-innocence is more general than valence tautomerism, as there is no need for localized valences and a resonance situation may also describe the coordination (compare with eq. (1.4)).

$$(NIL)^{x}M^{y}L_{n} \longleftrightarrow (NIL)^{x-1}M^{y+1}L_{n} \tag{1.5}$$

[2] It has to be noted that with modern techniques, a determination of electron distributions is almost always possible. However, the prediction of physical oxidation states for non-innocent ligands in contrast to formal oxidation states is rarely trivial.

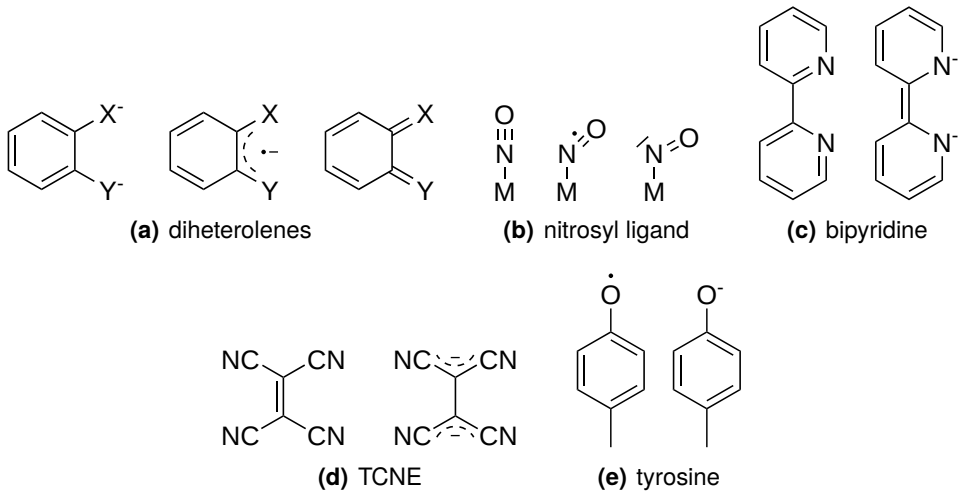

Fig. 1.7: Typical non-innocent ligands known from literature

Typical non-innocent ligands are depicted in fig. 1.7 and include the redox systems dioxygen O_2/superoxide $O_2^{\bullet -}$/peroxide O_2^{2-}, nitrosyl cation NO^+/nitric oxide radical $NO^\bullet$/nitroxide anion NO^-, dioxolenes, dithiolenes, 1,2-diimines or pyridine-2,6-diimine ligands as well as their derivatives.[50,51] In most cases, conjugated π systems are involved which are capable of either accepting or donating electrons.

The ability for ligand-based redox-activity equips non-innocent metal compounds with attractive properties. Complexes bearing non-innocent ligands often exhibit redox processes at mild potentials. Usually, oxidation or reduction reactions involve a structural change due to the oxidation of the non-innocent ligand whereas the oxidation state of the central metal remains constant (ligand-based redox activity). This property is of great importance for example in many biocatalytic processes mediated by metalloenzymes with non-innocent ligands, e.g. galactose oxidase.[52,53] Galactose oxidase is capable of oxidizing primary alcohols into aldehydes using molecular oxygen O_2 and releasing H_2O_2. The proposed catalytic mechanism of galactose oxidase (see fig. 1.8) involves a cysteine-modified tyrosyl radical as a non-innocent ligand. After the coordination of a primary alcohol as a substrate, an α-hydrogen is transfered from the alcoholate to the tyrosyl radical. Intramolecular electron transfer to the redox-active ligand enables the release of the aldehyde. Subsequently, two concerted 1 e^- oxidations of the tyrosine and the Cu^I regenerate the active catalyst species with its radical cofactor.

Among those non-innocent ligands which are best-known and attained most scientific interest, especially in the context of valence tautomerism, are dioxolene ligands.

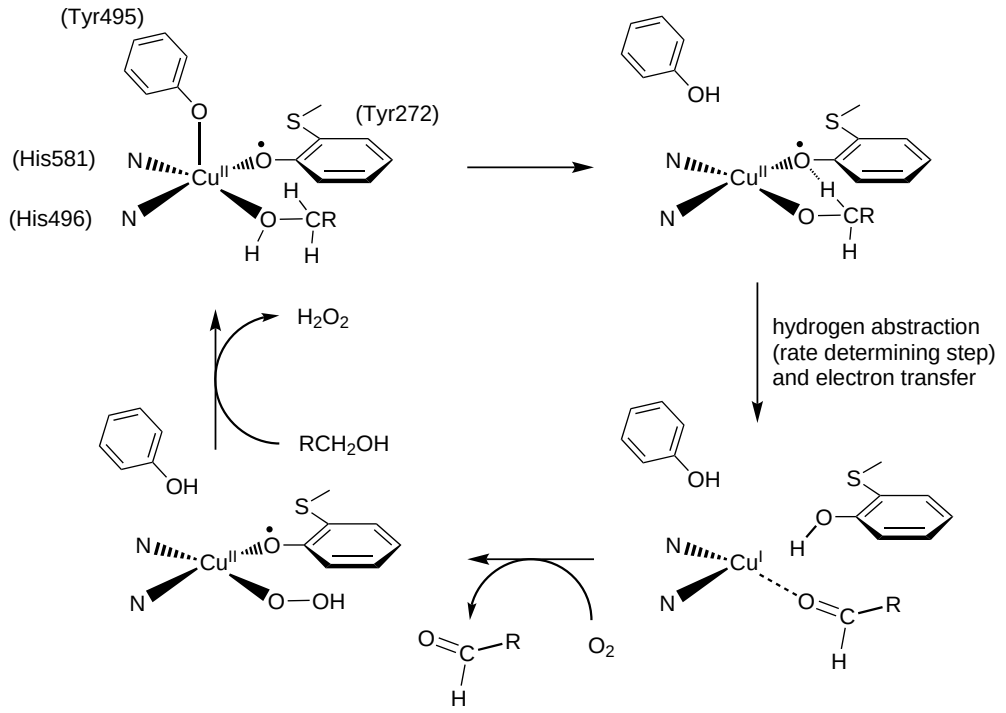

Fig. 1.8: Proposed mechanism for galactose oxidase[52,53]

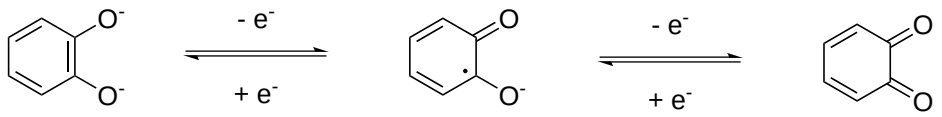

Fig. 1.9: The three members of the dioxolene redox series (catecholate, semiquinonate, quinone)[54]

This unique redox system can possess the oxidation states of a dianionic catecholate (1,2-benzenediolate), the monoanionic radical 1,2-benzosemiquinonate, and the uncharged 1,2-benzoquinone. Usually, their bonds to the metal ions have a low covalent character, which leads to well-defined charge-distributions and a low amount of delocalization.[55] This property makes dioxolene ligands promising candidates for the design of valence tautomeric complexes (see fig. 1.10). Some very common and frequently used dioxolene-type ligands are the substituted dihydroxybenzenes 3,5-di-*tert*-butyl catechol, 3,6-di-*tert*-butyl catechol, tetrachlorocatechol and tetrabromocatechol. Using steric effects as well as the absence of reactive hydrogen atoms in the aromatic ring, the corresponding semiquinonates are kinetically stabilized, which simplifies the isolation and characterization of semiquinonate complexes.

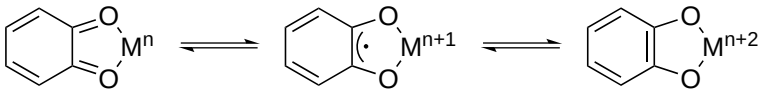

Fig. 1.10: Valence tautomers based on dioxolene ligands

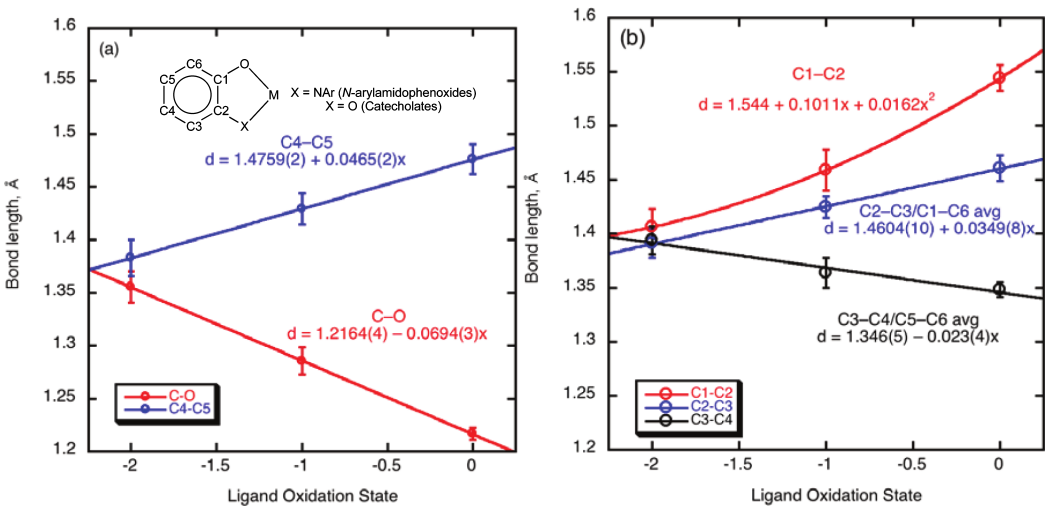

Fig. 1.11: Correlations of bond distances in catecholates with ligand oxidation state[56]

The significant structural changes which are observed for valence tautomeric transitions allow for an exact determination of charge distribution within the complexes. A very potent method for the assignment of (ligand) oxidation states is the analysis of bond lengths gained from crystallographic measurements. For the transition from a catechol to a semiquinone, C−O bonds are getting shorter due to a partial double bond character. In addition, all C−C bonds in catecholates are very similar (around 1.40 Å) whereas an alternating bond length pattern is found for semiquinones or quinones. M−O bond lengths can also be taken into account but strongly depend on the choice of metal ion. To quantify the analysis of dioxolene bond lengths, Brown established a set of correlations between intra-ligand bond distances and the ligand oxidation state based on a large collection of dioxolene complexes known from literature.[56] Using a least squares routine, a so-called “metrical oxidation state” can be calculated when structural data is available. The applied correlations are shown in fig. 1.11.

Due to the paramagnetic character of the dioxolene ligands, another method for the evaluation of the dioxolene redox state is EPR spectroscopy. In the case of negligible magnetic coupling to the central metal ion, g-values of about $g = 2.00$ are observed, which is typical for organic radicals such as semiquinones.[54] For this reason the complex $[Ru(3,5\text{-dbsq})(bipy)_2]^+$ exhibits a g-value of $g = 2.003$. Contrastingly, for its higher homologue $[Os(3,5\text{-dbcat})(bipy)_2]^+$ the EPR spectrum shows $g_1 = 2.448$ and $g_2 = 1.71$. These signals are typical for the rhombic structure of low spin Os(III). Thus, the ligand oxidation state of a dianionic catecholate can be assigned. Susceptibility measurements additionally provide easy access to the

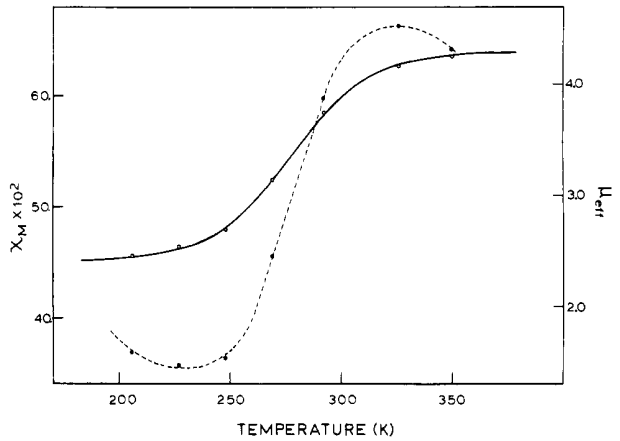

Fig. 1.12: Solution susceptibility (dotted line, $\chi_M \cdot 10^4$ in $cm^3\ mol^{-1}$) and magnetic moment (solid line, μ_{eff} in μ_B) of [Co(3,5-dbsq)$_2$(bipy)], obtained in toluene-d^8 by the Evans method[48]

overall magnetic moment of dioxolene complexes. Using temperature dependent measurements on [Co(3,5-dbsq)(3,5-dbdiox)(bipy)] (see fig. 1.12) Buchanan and Pierpont were able to observe valence tautomerism for dioxolene complexes for the first time.[48] Moreover, exchange interactions of semiquinonates with paramagnetic metal ions can be examined.

Electronic spectroscopy can be used to visualize charge transfer transitions. More information can be accessed in temperature dependent optical spectroscopy for which valence tautomeric conversions can be observed as a transition with several isosbestic points.[24]

Other methods for the characterization of dioxolene complexes include infrared or Raman spectroscopy, electrochemical methods, as well as NMR spectroscopy on diamagnetic catecholates.

1.3.3 Simplified Molecular Orbital Description

For the understanding of valence tautomeric conversions in dioxolene complexes, knowledge about the interplay of the involved molecular orbitals is necessary. Taking [M(diox)$_2$(bipy)] as an example, the π^* orbitals are singly occupied in the case of a semiquinone and doubly occupied for a catecholate. The metal t_{2g} orbitals possess the right symmetry for a π overlap with ligand π^* orbitals. Additionally, e_g orbitals can form σ-bonds with the dioxolene oxygen lone pair electrons (see fig. 1.13(a)).[25] The π^* orbitals are higher in energy than the t_{2g} orbitals and the mixing of metal and

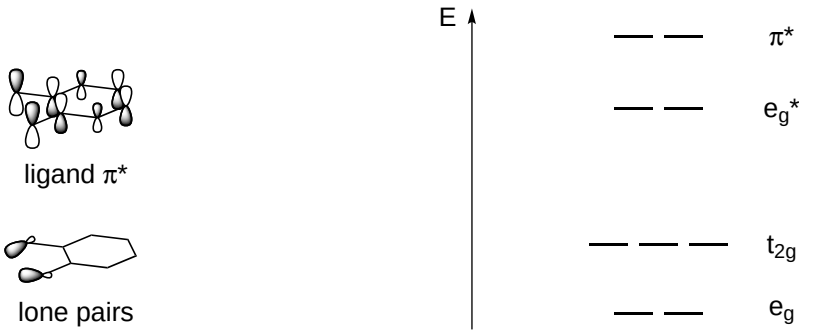

(a) Involved ligand orbitals

(b) Simplified scheme of the energetic sequence of molecular orbitals for M(diox)$_2$(N−N) type complexes. The small gap between the metal-based frontier orbitals (t_{2g} and e_g^*) allows spin crossover. The close energy spacing between metal-based π-bonding (t_{2g}) and ligand-based π-antibonding orbitals (π^*) permits valence tautomeric electron transfer.

Fig. 1.13: Simplified molecular orbital description for M(diox)$_2$(N−N) type complexes

ligand orbitals is rather weak. Therefore, the resulting set of π-bonding molecular orbitals retains metal-based (t_{2g} character), whereas the π-antibonding orbitals are ligand-based. Contrastingly, the lone pairs are low-lying and the e_g orbitals are higher in energy, leading to ligand-based σ-bonding MOs (e_g) and metal-based σ^* antibonding MOs (e_g^*). The resulting relative frontier orbital energies are shown in fig. 1.13(b). This fortunate sequence of orbitals meets the requirements for thermally induced electron transfer from the ligands to the metal ions or vice versa because of the close energy spacing of orbitals with metal- and ligand character as well as for simultaneous spin state transition. The involvement of antibonding orbitals further explains the changes in M−O and ligand bond lengths. More in-depth molecular orbital descriptions can be made using spin-unrestricted calculations as a basis,[57] which would exceed the intention of this section.

1.3.4 Thermodynamics of Valence Tautomeric Transitions

As already mentioned in the sections 1.2.1 and 1.3.1, thermodynamics play a key-role in the valence tautomeric equilibrium. For both tautomers to be thermally accessible, $\Delta H°$ needs to be in the order of kT. As the M−O-bonds for the *ls*-Co^{III} tautomer are stronger (less electron density in antibonding e_g orbitals) than for the *hs*-Co^{II} tautomer (occupied σ^* orbitals), the enthalpy for the equilibrium [Co^{III}(sq)(cat)(bipy)] $\rightleftharpoons$ [Co^{II}(sq)$_2$(bipy)] needs to be positive.

The change in entropy for valence tautomeric transitions can be estimated by the sum of electronic and vibrational contributions.

$$\Delta S^\circ = \Delta S_{el} + \Delta S_{vib} \tag{1.6}$$

The electronic contribution is primarily determined by the degree of electronic degeneracy, which is larger for the *hs*-Co^{II} tautomer. Due to the dioxolene mixed valence a degeneracy of 4 results for the contemplated tautomer [Co^{III}(sq)(cat)(bipy)], whereas spin coupling for the Co^{II} tautomer leads to a sextet ($S = \frac{5}{2}$), two quartets ($S = \frac{3}{2}$) and a doublet ($S = \frac{1}{2}$), and thus to an electronic degeneracy of 16.[25] ΔS_{el} can then be calculated.

$$\Delta S_{el} = R \ln \frac{g_{hs}}{g_{ls}} = R \ln \frac{16}{4} \approx 3\,\text{cal}\,\text{K}^{-1}\,\text{mol}^{-1} \tag{1.7}$$

The contribution of ΔS_{vib} typically is more important. Resulting from the occupation

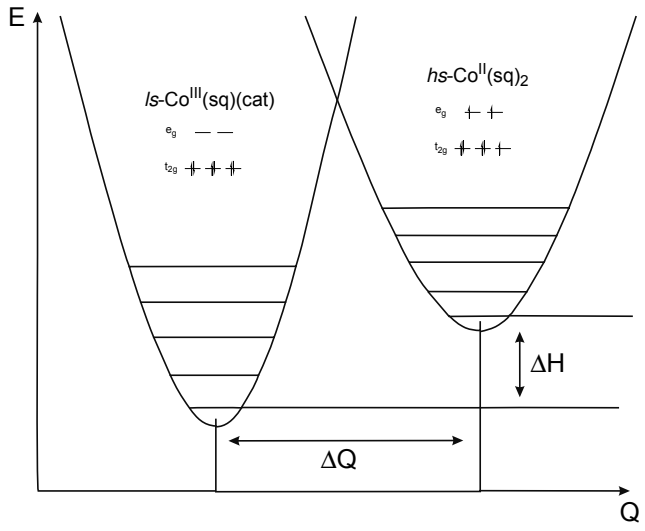

Fig. 1.14: Potential curves for valence tautomeric transitions[58]

of the antibonding σ^* orbitals and thus weaker bonds, the Co^{II} tautomer has a higher density of vibrational energy levels, which is the origin for the increased entropy. The exact vibrational contribution to the change in entropy can be calculated involving the vibrational partition functions $\prod(1 - \exp(-\nu/RT))$:

$$S_{vib} = R \ln \left[\frac{\prod(1 - \exp(-\nu_{ls}/RT))}{\prod(1 - \exp(-\nu_{hs}/RT))} \right] \tag{1.8}$$

Typically, ΔS_{vib} is in the order of 22 $\text{cal}\,\text{K}^{-1}\,\text{mol}^{-1}$, which corresponds to an enormous increase in vibrational frequencies for the Co^{III} tautomer, which is also experimentally

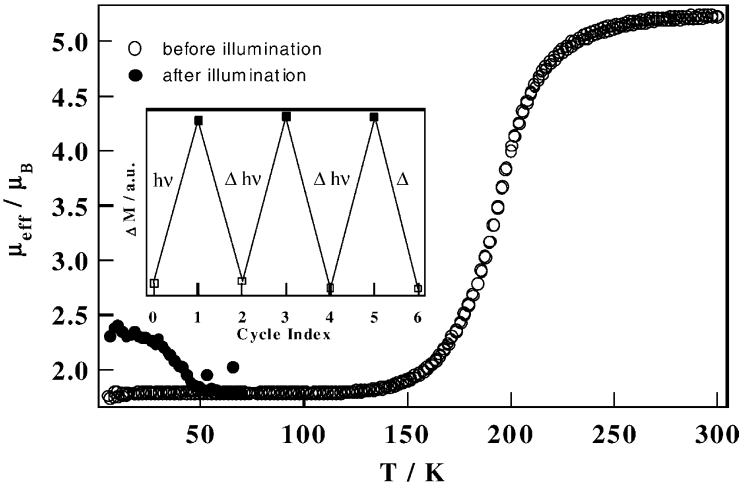

Fig. 1.15: μ_{eff} vs. T plots before and after illumination of [Co(3,5-dbsq)(3,5-dbcat)(tmeda)] $\cdot$ 0.5 $C_6H_5CH_3$[60]

found. Given these facts, the requirements discussed in section 1.2.1 (both positive $\Delta H°$ and $\Delta S°$) are met.

The thermodynamic parameters $\Delta H°$ and $\Delta S°$ can often be experimentally measured. Using for example temperature dependent magnetic or optical data, the molar fraction of the tautomers as a function of temperature $x = f(T)$ can be calculated. As this fraction is dependent on the thermodynamic parameters, $\Delta H°$ and $\Delta S°$ can be extracted.

$$x = \left[\exp\left(\frac{\Delta H°}{RT} - \frac{\Delta S°}{R} \right) + 1 \right]^{-1} \tag{1.9}$$

1.3.5 Dioxolene Complexes Showing Light-induced Valence Tautomerism

For the use of valence tautomeric complexes in future devices and technological applications, the ability for light-induced conversions is advantageous. First progress for this purpose has been made by conducting transient absorption studies, which proved that LMCT excited states can be generated by irradiation into the corresponding charge transfer band with a pulsed laser.[24] However, a fast Arrhenius-type relaxation in the order of nanoseconds was observed. For applications, a metastable excited state with reasonable lifetimes would be desirable. Indeed, several valence tautomeric complexes have been found, which show this property of excited valence tautomeric states with decay lifetimes in the order of 10×10^6 s at 10 K.[58–77]

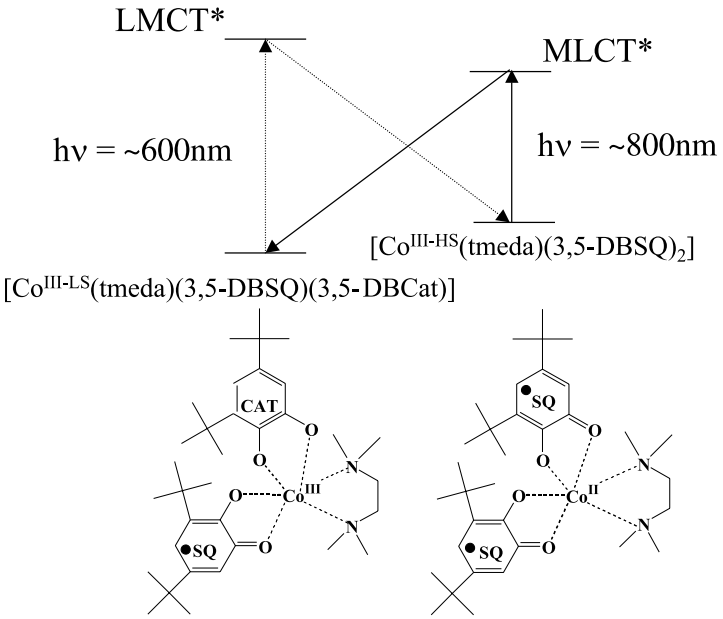

Fig. 1.16: Simplified Jablonski-type energy-level diagram for [Co(3,5-dbsq)(3,5-dbcat)(tmeda)] · 0.5 $C_6H_5CH_3$[59]

A typical example for a complex exhibiting a photo-induced valence tautomeric transition is [Co(3,5-dbsq)(3,5-dbcat)(tmeda)] · 0.5 $C_6H_5CH_3$.[60] The plot of the magnetic moment as a function of temperature shown in fig. 1.15 shows the characteristic step-like gradient at about 200 K, which is caused by thermal valence tautomeric conversion from the Co(II) bis-semiquinonate to the Co(III) semiquinonate at decreasing temperature. At 5 K, the sample was then illuminated with a green laser (λ = 532 nm), resulting in an increase of the magnetic moment. Corroborated by optical spectroscopy at low temperature, this effect was assigned to the generation of the charge transfer product [Co(3,5-dbsq)$_2$(tmeda)] · 0.5 $C_6H_5CH_3$. The lifetimes at 5 and 15 K are 175 and 70 min, respectively.[60] Figure 1.15 further shows the change of the magnetic moment after irradiation on warming. At 50 K the excited state completely relaxes back to the Co(III) tautomer. In some cases it is also possible to switch between the two tautomers by using light sources with different wavelengths and irradiating into the corresponding MLCT or LMCT bands. This effect is also observed for the latter complex for which the simplified Jablonski diagram is shown in fig. 1.16.

1.3.6 Biological Impact of Dioxolene Compounds

Due to their ubiquity in nature, their unique redox-activity and their excellent chelating properties (formation of five-membered rings with metal ions), the biological relevance of dioxolene ligands is obvious. Important examples include siderophoric iron transport, catecholamines as neurotransmitters or the presence and function of polyphenols in plant tissues (e.g. tannins).[54] In the context of this work, special attention has to be paid to metalloenzymes, where the non-innocence of dioxolene-type molecules plays an essential role. This attribute has been discussed for specific iron and copper enzymes, including catechol dioxygenases or catechol oxidases and tyrosinases.

1.3.6.1 Enzymatic Catechol Dioxygenation

Iron-containing catechol dioxygenases are responsible for catechol ring cleavage. This class of metalloenzymes can be divided into two groups, the intradiol or 1,2-dioxygenases and the extradiol or 2,3-dioxygenases, depending on the position of the oxidative cleavage of the catechol rings (see fig. 1.17(a)). For both classes of proteins, spectroscopic studies were conducted and model complexes were synthesized, which allowed an in-depth analysis of the catechol oxidation. Proposed mechanisms are shown in figs. 1.17(b) and 1.17(c). These findings clearly show the importance of the non-innocent character of catechol for the catalytic cycles in both cases, as the activation of the substrate is accomplished by intramolecular electron transfer to the central iron ion. The dioxolene then has a partial radical character which allows the attack of molecular or iron-bound oxygen to initiate the oxidative cleavage. In addition, also the dioxygen is activated in this way for extradiol oxygenases.

1.3.6.2 Enzymatic Catechol Oxidation

Beside the dioxygenase enzymes, which oxidatively cleave catechol rings, another important group of proteins for the oxidation of catechols are the catechol oxidases and tyrosinases. Both enzymes catalyze the aerobic oxidation of 1,2-dihydroxybenzenes to the corresponding *o*-quinones (see fig. 1.18).[3] The resulting quinone derivatives can then auto-polymerize to yield natural pigments like melanin, which

[3] In addition, tyrosinase catalyzes the monooxygenation of monophenols.

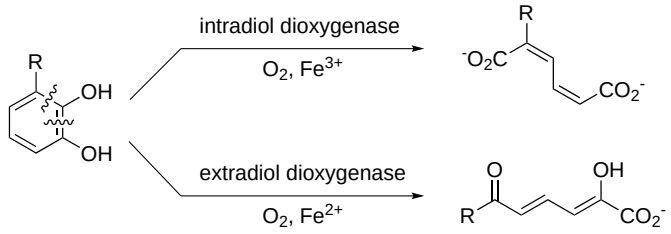

(a) Comparison of intradiol and extradiol catechol cleavage

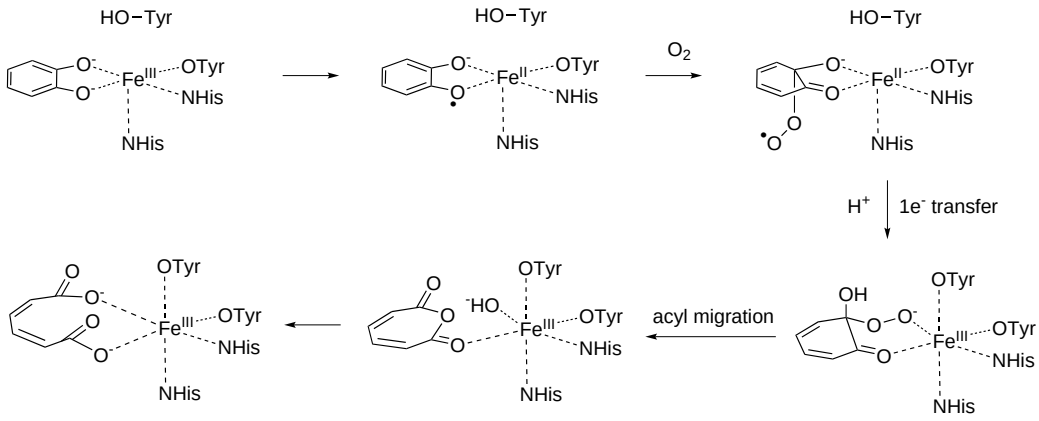

(b) Intradiol dioxygenase

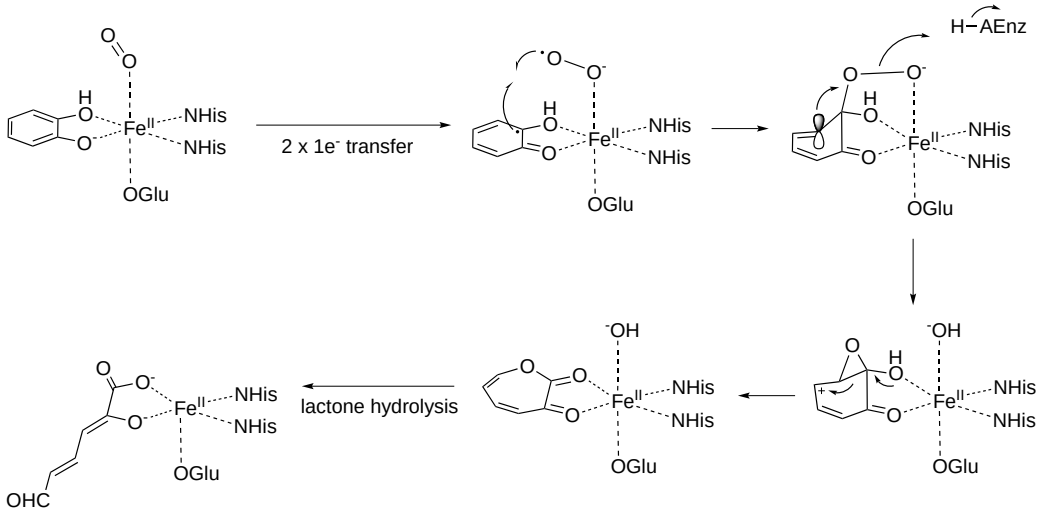

(c) Extradiol dioxygenase[78]

Fig. 1.17: Proposed catalytic mechanisms for catechol dioxygenases[79]

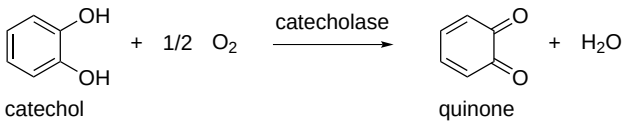

Fig. 1.18: Oxidation of catechol by catecholase enzymes

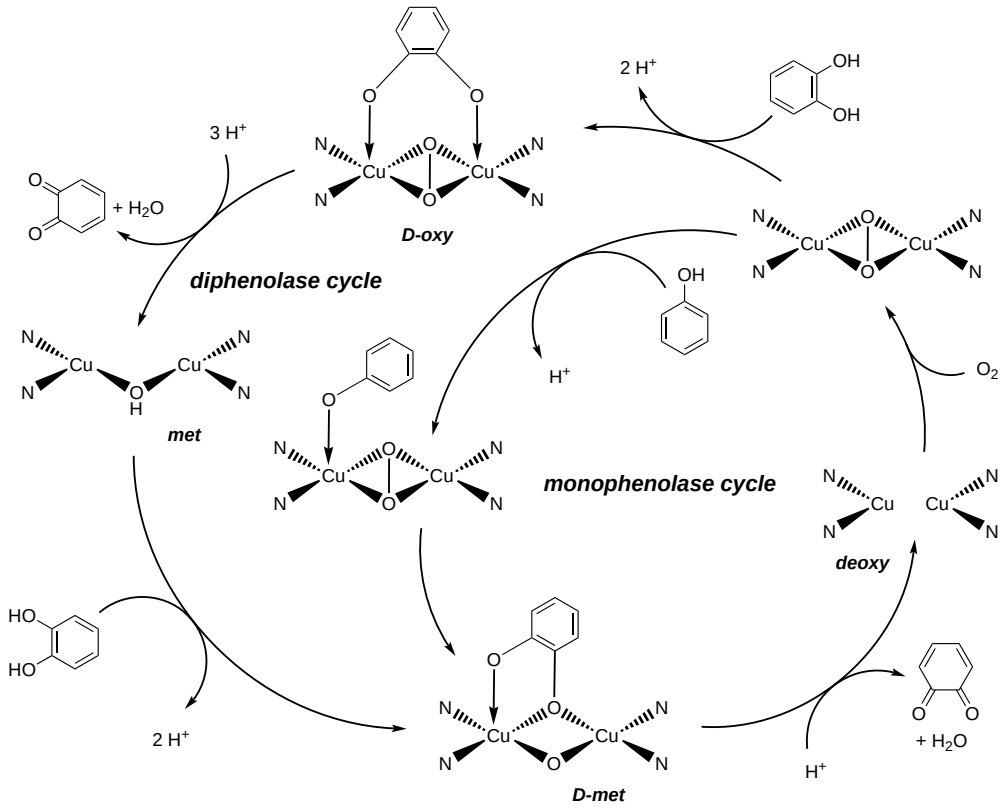

Fig. 1.19: Proposed mechanism of the mono- and diphenolase cycle of tyrosinase[87]

are thought to protect skin cells from UV radiation damage. These type III copper proteins are characterized by an antiferromagnetically coupled dinuclear copper active site. Although the exact mechanism of the catalytic cycle is still subject of heavy discussions,[80–86] there is the (maybe obvious) agreement that both the catechol and the oxygen are activated by the coordination to the copper ion(s). The catalytic cycle proposed by Solomon et al. for tyrosinase oxidation reactions shown in fig. 1.19 yields most assent. The diphenolase or catechol oxidase cycle includes the binding of dioxygen as peroxide in a side-on bridging coordination (μ-η^2:η^2) to the dimeric copper site being surrounded by histidines, accompanied by the oxidation of Cu^{I} to Cu^{II}. Catecholate substrates are bound to this *oxy* state, followed by the stepwise release of two *o*-quinones and the reformation of the *deoxy* state (see fig. 1.19). Distinct catalytic cycles including radical semiquinonate species have also been proposed.[81,88] However, there is still a lack of experimental confirmation.

To resolve the problem of the vague mechanistic ideas, several model complexes have been synthesized to mimic the reactive site of catecholase enzymes and spectroscopic and kinetic studies were conducted. Beside the fundamental understanding of reaction mechanisms, another scientific appeal is a potential application

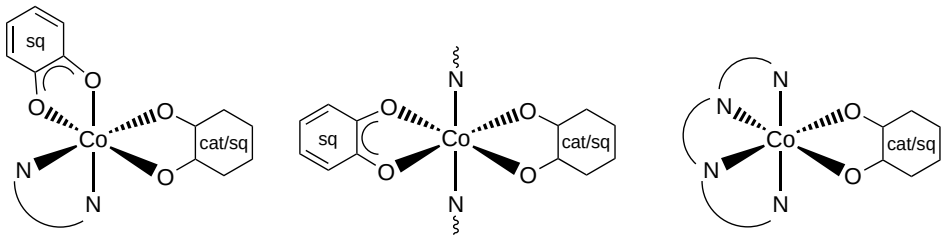

Fig. 1.20: Most common types of mononuclear valence tautomeric dioxolene complexes[90]

of nature-inspired catalysts for the oxidation of organic substrates with dioxygen under mild conditions, as this is of great interest from an economical and environmental point of view.[89]

1.3.7 Valence Tautomeric Dioxolene Complexes in Literature

1.3.7.1 Mononuclear Valence Tautomeric Dioxolene Complexes

Dioxolene Complexes with Cobalt

By far the major contribution for the investigation of valence tautomerism with dioxolene ligands is made by cobalt complexes. The research has focused on three main classes: $[Co(diox)(N_4L)]^+$, $[Co(sq)(diox)(N_2L)]$ and *trans*-$[Co(sq)(diox)(NL)_2]$ type complexes with N_xL as mono-, bi- or tetradentate nitrogen donor ancillary ligands (see fig. 1.20).

The complex [Co(3,5-dbsq)(3,5-dbdiox)(bipy)] (already introduced on page 14) is the dioxolene compound, where a valence tautomeric behavior was observed for the first time by Buchanan and Pierpont. This was accomplished mainly by carrying out temperature dependent measurements of the magnetic moment in toluene solution (see fig. 1.12) and later in solid state. These measurements revealed a transition from an $S = \frac{1}{2}$ ground state at low temperature to higher magnetic moments for increasing temperature. The explanation for this observation was found in a valence tautomeric conversion and could be confirmed by magnetic resonance as well as optical spectroscopy:

$$[Co^{III}(3,5\text{-dbsq})(3,5\text{-dbcat})(bipy)] \rightleftharpoons [Co^{II}(3,5\text{-dbsq})_2(bipy)] \qquad (1.10)$$

As discussed in sections 1.3.2 and 1.3.3, the changes of the electron distribution and the occupation of antibonding e_g^* orbitals lead to different bond lengths for both tautomers. Spectral changes allowed the quantitative determination of thermodynamic parameters in toluene as well as in solution, which confirmed the considerations made in section 1.3.4.

$$\Delta H^\circ_{\text{solid}} = 32\,\text{kJ mol}^{-1}$$
$$\Delta H^\circ_{\text{toluene}} = 34\,\text{kJ mol}^{-1}$$
$$\Delta S^\circ_{\text{solid}} = 98\,\text{J K}^{-1}\,\text{mol}^{-1}$$
$$\Delta S^\circ_{\text{toluene}} = 124\,\text{J K}^{-1}\,\text{mol}^{-1}$$

These findings and the quest for a further understanding of valence tautomerism and development of similar dioxolene complexes led to the synthesis of multiple complexes of the same structural type. Systematic exchange of nitrogen donor ancillary ligands led to some important conclusions: It was observed that a decrease of the transition temperature can be achieved by the introduction of electron withdrawing substituents. Due to the decreased ligand donor strength, the less hard Co^{II} is stabilized, leading to a dramatic influence on the transition temperature (see table 1.1(a)). Additionally, $T_{1/2}$ can also be tuned by varying the chelate ring flexibility of the co-ligands. For the ancillary ligand series tmmda ($n = 1$), tmeda ($n = 2$), tmpda ($n = 3$) bigger chelate ring sizes result in entropic stabilization of the Co^{II} redox isomer and hence decreasing transition temperature $T_{1/2}$ (listed in table 1.1(b)).

Tab. 1.1: Transition temperature dependence on ancillary ligand properties for [Co(3,5-dbsq)(3,5-dbdiox)(N_2L)]-type complexes[46]

(a) Dependence on ligand substituents

ligand N_2L	$T_{1/2}$ (toluene)
bipy	275 K
phen	265 K
NO_2-phen	100 K
$(NO_2)_2$-phen	90 K

(b) Dependence on chelate ring flexibility

ligand N_2L	$T_{1/2}$ (solid)
tmmda	375 K
tmeda	350 K
tmpde	178 K

It has been found that the same principles of ancillary ligand dependence also apply to complexes of the type *trans*-[Co(sq)(diox)$(NL)_2$] (with NL = pyridine derivatives), even though the dioxolenes are *trans* to each other rather than *cis*, as in the case for the chelating bidentate ligands. Furthermore, studies on this class of complexes

convincingly illustrated the influence of intermolecular interactions. Caused by cooperative effects, hysteresis in the valence tautomeric transition as well as high stabilities of photo-induced metastable states have been found.[70,71,91] The widest hysteresis of a valence tautomeric transition was found by Jung et al. for the complex [Co(3,5-dbsq)(3,5-dbdiox)(py_2O)]. The thermal hysteresis with an enormous width of about 230 K was reported to be caused by a conformational change of the bis(pyridine) ether ancillary ligand accompanied by changes in intermolecular interaction.[92]

Examples of the third important class of mononuclear cobalt dioxolenes are the 1:1 adducts $[Co(diox)(N_4L)]^+$. While studies of complexes with Me_ncyclam as tetradentate nitrogen donor ligands nicely illustrated the effect of donor atom strength as seen above,[93,94] Me_ntpa derivatives allowed the investigation of the effect of steric hindrance at the cobalt center.[66] For three methyl groups (strong steric hindrance) the Co^{III} tautomer is found in the temperature range 0 K to 300 K. Reducing the number of methyl groups n and thus weakening the hindrance stabilizes the Co^{II} tautomer so that for $n = 2$ thermal valence tautomerism around 280 K is observed and for $n = 0, 1$ the Co^{II} tautomer is apparent throughout the temperature range.

Dioxolene Complexes with Manganese

For manganese, the best accessible and most common redox states are Mn^{II} (*hs* d^5), Mn^{III} (*hs* d^4) and sometimes Mn^{IV} (d^3). Concerning the electronic and geometric properties there is an obvious analogy of Mn^{II} and Co^{II}, as well as of Mn^{IV} and Co^{III}. For instance, due to the d^3 electron configuration, Mn^{IV} prefers the formation of complexes with strong π-donor ligands (such as catecholates) to form strong bonds with only small deviations from the ideal octahedral geometry. The same is true for Co^{III} with d^6 configuration. Contrastingly, Mn^{II} is more flexible concerning the geometry and is stabilized by less charged, weakly donating ligands. Trivalent manganese is somehow in between these two extrema. The access to these three oxidation states is of interest as it offers the potential of multi-step valence tautomerism.

Initial observations of valence tautomeric transitions for manganese complexes were made for $[Mn(3,5\text{-dbdiox})_2(py)_2]$.[95]

$$\underset{\text{purple}}{[Mn^{IV}(3,5\text{-dbcat})_2(py)_2]} \rightleftharpoons \underset{\text{purple}}{[Mn^{III}(3,5\text{-dbcat})(3,5\text{-dbsq})(py)_2]} \rightleftharpoons \underset{\text{green}}{[Mn^{II}(3,5\text{-dbsq})_2(py)_2]} \tag{1.11}$$

Due to antiferromagnetic coupling between the semiquinonates and the manganese ions as well as the absence of spin state transitions, these transitions could not be observed magnetically ($S = \frac{3}{2}$ ground state for all tautomers), but by means of optical spectroscopy.[96] Similar observations were made for other manganese complexes of this structural class as well as for $[Mn(cth)(dbcat)]^+$ type complexes.[97]

Dioxolene Complexes with Copper

For copper complexes, the available oxidation states are Cu^I and Cu^{II}. Usually, hard nitrogen donor ligands do not allow Cu^I to be stabilized. Therefore, the inclusion of phosphine or similar π-acceptor ancillary ligands was found to be advantageous to synthesize copper complexes being capable of valence tautomerism. Another problem to overcome is the fact that Cu^I prefers tetrahedral complex geometry, while divalent copper favors square planar coordination. This rearrangement seems to present a kind of barrier for the realization of valence tautomeric conversions. However, inspired and motivated by copper containing amine oxidase enzymes,[98] observations of solvent and temperature-dependent valence tautomerism were observed for copper complexes containing softer sulfur or phosphorous-based ancillary ligands. Furthermore Speier et al. were able to characterize a copper phenanthrenediolate complex which showed temperature dependent EPR spectra, which were assigned to valence tautomerism (see fig. 1.21).[99]

Dioxolene Complexes with Other Metals

Nickel most commonly possesses the oxidation state +II. However, a series of complexes were found, where reversible valence tautomeric transitions to Ni^{III} with phenoxyl radicals[100,101] or porphyrin systems[102] were observed.

$$[Ni^{II}L] \rightleftharpoons [Ni^{III}L^-] \tag{1.12}$$

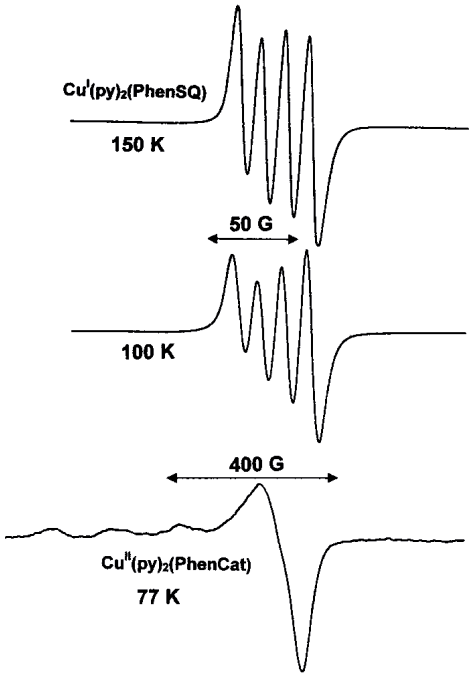

Fig. 1.21: EPR spectra recorded on [Cu(py)$_2$(phendiox)] in 1:10 pyridine/toluene solution showing the transition from [Cu^{I}(py)$_2$(phensq)] to [Cu^{II}(py)$_2$(phencat)].[99]

While there have not been reports of thermally induced valence tautomerism for nickel dioxolene complexes, it has been shown that the valence orbital energy of planar Ni^{II} is similar to the orbital energy of di-*tert*-butyl-1,2-semiquinonate ligands.[103,104] Only small modifications of nickel dioxolene complexes can result in the appearance of a different tautomer, but no equilibrium between two tautomers was observed yet.

As already seen in section 1.3.6.1, valence tautomeric transitions for Fe^{III} catecholates have been proposed in the catalytic cycles for catechol dioxygenase enzymes. However, in most cases, there is no thermodynamic driving force for a suchlike electron transfer. Provided that both tautomers contain iron in its *high spin* configuration (which is the usual case and expected), an electron transfer from the ligand to the metal ions would not involve a change in the population of the antibonding e_g orbitals, which are mainly responsible for the bond strength and thus $\Delta H°$. As discussed in sections 1.3.1 and 1.3.4, such a "tight-floppy-transition" is one of the prerequisites for valence tautomeric equilibria. Despite this problematic situation, the iron complex [Fe^{III}(bispicen)(Cl$_4$cat)(Cl$_4$sq)] · DMF containing tetrachlorocatechol was reported to exhibit a valence tautomeric equilibrium.[105] Even so, there are discussions about the validity of these results, because the reported temperature dependence of the optical spectra is not significant and the magnetic susceptibility

seems to remain unaffected by the proposed tautomeric conversion. Disregarding these findings, there is still the chance for the synthesis of iron dioxolene valence tautomers for *low spin* Fe^{III}(cat), because the resulting spin state transition would cause e_g orbital population changes. Nevertheless, this might be a synthetic challenge, as the required strong ancillary ligands would demand skillful electronic tuning and adaption of the dioxolene ligand.

1.3.7.2 Dinuclear Valence Tautomeric Dioxolene Complexes

In the field of Fe^{II} spin crossover compounds, the idea of linking two spin crossover units to larger, multinuclear entities is already well established.[106–108] These activities are stimulated by the fact that for certain dinuclear spin crossover complexes well-defined two-step transitions could be observed. The presence of the three distinct spin states *ls*-*ls*, *ls*-*hs* and *hs*-*hs* is due to an intramolecular cooperativity between the single metal centers or steric effects. The availability of these three states is of interest for the potential use as three-state switches or molecular ternary memories.[109] Additionally, some dinuclear spin crossover complexes were found to exhibit wider hysteresis, likewise caused by intramolecular interactions. Given the similarities of spin crossover and valence tautomerism, the same can be true for valence tautomeric complexes. Therefore, the logical consequence is the analog development of dinuclear valence tautomers.

For this realization of dinuclear valence tautomers, several strategies have been followed. The first and most intuitive approaches are based on the mononuclear valence tautomeric units presented in section 1.3.7.1 bridged by organic linkers. The most popular class of dimeric cobalt dioxolenes can be described by the general formula [{Co(sq)(diox)}$_2$(N_2LN_2)] with a bridging bis-bidentate nitrogen donor ancillary ligand N_2LN_2, such as bis(diimine ligands). Some of the employed ligands are depicted in fig. 1.22(a). The first reported complex from this class, a bipyrimidine bridged dimer, did not show thermally induced valence tautomerism and a $(Co^{II})_2$ state was found for the whole temperature range.[110] Contrastingly, for the phenylene-bridged bipy complexes [{Co(3,5-dbsq)(3,5-dbdiox)}$_2$(bipy-*m*/*p*-Ph-bpy)] a temperature-driven valence tautomeric conversion was observed.[111] However, the behavior was considerably dependent on the environment and solvation of the complex and showed no signs of two-step transitions or hysteretic effects. Similar results were found for other dimeric systems with weak coupling of the metal ions,

where the two valence tautomeric centers are more or less independent.[112,113] A stronger coupling, as found for [{Co(3,5-dbsq)(3,5-dbdiox)}$_2$(ppm)], led to a two-step thermally induced valence tautomeric transition, monitored by near infrared spectroscopy:[114]

$$\{Co^{III}(cat)\}_2 \rightleftharpoons \{Co^{III}(cat)\}\{Co^{II}(sq)\} \rightleftharpoons \{Co^{II}(sq)\}_2 \qquad (1.13)$$

Another approach for the synthesis of dinuclear valence tautomeric complexes is the utilization of redox-active bridging ligands in combination with N_4L ancillary ligands. Several comparative studies with bis-chelating bis-dioxolene ligands as bridging units diox−L−diox are found in literature (see fig. 1.22(b)).[58,115–118] Concerning valence tautomeric conversions, an interesting behavior was found for the complexes [{Co(Me$_n$tpa)}$_2$(diox−spiro−diox)]$^{2+}$.[118,119] In analogy to the corresponding mononuclear complexes, the employment of tpa and Me$_3$tpa resulted in {Co^{III}(cat)}$_2$ or {Co^{II}(sq)}$_2$ tautomers respectively. For the Me$_2$tpa derivative however, magnetic measurements as well as Co K-edge XANES studies provided evidence for a two-step conversion as described in eq. (1.13). Besides, photoinduced valence tautomeric transitions were observed.

Instead of bis-dioxolenes, ligands derived from 2,5-dihydroxy-1,4-benzoquinone (dhbq) can be used as bridging moieties.[58,64,120,121] For instance, the complexes [{Co(cth)}$_2$(dhbq)]$^{3+}$ and [{Co(tpa)}$_2$(dhbq)](PF$_6$)$_3$ revealed both thermally as well photoinduced valence tautomerism for one of the cobalt centers.[58,64] For the latter, a hysteresis loop in the thermal transition around 300 K is observed, which is explained by intermolecular interactions.

1.3.7.3 Polymeric Valence Tautomeric Dioxolene Complexes

Similar as for the dinuclear dioxolene complexes, two general strategies for the synthesis of polynuclear valence tautomeric complexes are possible: employing either a nitrogen donor ligand or a redox-active ligand as bridging moiety. The first approach was followed for instance using pyrazine (pyz) and 4,4'-bipyridine (4,4'-bipy) for the linkage of [Co(sq)(diox)] units to yield one-dimensional cobalt dioxolene complexes.[73,122–124] For the compounds [Co(3,6-dbdiox)$_2$(pyz)]$_n$ and [Co(3,5-dbdiox)$_2$(4,4'-bipy)]$_n$ magnetic measurements and near infrared spectra revealed thermal valence tautomeric conversions. The former also showed light-

induced transitions. Interestingly, as the polymer chains are arranged perpendicular to the plane of the crystal plates, a reversible bending of the crystals upon light irradiation is observed. This photomechanical effect was reported to be caused by the elongation of the Co−N bonds during the light-induced tautomeric conversion.[122]

For the second approach toward polymeric cobalt dioxolene complexes, ligands of the type diox−Ph−diox or diox−spiro−diox were reported[58,117,125–127] (see fig. 1.22(b)). The resulting compounds with N_2L ancillary ligands could not be analyzed crystallographically, but they are believed to have one-dimensional chain structures $[Co(diox-R-diox)(N_2L)]_n$ and showed thermally and light-induced valence tautomeric transitions.

The only example for higher dimensional cobalt dioxolene coordination networks is the two-dimensional metal-organic framework based on the tetrapyridyl bridging ligand tpom. The porous layers $[Co(3,5\text{-dbdiox})_2(tpom)]_n$ exhibit thermally and light-induced valence tautomerism. Surprisingly, the valence tautomeric transition was found to be gradual and shows no signs of cooperativity. This observation is explained by the rather high flexibility of the bridging ligand.

1.3.7.4 Dioxolene Coordination Clusters

While for most published dioxolene complexes, the dioxolene ligands coordinate as bidentate chelates with both oxygen donor atoms bound to the metal ion, some other coordination modes are frequently found. As represented in fig. 1.23, additional common binding modes for dioxolene ligands are a monodentate η^1 coordination of a protonated ligand or the μ^2 bridging coordination in a chelating $\eta^2{:}\eta^1$ or non-chelating $\eta^1{:}\eta^1$ fashion. For dioxolenes that are bridging more than two metal ions, additional coordination modes are found and will be discussed later. While there are many examples for bridging dioxolenes in polynuclear transition metal coordination clusters, none of them is reported to undergo valence tautomeric transitions.[128–130]

In preceding studies to the present work, I was able to achieve progress on the systematic examination of the electronic properties of oligonuclear iron dioxolenes in different oxidation states.[131] The reaction of basic iron carboxylates with dioxolene ligands permitted the synthesis of a series of di- and tetranuclear clusters with semiquinonates and catecholates in different coordination modes. Typical examples

are shown in fig. 1.24. Iron has been chosen as central ion, as it is magnetically isotropic (high spin d^5) and can thus be easily interpreted. Furthermore, despite its redox-activity, iron does not have the tendency to undergo valence tautomeric transitions, as this process would not involve a significant change in the M−L bond strength for both tautomers (see page 26). This fact enabled the assumption of localized and temperature-independent redox states for a straightforward evaluation. Extensive elaboration of the individual ligand and metal oxidation states using Brown's concept of *metrical oxidation states* as well as Mößbauer spectroscopy, magnetic measurements, electrochemical methods and optical spectroscopy allowed an unambiguous assignment of the electron distribution for both bridging and non-bridging dioxolenes. The most important finding was that *hs* iron(III) is able to stabilize both non-bridging semiquinonates and dianionic catecholates under ambient conditions, mainly dependent on the overall charge of the complex. Interestingly, for bridging dioxolenes (μ^2-η^2:η^1 coordination), only catecholate coordination was observed. Due to the increased electron withdrawal in comparison to ligands coordinated to only one metal ion, the less charged radical species seems to be energetically disfavored. Based on these findings, the empirical rules for polynuclear iron dioxolenes were established:

1. Bridging dioxolenes are only stable in the oxidation state of a dianionic catecholate.
2. For non-bridging dioxolenes, the oxidation state is mainly determined by the electronic withdrawal of the ancillary ligands and the overall charge of the complex.

A comparison with similar compounds known from literature showed that a change from a trivalent metal ion to divalent Co^{2+} yielded several complexes with μ^2-η^2:η^1 bridging semiquinonates, although the electronegativity of cobalt is slightly higher than that of iron. It can therefore be assumed that only a slight decrease in electron withdrawal by the metal ions is necessary to stabilize catecholates as well as semiquinonates in a bridging mode and therefore fulfill the main prerequisites for valence tautomeric transitions in polynuclear complexes with bridging monofunctional dioxolenes. However, suchlike coordination clusters have not been reported yet.

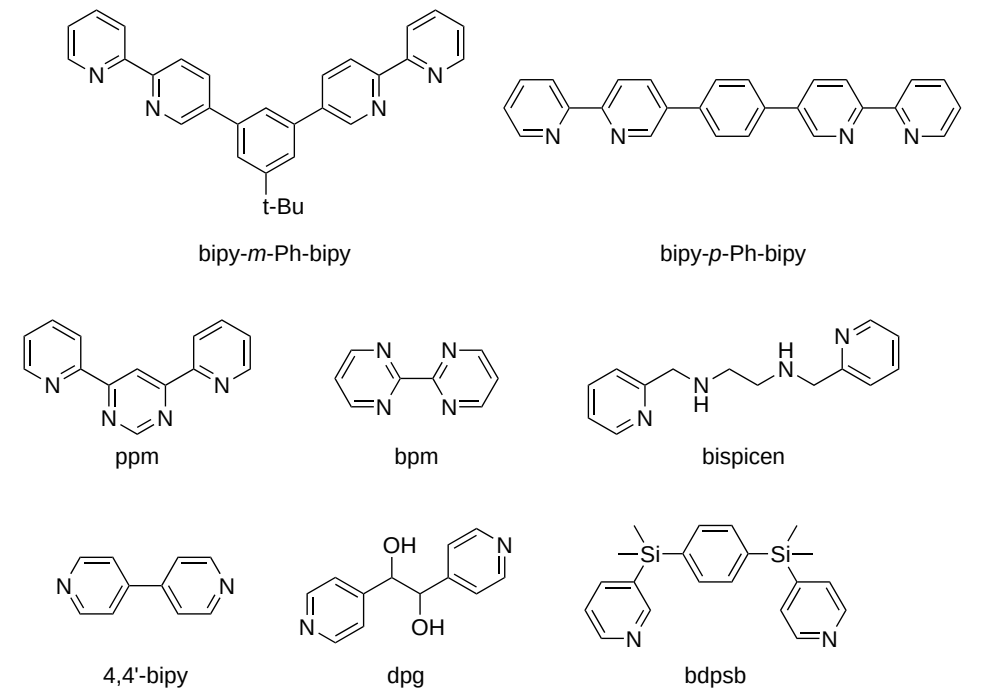

Fig. 1.22: Employed bridging ligands for polynuclear valence tautomeric complexes[90]

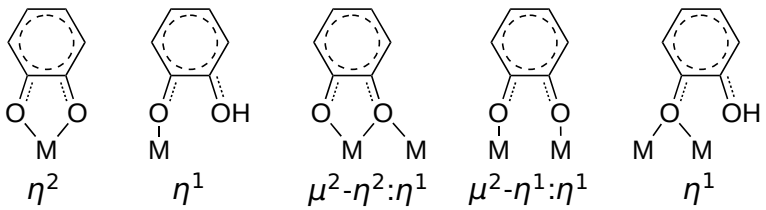

Fig. 1.23: Some possible coordination modes of dioxolene ligands

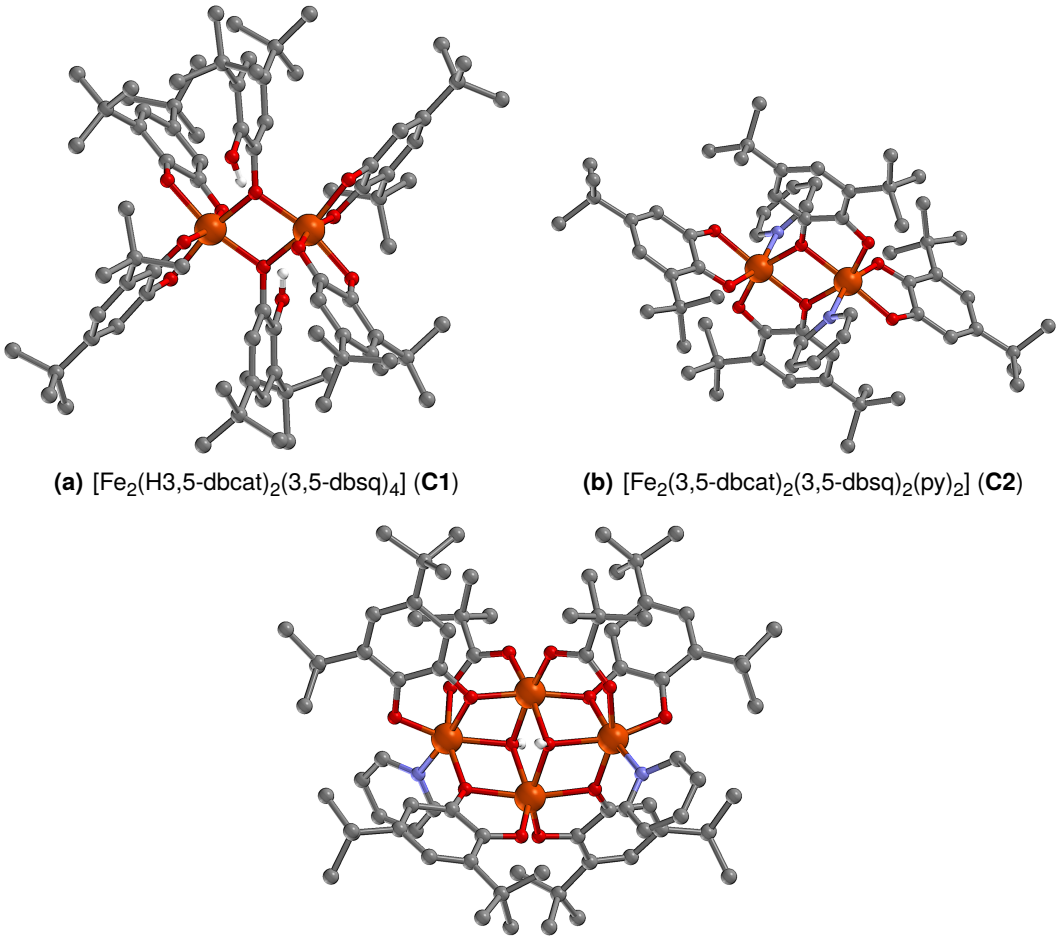

(a) $[Fe_2(H3,5\text{-dbcat})_2(3,5\text{-dbsq})_4]$ (**C1**)

(b) $[Fe_2(3,5\text{-dbcat})_2(3,5\text{-dbsq})_2(py)_2]$ (**C2**)

(c) $[Fe_4(OH)_2(3,5\text{-dbcat})_4(py)_2(piv)_2]$ (**C3**)

Fig. 1.24: Molecular structures of oligonuclear iron dioxolene complexes

2

Aim of the Work

As discussed in section 1.3.7 polynuclear dioxolene complexes are unique molecules providing the possibility of polymodal valence tautomerism and allowing the examination of intramolecular interaction of linked spin centers.The common concept of a linkage of known mononuclear fragments by bridging N-donor ligands or bis-dioxolenes as presented in section 1.3.7 however strongly limits the nuclearity of the resulting complexes as well as their structural variety. Up to now, the occurrence of *bridging* bidentate mono-dioxolenes has not been examined systematically and has even widely been avoided as the resulting complexes are more challenging and sophisticated than their mononuclear relatives. Recently, as presented on page 29, I was able to achieve first progress in the area of iron coordination clusters with bridging dioxolenes as a preliminary contribution to the present work. However, these complexes were designed to be redox-innocent with respect to valence tautomeric equilibria and only aimed at the understanding of ligand oxidation state stability in different bridging modes for iron complexes. More generally, for other transition metal ions, the influence of the coordination mode (see fig. 1.23) on the dioxolenes' redox-properties can hardly be predicted.

To overcome this issue, the present work aims at the synthesis of a variegated series of novel oligonuclear coordination clusters with redox-active dioxolene ligands with different coordination modes and various 3*d* transition metal ions. Beside the thorough assignment of the involved metal ions' and ligands' oxidation states, the temperature dependence of the valence tautomeric states in these clusters is a main objective of this thesis.

The work to achieve these goals can be classified into the following fields:

The first step is the synthesis of novel mononuclear dioxolene complexes. Being much simpler than polynuclear complexes with bridging ligands, these complexes serve as a reference for a comparison with polynuclear dioxolene complexes.

As a second step, the self-organized assembly of small components (metal precursors, dioxolene ligands and auxiliary ligands) to larger clusters is examined. This approach is capable of providing a number of complexes with a large structural variety. The self-assembly strategy ensures the formation of energetically favored structures, and hence provides information about the most stable electronic configuration.

A third step is the synthesis and establishment of appropriate multidentate auxiliary ligands and their utilization as structure-providing building blocks in oligonuclear dioxolene complexes. This method enables the targeted synthesis of clusters with a given structure and avoids arbitrary structures as expected for the method of self-organization.

Finally, the synthesized complexes are characterized and examined with respect to their ability to undergo valence tautomeric transitions. As an experimental proof of the electronic activation of the dioxolene ligands in addition to analytical data, the catalytic activity for the oxidative generation of quinones with molecular oxygen is measured (catecholase activity) for some showcase complexes.

The present work fills a gap in the literature as it provides new strategies toward the synthesis of oligonuclear transition metal dioxolene complexes and their characterization. The gained insights result in a much better understanding of the electronic structure, making the future development of switchable dioxolene clusters more feasible and thus allowing potential future applications. Based on the recent theoretical proposal of dinuclear valence tautomers as 2-qubit quantum gates for the development of quantum computers[22] (see section 1.1.1), the results of this study provide an important contribution to the experimental accessibility of suchlike complexes.

3 Results and Discussion

This chapter presents the strategies for the synthesis of the oligonuclear transition metal dioxolene complexes discussed in this work. For each followed synthetic methods the resulting coordination clusters are introduced and their structural, magnetic, spectroscopic and electronic properties are presented and interpreted. In the course of this chapter, the advantages and disadvantages of each synthetic route are discussed and the applied workflow is explained.

Most of the mono- and dinuclear complexes presented in the introductory section 1.3.7 were synthesized by reacting inorganic metal salts with catechols/catecholates or quinones in rather polar solvents like methanol. Due to the strong solvation under these conditions, the formation of small aggregates is preferred over the assembly of larger moieties.

For the targeted synthesis of complexes with higher nuclearity in this work the solvent polarity was decreased, which required the application of metal precursors soluble in apolar solvents. Polynuclear transition metal carboxylates, or more precisely pivalates (trimethyl acetates), were found to come up to this requirement, as they are easily soluble in manifold organic solvents. Furthermore, they offer pre-built multinuclear moieties with bridging pivalates for a subtle coordination of dioxolenes by substitution. A large variety of basic pivalates with different transition metal ions in several oxidation states is reported and their preparation is straightforward.

The synthesis of the polynuclear dioxolene complexes described in this thesis is based on the pivalates $[Co_2(OH_2)(piv)_4(Hpiv)_4]$ (**P1**), $[Co(piv)_2]_n$ (**P2**), $[Cu_2(piv)_4(EtOH)_2]$ (**P3**), $[Ni_2(H_2O)(piv)_4(Hpiv)_4]$ (**P4**), $[Ni(piv)_2]_n$ (**P5**), $[Fe_3O(piv)_6(H_2O)_3]piv$ (**P6**) and $[Fe_3O(piv)_6(py)_3]$ (**P7**). All the incorporated metal ions are redox-active and stable in more than one oxidation state. This suggests the theoretical possibility for intramolecular electron transfer in combination with dioxolene ligands. One exception is iron. Despite its redox activity it is not capable of valence tautomerism, as there is no thermodynamic driving force (see section 1.3.7.1). The resulting iron

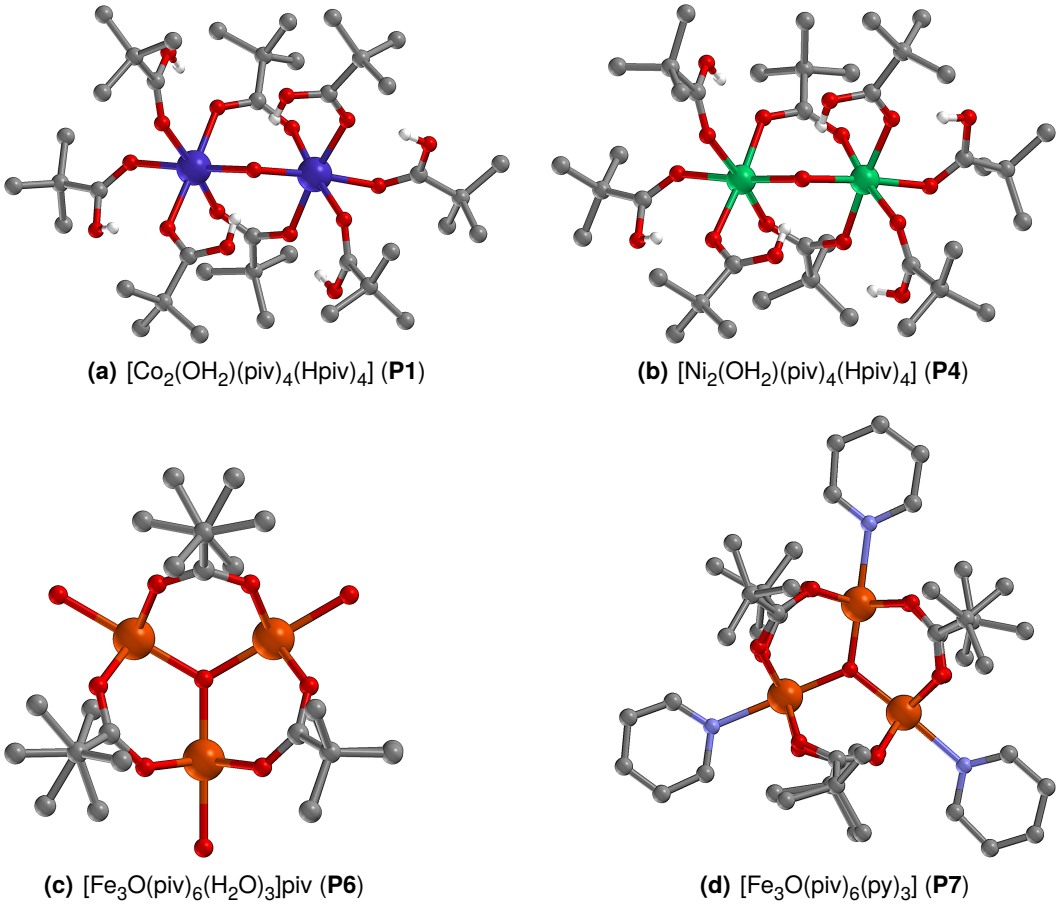

(a) $[Co_2(OH_2)(piv)_4(Hpiv)_4]$ (**P1**)

(b) $[Ni_2(OH_2)(piv)_4(Hpiv)_4]$ (**P4**)

(c) $[Fe_3O(piv)_6(H_2O)_3]piv$ (**P6**)

(d) $[Fe_3O(piv)_6(py)_3]$ (**P7**)

Fig. 3.1: Molecular structures of selected transition metal pivalate precursors

complexes are used as innocent references for the comparison with non-innocent relatives.

As dioxolene ligand, the alkylated derivative 3,5-di-*tert*-butyl-1,2-dioxolene **L1a** was used for the majority of syntheses in the oxidation state of a dianionic catecholate as well as the neutral quinone **L1b**. The catechol species **L1a** is a very strong chelate ligand with good electron donor abilities. The addition of an optional base further increases the ligand strength by deprotonation of the coordinating hydroxyl groups. As bases, different amines were used, both coordinating ones like pyridine or piperidine derivatives and less coordinating ones like triethylamine. In addition to the pure deprotonating role, these amines are able to saturate metal coordination spheres by coordination and thus enable crystallization. The oxidized ligand **L1b** in contrast, which has also been used for selected syntheses, is much weaker, as it does not carry a negative charge. However, the chosen reaction conditions allow the reduction of the quinones to semiquinones or catechols *in situ* while oxidizing the metal ions or other components and thus the binding affinity toward metal ions

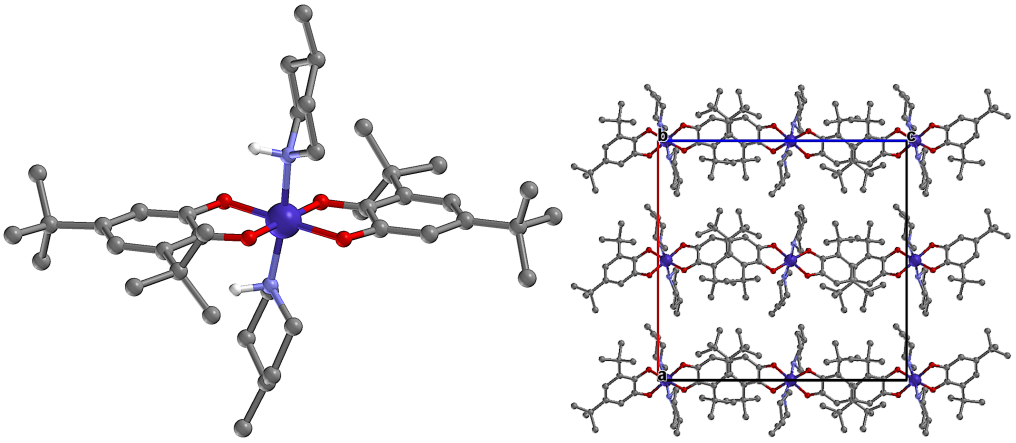

(a) Molecular structure of **C4** **(b)** Crystal packing of **C4**

Fig. 3.2: Structural representations of [Co(3,5-dbsq)(3,5-dbcat)(4-Mepip)$_2$] (**C4**)

may be dramatically increased. As a second dioxolene ligand tetrabromocatechol (tbcat) was chosen for selected syntheses.

3.1 Mononuclear Dioxolene Complexes

Mononuclear dioxolene complexes were synthesized as a reference without metal-metal-interactions and bridging dioxolene ligands. Those compounds easily allow for the comparison with literature-known complexes, because there are numerous similar examples (see section 1.3.7.1). The present section however makes no claim to review of the properties of mononuclear dioxolene complexes entirely, as a more detailed consideration would be beyond the scope of this thesis.

The first complex to be presented is [Co(3,5-dbsq)(3,5-dbcat)(4-Mepip)$_2$] (**C4**), for which the molecular structure is depicted in fig. 3.2(a). The mononuclear complex which crystallizes in the orthorhombic space group $Pca2_1$ was prepared from [$Co_2(OH_2)(piv)_4(Hpiv)_4$] (**P1**), 3,5-di-*tert*-butylcatechol (**L1a**) and 4-methylpiperidine as an ancillary ligand in acetonitrile. As determined from single crystal X-ray diffraction measurements at 173 K, the central cobalt ion is coordinated by two chelating 3,5-di-*tert*-butyl-1,2-dioxolene ligands and two 4-methylpiperidine ancillary ligands *trans* to each other. A close resemblance with the *trans*-[Co(sq)(diox)(NL)$_2$] type mononuclear complexes presented in section 1.3.7.1 can be seen. The main difference is the fact that all published complexes of this type are based on aromatic co-ligands such as pyridine, while in the present case the aliphatic methylpiperidine is enclosed. This difference mainly has an influence on the electronic properties, as

C4

Tab. 3.1: Metrical oxidation states for the dioxolene ligands in **C4** based on crystallographically determined bond lengths at 173 K

Ligand	Metrical oxidation state (*MOS*)
Dioxolene 1	−1.22
Dioxolene 2	−1.93

piperidine is a slightly better electron donor. Therefore, the ligand strength is slightly increased in comparison to the complexes based on pyridine derivatives. Another contrast to the pyridine adducts arises from the co-ligand symmetry. While pyridine is a flat molecule, piperidine exhibits lower symmetry due to its chair conformation. This in turn lowers the overall complex symmetry. A closer look at the crystal structure reveals that the N−H bonds of both piperidine rings are facing the same direction, breaking the complex' inversion symmetry. Consequently, also the dioxolene ligands are chemically (as well as crystallographically) non-equivalent. The coordination polyhedron around the central cobalt ion can be described as an octahedron slightly elongated along the Co−N axis. Co−O bond lengths of 1.884 Å to 1.905 Å and Co−N distances of 1.969 Å and 1.978 Å, respectively, clearly indicate trivalent cobalt. Thorough analysis of intra-ligand atom distances allows for an assignment of the physical oxidation state of the two dioxolene ligands. For the first dioxolene ligand (the one on the right in fig. 3.2(a)), alternating C−C bond lengths are found within the ring (cf. table B.5). Furthermore, comparatively short C−O bond lengths of 1.302 Å and 1.312 Å indicate a partial double bond character. In contrast, for the second dioxolene ligand a stronger bond lengths assimilation within the ring is observed and C−O distances are a bit longer (1.348 Å and 1.362 Å). These findings strongly suggest the assignment of dioxolene 1 as a monoanionic semiquinonate and dioxolene 2 as an aromatic, dianionic catecholate, which is in agreement with the overall charge balance of the complex. The complex can thus be written as $[Co^{III}(3,5\text{-dbsq})(3,5\text{-dbcat})(4\text{-Mepip})_2]$ with localized valences. A quantitative analysis by means of Brown's concept of metrical oxidation states[56] confirms this conclusion as there are good agreements with the theoretical *MOS* values of −1 and −2 for dioxolene 1 and 2 respectively (see table 3.1).

As these values extracted from the crystallographic data are only a snapshot of the electron distribution at 173 K, the magnetic susceptibility of **C4** was measured in the temperature range 2 K to 380 K at a magnetic field of 1 T to resolve the temperature dependence. The $\chi \cdot T$ vs. T plot in fig. 3.3(a) shows a fairly constant value of

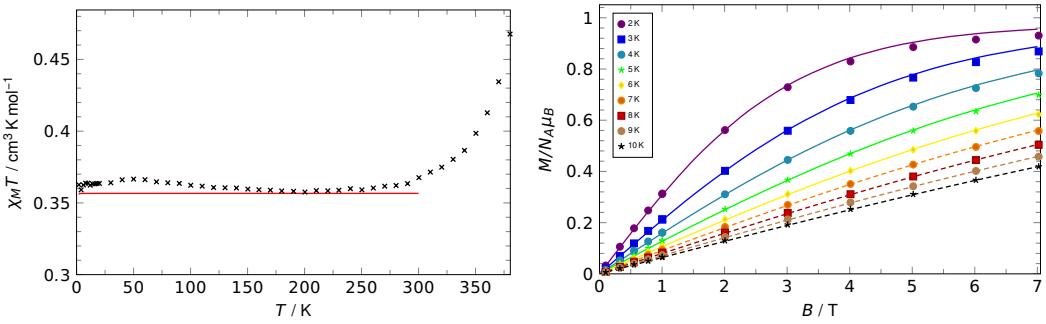

(a) Magnetic susceptibility ($B = 1\,\mathrm{T}$)

(b) Magnetization

Fig. 3.3: Magnetic data of **C4** ($g = 1.95$)

0.36 cm^3 K mol^{-1} in the range from 2 K to 300 K. Below 10 K measurements of the magnetization were conducted at various fields (depicted in fig. 3.3(b)). Both these magnetization values and susceptibility data below 300 K were simulated simultaneously. Choosing a single, isolated $S = \frac{1}{2}$ spin center for the semiquinonate ligand found in the single crystal structure with an isotropic g tensor of $g = 1.95$ as the underlying model using the Phi software, yields a good agreement of the simulation with the experimental findings (see solid lines). These parameters are reasonable for a magnetic spin located on the single semiquinonate ligand. Theoretically, a g value of approximately 2.00 is expected for suchlike organic radicals, as spin orbit coupling usually is negligible. However, the slightly lower value in this present case is still within the expected fault range. Above 300 K the product of the molar susceptibility and the temperature slightly increases to about 0.467 cm^3 K mol^{-1} at 380 K. This increase can be explained by an intramolecular electron transfer from the catecholate ligand (dioxolene 2) to the central cobalt(III) ion within the meaning of valence tautomerism resulting in a $Co^{II}(sq)_2$ species.

$$[Co^{III}(3,5\text{-dbsq})(3,5\text{-dbcat})(4\text{-Mepip})_2] \rightleftharpoons [Co^{II}(3,5\text{-dbsq})_2(4\text{-Mepip})_2] \qquad (3.1)$$

This transition is accompanied by a spin state transition from *low spin* Co(III) to *high spin* Co(II). As the expected (spin only) value for $\chi_M T$ for a $Co^{II}(sq)_2$ species is 2.625 cm^3 K mol^{-1} (assuming $g_{Co} = g_{el} = 2.0023$), the observed onset above 300 K only corresponds to a partial valence tautomeric transition. Due to technical limitations, the magnetic data could not be measured at higher temperatures to detect the complete transition.

The measurement of solid state reflectance spectra of **C4** in the range from 20 °C to 120 °C (shown in fig. 3.4) allowed the spectroscopic monitoring of the valence

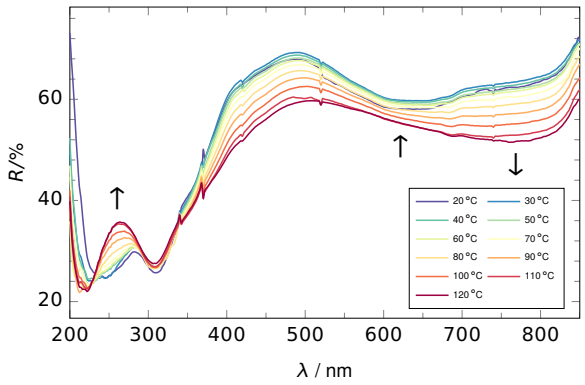

Fig. 3.4: Solid state reflectance spectra for [Co(3,5-dbsq)(3,5-dbcat)(4-Mepip)$_2$] (**C4**). The temperature dependence of the reflectance shows a valence tautomeric transition between 20 °C and 120 °C.

tautomeric transition. At 20 °C, for the Co^{III}(sq)(cat) species, the most prominent absorption bands are found at 244 nm, 310 nm and 638 nm. For increasing temperature, the intensity of the former and the latter decrease while new bands at 222 nm and 760 nm appear. This behavior and the position of the absorption bands are in good agreement with other thermochromic, valence tautomeric cobalt dioxolene complexes.[92,113] Above 120 °C, an irreversible decomposition of the compound is observed. Thus, similar to the magnetic measurements, only a partial valence tautomeric transition is experimentally accessible. The extraction of the molar fraction of the high spin tautomer and hence the calculation of the thermodynamic parameters $\Delta H°$ and $\Delta S°$ for this equilibrium is therefore impossible.

In comparison, the pyridine adduct [Co(3,5-dbsq)(3,5-dbcat)(py)$_2$] · 0.5py exhibits a valence tautomeric conversion temperature of about 250 K.[91] The higher transition temperature $T_{1/2}$ in the present case agrees with the stabilization of the Co^{III} tautomer due to the slightly stronger ligand field of methylpiperidine compared to pyridine. However, one has to keep in mind that in addition to electronic effects, the presence of valence tautomeric conversions is strongly dependent on the solvation and crystal packing.[70,91] In many examples, the inclusion of solvent molecules within the crystal structure led to steric hindrance and thus to shifts of the transition temperature or the suppression of valence tautomerism at all. For [Co(3,5-dbsq)(3,5-dbcat)(py)$_2$] · 0.5py for example, the embedded pyridine molecule prevents one of the crystallographically independent complexes from undergoing the required expansion upon a valence tautomeric transition. Therefore, only a 1:1 mixture of both tautomers is observed at room temperature. In the present case, no solvent molecules are included and the non-orthogonal, rather flexible

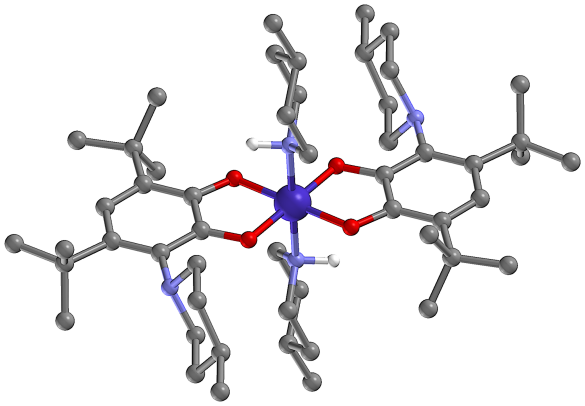

Fig. 3.5: Molecular structure of [Co(dbmpsq)(dbmpcat)(4-Mepip)$_2$] (**C5**)

packing allows a “breathing” of the complexes (see fig. 3.2(b)). Thus, no significant influence of intermolecular effects is expected in addition to the electronic properties determined by the ligands.

The structurally related compound [Co(dbmpsq)(dbmpcat)(4-Mepip)$_2$] (**C5**) could be prepared similarly. In this case [Co(piv)$_2$]$_n$ (**P2**) was used as a precursor instead of the dinuclear cobalt pivalate. Although the synthesis included the use of 3,5-di-*tert*-butylcatecholate just as in the case of **C4**, the crystal structure revealed the *in situ* formation of two 4,6-di-*tert*-butyl-3-(piperidin-1-yl)benzene-1,2-diolates, which coordinate to the cobalt ion in the same manner as the unmodified ligand. This formation may be explained by an oxidation of the catecholate to a radical semiquinone, which allows a hydrogen abstraction from the excessive methylpiperidine. High temperatures during the synthesis and the coordination of the ligand to the cobalt ion further increases its reactivity as electrons are withdrawn from the ligand backbone. This spontaneous and unexpected reaction nicely shows the effect of substrate activation analog to the processes found in the catechol dioxygenase enzymes as discussed in section 1.3.6.1. The reaction with methylpiperidine, which is much less reactive than dioxygen, highlights the strength of the activation additionally.

In contrast to **C4**, compound **C5** crystallizes in the monoclinic space group $C2/c$. An inversion center coincides with the location of the cobalt atom, thus the asymmetric unit only consists of half a molecule. Therefore, both dioxolene ligands are crystallographically equivalent and cannot be distinguished. Bond lengths analyses for the dioxolene ligand of the asymmetric unit are ambiguous as they correspond to an intermediate of catecholate and semiquinonate. A quantitative examination yields the *metrical oxidation state* $MOS = -1.54$, showing the intermediate character.

Tab. 3.2: Metrical oxidation states for the dioxolene ligands in **C5** based on crystallographically determined bond lengths at 173 K

Ligand	Metrical oxidation state (*MOS*)
Dioxolene 1	−1.54

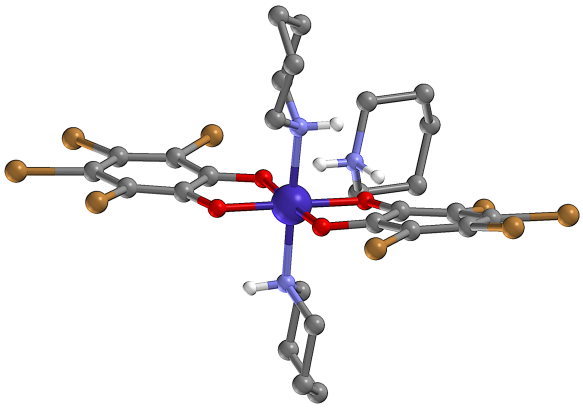

Fig. 3.6: Molecular structure of (HPip)[Co(tbcat)$_2$(pip)$_2$] (**C6**)

Using crystallography, it cannot be resolved if the valences are localized as for **C4** (Co(sq)(cat)) or delocalized with two intermediate ligands (Co(sq/cat)$_2$). Another structural ambiguity is the coordination of the 4-methylpiperidine. While for **C4** both N−H bonds face the same direction, for **C5** a 50 % mirror disorder is observed. Due to the inversion center, both methylpiperidine ligands (and their disordered counterparts) are crystallographically equivalent. Hence, a differentiation between the *syn* (as for **C4**) or the potential *anti* conformer cannot be made crystallographically.

C6

For the synthesis of (Hpip)[Co(tbcat)$_2$(pip)$_2$] (**C6**), the brominated catechol tetrabromocatechol was used. This ligand provides the same steric stabilization of a potential semiquinone radical, but is far more electron withdrawing than the corresponding alkylated catechol. Therefore, the redox potential is higher than for the butyl derivative and the oxidation to a semiquinone is hindered.[132]

The synthesis involved the reaction of [Co$_2$(OH$_2$)(piv)$_4$(Hpiv)$_4$] (**P1**) with tetrabromocatechol and piperidine in acetonitrile and yielded monoclinic crystal with the space group $P2_1$ with the molecular formula (Hpip)[Co(tbcat)$_2$(pip)$_2$]. In similarity to the former two mononuclear complexes, the central cobalt ion is coordinated by the two dioxolenes and two *trans* piperidines. Contrary to the arrangement in **C4**, both piperidine ligands and their N−H bonds face opposite directions. The main structural difference is the additional inclusion of a piperidinium cation, which is loosely bound over hydrogen bridges to two catecholate oxygen atoms (with donor-acceptor dis-

Tab. 3.3: Metrical oxidation states for the dioxolene ligands in **C6** based on crystallographically determined bond lengths at 173 K

Ligand	Metrical oxidation state (*MOS*)
Dioxolene 1	−1.60
Dioxolene 2	−1.73

tances of 2.771 Å and 2.819 Å). The Co−O and Co−N bond lengths (see table B.7) are in the same order of magnitude as found for **C4** and **C5**, which is typical for *low spin* cobalt(III) complexes.[133] The serious steric demand of the bromine groups is evident in a remarkable distortion of the complex, the angle between the two dioxolene ligand mean planes is 10.3°. This distortion might be the reason for the metrical oxidation states $MOS_{\text{lig 1}} = -1.60$ and $MOS_{\text{lig 2}} = -1.73$ to show comparatively large deviations from the expected value of $MOS = -2$. Nonetheless, the assignment of both ligands as catecholates is required to assure charge neutrality, is consistent with the expected behavior of the electron withdrawing bromine substituents and is considered to be unambiguous. In literature, only one further anionic cobalt bis(catecholate) complex with *trans* nitrogen donor ligands is reported. The compound $(Et_3NH)[Co(pym)_2(tbcat)_2] \cdot H_2O$ shows a weak temperature dependence of the electronic absorption in acetonitrile solution, which was attributed to thermal valence tautomerism.[134]

Magnetic measurements for **C6** revealed that the complex is diamagnetic in the temperature range 2 K to 380 K, which is a further confirmation of the redox states derived from the structural data. In contrast to the previously reported complex $(Et_3NH)[Co(pym)_2(tbcat)_2] \cdot H_2O$, a valence tautomeric transition has not been observed in the accessible temperature range in solid state. Strong electron withdrawal of the bromine substituents seems to disfavor the intramolecular electron transfer from one catecholate to the central cobalt ion in this mononuclear case. Assuming a polynuclear complex with a μ_2 coordination of this tetrabromocatecholate or a similar electronically modified ligand, where the withdrawal of multiple metal ions is stronger, this ligand may exhibit frontier orbitals which energetically allow valence tautomerism.

Regarding these three examples of mononuclear dioxolene complexes, which serve as a simple reference in the following sections, it can be seen that the valence tautomeric equilibrium is very sensitive to modifications in the dioxolenes as well as in the auxiliary ligands. It is expected, that the introduction of additional metal ions

further increases the number of parameters. Furthermore, bridging dioxolenes hold additional exchange and electron transfer pathways to the metal ions due to a different and more complex orbital overlap. The next section presents various polynuclear transition metal dioxolene complexes with the aim of a structural understanding.

3.2 Polynuclear Dioxolene Complexes

3.2.1 Polynuclear Dioxolene Complexes by Self-Organization of Ligands

The first concept for the synthesis of polynuclear dioxolene complexes is taking advantage of "self-organisation" of small components. As outlined in section 1.3.7.4, dioxolene ligands have the ability to build multinuclear complexes by coordinating in bridging modes. To foster the increase of the nuclearity, additional bridging co-ligands are used. Despite their bridging and chelating nature, those auxiliary ligands must not coordinate to the metal too strongly, as this would cause the risk of displacing the main dioxolene ligands. Due to their comparatively weak binding to transition metal ions and a manifold of possible coordination modes,[135] carboxylate ligands have proven to be appropriate for the purpose of bridging co-ligands. In the present case these carboxylates are already included in the transition metal precursors. In addition, the solvent choice is crucial for the generation of polynuclear complexes. High solvent polarity usually increases the solvation enthalpy and stabilizes charged, solvated complexes, while the aggregation to larger moieties with a lower charge density is disfavored. Too low solvent polarities (as for hydrocarbons) however impede a ligand oxidation from a catechol to a semiquinone, which is essential in many syntheses. For these reasons, the complexes presented on the following pages were prepared in moderately polar organic solvents, which are sufficiently polar to allow oxidation processes or other reactions, which involve charged particles, but also sufficiently apolar to favor larger coordination clusters.

3.2.1.1 Cobalt Dioxolene Clusters

C7

The reaction of $[Co(piv)_2]_n$ (**P2**), 3,5-dbcat (**L1a**) and triethylamine in acetonitrile afforded two crystalline conformers of $[Co_3(3,5\text{-dbsq})_2(piv)_4(NEt_3)_2]$ **C7**: the triclinic, synclinal conformer **C7a** (see fig. 3.7(a)) and the monoclinic, antiperiplanar

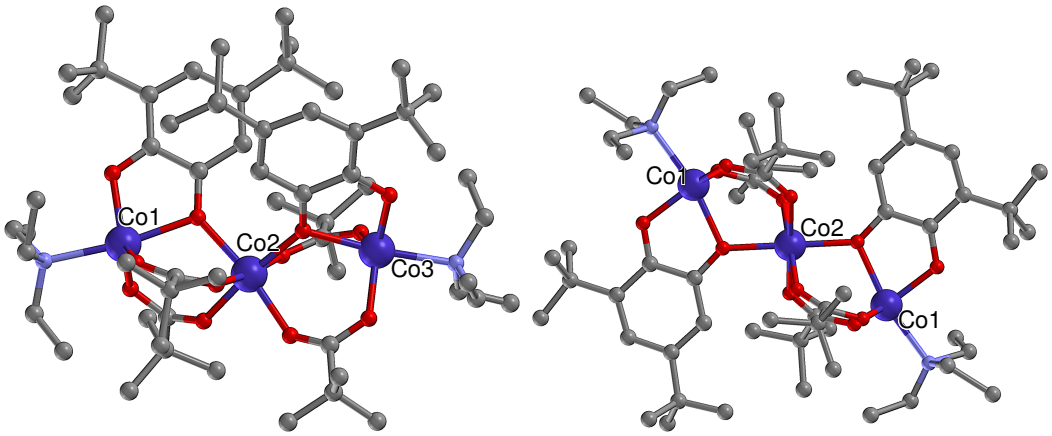

(a) Synclinal, triclinic **C7a** **(b)** Antiperiplanar, monoclinic **C7b**

Fig. 3.7: Molecular structures of $[Co_3(3,5\text{-dbsq})_2(piv)_4(NEt_3)_2]$ (**C7**)

conformer **C7b** (see fig. 3.7(b)). While most batches contained only the triclinic polymorph, the minority of batches contained small traces of monoclinic **C7b** as a side product.

C7b

Complex **C7b** crystallizes in the monoclinic space group $P2_1/c$ and contains three linearly arranged cobalt(II) ions, for which the central cobalt is positioned on an inversion center. For the nonbonded Co…Co distances 3.537 Å are found. Each of the outer metal ions is coordinated by a 3,5-di-*tert*-butyl-1,2-semiquinonate (coordinated in a μ_2-η^2:η^1 mode and bridging to the central cobalt ion), one terminal triethylamine ligand and two pivalate ligands, bridging to the central cobalt ion. This coordination results in an octahedral coordination sphere for the middle cobalt ion and distorted trigonal bipyramidal surroundings for the outer metals. Both dioxolene ligands are in an antiperiplanar configuration and *trans* with respect to the central cobalt ion. One of the pivalate *tert*-butyl groups and the triethylamine ligand are disordered over two positions. While the Co−O bond lengths around the central cobalt ion are concentrated around 2.08 Å with only small deviations, for the outer cobalt ions it has to be differentiated between the axial and equatorial bonds. The equatorial metal-oxygen bonds amount to about 1.97 Å. For the axial Co−O and Co−N distances much larger values are found with 2.169 Å and 2.232 Å, respectively. The Co−O bond lengths are consistently in the order of magnitude of distances found for similar *high spin* Co^{II} complexes with octahedral or trigonal bipyramidal coordination environment.[133,136–141] The bond distance to the axial triethylamine however is unusually long, and may be explained by the weak interaction with the metal ion, as well as by steric repulsion due to the *tert*-butyl groups. To confirm

Tab. 3.4: Metrical oxidation states for the dioxolene ligands in **C7b** based on crystallographically determined bond lengths at 173 K

Ligand	Metrical oxidation state (*MOS*)
Dioxolene 1	−0.95

the dioxolenes' oxidation state, a bond lengths analysis has been conducted. For both (crystallographically equivalent) ligands, alternating bond lengths patterns and comparatively short C−O bonds are found, which indicated semiquinonoid character, which is also confirmed by the calculated metrical oxidation state $MOS_{\text{lig 1/2}} = -0.95$. In comparison to the polynuclear iron dioxolene complexes **C1**, **C2** and **C3** examined in prior studies (see page 29), it is remarkable that for the present cobalt complex a bridging coordination of a semiquinone is possible. For the related iron complexes, the increased metal charge of the ferric iron only allows the dianionic oxidation state of a catecholate as a bridging moiety due to increased electron withdrawal and destabilization of soft, weakly charged ligands. Interestingly, this linear complex bears a strong resemblance to $[Co_3(piv)_6(NEt_3)_2]$, which was first reported by Denisova et al. in 2002. For this compound, additional pivalates are bound instead of the dioxolene ligands in the present complex. Due to the weaker chelating character of pivalate in comparison to *o*-semiquinones, an interesting structural rearrangement of the pivalate coordination with a change from trigonal bipyramidal to tetrahedral coordination of the outer cobalt ions is observed at room temperature.[136,142]

As the monoclinic polymorph **C7b** could only be separated in traces, an analysis beyond structural descriptions, such as the examination of the magnetic properties, was unfortunately not possible.

C7a

The triclinic polymorph which crystallizes in the space group $P\bar{1}$ exhibits the same molecular formula as well as the same bridging coordination modes of the ligands, just that in this case the two dioxolene ligands are not antiperiplanar. Half the molecule is rotated around one Co−Co axis to result in a synclinal configuration (see fig. 3.7(a)). As a consequence, the symmetry of the whole trinuclear moiety is reduced and both sides of the molecule are now crystallographically inequivalent. In contrast to the monoclinic polymorph, complex **C7a** is bent, the Co−Co−Co angle is found to be 155.7° with Co…Co distances of 3.522 Å and 3.541 Å. This deformation is due to the carboxylates' and dioxolenes' different number of atoms in the bridging parts. The resulting tilts cannot cancel each other out as it was the

Tab. 3.5: Metrical oxidation states for the dioxolene ligands in **C7a** based on crystallographically determined bond lengths at 173 K

Ligand	Metrical oxidation state (*MOS*)
Dioxolene 1	−0.95
Dioxolene 2	−0.96

case for the inversion symmetric **C7b**. Despite this quite remarkable rearrangement, the bond lengths are rather equal for both rotational conformers. Accordingly, the Co−O/N distances and the metrical oxidation states of $MOS_{\text{lig 1}} = -0.95$ and $MOS_{\text{lig 2}} = -0.96$ for both ligands (which are now crystallographically independent) resemble those of the monoclinic conformer.

Figure 3.8(a) shows the temperature dependence of $\chi_M T$ for **C7a** at 1 T. The curve continuously decreases as the temperature is decreased, indicating dominant antiferromagnetic couplings between the five spin centers. At 300 K a value of $\chi_M T = 6.9\,\text{cm}^3\,\text{K}\,\text{mol}^{-1}$ is measured, which is above the spin only value of $6.375\,\text{cm}^3\,\text{K}\,\text{mol}^{-1}$, despite of the absence of a plateau at high temperatures. Therefore, the contributions of the cobalt orbital momentum needs to be taken into account, which is in agreement with the T ground term for the central, octahedral *hs* cobalt(II).[1] At 2 K, a value of $0.601\,\text{cm}^3\,\text{K}\,\text{mol}^{-1}$ is observed. As the magnetization measurements shown in fig. 3.8(b) do not reveal a saturation magnetization at low temperatures and high fields, a corresponding spin ground state cannot be determined. Obviously, multiple low lying states are present in energetic proximity instead of one single well-isolated ground state. However, a simulation of the susceptibility and magnetization data was not possible, due to the intricate coupling scheme with five spin centers.

In addition to the common measurements of the magnetic susceptibility and magnetization, laser irradiation experiments were carried out. For this purpose, a powdered sample of **C7a** was cooled down to 10 K within a SQUID magnetometer and irradiated with a laser of a wavelength of $\lambda = 520\,\text{nm}$ while the susceptibility was monitored. Upon irradiation, an immediate drop of the susceptibility is observed. Local light-induced heating of the sample was determined to be one contribution to this decrease. However, even after switching off the laser, a residual drop of the magnetic moment is evident. Subsequently, the temperature of the sample is

[1] The possible orbital contribution for trigonal bipyramidal cobalt(II) ions is discussed in more detail on page 66.

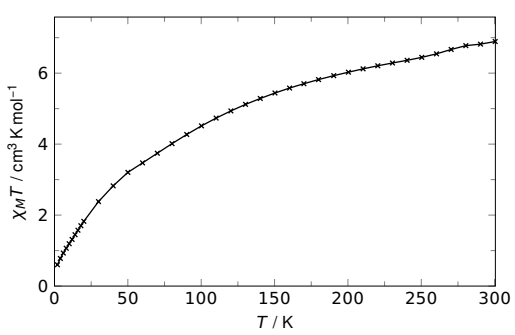

(a) Temperature dependence of the magnetic susceptibility for **C7a**

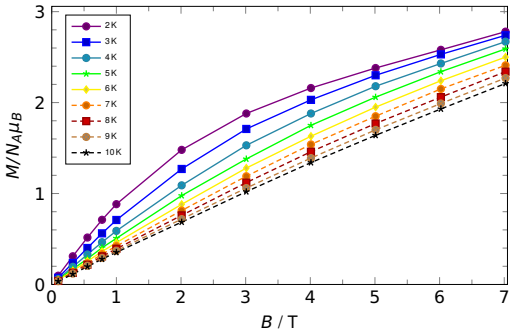

(b) Magnetization measurements for **C7a**

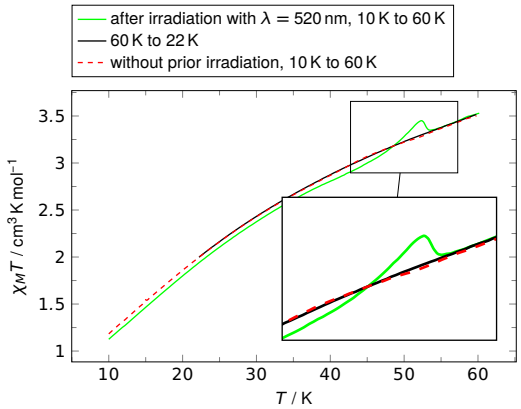

(c) Irradiation experiments for containing **C7a**

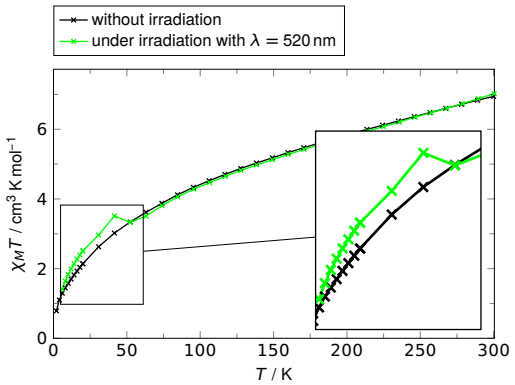

(d) Irradiation experiments for a PVC foil containing **C7a**

Fig. 3.8: Magnetic measurements for **C7a**

slowly increased at a rate of 0.3 K min^{-1} (see green curve in fig. 3.8(c)). At 47 K, the $\chi_M T$ value of the irradiated sample increases and the unirradiated sample's curve is crossed. A maximum is observed at 52 K, after which the susceptibility relaxes to the value of the unirradiated sample. This behavior is associated with the light-induced generation of a metastable state with a different magnetic moment. As the examined bulk powder sample of **C7a** is very opaque and strongly absorbing, the laser light is expected to only very weakly penetrate into the surface. Therefore, the light-induced excitation of only a small percentage of the sample is possible and the small differences of irradiated and unirradiated sample in fig. 3.8(c) are explained.

Furthermore, the properties under continuous irradiation were examined. To overcome the challenge of the complex' strong absorbance, a polyvinyl chloride foil containing 8 % of compound **C7a** was prepared by dissolving defined amounts of **C7a** and PVC in tetrahydrofuran, followed by the evaporation of the solvent in a vac-

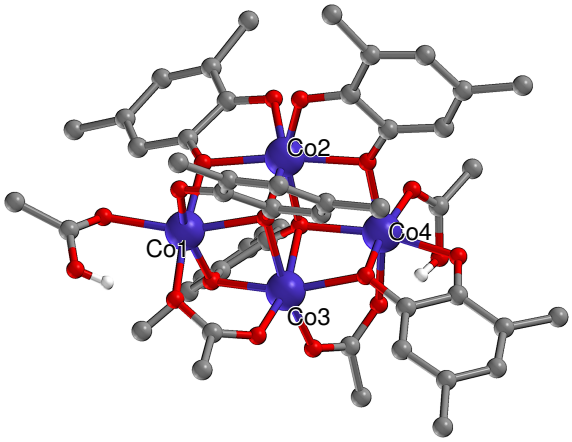

Fig. 3.9: Molecular structure of $[Co_4(3,5\text{-dbsq})_4(3,5\text{-dbcat})(piv)_2(Hpiv)_2]$ (**C8**). Methyl groups have been omitted for clarity.

uum. The resulting foil is much more transparent and allows a better penetration by light. The measurement of $\chi_M T$ as a function of temperature is shown in fig. 3.8(d). Without irradiation (see black curve), the curve resembles that of the bulk material. Under continuous irradiation with a laser of 520 nm an increase of $\chi_M T$ below 45 K is observed.

Obviously, the metastable state of the bulk material described above differs from the photostationary state found under continuous irradiation. For an insight into the electronic nature of these excited states, electron density measurements at the SPring-8 synchrotron in Hyōgo Prefecture, Japan were anticipated. Unfortunately, X-ray diffraction measurements below 60 K were impossible due to radiation damage of the cryocooled crystals. Additionally, EPR spectra of **C7a** were recorded at low temperatures. However, an irradiation during the measurements did not change the resulting resonance significantly. For these reasons, no further statements about the character of the excited states can be made.

In a similar reaction, using $[Co_2(OH_2)(piv)_4(Hpiv)_4]$ (**P1**) as a starting material, the complex $[Co_4(3,5\text{-dbsq})_4(3,5\text{-dbcat})(piv)_2(Hpiv)_2]$ (**C8**, see fig. 3.9) could be prepared as monoclinic crystals with the space group $P2_1/c$. In contrast to **C7**, its molecular structure is rather complex and asymmetric. The compound consists of four divalent cobalt ions in distorted octahedral ligand surroundings to form a butterfly-like $[Co_4(\mu_3\text{-}O)_2]^{4+}$ core. While the two deprotonated pivalate ligands form a bridging coordination between Co1 and Co3 or Co3 and Co4, respectively, the two protonated pivalates are loosely bound to Co1 and Co4 with one oxygen atom and form hydrogen bridges to the neighboring carboxylates. Three of the five dioxolene

Tab. 3.6: Metrical oxidation states for the dioxolene ligands in **C8** based on crystallographically determined bond lengths at 173 K

Ligand	Metrical oxidation state (*MOS*)
Dioxolene 1	−1.02
Dioxolene 2	−1.09
Dioxolene 3	−1.00
Dioxolene 4	−2.09
Dioxolene 5	−1.14

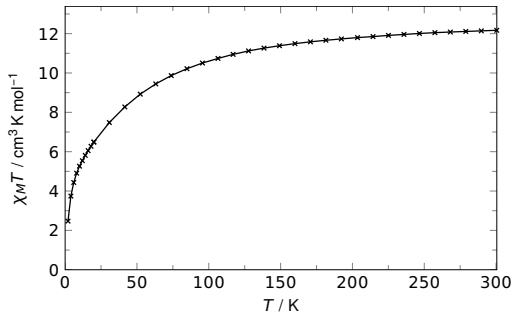

Fig. 3.10: Temperature dependence of the magnetic susceptibility of **C8** ($B = 1$ T). Black solid lines are for guidance only.

ligands are coordinated in a 1:2κ^2O^1,2κO^2 ($\equiv \mu_2$-η^2:η^1) manner (dioxolene 1 bridges Co2 and Co1, dioxolene 2 bridges Co2 and Co4, dioxolene 3 bridges Co4 and Co3). The remaining two dioxolene ligands are part of the $[Co_4(\mu_3\text{-}O)_2]^{4+}$ butterfly core and thus contain μ_3-bridging oxygen donor atoms. For dioxolene 4 a 2:3:4κ^3O^1,1:3κ^2O^2 coordination is found, whereas dioxolene 5 exhibits a 1:2:3κ^3O^1,1κO^2 bonding. Regarding the ligand bond lengths, ligand 4, which bonds to all four cobalt ions and thus experiences the strongest electron withdrawal, is found to have a dianionic catecholate character. The remaining dioxolenes show shorter C−O bond lengths and alternating short-long patterns of the C−C bonds and are hence best described as semiquinones, which is also confirmed by the metrical oxidation states (see table 3.6). Together with the two negatively charged pivalates, the eight positive charges from the *hs*-cobalt(II) ions can be neutralized.

Figure 3.10 shows the temperature dependence of the product $\chi_M T$ for **C8**. In the present case, a simulation of the magnetic data would not be reasonable, as the complex contains eight different spin centers with numerous exchange pathways. Even if additional effects such as spin orbit coupling or zero-field-splitting were excluded from the simulations (which is not appropriate in this case), the fitting of this rather simple curve would be too overparameterized. Therefore, only a qualitative discussion is possible. At high temperatures, the curve converges towards a plateau

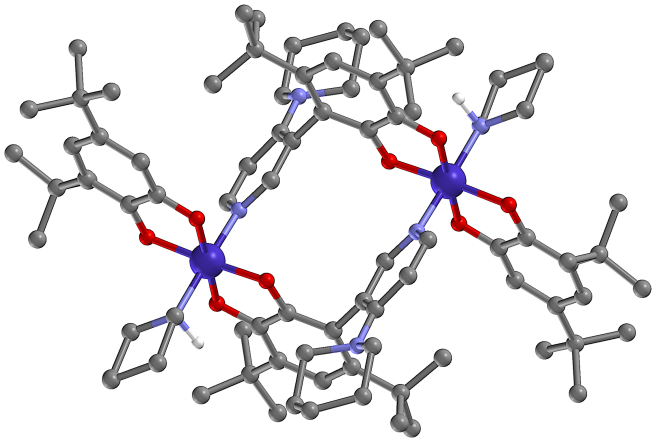

Fig. 3.11: Molecular structure of $[Co_2(3,5\text{-dbsq})_2(pipycat)_2(pip)_2]$ (**C9**)

with 12.17 $cm^3\,K\,mol^{-1}$, which is significantly larger than the expected spin-only value for four non-interacting $S = \frac{3}{2}$ and four $S = \frac{1}{2}$ centers (corresponding to the four *high spin* Co(II) ions and four semiquinonates) with $g = 2$ (9 $cm^3\,K\,mol^{-1}$). Therefore, orbital contributions have to be taken into account for the cobalt ions. Given that the semiquinones adopt the g-tensor of a free electron $g_{sq} = 2.0023$, that all *hs*-cobalt(II) ions have the same g-factor and that the thermal energy at 300 K is sufficiently large to overcome all exchange interactions, the effective mean g-factor for the cobalt ions can be calculated using the spin-only formula. The obtained value $g_{Co} = 2.43$ is in good agreement with the g-values found for similar *hs*-cobalt(II) complexes. At low temperatures, a continuous decrease of $\chi_M T$ is observed, presumably caused by dominant antiferromagnetic couplings between the spin centers. As this degrease is gradual and without any steps, no signs of a valence tautomeric conversion to a (partial) Co^{3+}(cat) tautomer at lower temperatures are apparent.

Complex **C9**, which is shown in fig. 3.11, was synthesized from the starting materials $[Co(piv)_2]_n$ (**P2**), 3,5-di-*tert*-butylcatechol (**L1a**) and piperidine in acetonitrile. The formation of this dinuclear compound includes an unusual derivatization of the dioxolene ligand to 3-(4-piperidino-3-pyridyl)-4,6-di-*tert*-butylcatecholate (pipycat) *in situ*. This reaction, whose exact mechanism is still unknown, involves two oxidative ring fusions and the oxidation of one piperidine to a pyridyl unit. In similarity to the formation of 4,6-di-*tert*-butyl-3-(piperidin-1-yl)benzene-1,2-diolates for **C5**, this reaction is presumably driven by a metal-mediated activation of the catecholate, followed by radical oxidation with atmospheric dioxygen. The resulting ligand offers two donor functionalities, the bidentate catecholate unit and the pyridyl nitrogen

Tab. 3.7: Metrical oxidation states for the dioxolene ligands in **C9** based on crystallographically determined bond lengths at 173 K

Ligand	Metrical oxidation state (*MOS*)
Dioxolene 1	−1.17
Dioxolene 2	−1.85

atom. As the coordination angle between these two sites is approximately 90° in the energetically most favored conformation, the ligand can be understood as a '90° donor building block' as defined for supramolecular self-assembly and the *directional bonding approach*.[143,144] On the other hand, a $[Co(3,5\text{-dbsq})(pip)]^{2+}$ unit can be regarded as a '90° acceptor'. The combination of two '90° donor' ligands with two 90° cobalt units allows the formation of a molecular square with the formula $[Co_2(3,5\text{-dbsq})_2(pipycat)_2(pip)_2]$. This complex crystallizes in the triclinic space group $P\overline{1}$ and the asymmetric unit, which includes half the square and an additional acetonitrile solvent molecule, bears a disordered *tert*-butyl and piperidyl residue. The slightly distorted octahedral coordination sphere around the cobalt ions contains four dioxolene oxygen donor atoms as well as a piperidine and pyridine nitrogen. All cobalt–donor atom bond lengths (approximately 1.89 Å and 2.00 Å for O and N donation, respectively) are in good agreement with the expected geometry for *ls*-cobalt(III) complexes.[133] The two different dioxolene ligands exhibit structural differences. While the unmodified dioxolene ligand (dioxolene 1) shows the typical pattern of alternating bond lengths, the modified dioxolene is found to have characteristic aromatic bond lengths. Consistently, the calculated metrical oxidation states are $MOS_{\text{lig 1}} = -1.17$ and $MOS_{\text{lig 2}} = -1.85$.

Figure 3.12 shows the measurements of the magnetic susceptibility, the magnetization and the applied coupling scheme. Over the whole temperature range $\chi_M T$ takes a constant value of 0.82 $cm^3\,K\,mol^{-1}$ with only a slight decrease at very low temperatures. The field dependent magnetization measurements shown in fig. 3.12(b) exhibits a saturation magnetization corresponding to two unpaired electrons at 2 K and strong magnetic fields. These observations are in good agreement with the fact, that the only two paramagnetic centers in **C9** are the semiquinones with $S = \frac{1}{2}$ each. For the same reason, the coupling scheme applied for the simulation of the magnetic data as depicted in fig. 3.12(c) is rather simple, as only the two $S = \frac{1}{2}$ semiquinones are involved. The best simultaneous fit of the susceptibility and magnetization data is yielded with $-0.33\,cm^{-1}$ for the exchange parameter J and

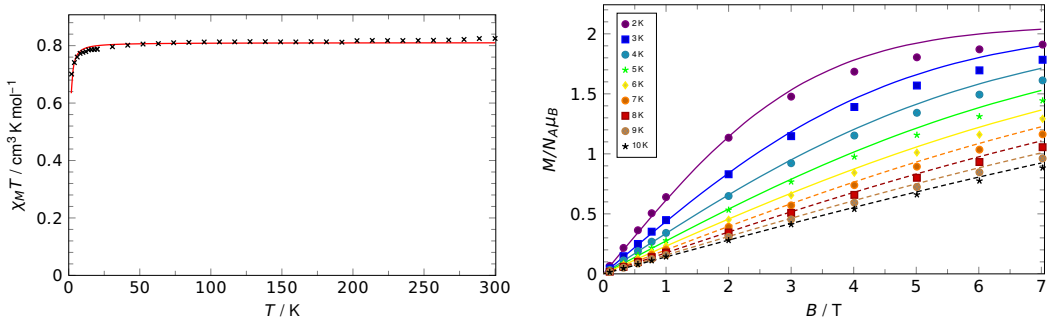

(a) Magnetic susceptibility

(b) Magnetization

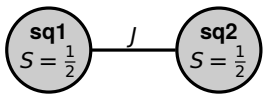

(c) Coupling scheme

Fig. 3.12: Magnetic data of **C9** ($J = -0.33\,\mathrm{cm}^{-1}$, $g = 2.08$)

a Landé factor of $g = 2.08$. Given the organic character of the two spin centers, the g factor without significant orbital contributions is justified. The fact that the two semiquinonate ligands are located at opposite ends of the dinuclear complex without direct bonding interactions further explains the very small, almost negligible exchange interaction resulting from the fit of the magnetic data. A simulation as two uncoupled $S = \frac{1}{2}$ centers only slightly increases residual error of the fit and would also be reasonable.

3.2.1.2 Copper Dioxolene Cluster

As a second redox-active metal, which provides the possibility of a valence tautomeric transition, copper was chosen. In analogy to the self-assembly of cobalt dioxolenes, basic copper pivalate **P3** was used as starting material.

The reaction of $[Cu_2(piv)_4(EtOH)_2]$ (**P3**) and 3,5-di-*tert*-butylcatechol (**L1a**) in acetone yielded the hexanuclear copper dioxolene $[Cu_6(3,5\text{-dbsq})_4(3,5\text{-dbcat})_2(piv)_4]$ (**C10**), which crystallizes in the triclinic space group $P\overline{1}$. The molecular structure of this complex (see fig. 3.13) is best described as a central tetranuclear moiety with capping planar $[Cu(3,5\text{-dbsq})_2]$ units which are weakly bound at both sides. In the inner $[Cu_4(3,5\text{-dbcat})_2(piv)_4]$ part the two catecholate ligands are bridging two paddle wheel-like $[Cu_2(piv)_2]$ units in a 1:2:3κ^3O^1,4:5κ^2O^2 fashion. This type of bridging mode of a catecholate ligand is very unusual and has not been observed before in the complexes published in the Cambridge Structural Database. For the

C10

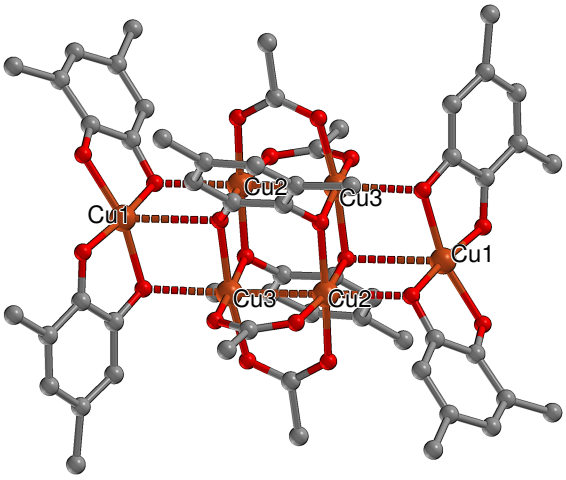

Fig. 3.13: Molecular structure of $[Cu_6(3,5\text{-dbsq})_4(3,5\text{-dbcat})_2(piv)_4]$ (**C10**). Methyl groups have been omitted for clarity.

Tab. 3.8: Metrical oxidation states for the dioxolene ligands in **C10** based on crystallographically determined bond lengths at 173 K

Ligand	Metrical oxidation state (*MOS*)
Dioxolene 1	−1.14
Dioxolene 2	−1.12
Dioxolene 3	−1.99

related polydentate bridging modes 1:2κ^2O^1,3:4κ^2O^2 and 1:2:3κ^3O^1,3:4κ^2O^2 only a handful of other complexes are reported.[145–148] For the five-coordinate copper ions of the inner $[Cu_2(piv)_2]$ units, short Cu−Cu distances of 2.66 Å are found, which is similar to the metal-to-metal distance in metallic copper. All six copper atoms are in square pyramidal oxygen environment. While the planar Cu−O distances are in the region of 1.95 Å, the axial bond lengths are longer with about 2.25 Å. These values are within the range typically found for copper(II) complexes with oxygen donor ligands and square pyramidal geometry.[149–151] A bond lengths analysis of the dioxolene ligands revealed the metrical oxidation states to be $MOS_{lig\,1} = -1.14$ $MOS_{lig\,2} = -1.12$ $MOS_{lig\,3} = -1.99$, where dioxolene 1 and 2 are the terminal dioxolenes of the outer $[Cu(3,5\text{-dbsq})_2]$ unit and dioxolene 3 is the inner bridging catecholate. Again in this complex, it is observed that increased electron withdrawal by multiple metal ions stabilizes the higher charged dianionic catecholate.

For the quantification of the coupling strengths between the individual spin centers, the temperature dependence of the magnetic susceptibility and the field-dependent magnetization were measured (see fig. 3.14). At 2 K, the product $\chi_M T$ converges towards the value 0.914 $cm^3\,K\,mol^{-1}$. For increasing temperatures, the curve grad-

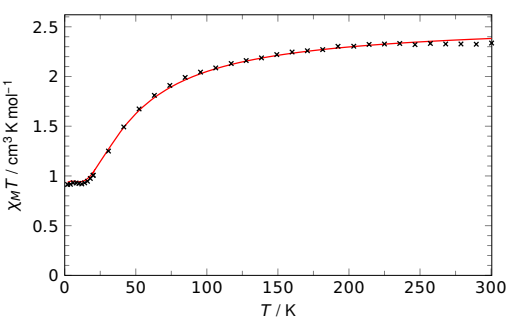

(a) Magnetic susceptibility

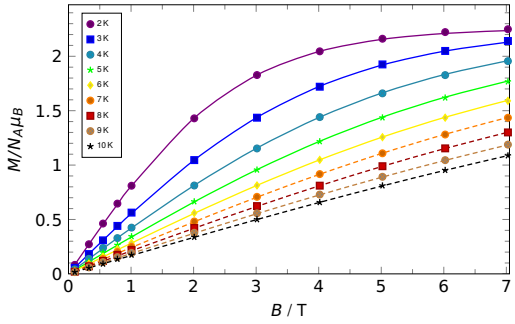

(b) Magnetization

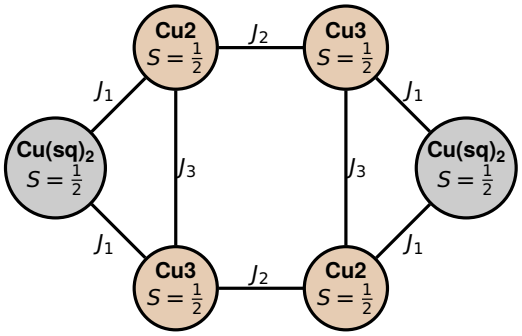

(c) Coupling scheme

Fig. 3.14: Magnetic data of **C10** ($J_1 = -17.0\,\mathrm{cm}^{-1}$, $J_2 = -0.1\,\mathrm{cm}^{-1}$, $J_3 = -8.6\,\mathrm{cm}^{-1}$, $g = 2.19$)

ually increases and approaches a plateau with $\chi_M T = 2.33\,\mathrm{cm}^3\,\mathrm{K\,mol}^{-1}$ at high temperatures. The magnetization curve at 2 K converges to a saturation magnetization corresponding to two unpaired electrons. The interpretation of this complex entity of ten interacting spin centers with $S = \frac{1}{2}$ requires some simplifications. Based on the evaluation of similar copper dioxolenes, very strong antiferromagnetic copper–semiquinonate couplings are expected within the capping moieties [Cu(3,5-dbsq)$_2$].[152] Supposing these coupling strengths exceed the thermal energy, [Cu(3,5-dbsq)$_2$] may be described as a single spin center with $S = \frac{1}{2}$. This reduces the number of spin centers to six and allows the simulation of the susceptibility and magnetization data with an effective exchange Hamiltonian according to the coupling scheme depicted in fig. 3.14(c). With fixed $g_{\mathrm{Cu(sq)_2}} = 2.00$ the iterative fit of the susceptibility and the magnetization yielded $J_1 = -17.0\,\mathrm{cm}^{-1}$, $J_2 = -0.1\,\mathrm{cm}^{-1}$, $J_3 = -8.6\,\mathrm{cm}^{-1}$ and a mean Landé factor $g_{\mathrm{Cu}} = 2.19$. The most interesting and unexpected result of these simulations is the negligible value found for J_2, the Cu…Cu exchange within the [Cu(piv)$_2$]$^{2+}$ fragment. For the structurally related dinuclear copper carboxylates, it is known that a strong antiferromagnetic coupling between the copper ions is favored, which is due to superexchange interaction over the triatomic

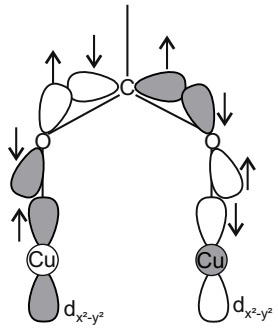

Fig. 3.15: Superexchange pathway for copper carboxylates leading to antiferromagnetic interaction of the copper cores[154]

π delocalized carboxylate ligands (see superexchange pathway in fig. 3.15).[153] The weak δ interaction of the two spin-carrying copper $d_{x^2-y^2}$ orbitals was found to be negligible in spite of the comparatively short Cu…Cu distance of 2.66 Å. In the present case, however, not only carboxylate bridges, but also catecholate bridges are involved. These ligands provide a tetra-atomic exchange pathway, which in contrast to the pivalate bridges favor a ferromagnetic coupling of the two coordinated copper ions. The coupling parameter of about $J = 0\,\mathrm{cm}^{-1}$ may thus be interpreted as a result of the competition of both exchange pathways, which cancel each other out. However, the magnetic data shows no signs of valence tautomeric transitions to a Cu^{I}(sq) species.

3.2.1.3 Nickel Dioxolene Cluster

C11

On the way to novel polynuclear dioxolene complexes, the nickel coordination cluster $[Ni_4(3,5\text{-dbcat})_2(H3,5\text{-dbcat})(piv)_2(MeCN)_4]$ (**C11**) has been synthesized. The starting material $[Ni(piv)_2]_n$ (**P5**) was reacted with 3,5-di-*tert*-butylcatechol (**L1a**) and triethylamine to yield the tetranuclear acetonitrile solvate which crystallizes in the triclinic space group $P\bar{1}$. The complex is best described as a stack of two $[Ni_2(3,5\text{-dbcat})(H3,5\text{-dbcat})(piv)(MeCN)_2]$ units with a bridging pivalate and two catecholates as shown in fig. 3.16(b). A stacking of two of these units under the formation of four Ni−O bonds with an average bond length of 2.07 Å yields distorted octahedral environments for all nickel(II) ions, building up a distorted $[Ni_4O_4]$ cube. The analysis of the Ni−O bond lengths clearly indicate divalent nickel in all four positions.[133] For the four dioxolene ligands, an assimilation of the C−C bond lengths and comparatively long C−O distances (see table B.13) are found in all cases, clearly indicating aromaticity. The metrical oxidation states of about −2 as listed in table 3.9 confirm these findings. Summing up the charges of the metal ions, dioxolene ligands

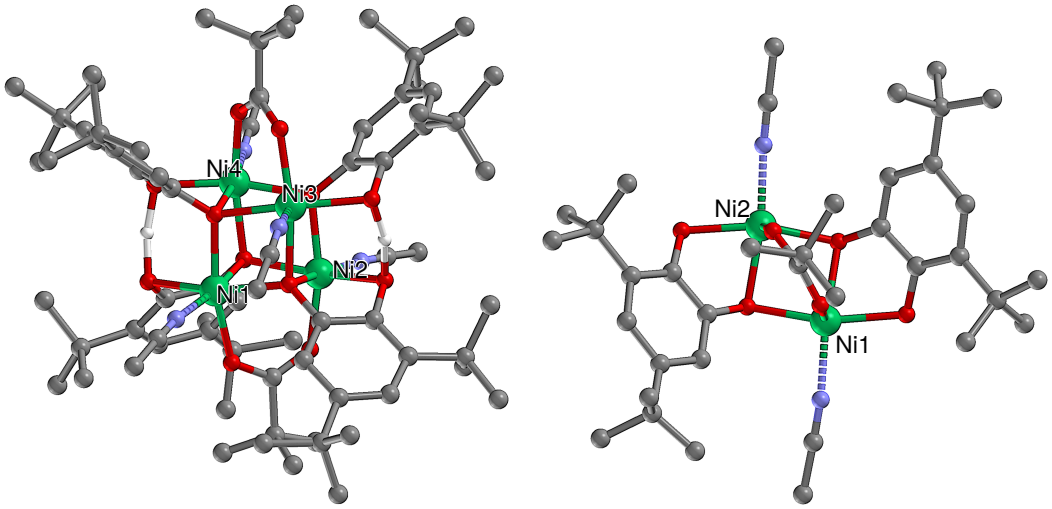

(a) Complete molecule **(b)** Half molecule in top view

Fig. 3.16: Molecular structure of $[Ni_4(3,5\text{-dbcat})_2(H3,5\text{-dbcat})(piv)_2(MeCN)_4]$ (**C11**)

Tab. 3.9: Metrical oxidation states for the dioxolene ligands in **C11** based on crystallographically determined bond lengths at 173 K

Ligand	Metrical oxidation state (*MOS*)
Dioxolene 1	−2.11
Dioxolene 2	−2.28
Dioxolene 3	−2.18
Dioxolene 4	−1.98

and pivalates, there are two excessive negative charges to be balanced. As the assignment of the oxidation states of the nickel ions and the catecholates is very reliable due to the significance of the bond lengths, two protons need to be added delocalized between the non-bridging catecholate oxygens. Although no residual electron density was found at these positions, the adjacent oxygen atoms point towards each other and have the perfect distance for a hydrogen bond. Hence, these two hydrogen atoms were added at the calculated positions and further refined.

The temperature dependence of the magnetic susceptibility is shown in fig. 3.17(a). For the high temperature regime values of $\chi_M T = 3.90\,\mathrm{cm^3\,K\,mol^{-1}}$ are detected, which is in the order of the spin only value for four uncoupled $S = 1$ nickel(II) centers ($\chi_M T = 4.00\,\mathrm{cm^3\,K\,mol^{-1}}$). With decreasing temperature, the magnetic moment gradually decreases, at first only slowly, below 80 K a faster decrease is observed. At very low temperatures, the curve approaches zero, reaching $0.10\,\mathrm{cm^3\,K\,mol^{-1}}$ at 2 K. Using the coupling scheme shown in fig. 3.17(b), it was possible to simulate the measured data. Two different types of exchange coupling were introduced:

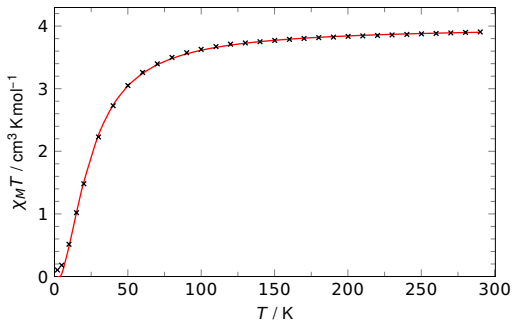

(a) Magnetic susceptibility

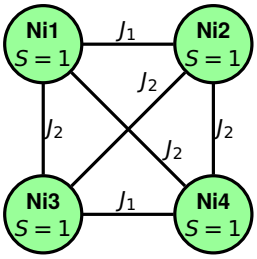

(b) Coupling scheme

Fig. 3.17: Magnetic data of **C11** ($J_1 = -8.64\,\mathrm{cm}^{-1}$, $J_2 = 2.70\,\mathrm{cm}^{-1}$, $g = 2.00$)

J_1, which corresponds to the Ni1–Ni2 and Ni3–Ni4 interactions (along the pivalate ligand) and J_2 for the remaining couplings. With Ni−O−Ni angles of about 90° for the J_1 exchange pathways and much larger angles for the latter paths (98.4° on average), significant differences of the geometries are present, which legitimate the assumption of two different exchange parameters. For the g values however a mean value for all nickel ions was assumed. A fit of the experimental curve led to $J_1 = -8.64\,\mathrm{cm}^{-1}$, $J_2 = 2.70\,\mathrm{cm}^{-1}$ and $g = 2.00$ as final values. The Landé factor close to the value for an isolated electronic spin is in agreement with the non-degenerate $^3A_{2g}$ ground state for octahedral nickel(II) ions (d^8), with low orbital contributions to the spin-only moment. The weak ferromagnetic interaction for J_1 is explained by the 90° Ni−O−Ni superexchange according to the Goodenough–Kanamori–Anderson rules[155–157] for two filled orbitals. For larger angles, an antiferromagnetic contribution becomes dominant due to a partial overlap of the spin-carrying orbitals involved in the superexchange. Therefore, an antiferromagnetic coupling parameter of $J_2 = -8.64\,\mathrm{cm}^{-1}$ is found. The gradual increase of the magnetic susceptibility with the temperature without steps and the goodness of the fit indicate the absence of valence tautomeric transitions for all catecholates. Due to the μ_3 bridging mode for all ligands and the (partial) protonation, this localization of valences is in accordance with the expectations.

3.2.1.4 Heterometallic Dioxolene Cluster

The first results of section 3.2.1.1 showed that polynuclear cobalt dioxolenes exhibit some interesting properties related to their nuclearity. For **C7a** for instance, the low temperature laser excitation experiments revealed an electronic transition to a metastable species, which might be a corresponding valence tautomer. One

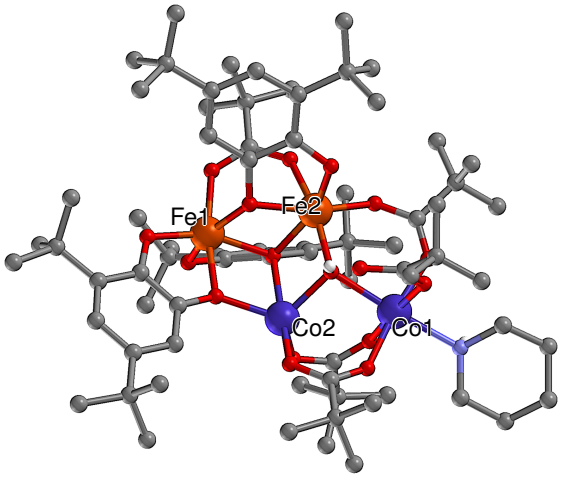

Fig. 3.18: Molecular structure of $[Co_2Fe_2(OH)(3,5\text{-dbcat})_3(piv)_5(pip)]^{2-}$ (**C12**). Piperidinium ions have been omitted for clarity.

main challenge, however, is the huge amount of parameters for the analysis of the magnetic data for increased nuclearity. Especially for magnetically complex ions like cobalt(II), which is subject to spin-orbit coupling, a simulation of the measured data sometimes is overparameterized. To overcome this issue, one idea was to rely on the knowledge about polynuclear iron dioxolenes, which are much easier to understand, as they will not undergo valence tautomeric transitions and do not exhibit spin-orbit coupling, and combine those with the more intriguing cobalt dioxolenes. The aim was the synthesis of a polynuclear complex, for which the generation of higher nuclearity is based on an iron backbone, while the redox-activity is found for the incorporated cobalt.

Substantial progress in this field was made with the synthesis of the heteronuclear iron–cobalt complex $(Hpip)_2[Co_2Fe_2(OH)(3,5\text{-dbcat})_3(piv)_5(pip)]$ (**C12**), which crystallized in the triclinic space group $P\overline{1}$. It was synthesized by reacting the heterometallic precursor $[Fe_2CoO(piv)_6(pip)_3]$ (**P8**) with 3,5-di-*tert*-butylcatechol (**L1a**) in acetone. The resulting tetranuclear complex with an asymmetric butterfly-like structure holds a $[Co_2Fe_2O_2]^{6+}$ core. While the μ_3 moiety of the Co_2Fe triangle is a hydroxyl ligand, the other $CoFe_2$ "wing" is bridged by the oxygen O3 of dioxolene 2, which is chelating this wing atom. Dioxolene 1 is similarly coordinated to the wing iron, but only bridging to the cobalt "body" atom. The third dioxolene ligands is coordinated to the body iron atom and bridging to the iron wing. Pivalate bridges account for the residual connections of adjacent metal ion. Additionally, a piperidine ligand and a non-bridging pivalate is bound at the wing cobalt ion. The coordination spheres are distorted octahedral except for the body cobalt ion, which is found in a

C12

Tab. 3.10: Metrical oxidation states for the dioxolene ligands in **C12** based on crystallographically determined bond lengths at 173 K

Ligand	Metrical oxidation state (*MOS*)
Dioxolene 1	–1.83
Dioxolene 2	–2.18
Dioxolene 3	–1.97

distorted trigonal bipyramidal surrounding. The assignment of the metal centers in the X-ray structure refinement was made based on small differences in the electron density, as well as on bond lengths and coordination sphere analyses. The resulting geometries are characteristic for the respective metal ions – rather isotropic octahedra with M−O bond lengths of approximately 2.00 Å for *high spin* iron(III) or an elongated octahedron and trigonal bipyramid with typical bond lengths for *high spin* cobalt(II).[133] This assignment was corroborated, as a Co:Fe ratio of 1:1 was found with atomic absorption spectroscopy for **C12**. For all bond dioxolene ligands the bond lengths indicate the oxidation state of catecholates, which is also quantified by the calculated metrical oxidation states (see table 3.10). As all dioxolenes are solely coordinated to the iron ions, it stands to reason that the same empirical rules as valid for homonuclear iron dioxolenes (see section 1.3.7.4) apply and that the influence of tho cobalt ions is negligible. The presence of bridging catecholates instead of semiquinones corroborates this hypothesis.

For the analysis of the magnetic exchange interaction between the metal centers, the temperature dependence of the magnetic susceptibility and the field-dependence of the magnetization were measured (see fig. 3.19). The $\chi_M T$ vs. T plot shows a nearly linear increase from 2.9 $cm^3\,K\,mol^{-1}$ at 6 K to 6.1 $cm^3\,K\,mol^{-1}$ at high temperatures. Below 6 K a steep decrease of $\chi_m T$ is observed. The room temperature value of 6.1 $cm^3\,K\,mol^{-1}$ is far below the theoretical spin-only value of 12.5 $cm^3\,K\,mol^{-1}$ for two uncoupled *hs*-iron(III) and two *hs*-cobalt(II) ions. Accordingly, strong antiferromagnetic couplings are estimated, which exceed the thermal excitation. The field-dependent measurements of the magnetization indicate a $S = 1$ ground state. Using the approximation of a fixed g factor $g = 2.00$ for the isotropic ferric irons, an iterative regression yielded the exchange parameters $J_1 = -25.4\,cm^{-1}$, $J_2 = -37.2\,cm^{-1}$, $J_3 = -38.1\,cm^{-1}$, $J_4 = 1.0\,cm^{-1}$ and $J_5 = -15.3\,cm^{-1}$ according to the coupling scheme in fig. 3.19(c) and the cobalt Landé factor $g_{Co} = 2.20$. It has to be noted that the large amount of parameters leads to poorly defined absolute values. However, a consolidation of coupling constants to reduce the number of

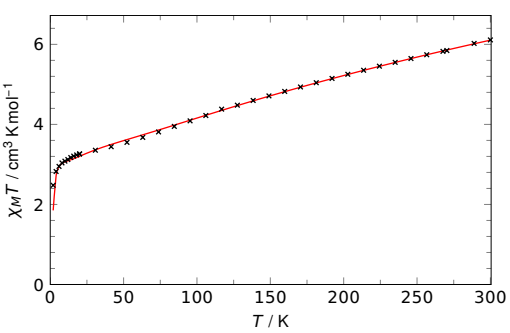

(a) Magnetic susceptibility

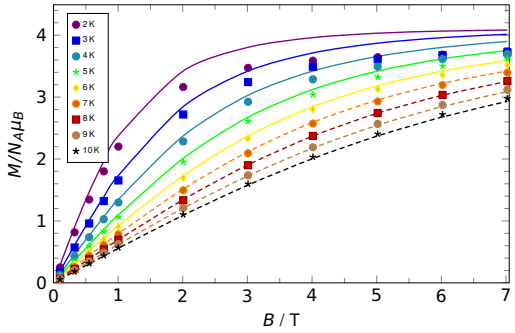

(b) Magnetization

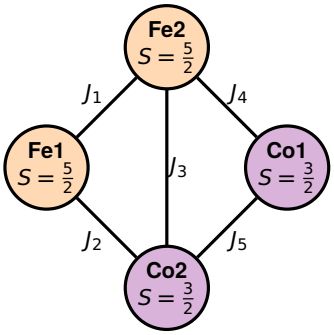

(c) Coupling scheme

Fig. 3.19: Magnetic data of **C12** ($J_1 = -25.4\,\mathrm{cm}^{-1}$, $J_2 = -37.2\,\mathrm{cm}^{-1}$, $J_3 = -38.1\,\mathrm{cm}^{-1}$, $J_4 = 1.0\,\mathrm{cm}^{-1}$, $J_5 = -15.3\,\mathrm{cm}^{-1}$, $g_{\mathrm{Fe}} = 2.00$ (fixed), $g_{\mathrm{Co}} = 2.20$)

parameters is not reasonable, as the corresponding exchange pathway geometries are very different due to the complex' asymmetry.

3.2.2 Polynuclear Dioxolene Complexes with Chelating Ancillary Ligands

The manifold of different dioxolene coordination clusters presented in section 3.2.1 nicely shows the potential of the chosen synthesis route involving the self-organization of small bridging ligands in rather apolar solvents. Numerous polynuclear complexes could be established in this way, which enable an insight into the enormous structural variety and the coordination mode's influence on the oxidation state properties for several redox-active metal ions. The chosen reaction conditions allow for a feasible, fast and straightforward synthesis of the desired complexes. Despite these arguments, syntheses of this type always require an extended period of trial and error with large numbers of rejects. Due to the low structural selectivity and preference of the ligands, the outcome of these self-organizing reactions is often the result of serendipity. Although this strategy opens the door to numerous unprece-

dented, unique complexes, the establishment of a closer related series of molecules or the targeted synthesis of an anticipated structural type is rather unlikely.

To overcome this issue, chelating ancillary ligands with defined coordination modes can be used. With the right choice of co-ligands the formation of the desired structures can be stimulated. Even so the selection of suitable ligands seems trivial, there are many demands to meet in the present work. First and most importantly, the ancillary ligand needs to allow defined polynuclear arrangements. Most of the common multidentate ligands known in literature favor the formation of mononuclear chelates. The introduction of a second or further chelating coordination pocket requires much more elaborate organic syntheses. Secondly, multidentate ligands usually form very stable complexes due to the entropic chelate effect. What sounds like an advantage may also cause trouble if one of the requirements is the additional coordination of a smaller ligand (e.g. the dioxolene ligands). Although dioxolenes are comparatively strong chelating ligands, multidentate co-ligands might easily suppress their coordination. Therefore, a compromise between counter-ligand strength and flexibility is necessary. A third requirement is the creation of a suitable environment for the dioxolene ligands. This includes covering of the dioxolene's steric demands as well as the offer of the right number and geometry of metal vacancies for a coordination.

The following sections will present the complexes resulting from syntheses with chelating ancillary ligands. This work can be divided into two general approaches: the use of salicylhydroxamic acid (H_3shi) as a pseudo-multi-chelating ligand (see section 3.2.2.1) and the utilization of specially synthesized bis-chelating ancillary ligands (sections 3.2.2.2 and 3.2.2.3).

3.2.2.1 Cobalt Complexes with Salicylhydroxamate Ancillary Ligands

Salicylhydroxamic acid (short H_3shi, see fig. 3.20) is an archetypal ligand for the synthesis of a special subtype of polynuclear complexes, the so-called metallacrowns.[158–163] An example of a general structure of a metallacrown backbone, the so-called 12-MC-4[2] [$M_4M'shi_4$], based on salicylhydroxamic acid is shown in fig. 3.21. This class of molecules reveals a cyclic repetition of the atom sequence [M−O−N−] to form structural analogs to the organic crown ethers with the sequence

[2]This nomenclature is in analogy to the nomenclature of organic crown ethers. The first number represents the ring size, the second determines the number of oxygen atoms.

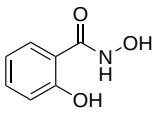

Fig. 3.20: Salicylhydroxamic acid (H_3shi)

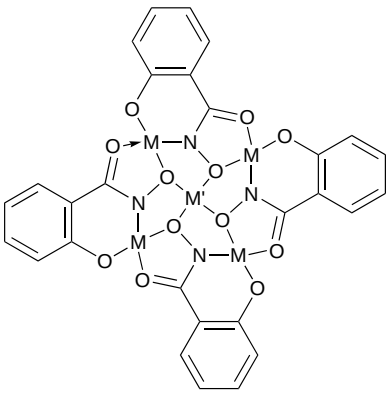

Fig. 3.21: General structure of a metallacrown backbone (12-MC-4) based on salicylhydroxamic acid (axial ancillary ligands omitted for clarity)

[C−C−O−]. As the donor atoms point towards the center of the ring, an additional cation (M' in fig. 3.21) can be enclosed. Without working out every single detail about the properties commonly found for metallacrowns, it is notable, that suchlike complexes feature a high solvent stability, are easily modified and have found widespread application in the fields of catalysis, single-molecule magnetism, magnetic resonance imaging, modeling of active sites in enzymes or molecular recognition. The synthesis of metallacrowns based on salicylhydroxamic acid was found to be straightforward, because the coordination of salicylhydroxamate to metal ions follows the rules of self-assembly, favoring a 12-MC-4 arrangement (see fig. 3.21). Despite the small size of the employed ligands, molecules with predictable structures can thus be synthesized reliably under suitable reaction conditions.

For the present work, advantage was derived from the unique self-assembly of metallacrowns. To tackle the problem of the unpredictable formation of polynuclear dioxolene complexes as presented in section 3.2.1, salicylhydroxamic acid was used as an ancillary ligand. The idea was that the simultaneous use of dioxolene ligands and H_3shi results in the assembly of a rigid pre-built metallacrown fragment in solution which is available for a coordination of the dioxolene ligand. This concept is illustrated in fig. 3.22. In the resulting complexes, the metallacrown fragment fulfills the task of an intricate ancillary ligand, which retains multiple metal ions at defined positions within the molecule. Likewise, the metallacrown entity is sufficiently flexible and little sterically demanding so that the additional coordination of dioxolene ligands is possible. The most important advantage over conventional co-ligands beside the synthetic feasibility is the comparable ligand strength of cate-

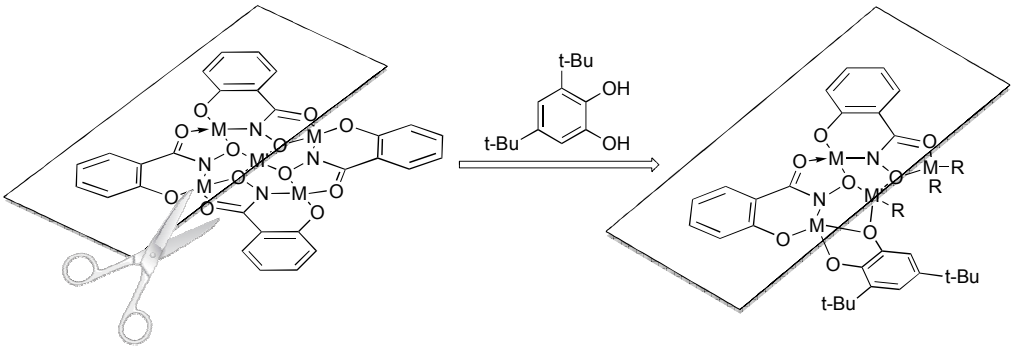

Fig. 3.22: Concept of using metallacrown fragments as a complex backbone

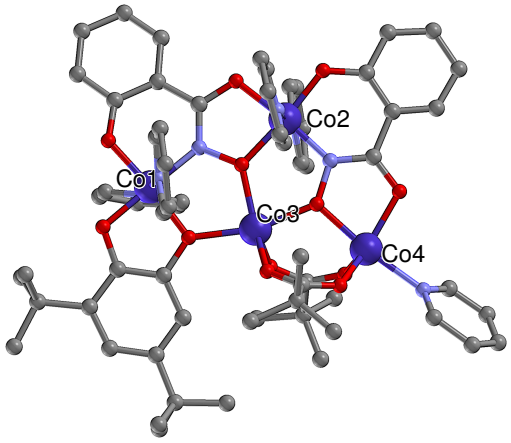

Fig. 3.23: Molecular structure of $[Co_4(shi)_2(3,5\text{-dbcat})(piv)_2(py)_5]$ (**C13**)

cholates/semiquinonates and hydroxamates. While common multidentate chelate ligands (given EDTA for example) exhibit very high complex association equilibrium constants, dioxolenes can easily compare with the bidentate salicyl hydroxamate and are thus not suppressed from a coordination to the metal.

C13

To implement this concept, $[Co_2(OH_2)(piv)_4(Hpiv)_4]$ (**P1**), salicylhydroxamic acid (H_3shi) and pyridine were reacted with 3,5-di-*tert*-butyl-1,2-benzoquinone (**L1b**) in acetonitrile. From this synthesis the tetranuclear cobalt complex $[Co_4(shi)_2(3,5\text{-dbcat})(piv)_2(py)_5]$ (**C13**) emerged, which crystallized in the monoclinic space group $P2_1/c$. This compound perfectly corresponds to the anticipated structural idea worked out in fig. 3.22. A major part of the molecule shows the typical coordination of two salicylhydroxamates to form a rather planar metalorganic metallacrown-like $[Co_4(shi)_2]^{4+}$ backbone. Instead of additional salicylhydroxamates, a 3,5-di-*tert*-butylcatecholate ligand binds to two of the cobalt ions in a μ_2-η^2:η^1 mode, extending the molecule plane. The residual vacant coordination sites are occupied by two bridging pivalates as well as five pyridines. For the two cobalt

Tab. 3.11: Metrical oxidation states for the dioxolene ligands in **C13** based on crystallographically determined bond lengths at 173 K

Ligand	Metrical oxidation state (*MOS*)
Dioxolene 1	−1.89

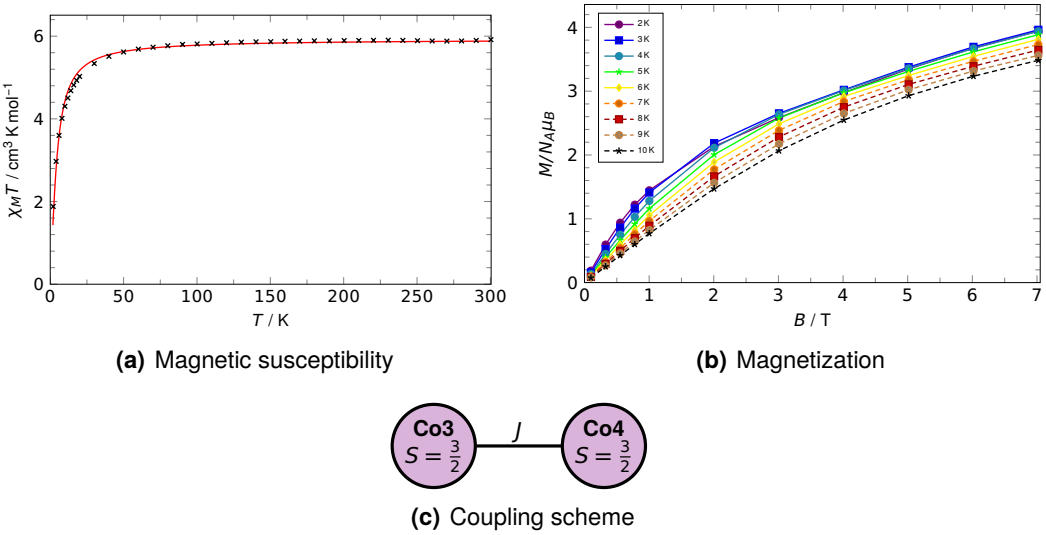

(a) Magnetic susceptibility

(b) Magnetization

(c) Coupling scheme

Fig. 3.24: Magnetic data of **C13** ($J = -0.68\,\mathrm{cm}^{-1}$, $g = 2.51$)

ions coordinated by the hydroxamate ligand's phenolate moieties (Co1 and Co2), slightly elongated octahedral coordination spheres with planar bond lengths of about 1.89 Å and axial bond lengths of about 1.96 Å are observed, indicating *low spin* cobalt(III) ions. The remaining metal centers exhibit distorted trigonal bipyramidal geometries with Co−O distances of approximately 2.00 Å as commonly found for *high spin* cobalt(II). Regarding the atom distances for the dioxolene ligand, a metrical oxidation state of $MOS = -1.89$ can be calculated, corresponding to the oxidation state of a dianionic catecholate. As this catecholate is bidentately coordinated to a trivalent cobalt ion, the complex offers the opportunity of a valence tautomeric transition caused by an intramolecular electron transfer from the catecholate to the metal ion at higher temperatures.

To evaluate this option, magnetic studies were conducted (see fig. 3.24). The $\chi_M T$ value at room temperature is $5.9\,\mathrm{cm}^3\,\mathrm{K\,mol}^{-1}$, which is much larger than the spin-only value for two independent $S = \frac{3}{2}$ *high spin* cobalt(II) centers. Therefore, a contribution of the orbital angular momentum needs to be taken into account. For decreasing temperatures, the magnetic moment of **C13** decreases to $1.88\,\mathrm{cm}^3\,\mathrm{K\,mol}^{-1}$ at 2 K. This observation is referred to an antiferromagnetic coupling of the two cobalt

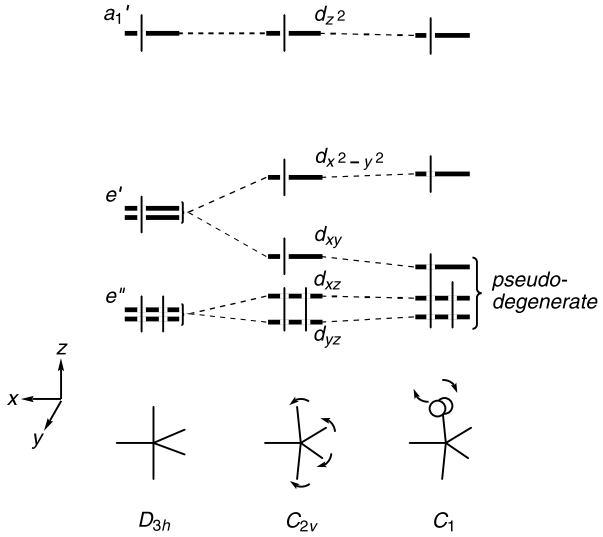

Fig. 3.25: Energy diagram of d-d separation for trigonal bipyramidal cobalt(II) showing the generation of pseudo-degenerate states with an orbital momentum under C_1 symmetry[164]

centers. In order to quantify the strength of this coupling the experimental susceptibility data were simulated using two exchange-coupled spin centers with $S = \frac{3}{2}$ as an underlying model (see fig. 3.24(c)). A good agreement with the measured data was found for the parameters $J = -0.68\,\mathrm{cm}^{-1}$ and $g = 2.51$. The obtained antiferromagnetic coupling is very weak, which explains the rather constant magnetic moment above 20 K. The large value found for g is somehow surprising, as the $^4A_2'$ ground term for a d^7 ion in an ideal D_{3h} trigonal bipyramidal symmetry does not have an orbital momentum. Hence, this effect has to be caused by either an admixing of excited states (e.g. the $^4E''$ state) or the geometric distortion to lower symmetries, causing pseudo-degenerate states (pseudo-T term) with an intrinsic angular momentum (see fig. 3.25).[164] Unfortunately, the magnetization data could not be fitted satisfactorily, even if including additional parameters like zero-field splitting. Apparently, the proper treatment of the low temperature regime, which is very sensitive to small changes within the close sequence of the electronically lowest lying states, requires the introduction of additional higher order effects. Given these rather featureless curves, an overparameterization of the simulation would be the consequence. The rather constant value at higher temperatures of $5.9\,\mathrm{cm}^3\,\mathrm{K\,mol}^{-1}$ indicates the absence of valence tautomeric transitions. Evidently, the hard donor ligand environment around the respective cobalt ion seems to stabilize the higher charged trivalent metal ion with a coordinated catecholate. To foster a valence tautomeric transition within the experimentally accessible temperature range, sub-

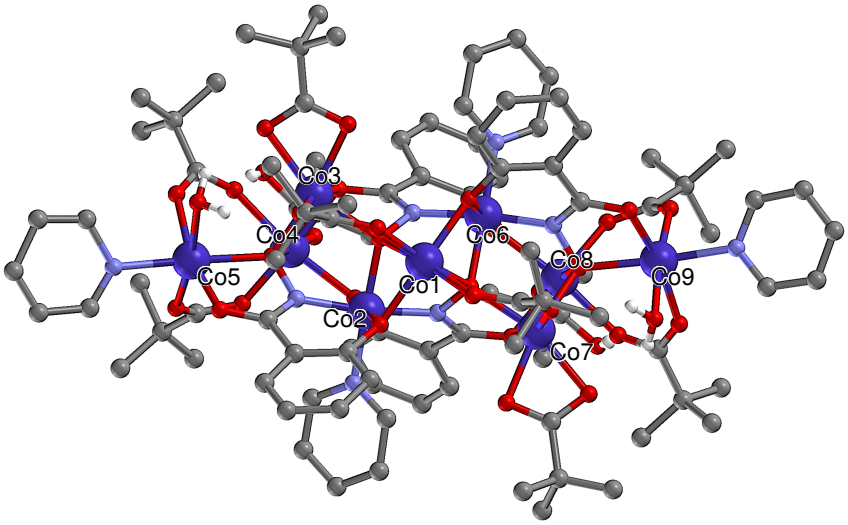

Fig. 3.26: Molecular structure of $[Co_2^{III}Co_7^{II}(shi)_4(piv)_8(Hpiv)_2(H_2O)_2(py)_4]$ (**C14**)

stantial modifications of the electronic ligand and co-ligand characters would be necessary.

Based on this successful synthesis using metallacrown fragments as preorganizing building blocks, numerous additional syntheses were prepared. One particular aim was the generation of an electronically modified complex with structural similarity to **C13** to enable valence tautomeric transitions. However, it became apparent that the use of salicylhydroxamic acid as ancillary ligands also can be somehow problematic, because dioxolene ligands were often found to be displaced and did not show up in the resulting compounds.

One exemplary complex with excluded dioxolenes is the nonanuclear cobalt coordination cluster $[Co_2^{III}Co_7^{II}(shi)_4(piv)_8(Hpiv)_2(H_2O)_2(py)_4]$ (**C14**). This intricate complex crystallizes in the triclinic space group $P\overline{1}$ and is C_2 symmetric. Distorted octahedral coordination spheres are found for all cobalt ions. Except for Co2 and Co6 Co−O and Co−N bond lengths of 2.00 Å to 2.25 Å are found, indicating divalent cobalt ions. The large deviations arise from Jahn-Teller distortions as well as steric effects due to strongly strained bridging ligands. Furthermore, two of the pivalates exhibit chelating coordination modes very small bite angles, again leading to strong distortions. Co2 and Co6, the two ions bridged to the central metal ion via phenolates, exhibit a more regular octahedral coordination environment with Co−O and Co−N distances of 1.89 Å to 1.97 Å and can thus be considered to be cobalt(III) ions. Interestingly, the two salicylhydroxamate ligands have very high bridging indices of μ_4 and μ_6, respectively.

C14

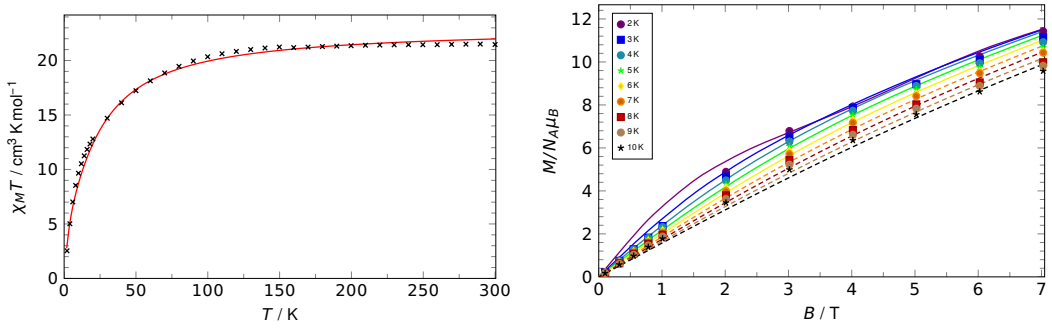

(a) Magnetic susceptibility

(b) Magnetization

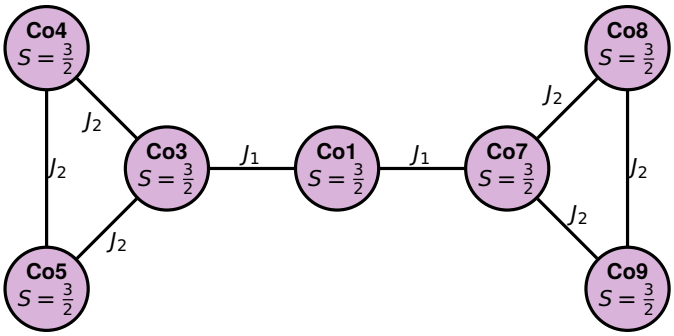

(c) Scheme

Fig. 3.27: Magnetic data of **C14**. $g_{\text{all}} = 2.65, J_1 = -0.33\,\text{cm}^{-1}, J_2 = -2.28\,\text{cm}^{-1}$

To get an insight into the electronic nature of the complex' metal centers, measurements of the magnetic susceptibility and the field-dependent magnetization were taken. Temperature dependent measurements of the susceptibility (see fig. 3.27(a)) show a constant value of $\chi_M T = 21.5\,\text{cm}^3\,\text{K}\,\text{mol}^{-1}$ at high temperatures, which is larger than the spin only value of $13.125\,\text{cm}^3\,\text{K}\,\text{mol}^{-1}$. Therefore, as anticipated for octahedral *high spin* cobalt(II) ions with their T ground terms, orbital contributions need to be taken into account. For decreasing temperatures, smaller $\chi_M T$ values are found, reaching $2.5\,\text{cm}^3\,\text{K}\,\text{mol}^{-1}$ at 2 K, which are supposed to be provoked by antiferromagnetic couplings of the paramagnetic centers. The field-dependent magnetization measurements (see fig. 3.27(b)) yield a narrow set of similarly shaped, nearly linear isotherms. This small influence of the temperature corresponds to the fact that there are many energetically low lying states in close proximity instead of one single separated ground state, which is in agreement with the presence of numerous interconnected metal centers with large numbers of interacting states. Even at 2 K and high fields, no saturation of the magnetization is achieved, which is also a result of energetically similar and weakly separated low lying states. Using simulations, the attempt of a quantification of the antiferromagnetic couplings was made. The underlying model was chosen according to the scheme depicted in

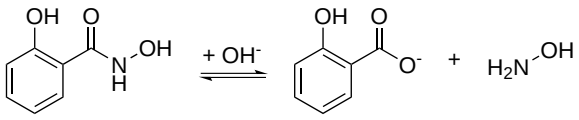

Fig. 3.28: Alkaline hydrolysis of salicylhydroxamic acid H_3shi

fig. 3.27(c), including seven $S = \frac{3}{2}$ centers and two different exchange coupling parameters. It was assumed, that J_1 value is smaller than J_2 as the corresponding metal–metal distances in the crystal structure are significantly longer and there is only one direct Co−O−Co bridge serving as exchange path for the connection of Co1 and Co3 or Co7. The best fit (see solid lines in figs. 3.27(a) and 3.27(b)) yielded an average Landé factor $g_{\text{all}} = 2.65$ and the isotropic Heisenberg exchange coupling constants $J_1 = -0.33\,\text{cm}^{-1}$ and $J_2 = -2.28\,\text{cm}^{-1}$. Very strong spin orbit coupling leads to a g factor significantly larger than g_{el} for a free electron. The exchange coupling parameters J_1 and J_2 show the expected proportions ($J_1 < J_2$) and are rather weak. Any remaining deviation from the experimental susceptibility and magnetization data is due to the rough approximations made for the simulations. For a more exact fit of the susceptibility data, independent cobalt sites and coupling parameters for each exchange pathway between Co3/7, Co4/8 and Co5/9 would be needed, as the corresponding superexchange paths and geometric environments are slightly different. This would result in a model based on at least four different cobalt atoms with four coupling constants, which would be a severe overparameterization. Furthermore, zero-field splitting would need to be taken into account. Even without a more complex coupling scheme, the introduction of magnetic anisotropy exceeds the capabilities of available software and computational power.

Another difficulty for the use of salicylhydroxamic acid as an ancillary ligand is the limited stability of the hydroxamate. Although this class of carbonyl derivatives is usually quite stable due to its tautomerism, it was found that the alkaline reaction conditions in combination with elevated temperatures, protracted reaction times and remaining water contents in the applied solvents or reactants led to a hydrolysis to salicylates (see fig. 3.28).

For the reaction of $[Co_2(OH_2)(piv)_4(Hpiv)_4]$ (**P1**) with salicylhydroxamic acid (H_3shi), 3,5-di-*tert*-butyl-1,2-benzoquinone (**L1b**) and pyridine in acetonitrile the formation of the three-dimensional coordination polymer $[Co_2^{III}Co^{II}(sal)_4(py)_4]$ (**C15**) was observed. In this structure, which crystallizes in the tetragonal space group $I4_1/a$, no coordination of a dioxolene species is observed. This however may be related to the

C15

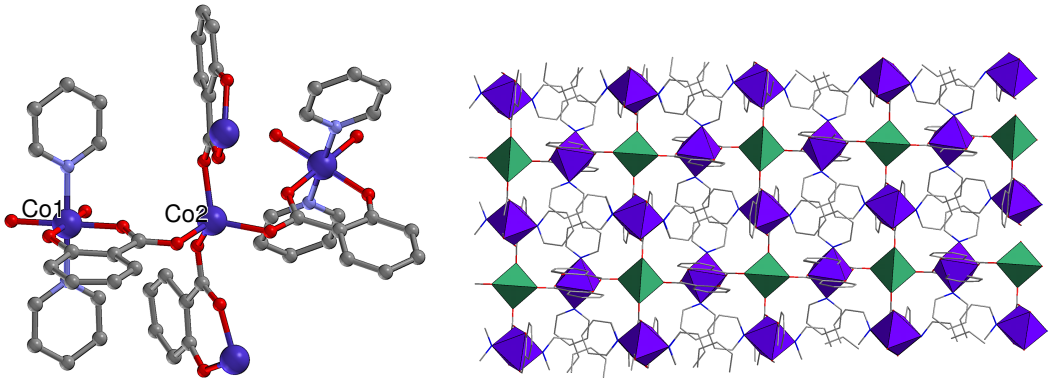

(a) Detail view **(b)** Two unit cells

Fig. 3.29: Crystal structure of $[Co_2^{III}Co^{II}(sal)_4(py)_4]$ (**C15**)

fact, that this ligand was used in its weakly coordinating neutral quinone redox state. The salicylate, which presumably emerged from the alkaline hydrolysis as discussed above, coordinates to Co1 with the phenolic and carboxylic oxygen atoms to form a six-membered chelate ring. The third ligand oxygen atom bridges to a neighboring Co2. Additionally, two pyridines are bound *anti* to Co1 to complete the octahedral coordination sphere. For Co2 a tetrahedral surrounding is found. The measured bond lengths (listed in table B.17) indicate *low spin* cobalt(III) for Co1 and tetrahedral *high spin* cobalt(II) for Co2. Extending the structure in all spatial directions, the three-dimensional coordination network shown in fig. 3.29(b) is assembled. Within this metal-organic framework, several voids are present. Although the total void volume makes up about 33.9 percent of the cell size (1487.8 Å^3), only few pores are sufficiently large to be accessible by solvent molecules (about 297.6 Å^3 per cell, 6.8 % with a 1.2 Å probe radius).

3.2.2.2 Complexes with Bis-chelating Ancillary Ligands

The successful synthesis of the complex **C13** as anticipated shows that it is possible to prepare tailor-made complexes using self-assembled fragments of small components such as salicylhydroxamic acid as building blocks. This concept allows for the rational synthesis of polynuclear complexes with a well defined coordination of dioxolene ligands. Trying to synthesize structural analogs of **C13**, it has been found that this method however still causes some difficulties. The latter two compounds **C14** and **C15** indicate that the main challenges of the use of salicylhydroxamic acid as preorganizing ancillary ligands are related to the ligand strength, instability and still too high structural flexibility. For instance, **C14** does not contain the typical,

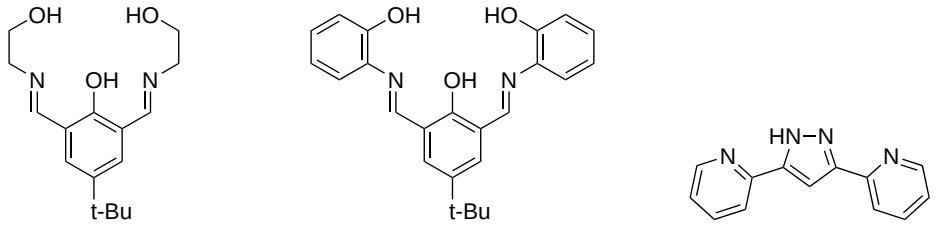

(a) H_3debup (**L3**) **(b)** H_3dabup (**L4**) **(c)** Hbpp (**L9**)

Fig. 3.30: Bis-chelating, planar ancillary ligands

anticipated metallacrown backbone, which is essential for the desired formation of **C13** analogues. Furthermore, hydroxamic acids are good chelating agents and form very stable complexes with numerous transition metal ions. This tendency may be the reason for the unintentional displacement of the employed dioxolene ligands seen in **C14**. Additionally, the regularly observed hydrolysis of salicylhydroxamic acid is a reaction to be avoided.

For these reasons, the more obvious route for the rational prearrangement of multiple metal ions for the coordination of additional dioxolene ligands was taken in addition to the previous syntheses: the use of bis-chelating ancillary ligands. Using appropriate organic syntheses suitable ligands with tailor-made properties can be designed. To foster the formation of predictable structures, rigid molecules are advantageous.

For the present work, three bis-chelating, planar ancillary ligands were synthesized (see fig. 3.30). 4-*tert*-butyl-2,6-bis(((2-hydroxyethyl)imino)methyl)phenol (H_3debup, **L3**) and 4-*tert*-butyl-2,6-bis(((2-hydroxyphenyl)imino)methyl)phenol (H_3dabup, **L4**) are two structurally related bis(iminomethyl) phenols. While **L3** contains two rather flexible ethanolamine residues, **L4** with its aminophenol groups is more rigid and planar. Both ligands offer two sites for the coordination of transition metal ions with a total number of three oxygen and two nitrogen donor atoms. The third ligand which was used for a preorganization of the metal ions is 3,5-bis(pyridine-2-yl)pyrazole (Hbpp, **L9**). In this case, two bidentate coordination pockets are available.

The reaction of $[Co_2(OH_2)(piv)_4(Hpiv)_4]$ (**P1**) and H_3debup (**L3**) resulted in the crystallization of the hexanuclear cobalt complex $[Co_6(OH)_2(Hdebup)_2(piv)_8]$ (**C16**). The addition of excessive catecholate **L1a** with or without triethylamine as a deprotonating base did not have an influence on the outcome of this synthesis. This obstruction of the dioxolene ligands is referred to the strong binding of the chelating ancillary ligands to the metal ions. Furthermore, as these ligands enclose the metal ions

C16

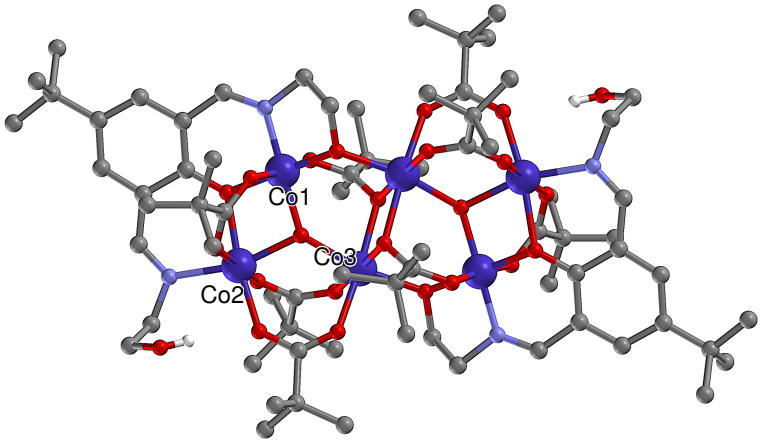

Fig. 3.31: Molecular structure of $[Co_6(OH)_2(debup)_2(piv)_8]$ (**C16**)

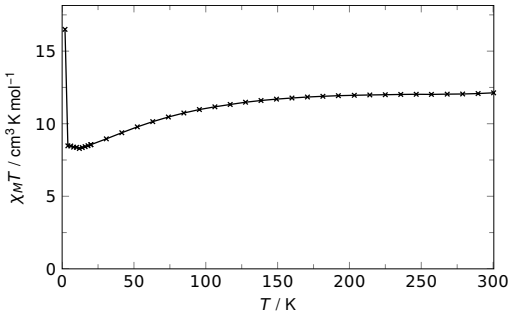

Fig. 3.32: Temperature dependence of the magnetic susceptibility of **C16** for an immobilized polycrystalline sample, $B = 0.1\,\mathrm{T}$

much more than those smaller co-ligands used in prior syntheses, a steric hindrance is present. **C16** is a centrosymmetric molecule and crystallizes in the monoclinic space group $P\overline{1}$. The crystal structure's asymmetric unit contains a $Co_2^{II}Co^{III}(\mu_3\text{-OH})$ triangle held together by four pivalate ligands and a twofold deprotonated $Hdebup^{2-}$ ligand. Two of these units are bridged by two debup hydroxyl and two pivalate oxygen atoms to form an inversion symmetric coordination cluster. Most striking is the presence of two non-coordinating, protonated ethanolamine groups. These flexible residues are freely dangling and are disordered over two positions. This lack of a coordinative bond leads to the fact that the anticipated structural type according to prior considerations cannot form. Regarding the Co−O and Co−N bond lengths, it is found that two different oxidation states for the cobalt ions are observed. While for Co1 short bond lengths of 1.869 Å to 1.917 Å and a rather strictly octahedral coordination sphere are measured, for Co2 and Co3 the distances to the neighboring atoms average to 2.08 Å with more distorted octahedral coordination environments. Consequently, Co1 is identified as a *low spin* cobalt(III) ion, whereas the oxidation state of a *high spin* cobalt(II) ion is assigned to Co2 and Co3.[133]

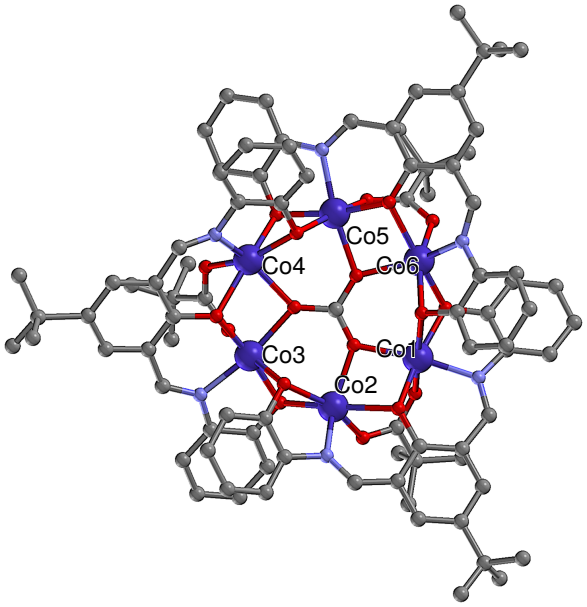

Fig. 3.33: Molecular structure of $(HNEt_3)_2[Co_6(CO_3)(dabup)_3(piv)_3]$ (**C17**)

Despite the fact that the desired structural type failed to appear, the temperature dependence of the magnetic susceptibility was examined to evaluate the strength of exchange coupling of the metal ions. Unfortunately, the compound suffered from strong orientation effects under applied fields at low temperatures, visible in strong field dependence of the susceptibility. Therefore, the sample was immobilized using highly viscous grease. Even under these precautions, slight inconsistencies at low temperature were measured. For this reason and the fact that the underlying model would be too complex for a meaningful simulation, the data can only be discussed qualitatively. The $\chi_M T$ curve depicted in fig. 3.32 takes a constant value of 12.1 $cm^3\,K\,mol^{-1}$. As the spin only value for four individual *high spin* cobalt(II) centers ($S = \frac{3}{2}$) would only be 7.5 $cm^3\,K\,mol^{-1}$, strong orbital contributions need to be taken into account. Assuming weak couplings at high temperatures, an average Landé factor of $g = 2.54$ for all cobalt ions can be extracted.

To overcome the issue of the dangling ethanolamine residues, more rigid aminophenol groups were attached for the ligand 4-*tert*-butyl-2,6-bis(((2-hydroxyphenyl)imino)methyl)phenol (H_3dabup **L4**, see fig. 3.30).

A reaction of $[Co_2(OH_2)(piv)_4(Hpiv)_4]$ (**P1**) and triethylamine involving **L4** as an ancillary ligand afforded the formation of $(HNEt_3)_2[Co_6(CO_3)(dabup)_3(piv)_3]$ (**C17**). An excessive addition of 3,5-dbcat (**L1a**) did not have an influence on the synthesis, the dioxolene was hindered from a coordination by the strongly chelating ligand **L4**.

C17

Surprisingly, a carbonate was found to build the center of this molecule, despite the fact that no carbonate precursors were used for the syntheses. As the reaction was carried out under air, it is believed that this structural feature has its origin in atmospheric carbon dioxide. In spite of the low natural amount of this trace gas of about 400 ppm,[165] the generation of this crystalline complex is somehow unexpected and is a proof of a high binding affinity for this structural type. The present hexanuclear cobalt complex crystallizes in the orthorhombic space group *Pbcn*. The complex anion exhibits C_3 symmetry with the central CO_3^{2-} carbonate which serves as a template for the coordination of all six cobalt ions, which is a very rare bridging mode for carbonate as a ligand and only few similar structures are known.[166–168] Three threefold deprotonated dabup^{3-} ligands are helically arranged around this $[Co_6(CO_3)]^{10+}$ core, each enclosing two cobalt ions and bridging to the neighboring metals via the phenolate oxygens. The short phenyl ring distances indicate π/π interactions. Additionally, three pivalate ligands are bound at one side of the molecule plane, each bridging two cobalt ions. As a result of this asymmetry, the anion exhibits a rather polar and an apolar side. While the dabup side of the plane contains many heteroatoms available for hydrogen bonds, the other side is sterically shielded by the pivalate *tert*-butyl groups and thus rather hydrophobic. This property is also seen in the binding to the two triethylammonium ions, which balance the two negative charges of the $[Co_6(CO_3)(dabup)_3(piv)_3]^{2-}$ anion. While the cations on the polar side of the anion is weakly bound via a N–H···O hydrogen bridge, the N–H bond of the cation on the rather apolar side points away from the molecule and forms loose hydrophobic ethyl–*tert*-butyl interactions. All cobalt ions have distorted octahedral CoO_5N coordination spheres with donor atom distances of 2.011 Å to 2.268 Å, which indicates the presence of *high spin* cobalt(II).

The carbonate's μ_6 coordination mode was first found for the hexanuclear oxovanadium(IV) complex $(NH_4)_5[(VO)_6(CO)_4(OH)_9]\cdot 10\,H_2O$ in the year 1986.[169] Since then, several similar assemblies with μ_6 carbonates serving as templates have been published with different transition metal ions.[167,168,170–174] Although the use of carbonate sources such as sodium carbonate is quite usual in the syntheses of theses complexes, the capture of atmospheric carbon dioxide has been observed in some cases, especially for late 3*d* transition metals.[167,173,174] Despite the carbonate's template effect, different metal arrangements are found. For sterically less demanding ancillary ligands, cage-like structures are commonly observed.[167,175,176] The hexagonal, rather planar placement of metal ions found in the present complex is

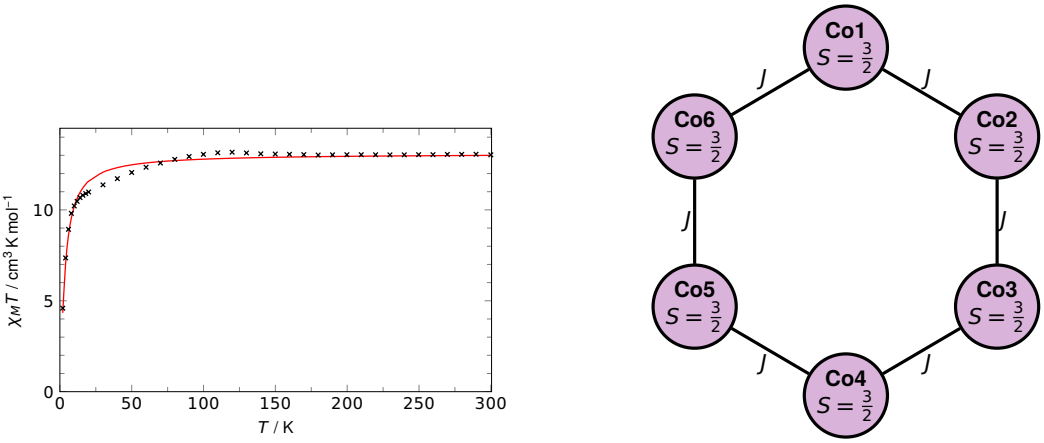

(a) Plot of $\chi_M T$ vs. T

(b) Coupling scheme

Fig. 3.34: Temperature dependence of the magnetic susceptibility of **C17** at $B = 1\,\mathrm{T}$. $g = 2.16$, $J = -0.33\,\mathrm{cm}^{-1}$

favored due to the flat, helically arranged dabup^{3-} ancillary ligands available for inter-ligand π–π interactions.

The temperature dependence of the magnetic susceptibility for compound **C17** is shown in fig. 3.34. A constant $\chi_M T$ value of $13.0\,\mathrm{cm}^3\,\mathrm{K\,mol}^{-1}$ is measured above approximately 90 K. Comparing with the spin only value of $11.25\,\mathrm{cm}^3\,\mathrm{K\,mol}^{-1}$ for six uncoupled $S = \frac{3}{2}$ centers, it is evident that a contribution of the orbital momentum must be taken into account, as expected for *high spin* cobalt(II). At low temperatures, a decrease of the magnetic moment is observed, which is explained with dominant antiferromagnetic interactions between the cobalt ions, leading to an $S = 0$ ground state. For the simulation of the magnetic data, a very simplified coupling scheme with a cyclic arrangement of six equal $S = \frac{3}{2}$ centers and six equal coupling constants J was applied (see fig. 3.34(b)). A simplex fit of the experimental data yielded $g = 2.16$ and a weak antiferromagnetic coupling of $J = -0.33\,\mathrm{cm}^{-1}$. These values are within the expected range for *high spin* cobalt(II) ions with a certain amount of unquenched orbital contribution due to its T term ground state. According to the Goodenough–Kanamori–Anderson rules and other elaborate magnetostructural correlations, the weak coupling between the cobalt ions can be correlated with small Co−O−Co angles of 94.4° in average.[155–157] This finding is experimentally confirmed for several phenoxyl bridged cobalt complexes.[157] More complex underlying models, such as the consideration of weak couplings for the *syn–anti*- and *anti–anti*coordination modes for carbonate, would probably improve the goodness

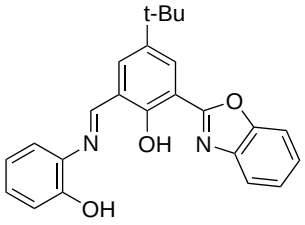

Fig. 3.35: H_2bobupimp

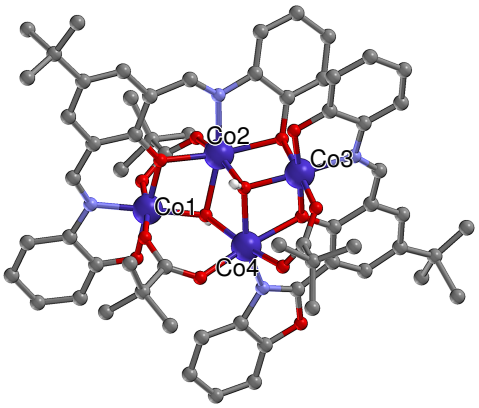

Fig. 3.36: Molecular structure of $[Co_4(OH)_2(dabup)(bobupimp)(piv)_3]$ (**C18**)

of the fit, especially at low temperatures, but on the other hand overparameterize the problem and lead to excessive computational demands.

The formation of **C17** nicely shows the success of the introduction of the more rigid aminophenol residue to foster a bis-chelating coordination with two ONO pockets. The stiffness of the aromatic rings as well as the possibility for an extended π overlap promotes the tendency towards a planar configuration of the ligand, which dramatically reduces the degrees of freedom. With this ligand property, the assembly of more predictable polynuclear structures should be possible. On the other hand, the additional coordination of dioxolene could not be achieved. Looking at the crystal structure of **C17** this is mainly due to two reasons: Firstly, dabup can be considered as a very strong ligand due to its chelating character. Similar to the metallacrown fragments discussed in section 3.2.2.1, a coordination of the catecholates is hindered simply because they are much weaker. Secondly, the ligand **L4** is intendedly rigid. Although the coordination found in **C17** shows that this molecule is able to coordinate in a facial as well as in a meridional manner, it does not show sufficient flexibility to adapt to sterically more demanding ligands such as the catecholate derivative. A strong steric tension between the *tert*-butyl residues of the catecholate and the phenyl groups of the ancillary ligand would result.

C18

A third difficulty with the use of **L4** as a co-ligand for the formation of polynuclear dioxolene complexes is evident in complex $[Co_4(OH)_2(dabup)(bobupimp)(piv)_3]$ (**C18**). The tetranuclear complex, which is the product from the reaction of $[Co_2(OH_2)(piv)_4(Hpiv)_4]$ (**P1**), H_3dabup (**L4**) and the non-coordinating 3,5-di-*tert*-butyl-1,2-benzoquinone (**L1b**), shows that the ligand dabup^{3-} is not stable but is

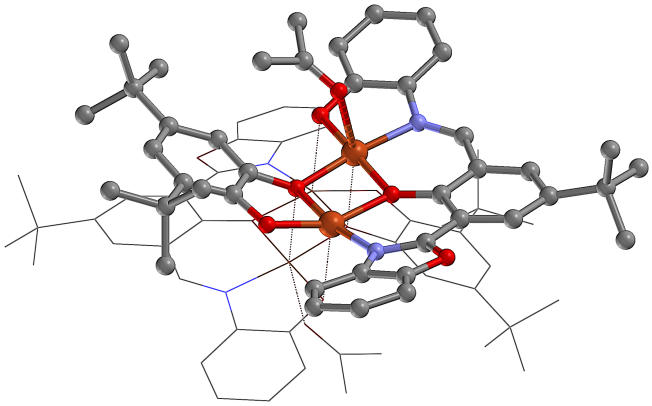

Fig. 3.37: Molecular structure of $[Cu_4(3,5\text{-dbcat})_2(\text{bobupimp})_2(\text{acetone})_2]$ (**C19**)

able to rearrange to bobupimp^{2-} (see fig. 3.35). This *in situ* modification of the ligand involves a nucleophilic attack of one hydroxyl group at the neighboring imine group followed by an oxidation to an aromatic benzoxazole. Because this reaction only occurs at one side of the ligand, an asymmetry is generated. The complex **C18** crystallizes in the triclinic space group $P\overline{1}$. In the resulting complex asymmetric unit one planar $[Co_2(\text{dabup})(\text{piv})]^+$ unit is connected to a $[Co_2(\text{bobupimp})(\text{piv})]^{2+}$ fragment via two bridging μ_3 hydroxyl groups and one pivalate. An additional pivalic acid molecule is loosely bound to a hydroxyl and a phenolate group via hydrogen bonds. Intramolecular π/π interactions are observed for the stacking of the two main ancillary ligands dabup and bobupimp. The cobalt–donor atom bond lengths average to 1.894 Å for Co1 and Co3, and 2.088 Å for Co2 and Co4, respectively. Furthermore, it is evident, that the octahedral coordination spheres are much more symmetric for Co1 and Co3 than they are found for Co2 and Co4, which show certain amounts of distortion. For these reasons, Co1 and Co3 are assigned to *low spin* cobalt(III) ions with t_{2g}^6 electron configuration and Co2 and Co4 to *high spin* cobalt(II).

The same oxidation of H_3dabup to H_2bobupimp is found in a similar reaction with copper pivalate $[Cu_2(\text{piv})_4(\text{EtOH})_2]$ (**P3**) and 3,5-di-*tert*-butylcatechol (**L1a**) in acetone, which yielded the complex $[Cu_4(3,5\text{-dbcat})_2(\text{bobupimp})_2(\text{acetone})_2]$ (**C19**). The centrosymmetric complex, which crystallizes in the triclinic space group $P\overline{1}$, consists of two rather planar, slightly bowl-shaped $[Cu_2(\text{bobupimp})(3,5\text{-dbcat})(\text{acetone})]$ moieties, which are stacked via four dative Cu−O interactions. This ligand arrangement results in square pyramidal CuO_5 coordination spheres for Cu1 and elongated octahedral CuO_6 surrounding for Cu2. It has to be noted that the coordination of the catecholates is only possible due to the oxidation of the ancillary ligand, which is

Tab. 3.12: Metrical oxidation states for the dioxolene ligands in **C19** based on crystallographically determined bond lengths at 173 K

Ligand	Metrical oxidation state (*MOS*)
Dioxolene 1	−1.94

sterically less demanding than the preliminary ligand dabup and leaves an additional vacant coordination site. For both metal centers planar bond lengths of 1.94 Å and long axial donor atom distances of 2.41 Å to 2.68 Å are measured, which indicate the typical Jahn-Teller distortion found for a Cu^{2+} d^9 electron configuration. To confirm the oxidation state of the μ_2-η^2:η^1 dioxolene ligand, the intraligand atom distances were considered. Comparatively long C−O distances, the C−C bond lengths assimilation and the requirement of charge balance clearly indicate the oxidation state of a dianionic catecholate. A metrical oxidation state of $MOS = 1.94$ confirms this qualitative consideration.

As seen for the compounds **C17**, **C18** and **C19**, the ligand H_3dabup (**L4**) much more reliably coordinates in a bis-chelating manner and in the anticipated coordination mode than observed for H_3debup (**L3**). This reliability is essential for the prediction and prognosis of the resulting complexes based on this ligand. However, it is seen that the observed ligand oxidation to H_2bobupimp alters the coordination pockets so that this forecast again is less reliable. However, this unexpected rearrangement offered insights into the required steric demands to enable the secondary coordination of dioxolene ligands. For **C17** and **C18** an additional coordination could not be achieved, which is referred to the steric demands and the high binding affinity for H_3dabup. For **C19** however, the unexpected oxidation of the ancillary ligand led to a vacancy of one coordination site at the copper ion coordinated by the benzoxazole. Taking these observations as an input for the development for a different, more appropriate co-ligand, some additional requirements have to be met: The ligand must not undergo reactions under the established reaction conditions. Furthermore, less steric hindrance is required for the subsequent coordination of dioxolene ligands.

To meet these demands, the ligand 3,5-bis(pyridine-2-yl)pyrazole (Hbpp, **L9**, see fig. 3.30(c)) was employed. While at first sight is has little in common with the first attempts **L3** and **L4** it is considered to be appropriate for the synthesis of polynuclear dioxolene with a rigid ligand backbone. The ligand exhibits two bidentate nitrogen

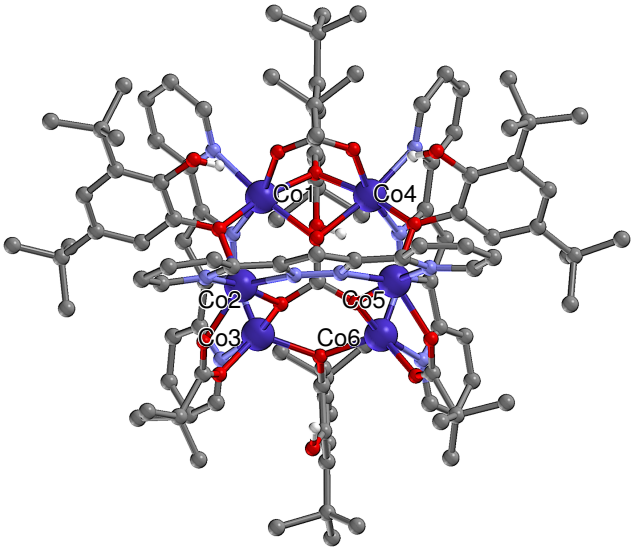

Fig. 3.38: Molecular structure of $[Co_6(CO_3)(bpp)_3(H3,5\text{-dbcat})_4(piv)_3]$ (**C20**)

donor coordination pockets and offers a planar, rigid backbone. Contrary to the phenol diimine ligands, the present ligand is not enclosing the coordinated metal ions but leaves room for the additional coordination of additional substrates such as dioxolenes.

The reaction of Hbpp (**L9**) with $[Co(piv)_2]_n$ (**P2**) and 3,5-di-*tert*-butylcatechol (**L1a**) yielded the complex $[Co_6(CO_3)(bpp)_3(H3,5\text{-dbcat})_4(piv)_3]$ (**C20**), which crystallized in the monoclinic space group $P2_1/c$. Similar as in compound **C17** a carbonate forms the central element of the complex, which coordinates to all six cobalt ions. In the present case, however, a boat-like arrangement of the metal ions is found instead of a rather planar, cyclic one. Three bpp^- ligands, three pivalates and four catecholates are additional bridging ligands to form the mirror symmetric complex **C20**. Interestingly, all catecholate ligands are only singly deprotonated and bind with only one oxygen atom in a μ_2 bridging mode. The ligand oxidation states were identified using metrical considerations. In every case C−C and C−O bond lengths indicated aromaticity due to bond lengths assimilation and C−O single bonds. Calculated metrical oxidation states of approximately $MOS = -2.0$ (see table 3.13) support this finding. As it first was believed that this coordination of protonated catecholates is due to a lack of base, further reactions were carried out using different amine bases. However, no complexes could be synthesized under these conditions.

Tab. 3.13: Metrical oxidation states for the dioxolene ligands in **C20** based on crystallographically determined bond lengths at 173 K

Ligand	Metrical oxidation state (*MOS*)
Dioxolene 1	−2.29
Dioxolene 2	−2.09
Dioxolene 3	−2.08
Dioxolene 4	−2.11

3.2.2.3 Targeted synthesis of [diox−Co−N_4LN_4−Co−diox] type complexes

As worked out in sections 1.3.7.2 and 1.3.7.3, several approaches for the synthesis of di- and polymeric cobalt dioxolene complexes have been followed. All approaches have in common, that they are based on known mononuclear valence tautomeric complex types which are coupled by simply doubling the ancillary ligand denticity or exchanging dioxolenes by bis-dioxolenes.

$$[Co(sq)(diox)(N_2L)] \Rightarrow [\{Co(sq)(diox)\}(N_2LN_2)]$$

$$[Co(sq)(diox)(NL)_2] \Rightarrow [Co(sq)(diox)(NLN)]_n$$

$$[Co(diox)(N_4L)]^+ \Rightarrow [\{Co(N_4L)\}_2(diox{-}L{-}diox)]^{2+}$$

However, the approach of using an octadentate ligand to couple two redox-active $[Co(diox)]^+$ units has not been followed before.

$$[Co(diox)(N_4L)]^+ \Rightarrow [\{Co(diox)\}_2(N_4LN_4)]^{2+}$$

This concept has some downright advantages. First of all, a suchlike dinuclear complex only consists of the absolutely necessary building blocks, two centers which enable valence tautomeric transitions and bridge with an adjustable coupling strength. Contrastingly, the dinuclear dioxolene complexes known from literature, incorporate additional (valence tautomerically innocent) semiquinonates. Therefore, even in the low spin state, a paramagnetic moment is measured. In the present case, the low spin state would be diamagnetic, which makes these complexes attractive for potential applications and facilitates analysis. Depending on the choice of the bridge, different gradations of intramolecular communication can be realized, leading to adjustable cooperativity of the valence tautomeric conversions from independent transitions to multi-step transitions. All previous dimeric complexes included some

"decorative" additional dioxolene or ancillary ligands, which were not involved in the valence tautomeric transition(s). Therefore, the understanding and modeling of analytical data is much easier in the present case, as fewer simplifications are needed. Furthermore, the resulting complexes can be regarded as model complexes for the experimental realization of 2-qubit quantum gates as proposed by Minkin et al. (see section 1.1.1).[22] On the other hand, the synthesis of an appropriate octadentate bridging ligand requires more elaborate syntheses and is an additional challenge. Furthermore, one has to keep in mind that the hypothetic products of the type $[\{Co(diox)\}(N_4LN_4)]^{2+}$ exhibit two positive charges. This requires the addition of suitable anions during the syntheses. As the intermolecular interaction and solvent or counter ion effects have a strong influence on the valence tautomeric equilibrium, the feasibility of an anion exchange may also be seen as a chance and advantage. For its use as quantum gates, negative charges are admittedly counterproductive.

The ligand N_4LN_4 needs to exhibit two tetradentate chelating coordination pockets, which enable the capture of a cobalt ion while allowing the binding of additional dioxolenes (*cis*-coordination). For this work, the ligand *N*,*N*,*N*',*N*'-tetra-2-picolyl-1,4-bis(2-aminoethyl)piperazine (tpbap, **L7**) was developed. Due to the piperazine body's chair configuration, this molecule's coordination sites face opposite directions. The aliphatic backbone is expected to lead to a weak interaction ("entanglement") between the two redox-active centers, which is also a requirement for the design of 2-qubit quantum gates.

The first step for the synthesis of **L7** is the symmetrical cyanomethylation of piperazine with chloroacetonitrile. In a second step, the dinitrile is reduced to the corresponding diamine. A reductive amination of four equivalents of 2-pyridinecarboxaldehyde results in the formation of tpbap **L7** in good yields.

Reacting this octadentate ligand **L7** with cobalt sulfate or perchlorate salts and 3,5-di-*tert*-butylcatechol (**L1a**) in stoichiometric amounts, the complexes $[Co_2(tpbap)(3,5\text{-}dbcat)_2](SO_4)$ (**C21a**) and $[Co_2(tpbap)(3,5\text{-}dbcat)_2](ClO_4)_2$ (**C21b**) could be synthesized.

Both isostructural complexes exhibit the expected structures with cobalt–dioxolene fragments oriented in opposing directions. While the sulfate **C21a** crystallizes in the monoclinic space group $C2/c$, the perchlorate exhibits lower crystal symmetry (triclinic, $P\bar{1}$). For both ligands the cobalt ions show a strictly octahedral coordination

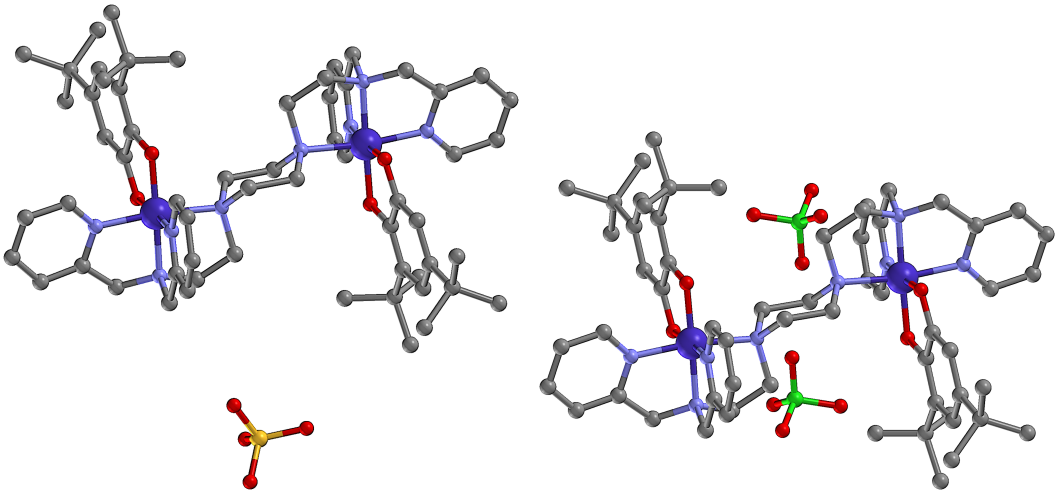

(a) Molecular structure of $[Co_2(tpbap)(3,5\text{-}dbcat)_2](SO_4)$ (**C21a**)

(b) Molecular structure of $[Co_2(tpbap)(3,5\text{-}dbcat)_2](ClO_4)_2$ (**C21b**)

Fig. 3.39: Molecular structures of $[Co_2(tpbap)(3,5\text{-}dbcat)_2]X_n$ complexes **C21a** and **C21b**

Tab. 3.14: Metrical oxidation states for the dioxolene ligands in **C21a** and **C21b** based on crystallographically determined bond lengths at 173 K

Complex	Metrical oxidation state (*MOS*)
C21a	−2.02
C21b	−1.94

sphere with Co−O bond lengths of approximately 1.85 Å and average Co−N distances of 1.95 Å. These close contacts and the weak distortion of the coordination octahedra clearly indicate the presence of *low spin* cobalt(III). For the dioxolene ligands comparatively long C−O distances corresponding to single bonds and aromatic C−C bond lengths are found. The metrical oxidation states confirm the oxidation state of a catecholate at 173 K in both cases (see table 3.14).

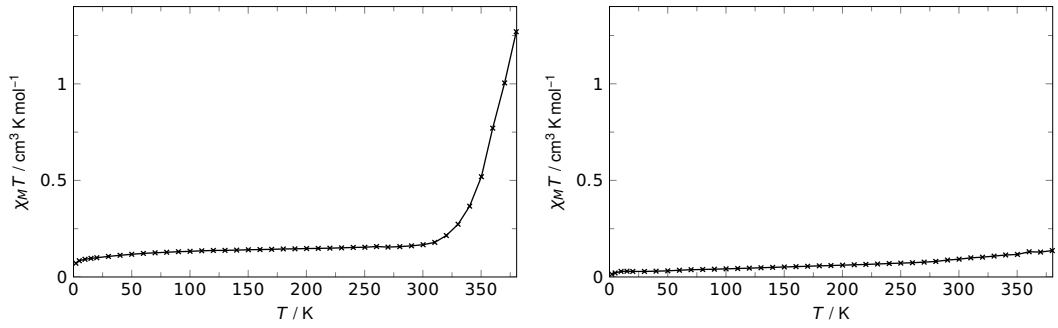

(a) Magnetic susceptibility of **C21a**

(b) Magnetic susceptibility of **C21b**

Fig. 3.40: Magnetic susceptibility of **C21a** and **C21b** ($B = 1$ T)

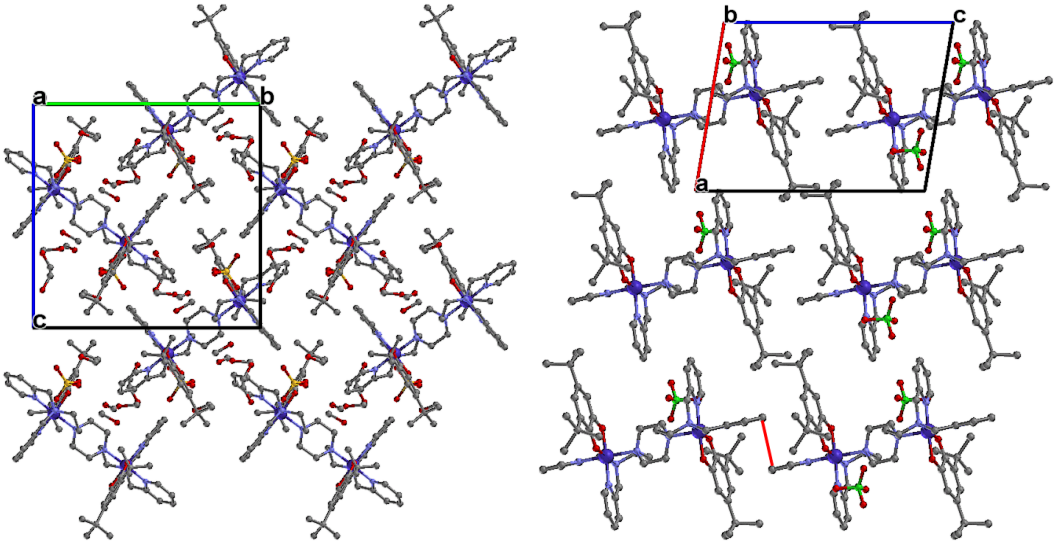

(a) Crystal packing of **C21a** along the *b*-*c* plane **(b)** Crystal packing of **C21b** along the *a*-*c* plane

Fig. 3.41: Differences in the crystal packing of **C21a** and **C21b**

For the examination of valence tautomerism, the magnetic susceptibility was measured between 2 K to 380 K for the complexes **C21a** and **C21b**. The obtained curves for $\chi_M T$ are shown in figs. 3.40(a) and 3.40(b). Both complexes show low $\chi_M T$ values below 300 K, as expected for the diamagnetic $Co_2^{III}(cat)_2$ species found in the structural data measured at 173 K. The residual magnetic moment is due to a deficient diamagnetic correction or small amounts of paramagnetic impurities. For the sulfate **C21a**, however, a steep increase of the magnetic moment is observed above 320 K, which can be attributed to a valence tautomeric interconversion to a cobalt(II) semiquinonate accompanied by a spin state transition to *high spin*. At 380 K a value of 1.26 $cm^3\,K\,mol^{-1}$ is reached. As one (uncoupled) Co^{II}(sq) moiety would correspond to a $\chi_M T$ value of (at least) 2.25 $cm^3\,K\,mol^{-1}$, the observed transition within the accessible temperature range unfortunately is incomplete. For this reason, it is not possible to identify, if a one-step transition to a $Co_2^{II}(sq)_2$ species or a two-step transition via $Co^{II}(sq)Co^{III}(cat)$ occurs. Interestingly, the corresponding isostructural perchlorate **C21b** exhibits low magnetic moments throughout the measurement range. It therefore exists in the tautomeric state of a $Co_2^{III}(cat)_2$ species without any sign of valence tautomerism. As the cation structures for **C21a** and **C21b** perfectly resemble each other (root-mean-square deviation of atomic positions $\mathrm{RMSD} = \sqrt{\frac{1}{N}\sum_{i=1}^{N}\delta_i^2} = 0.1254$), this striking difference needs to originate from packing, solvent or anion effects.

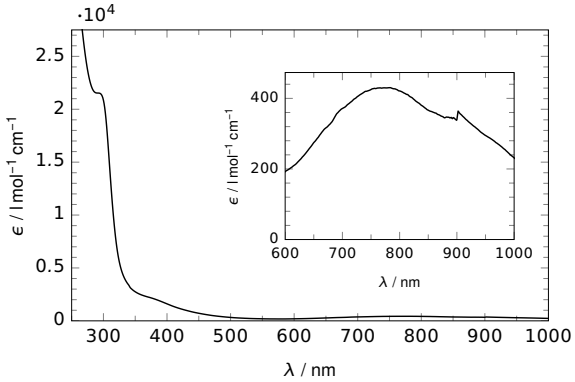

Fig. 3.42: UV/Vis spectrum for $[Co_2(tpbap)(3,5\text{-}dbcat)_2](SO_4)$ (**C21a**) in methanol at 25 °C

During a valence tautomeric conversion from *ls*-Co^{III} to *hs*-Co^{II} the Co−O and Co−N bond lengths are generally elongated by approximately 0.15 Å.[177] To accommodate the resulting "breathing" of the molecules upon valence tautomerism, the crystalline lattice must be soft enough. For **C21b**, all molecules in the crystal structure have the same orientation within the cell. Thus, only translational symmetry is found in the crystal lattice. The perchlorate ions are not involved in hydrogen bridges and very weak π-π interactions between the pyridyl residues of neighboring tpbap ligands are observed with ring plane distances of 3.38 Å and only a negligible overlap (see red line in fig. 3.41(b)). However, due to the molecule's angularity and the interlaced arrangement, a dense and rigid lattice is formed. This stiffness of the crystal packing impedes the molecular expansion during a valence tautomeric conversion. Contrastingly, for **C21a**, a herringbone packing motif with a herringbone angle of 72.4° is found for the arrangement of $[Co_2(tpbap)(3,5\text{-}dbcat)_2]^{2+}$ cations. Due to the asymmetric packing, molecular anions are not interlaced as seen for **C21b**. The voids between those moieties are not only filled with the sulfate counter ions, but also contain a large number of methanol solvent molecules. For this reason, the structure possesses an extended hydrogen bond network, which leads to intermolecular interactions and cooperativity. Further, it provides the required lattice flexibility to allow the expansion of the cobalt coordination spheres. For these reasons, a valence tautomeric transition is observed for sulfate **C21a** at ≈ 380 K whereas the perchlorate **C21b** is redox-innocent in the accessible temperature range. Similar impact of crystal packing, solvent incorporation and hydrogen bonding as lattice softening components is also reported for mononuclear cobalt dioxolene valence tautomers.[70,71]

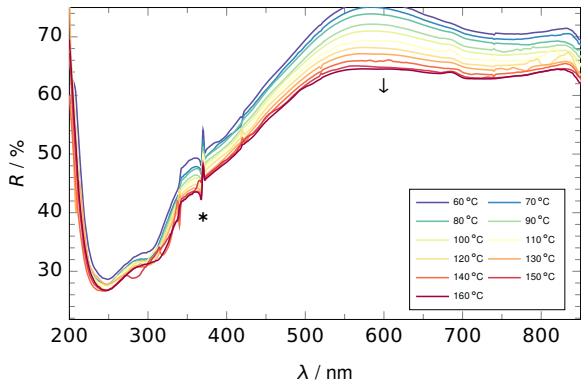

Fig. 3.43: Solid state reflectance spectra for $[Co_2(tpbap)(3,5\text{-dbcat})_2](SO_4)$ (**C21a**). Weak temperature dependence of the reflectance can be attributed to the valence tautomeric transition observed in the magnetic data.

The electronic spectrum in methanolic solution at 25 °C shown in fig. 3.42 features a broad band with a maximum absorption at about 780 nm, which is consistent with a symmetry-forbidden ligand-to-metal charge transfer transition expected for the Co^{III}(3,5-dbcat) tautomer.[66] The absorption shoulder at 380 nm is attributed to a $^1A_{1g} \rightarrow {}^1T_{1g}$ *d–d* transition commonly found for octahedral symmetry.[178]

Figure 3.43 shows the temperature dependence of the solid state optical reflectance in the range from 60 °C to 160 °C where the valence tautomeric transition is expected according to the magnetic data. The spectrum at 60 °C exhibits the same absorption maxima as in solution, but slightly red-shifted by about 20 nm. Although the differences of the diffuse reflectance spectra are less pronounced than it was observed for **C4**, the increase of the absorption at 600 nm with increasing temperature may be attributed to the generation of the Co^{II}(3,5-dbsq) tautomer, for which a metal-to-ligand charge transfer band is expected in this range.[66] Above 170 °C an irreversible decomposition of the complex is observed.

In order to evaluate the redox-activity of the non-innocent dioxolene ligands and the metal centers, cyclic voltammograms were recorded for **C21a** in acetonitrile (see fig. 3.44). In the available potential range the complex exhibits a quasi-reversible oxidation at −0.023 V ($E_{1/2}$ = −0.062 V, ΔE_p = 74 mV) versus Fc/Fc^+, which can be assigned to the feasible ligand-centered oxidation of the catecholates to semiquinonates. Notably, only one oxidation process is found. Therefore, a negligible exchange interaction of the two ligands is assumed, which is in accordance with the aliphatic bridging ligand and the long distances. In addition to this ligand-centered oxidation process, an irreversible reduction wave is measured at

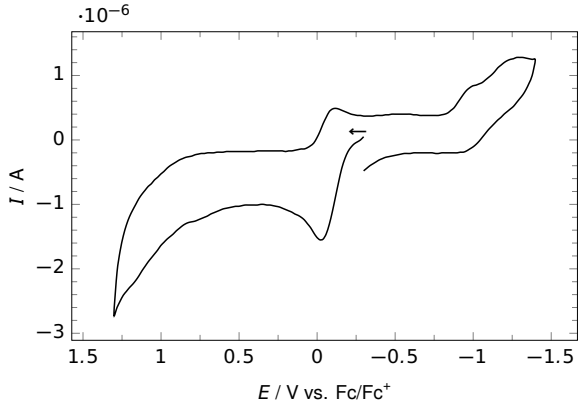

Fig. 3.44: Cyclic voltammogram for **C21a**. Conditions: 1 mmol l^{-1} in acetonitrile, supporting electrolyte 0.1 mol l^{-1} NBu_4PF_6, scan rate 200 mV s^{-1}.

$E_p = -0.584$ V, which is assigned to the reduction of Co^{III} to Co^{II}. Again, only one wave is resolved, consistent with two independent redox centers without notable coupling.

The structures of **C21a** and **C21b** are comparable to the mononuclear complexes $[Co(Me_ntpa)(3,5\text{-dbdiox})]PF_6 \cdot sol$ ($n = 0 \ldots 3$).[66] As already presented in section 1.3.7.1, a dependence of the valence tautomeric transition temperature from the ancillary ligand substitution level is found for these compounds. The Me_2tpa derivative best resembles the present dinuclear complex as it also shows a transition at an estimated temperature of 370 K. This phenomenological similarity is also reflected by the similar redox potentials for the process $[Co^{III}(cat)(L)]^+ + e^- \rightleftharpoons [Co^{II}(cat)(L)]$ with values of 0.674 V and 0.584 V vs. Fc/Fc^+ for **C21a** and the mononuclear complex, respectively. For the complex $[Co(L{-}N_4Bu_2)(3,5\text{-dbsq})](B(C_6H_4Cl)_4)$ containing the di-*tert*-butyl derivative of the tetraazamacrocyclic ligand 2,11-diaza[3.3](2,6)pyridinophane ($L{-}N_4Bu_2$), which was published by Graf et al., an even more pronounced structural similarity is apparent, because this ligand coordinates with two pyridyl moieties and two tertiary amines. Most remarkably, this complex does not exhibit valence tautomeric transitions at all, but a spin crossover above 200 K from *low spin* to *high spin* cobalt(II) is observed instead.[179] The absence of a valence tautomeric transition is explained by the steric tension of the ligand and the associated distortion of the cobalt coordination sphere. Regarding these comparisons, it is evident, that steric influences and the impact of solvents, anions and packing effects have an enormous influence on the valence tautomeric equilibrium, which must not be neglected. The mere comparison and tuning of electronic properties is therefore insufficient. The same applies to

quantum theoretical calculations to some extent, as those secondary effects beyond the electronic properties are only hard to embed in common theoretical methods.

3.3 Catecholase Activity for Polynuclear Dioxolene Complexes

Catecholase activity is referred to the catalytic oxidation of catechols to the corresponding 1,2-benzoquinones according to fig. 1.18. As outlined in section 1.3.6.2, the active sites of catechol oxidase or tyrosinase enzymes contain dinuclear copper centers. During the last years numerous dicopper complexes were synthesized to mimic the biologically active sites.[89,180–185] Although the catalytic activity of tyrosinase enzymes relies on the unique dinuclear type III copper center, a catecholase activity was also found for several model complexes not only limited to copper but based on different transition metal ions and nuclearities.[186–192] Even though there are many examples of functional models for catechol oxidase enzymes, the exact correlation between their structure and the efficiency of the catalytic oxidation of catechols is yet to be examined.

Most of the complexes presented in this work exhibit bridging dioxolenes. Spectroscopic studies on tyrosinase enzymes showed that this structural characteristic plays an important role in the catalytic diphenolase cycle which enables the oxidation to *o*-quinones. Therefore, the complexes discussed in this work can be considered as catalyst–substrate adducts “ES”. As all presented polynuclear dioxolene complexes are based on redox-active metal ions, it stands to reason, that they are also able to perform the other steps of the catalytic cycle beside dioxolene binding and therefore exhibit catecholase activity. In order to examine this ability, spectroscopic studies of the catalytic oxidation of 3,5-di-*tert*-butylcatechol to the corresponding 1,2-benzoquinone in methanolic solution were conducted, for which the results are presented in the following section. One particular aim of this little excursion into enzymology is the examination of the influence of the number of coordinated dioxolene ligands and their bridging mode on the catalytic efficiency.

For the spectrophotometric studies of the catecholase activity, defined amounts of **C3**, **C7a** and **C13** were dissolved in oxygen-saturated methanol.[3] Subsequently, a defined excess of 3,5-di-*tert*-butylcatechol was added as a substrate, which only shows an absorption at 282 nm. After this addition, time dependent spectral scans in the range from 300 nm to 800 nm were measured (see figs. 3.45(a), 3.46(a) and 3.47(a)). In all cases, the development of an intense absorption band at 401 nm was observed, which is characteristic for the formation of the corresponding quinone species 3,5-di-*tert*-butyl-1,2-benzoquinone 3,5-dbbq (**L1b**).[192] In order to study the reaction kinetics and determine the initial rates for the catalytic conversion of 3,5-dbcat to 3,5-dbbq, the time dependent changes in absorbance at 401 nm were monitored at 25 °C. Linear fits of the plots of the quinone extinction as a function of time yielded the respective initial rates. To determine the substrate concentration of these rates, these spectrophotometric experiments were repeated for different concentration of 3,5-dbcat from 5 to 200 equivalents. At low substrate concentrations, first order kinetics were observed in all three cases. At higher substrate concentrations, saturation of the rates is observed. This indicates the preceding formation of a complex–substrate adduct which in turn releases the product in the rate-determining step. For this reason the reaction kinetics can be analyzed by means of the Michaelis–Menten theory.[193]

Given a catalytic reaction that can be split into the bimolecular formation of an enzyme–substrate complex ES and the subsequent unimolecular catalytic generation of the product P, the overall reaction is represented as

$$\mathrm{E} + \mathrm{S} \underset{k_{-1}}{\overset{k_1}{\rightleftharpoons}} \mathrm{ES} \xrightarrow{k_2} \mathrm{E} + \mathrm{P} \tag{3.2}$$

with k_1, k_{-1} k_2 as the respective rate constants. Assuming a quasi-steady-state ($\frac{\mathrm{d}[\mathrm{ES}]}{\mathrm{d}t} = 0$, $k_1 = k_{-1} > k_2$) and a constant total enzyme concentration during the reaction time, the rate for the generation of P is given by

$$v = \frac{\mathrm{d}[\mathrm{P}]}{\mathrm{d}t} = \frac{v_{\max}[\mathrm{S}]}{K_{\mathrm{M}} + [\mathrm{S}]} \tag{3.3}$$

[3] Indeed, also the other complexes presented in this work were studied with respect to catecholase activity. These however were either insoluble in the required polar solvents, decomposed in solution or showed no activity.

with

$$v_{max} = k_{cat}[E]_0 \tag{3.4}$$

as the maximum rate, which is asymptotically approached and k_{cat} as the turnover frequency[4] (converted substrate molecules per catalyst molecule and second). The Michaelis constant K_M is an inverse measure of the enzyme's affinity for the converted substrate as it represents the concentration for which $v = \frac{v_{max}}{2}$. As an effective enzyme or catalyst requires both a high turnover frequency and a small Michaelis constant, the constant k_{cat}/K_M is usually used when comparing results.

For the feasible evaluation of K_M and k_{cat}, three different plot types for the linearization are common:

- Lineweaver–Burk[194] diagram: $1/v$ against $1/[S]$

$$\frac{1}{v} = \underbrace{\frac{K_M}{v_{max}}}_{\text{slope}} \cdot \frac{1}{[S]} + \underbrace{\frac{1}{v_{max}}}_{y\text{-intercept}} \tag{3.5}$$

- Eadie–Hofstee[195,196] diagram: v against $v/[S]$

$$v = \underbrace{-K_M}_{\text{slope}} \cdot \frac{v}{[S]} + \underbrace{v_{max}}_{y\text{-intercept}} \tag{3.6}$$

- Hanes–Woolf[197,198] diagram: $[S]/v$ against $[S]$

$$\frac{[S]}{v} = \underbrace{\frac{1}{v_{max}}}_{\text{slope}} \cdot [S] + \underbrace{\frac{K_M}{v_{max}}}_{y\text{-intercept}} \tag{3.7}$$

The classical Lineweaver–Burk plot is most widely used to determine k_{cat} and K_M. However, due to its double reciprocal nature, the points are unevenly weighted and small errors in the measurement are amplified. A better choice is found in the Eadie–Hofstee or the Hanes–Woolf diagram with an even weighting of all points. However, as in these linearizations the ordinates and abscissas are dependent variables, measurement errors affect x- as well as y-values and a good fit does not necessarily correlate with faultless data.

[4] in enzymology also *turnover number*

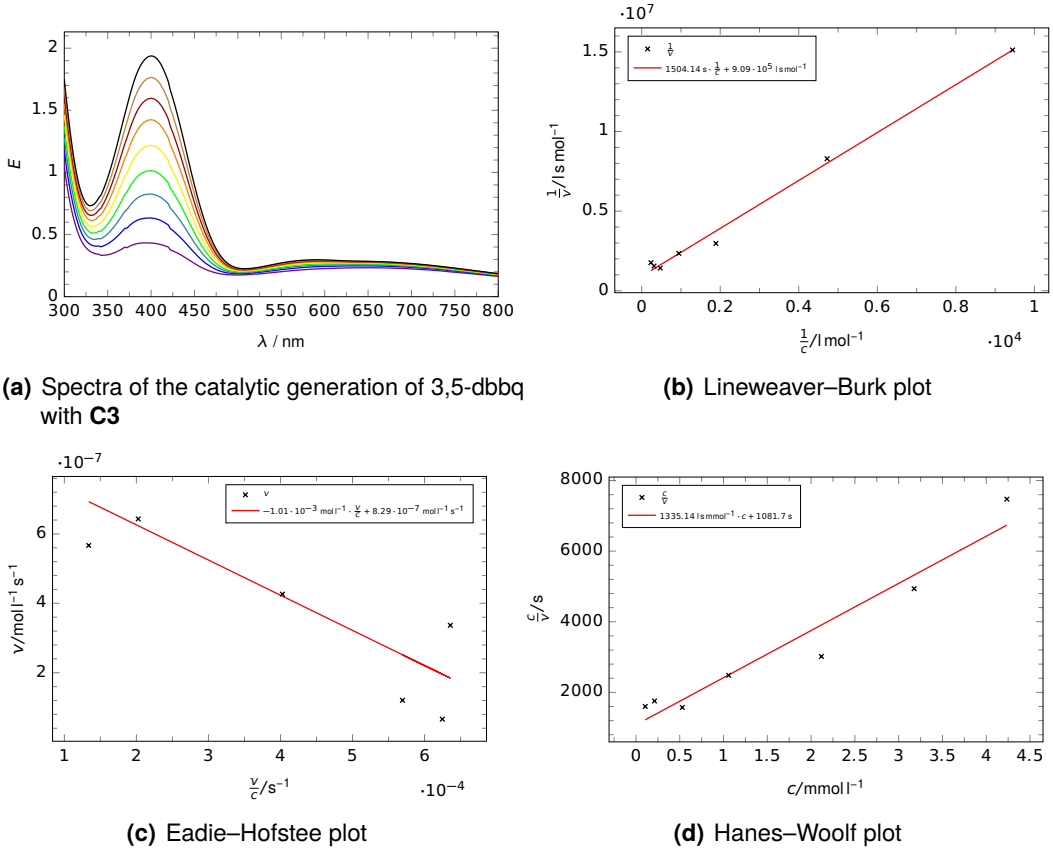

(a) Spectra of the catalytic generation of 3,5-dbbq with **C3**

(b) Lineweaver–Burk plot

(c) Eadie–Hofstee plot

(d) Hanes–Woolf plot

Fig. 3.45: Catecholase activity of **C3**

From figs. 3.45(a) to 3.45(d) it is seen that the tetranuclear iron catecholate $[Fe_4(OH)_2(3,5\text{-dbcat})_4(py)_2(piv)_2]$ (**C3**) shows significant catalytic activity on the oxidation of 3,5-di-*tert*-butylcatechol to the corresponding quinone. The development of the absorption band at 401 nm clearly corresponds to the generation of 3,5-di-*tert*-butyl-1,2-benzoquinone. The initial rate's dependence on the substrate concentration agrees with the Michaelis–Menten theory, as all three types of representations in figs. 3.45(b) to 3.45(d) yield reasonable linear trends. Consequently, the parameters K_M and k_{cat} were extracted from the respective linear fits and listed in table 3.15. It is to be noted that the three types of linear fits lead to different absolute values for K_M and k_{cat}. This is due the different weighting of measurement parameters for the plots. However, the same orders of magnitude are found for both values. In the following, only the values gained from Hanes–Woolf analysis are discussed, as this method provides an equal weighting of measured data points (see above) and yields reasonable errors. The turnover frequencies $k_{cat} = 127(15)\,h^{-1}$ are well comparable to the values found for some dinuclear copper complexes, specially designed to mimic the active site of copper proteins, which range from

$4\,h^{-1}$ to $214\,h^{-1}$.[89] However, also significantly more efficient functional models with turnover frequencies in the order of $1 \times 10^4\,h^{-1}$ are reported.[181,199] The Michaelis constant seems to be less affected by structural modifications than the turnover frequency, as it averages to approximately $1 \times 10^{-3}\,mol\,l^{-1}$ for all reported catecholase model complexes, independent from the ligand environment or transition metal. The affinities found for the present iron complex corroborate this finding.

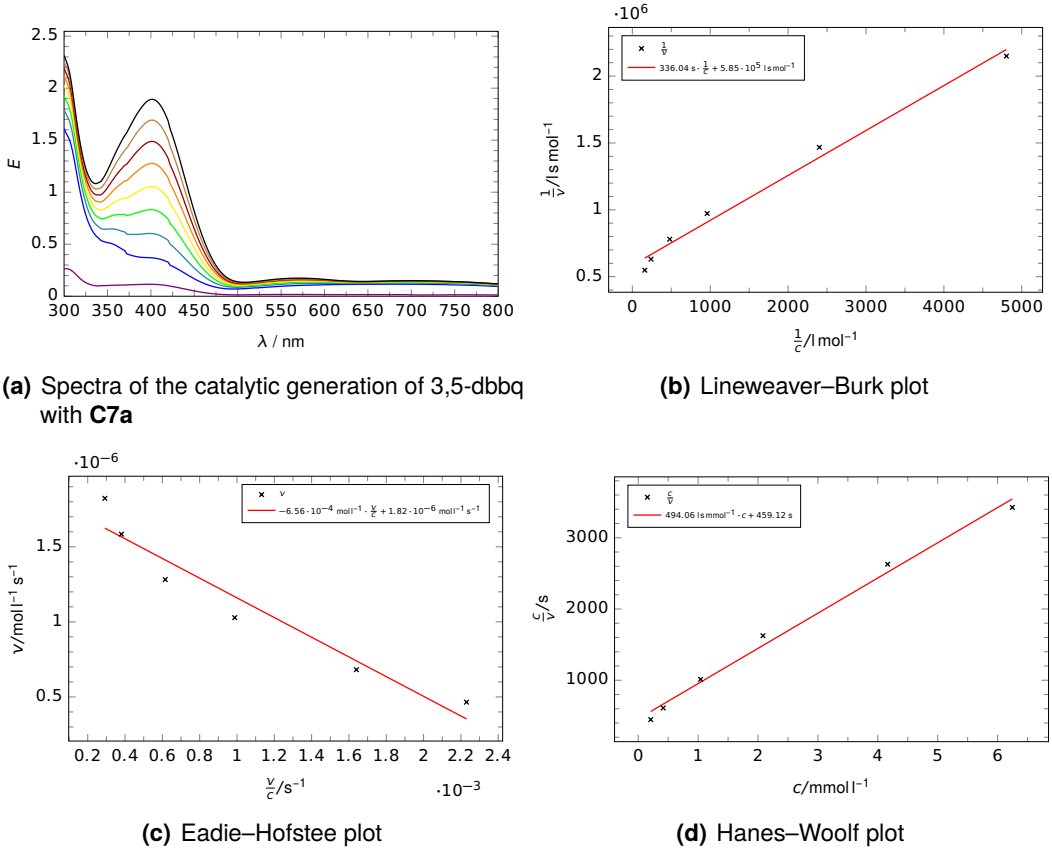

(a) Spectra of the catalytic generation of 3,5-dbbq with **C7a**

(b) Lineweaver–Burk plot

(c) Eadie–Hofstee plot

(d) Hanes–Woolf plot

Fig. 3.46: Catecholase activity of **C7a**

For the trinuclear cobalt semiquinonate $[Co_3(3,5\text{-dbsq})_2(piv)_4(NEt_3)_2]$ in its triclinic, synclinal conformation (**C7a**) and the tetranuclear metallacrown-based cobalt complex $[Co_4(shi)_2(3,5\text{-dbcat})(piv)_2(py)_5]$ (**C13**), which both show catecholase activity, the efficiency for catechol oxidase reaction was determined in the same way as described for **C3**. The Michaelis–Menten approach is legitimated in both cases, as the linearizations yield reasonable fits. It is to be noticed that all three complexes bear different numbers of coordinating dioxolene ligands. If those dioxolenes were the only active sites for the catalytic activity, their number would have a significant influence on the conversion rate. The rationalized Michaelis–Menten parameters are listed in table 3.15. While the catalytic activity of **C7a** resembles that of the iron

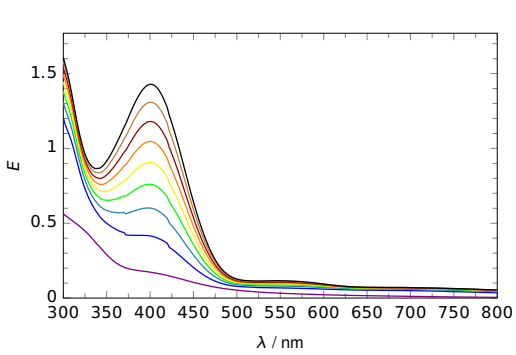

(a) Spectra of the catalytic generation of 3,5-dbbq with **C13**

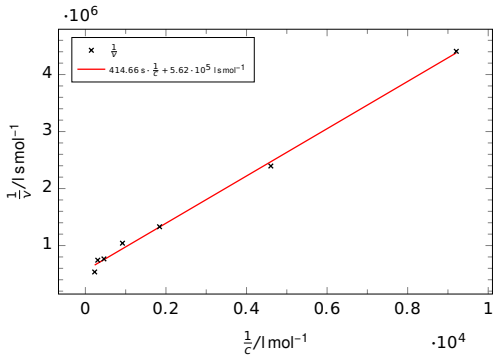

(b) Lineweaver–Burk plot

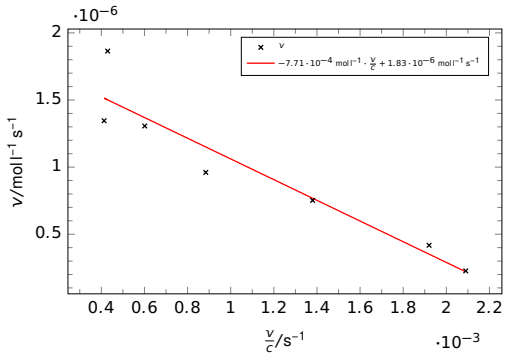

(c) Eadie–Hofstee plot

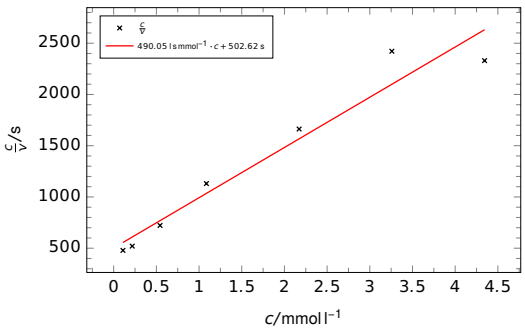

(d) Hanes–Woolf plot

Fig. 3.47: Catecholase activity of **C13**

Tab. 3.15: Michaelis constants K_M and turnover frequencies k_{cat} of **C3**, **C7a** and **C13**

Catalyst	method	K_M/mol l^{-1}	k_{cat}/h^{-1}	$\frac{k_{cat}}{K_M}$/l s^{-1} mol^{-1}
C3	Lineweaver–Burk	$1.65 \pm 0.40 \times 10^{-3}$	187 ± 45	31 ± 11
	Eadie–Hofstee	$1.01 \pm 0.31 \times 10^{-3}$	141 ± 24	39 ± 13
	Hanes–Woolf	$8.10 \pm 2.72 \times 10^{-4}$	127 ± 15	44 ± 16
C7a	Lineweaver–Burk	$5.74 \pm 0.52 \times 10^{-4}$	148 ± 11	71 ± 8
	Eadie–Hofstee	$6.55 \pm 0.89 \times 10^{-4}$	157 ± 10	67 ± 10
	Hanes–Woolf	$9.29 \pm 1.59 \times 10^{-4}$	175 ± 8	52 ± 9
C13	Lineweaver–Burk	$7.38 \pm 0.56 \times 10^{-4}$	295 ± 21	111 ± 12
	Eadie–Hofstee	$7.71 \pm 1.18 \times 10^{-4}$	304 ± 25	109 ± 19
	Hanes–Woolf	$1.03 \pm 0.27 \times 10^{-3}$	338 ± 37	92 ± 26

complex, it is found that **C13** is twice as active as **C3**. Interestingly, **C13** is the complex with the smallest number of coordinated dioxolene ligands. The hypothesis that the conversion rate depends on the number of dioxolene sites can thus be disproved. Presumably, for **C13** the catalytic activity is not based on the coordinated "in-plane" dioxolene, but on the axial coordination sites. The comparatively loosely bound axial pyridine ligands can be displaced by weakly coordinating catecholate anions, which in turn are activated and subsequently oxidized. Similar catalytic activity has been found for other mono-, di- and tricnuclear complexes with di-, tri- or heterovalent cobalt ions.[191,192,200–204] For these complexes, mechanistic studies revealed, that in a first step, a catalyst–substrate intermediate is formed by a coordination to cobalt(III). It is assumed that the following steps of the catalytic cycle include a valence tautomeric electron transfer to the metal ion, followed by the reaction with dioxygen, leading to the formation of the quinone and hydrogen peroxide as a byproduct while reoxidizing the catalyst. To check whether this mechanism may also be valid for the present complex **C13**, a qualitative test for hydrogen peroxide in the reaction solution was conducted. An iodide–starch test on 1 mg **C13** and 7.8 mg 3,5-di-*tert*-butylcatechol (**L1a**) dissolved in 10 ml of methanol indeed showed a bluish color, indicating the generation of hydrogen peroxide.

$$H_2O_2 + 2\,I^- + 2\,H^+ \longrightarrow I_2 + 2\,H_2O \tag{3.8}$$

$$I_2 + I^- + \text{starch} \longrightarrow \underset{\text{blue}}{I_3^-@\text{starch}} \tag{3.9}$$

This production of hydrogen peroxide shows a difference to the catalytic mechanism for native catecholase enzymes (see fig. 1.19) but is similar to many other model complexes in literature.[185,191,205] To get a structural idea of the intermediate catalyst–substrate complex ES, ESI mass spectrometric data were recorded on a catalyst solution ($c_{cat} = 0.1\,mg\,ml^{-1}$) with 50 equivalents of 3,5-di-*tert*-butylcatechol. In these studies, a *m/z* peak of 1497.79 is found, corresponding to the adduct $[Co_4(shi)_2(3,5\text{-dbcat})(piv)_2(py)_4 + 3,5\text{-dbcat} + H^+]^+$ (calc. $m/z = 1497.38$), which is assumed to be an intermediate of the catalytic cycle. In this intermediate cation, one of the (presumably axial) pyridine ligands is exchanged by a catechol. The observed protonation is believed to occur in methanolic solution under mass spectral conditions. Additionally, the analog adduct with only three pyridine ligands is observed in the ESI-MS experiment with a *m/z* peak of 1418.48 (calc. $m/z = 1418.33$). Therefore, the mechanistic assumptions made above are validated for the present compound and a schematic catalytic cycle can be postulated. This proposed mech-

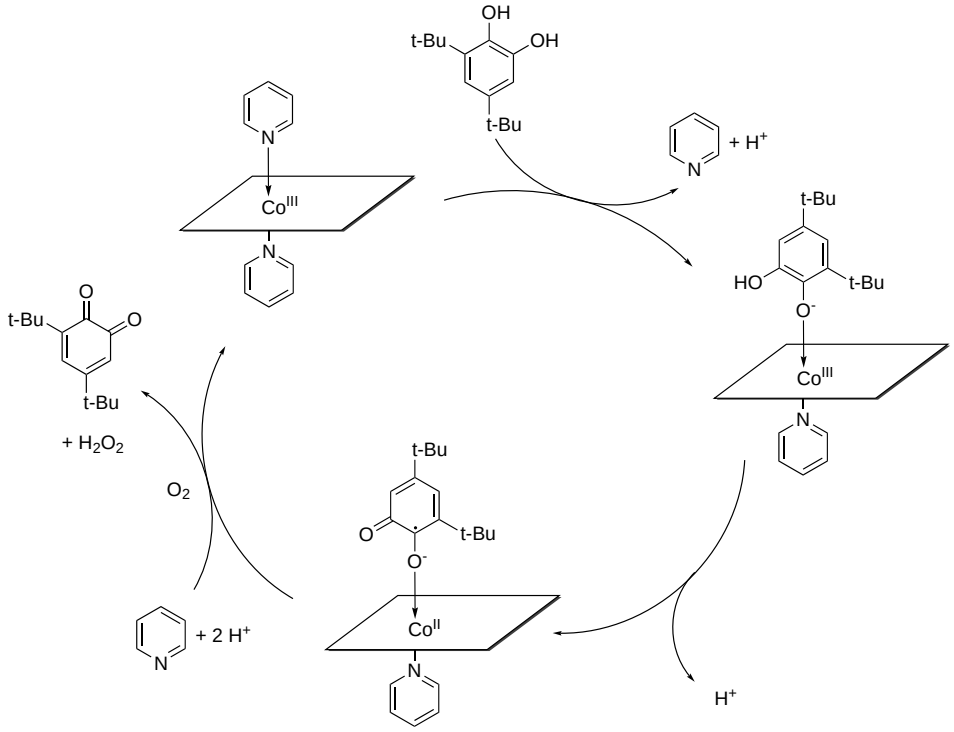

Fig. 3.48: Proposed mechanism for the catalytic cycle of the oxidation of 3,5-di-*tert*-butylcatechol by **C13**

anism for the oxidation of 3,5-di-*tert*-butylcatechol to the corresponding quinone is depicted in fig. 3.48. For the complexes **C3** and **C7a** similar mechanisms are expected.

4

Summary

The purpose of the present study was the development of novel routes for the synthesis of polynuclear transition metal dioxolene complexes with different metal ions. These various synthesis routes allowed studying the influence of the nuclearity and dioxolene bridging mode on the electronic properties of the complexes.

Preliminary preparation and magnetic characterization of the mononuclear dioxolene complexes [Co(3,5-dbsq)(3,5-dbcat)(4-Mepip)$_2$] (**C4**), [Co(dbmpsq)(dbmpcat)(4-Mepip)$_2$] (**C5**) and (Hpip)[Co(tbcat)$_2$(pip)$_2$] (**C6**) served as a reference for the polynuclear ones. For **C4**, a valence tautomeric transition to the cobalt(II) bis-semiquinone tautomer above room temperature was monitored by means of magnetic and spectroscopic studies.

Subsequently, the development of different strategies for the synthesis of polynuclear dioxolene complexes was presented. The first employed strategy of a self-assembly starting from transition metal pivalates, dioxolene ligands and small, non-chelating ancillary ligands was found to be very potent and allowed the synthesis of numerous polynuclear dioxolene complexes. Thorough investigation of structure–oxidation state relations for [Co$_3$(3,5-dbsq)$_2$(piv)$_4$(NEt$_3$)$_2$] (**C7a** and **C7b**), [Co$_4$(3,5-dbsq)$_4$(3,5-dbcat)(piv)$_2$(Hpiv)$_2$] (**C8**), [Co$_2$(3,5-dbsq)$_2$(pipycat)$_2$(pip)$_2$] (**C9**), [Cu$_6$(3,5-dbsq)$_4$(3,5-dbcat)$_2$(piv)$_4$] (**C10**), [Ni$_4$(3,5-dbcat)$_2$(H3,5-dbcat)(piv)$_2$(MeCN)$_4$] (**C11**) and (Hpip)$_2$[Co$_2$Fe$_2$(OH)(3,5-dbcat)$_3$(piv)$_5$(pip)] (**C12**) by means of crystallographic and magnetic examination led to a deeper understanding of the electronic properties for bridging dioxolenes coordinated to different transition metal ions. Laser irradiation experiments at low temperatures on **C7** further revealed the light-induced generation of a metastable state, whose exact nature is still subject to further research.

For more structural control and a predictable formation of polynuclear complexes, a metallacrown fragment based on salicyclhydroxamic acid was successfully employed as a planar complex backbone and structure dictating unit for the rational synthesis of the tetranuclear cobalt dioxolene complex [Co$_4$(shi)$_2$(3,5-dbcat)(piv)$_2$(py)$_5$] (**C13**).

This novel concept provides a powerful framework for the targeted synthesis of polynuclear complexes within the meaning of the directional bonding approach.

In further syntheses, the rigid, bis-chelating ancillary ligands 4-*tert*-butyl-2,6-bis(((2-hydroxyethyl)imino)methyl)phenol (H_3debup, **L3**), 4-*tert*-butyl-2,6-bis(((2-hydroxyphenyl)imino)methyl)phenol (H_3dabup, **L4**) and 3,5-bis(pyridine-2-yl)pyrazole (Hbpp, **L9**) were employed. For the resulting complexes $[Co_6(OH)_2(Hdebup)_2(piv)_8]$ (**C16**), $(HNEt_3)_2[Co_6(CO_3)(dabup)_3(piv)_3]$ (**C17**), $[Co_4(OH)_2(dabup)(bobupimp)(piv)_3]$ (**C18**), $[Cu_4(3,5\text{-dbcat})_2(bobupimp)_2(acetone)_2]$ (**C19**) and $[Co_6(CO_3)(bpp)_3(H3,5\text{-dbcat})_4(piv)_3]$ (**C20**) the impact of ligand geometry and properties on the complex formation were discussed.

Section 3.2.2.3 presents the synthesis of the octadentate nitrogen donor ligand *N*,*N*,*N*',*N*'-tetra-2-picolyl-1,4-bis(2-aminoethyl)piperazine (tpbap, **L7**) for the rational assembly of the first known dinuclear dioxolene complexes of the type $[\{Co(diox)\}_2(N_8L)]^{2+}$ as the perchlorate salt **C21b** and the valence tautomeric sulfate $[Co_2(tpbap)(3,5\text{-dbcat})_2](SO_4)$ (**C21a**), as inspired by the approved mononuclear, valence tautomeric cobalt dioxolenes $[Co(diox)(N_4L)]^+$. These dinuclear complexes with two well-defined and weakly coupled redox centers are regarded as ideal test objects for the systematic examination of two interacting switchable moieties. The magnetic and spectroscopic measurements on these dinuclear structures, which revealed a valence tautomeric transition for **C21a**, nicely illustrated the influence of crystal packing effects and lattice flexibility on the valence tautomeric equilibria. Notably, a diamagnetic state at low temperatures is found for this valence tautomer, which is in contrast to the conventional dinuclear dioxolene complexes but will be beneficial for potential applications or analysis. Due to their unique structures with two weakly coupled switchable centers, these complexes may serve as model systems for the experimental realization of molecular 2-qubit quantum gates, which before had been a synthetic challenge.

Finally, the polynuclear dioxolene complexes $[Fe_4(OH)_2(3,5\text{-dbcat})_4(py)_2(piv_2)]$ (**C3**), **C7a** and **C13** were identified to exhibit biomimetic catecholase activity, which demonstrates the metal-mediated electronic activation of the dioxolene ligands. Spectroscopic studies allowed the determination of Michaelis–Menten reaction kinetics for the oxidation of 3,5-di-*tert*-butylcatechol in all three cases. The catalytic activity was found to be independent from the complexes' nuclearity and the number of coordinated dioxolenes. The detection of hydrogen peroxide generated within the

catalytic cycle and ESI mass spectrometric studies enabled a mechanistic insight which enables the development of more efficient catalysts.

5 Outlook

This research will serve as a basis for future studies, as it provides multiple potent synthesis strategies for polynuclear dioxolenes with different transition metal ions and ligand oxidation states and coordination modes. The ability for a targeted, projectable synthesis may concern and stimulate various different areas of research.

One aim of subsequent activities should be the realization of well-characterized multi-step valence tautomerism. Based on this work's structural understanding and the acquired ability to synthesize multifaceted polynuclear dioxolene complexes, now additional attention is to be payed to the electronic modification and adaption of dioxolenes and ancillary ligands to the increased electron withdrawal for bridging coordination modes to enable valence tautomeric equilibria. An appropriate derivatization with electron withdrawing and donating groups could lead to an assimilation of ligand and metal frontier orbital energies to allow valence tautomerism at ambient temperatures. Taking complex **C21a** as an example, which shows a valence tautomeric transition at the border of the accessible temperature range, further studies could examine the electronic and steric modification of the tpbap ligand. Based on the trends for mononuclear complexes as summarized in table 1.1, it is expected that the derivatization with electron withdrawing groups or the increase of chelate ring flexibility allow the shift of the transition temperature towards lower temperatures, which facilitates an in-depth study of two-step valence tautomerism. Two appropriate ligands are shown in fig. 5.1. Additionally, asymmetric derivatization or chelate ring

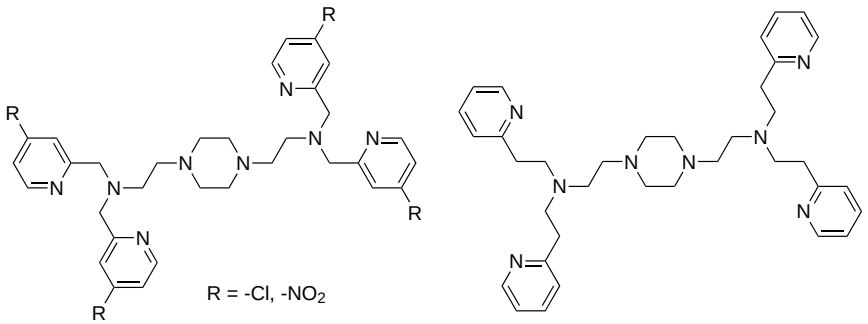

Fig. 5.1: Possible tpbap derivatives for the lowering of valence tautomeric transition temperatures of dinuclear cobalt complexes

enlargement would be possible, to foster the non-synchronous switching of the valence tautomeric centers.

In order to establish dinuclear cobalt dioxolenes like the herein presented complexes **C21a** and **C21b** as building blocks for the realization of quantum computers, still many obstacles are to overcome. To reduce spin coherence, the absence of moving charges in ionic structures is advantageous. Therefore, the utilization of electrically neutral complexes and thus some modifications of the molecular structure of the presented complexes would be necessary (e.g. the use of negatively charged ancillary ligands). Even with acceptable spin decoherence times for suchlike molecular units, further progress is required in the fields of organizing these molecules into devices or addressing and reading out of qubits. Despite all these challenges, the next decades will certainly afford exciting developments in this multidisciplinary topic of quantum computing, with coordination chemistry and molecular architecture as an essential contribution. The herein presented strategies for the synthesis of polynuclear dioxolene complexes can someday provide the required tools from a chemist's point of view.

6 Experimental Part

6.1 Methods

6.1.1 X-ray Crystallography

For the crystallographic characterization single crystals of the reported compounds were coated with perfluoropolyether, picked up with a nylon loop, and mounted on a SMART APEX II CCD diffractometer equipped with a nitrogen cold stream operating at 173(2) K. Graphite monochromated Mo-Kα radiation (λ = 0.710 69 Å) from a fine-focus sealed tube was used throughout. The crystallographic data of the compounds are listed in B. Cell constants were obtained from a least-squares fit of the diffraction angles of several thousand strong reflections. The data reduction was done with APEX2 v2.0[206], while SIR-97[207], SIR-2002[208] or Superflip[209] were used for the structure solution. The refinement of the structural model was processed with SHELXL 2014/7.[210] As a graphical front end Olex2 was utilized.[211]

6.1.2 SQUID Measurements

Magnetic susceptibility data of and magnetization measurements were collected with a SQUID magnetometer (Quantum Design MPMS XL-7). Powdered samples were filled in gelatin capsules and placed in a plastic straw. The measurements were carried out over a length of 4 cm with 24 data points. The temperature dependent magnetic contribution of the holder and capsule was experimentally determined and subtracted from the measured response function of the volume magnetization. With the molecular weight of the sample, the molar susceptibility was calculated using the julX 1.4.1 program by Bill.[212] Diamagnetic contributions of the samples were taken into account using Pascal constants. The simulation and fitting of the corrected data was performed using the PHI program.[213] For these simulations the Hamiltonian

$$\hat{H} = \hat{H}_{SO} + \hat{H}_{EX} + \hat{H}_{CF} + \hat{H}_{ZEE} \tag{6.1}$$

is used with $\hat{H}_{SO}$ (spin-orbit operator), $\hat{H}_{EX}$ (exchange operator) $\hat{H}_{CF}$ (crystal field operator) and $\hat{H}_{ZEE}$ (Zeeman operator). Due to the simplified nature of the simulations performed in this work, only the isotropic Heisenberg-Dirac-VanVleck effective Hamiltonian $\hat{H}_{EX}$ and $\hat{H}_{ZEE}$ were taken into account.

$$\hat{H}_{EX} = -2 \sum_{i<j}^{i,j \in N} J_{ij} \vec{\hat{S}}_i \cdot \vec{\hat{S}}_j \tag{6.2}$$

$$\hat{H}_{ZEE} = \mu_B \sum_{i=1}^{N} g_i \vec{\hat{S}}_i \vec{B} \tag{6.3}$$

6.1.3 NMR Spectroscopy

The NMR spectra were collected on a Bruker DRX 400 at room temperature ($\nu(^1\mathrm{H}) = 400.13\,\mathrm{MHz}$, $\nu(^{13}\mathrm{C}) = 100.61\,\mathrm{MHz}$). Tetramethylsilane and the solvent residual peaks were used as internal standard. For the processing and analysis of the spectra, the programs Bruker TopSpin 1.3 and MestreNova were utilized.

6.1.4 UV/Vis Spectroscopy

The UV/Vis spectra were measured on a Jasco V-570 UV/Vis/NIR spectrophotometer. For the measurements of solutions, quartz glass cells with an optical path length of 1 cm or 0.1 cm were used. Solid state reflectivity spectra were collected with the Harrick Scientific Praying Mantis™Diffuse Reflection Accessory with a low temperature reaction chamber. Potassium bromide was used for the optical dilution of the samples.

6.1.5 Infrared Spectroscopy

Infrared spectra were recorded in the $400\,\mathrm{cm^{-1}}$ to $4000\,\mathrm{cm^{-1}}$ range with a Jasco FT/IR-4200 spectrometer at room temperature. The samples were measured as pellets, using potassium bromide for the optical dilution.

6.1.6 Cyclic Voltammetry

The cyclic voltammograms were recorded with a three electrode cell setup using a Princeton Applied Research model 263 A potentiostat. A glassy carbon working electrode and a platinum counter electrode were utilized. A Ag/Ag^+ electrode (0.01 mol l^{-1} $AgNO_3$ in acetonitrile, silver wire) with salt bridge served as reference electrode in organic solvents. The sample concentration was 1 mmol l^{-1} if the solubility allowed it. tetrabutylammonium hexafluorophosphate (0.1 mol l^{-1}) was added as supporting electrolyte. The redox couple ferrocene–ferrocenium served as an internal standard, as the differences of the enthalpy of solution for ferrocene and ferrocenium are rather small, and therefore low solvent dependence is found for the reference potential. For the acquisition of data, the eDAQ EChem software (DOS version 4.30) was used.

6.1.7 ESI-MS

The ESI mass spectra were recorded on a Waters/MicroMass Q-Tof Ultima 3 spectrometer in the positive ion mode with LockSpray source at the Institute of Organic Chemistry at the Johannes Gutenberg University Mainz. A cone voltage of 52 V and a capillary voltage of 2.9 kV were applied.

6.1.8 Elemental Analysis

Elemental analyses (C, H and N) were carried out at the microanalytical laboratory of the Johannes Gutenberg University Mainz with a Foss Heraeus Vario EL elemental analyzer. The theoretical compositions were calculated without solvent molecules unless explicitly stated.

6.2 Syntheses

All chemicals used for the syntheses were obtained from commercial sources (Acros Organics, Alfa Aesar, Sigma-Aldrich, Fisher Scientific) and used as received without further purification, unless otherwise stated. Most reactions were carried out under air with spectrophotometrical grade solvents. A solvent purification system (MBRAUN MB-SPS-800) was used when dried solvents were required. For the

synthesis of air and moisture sensitive samples, Schlenk techniques were applied using argon 4.6.

6.2.1 Precursor Complexes

6.2.1.1 $[Co_2(OH_2)(piv)_4(Hpiv)_4]$ (P1)

40.0 g (392 mmol) of pivalic acid and 4 ml of water were added to 8.0 g (68 mmol) of cobalt carbonate hydrate ($CoCO_3 \cdot xH_2O$). The mixture was heated to 100 °C for 24 h. After the mixture had cooled down to 80 °C 100 ml acetonitrile were added and the resulting deep purple solution was filtered to remove seed crystals. After standing overnight the product **P1** could be separated by filtration as large, purple crystals.

Yield: 19.8 g purple crystals (20.9 mmol, 61.4 %).
IR (KBr): Figure A.1 on page 137.
$\tilde{\nu}$ (cm^{-1}) = 3415 (m), 2962 (s), 2929 (m), 2872 (m), 2698 (w), 2584 (w), 1678 (m), 1599 (s), 1524 (s), 1484 (s), 1459 (m), 1426 (s), 1361 (s), 1321 (m), 1227 (m), 1208 (m), 1031 (w), 937 (w), 897 (w), 872 (w), 791 (w), 611 (m), 539 (w), 460 (w), 418 (w).
Literature: G. Aromí et al., *Chem. Eur. J.* **2003**, *9*, 5142–5161.[214]

6.2.1.2 $[Co(piv)_2]_n$ (P2)

2.0 g (2.11 mmol) of powdered $[Co_2(OH_2)(piv)_4(Hpiv)_4]$ (**P1**) was heated to 180 °C under Argon with an electric Abderhalden's drying pistol. Water and pivalic acid evaporated from the sample and the color of the substrate changed from deep purple to pale violet.

Yield: 1.12 g violet powder (2.11 mmol, 100 %).
IR (KBr): Figure A.2 on page 137.
$\tilde{\nu}$ (cm^{-1}) = 3437 (br), 2962 (m), 2929 (m), 2871 (w), 1676 (w), 1599 (s), 1552 (s), 1524 (s), 1485 (s), 1458 (m), 1428 (s), 1361 (m), 1228 (m), 1032 (w), 939 (w), 898 (w), 792 (w), 613 (m), 583 (w), 540 (w), 459 (w).
Literature: G. Aromí et al., *Chem. Eur. J.* **2003**, *9*, 5142–5161.[214]

6.2.1.3 $[Cu_2(piv)_4(EtOH)_2]$ (P3)

11.86 g (32 mmol) of copper perchlorate hexahydrate and 8.97 g (64 mmol) of potassium pivalate were dissolved in 200 ml of ethanol to form a blue solution. The resulting $KClO_4$ precipitate was filtered off after 15 min and the filtrate was allowed to stand for 24 h. Large crystals of **P3** were isolated by filtration and washed with cold ethanol.

Yield: 8.08 g turquoise crystals (12.95 mmol, 81.0 %).
IR (KBr): Figure A.3 on page 138.
$\tilde{\nu}$ (cm^{-1}) = 3446 (br), 2960 (m), 2931 (m), 2873 (w), 1578 (s), 1531 (m), 1484 (m), 1460 (m), 1419 (s), 1377 (m), 1362 (m), 1223 (m), 1031 (w), 939 (w), 899 (w), 787 (w), 622 (m), 451 (m).
Literature: Variation of T. O. Denisova et al., *Russ. J. Inorg. Chem.* **2006**, *51*, 1020–1064.[215]

6.2.1.4 $[Ni_2(H_2O)(piv)_4(Hpiv)_4]$ (P4)

4.0 g (10.6 mmol) of $2\,NiCO_3 \cdot 3\,Ni(OH)_2 \cdot 4\,H_2O$ and 25.0 g (245 mmol) of pivalic acid were heated under reflux for 3 h with vigorous stirring. After the solution had been cooled down to 30 °C 20 ml diethyl ether were added and the mixture was filtered. 50 ml were added and the solution was allowed to stand still. After 48 h **P4** was filtered off as large green crystals, which were washed with cool acetonitrile.

Yield: 11.89 g green crystals (12.5 mmol, 80.1 %).
IR (KBr): Figure A.4 on page 138.
$\tilde{\nu}$ (cm^{-1}) = 3431 (br), 2972 (s), 2874 (m), 2703 (m), 2590 (m), 2361 (w), 1678 (s), 1607 (s), 1543 (m), 1482 (s), 1459 (m), 1408 (s), 1361 (s), 1208 (s), 1075 (w), 1033 (w), 876 (m), 798 (m), 612 (m), 543 (m).
Literature: G. Chaboussant et al., *Dalton Trans.* **2004**, 2758.[216]

6.2.1.5 $[Ni(piv)_2]_n$ (P5)

$[Ni_2(H_2O)(piv)_4(Hpiv)_4]$ (**P4**) (3.822 g, 4.0 mmol) was heated to 200 °C under Argon with an electric Abderhalden's drying pistol to evaporate the included water and pivalic acid. After one hour the product could be obtained as a green and amorphous powder.

Yield: 2.10 g pale green powder (4.0 mmol, 100 %).
IR (KBr): Figure A.5 on page 138.
$\tilde{\nu}$ (cm^{-1}) = 3429 (br), 2964 (s), 2930 (m), 2872 (m), 2589 (w), 1674 (s), 1605 (s), 1484 (s), 1460 (m), 1410 (s), 1361 (s), 1324 (m), 1210 (s), 1032 (w), 938 (w), 876 (m), 788 (w), 612 (w), 542 (w), 420 (w).
Literature: Z. V. Dobrokhotova et al., *Russ. Chem. Bull.* **2006**, *55*, 256–266.[217]

6.2.1.6 $[Fe_3O(piv)_6(H_2O)_3]piv$ (P6)

Iron(III) nitrate nonahydrate (24.24 g, 60 mmol) was dissolved in molten pivalic acid (90.13 g, 720 mmol) and heated to 165 °C. During the heating, first water evaporated, then nitrous gases evolved. When no further gases were produced, the mixture was cooled to 78 °C and 220 ml of ethanol followed by 50 ml of water were added in small portions. After 24 h red hexagonal crystals were separated by filtration, which were washed with toluene and η-hexane and dried in air.

Yield: 18.56 g red hexagonal crystals (19.6 mmol, 98 %).
IR (KBr): Figure A.6 on page 139.
$\tilde{\nu}$ (cm^{-1}) = 3417 (br), 2962 (m), 2929 (m), 2872 (m), 1592 (s), 1486 (s), 1458 (m), 1427 (s), 1381 (m), 1363 (m), 1230 (m), 1045 (w), 939 (w), 899 (w), 868 (w), 788 (w), 607 (m), 445 (m).
Literature: Variation of M. A. Kiskin et al., *Russ. Chem. Bull.* **2004**, *53*, 2508–2518.[218]

6.2.1.7 $[Fe_3O(piv)_6(py)_3]$ (P7)

13 g (65.4 mmol) of iron(II) chloride tetrahydrate was dissolved in 50 ml of water. Separately, 32 g (313 mmol) pivalic acid and 6.4 g (160 mmol) of sodium hydroxide were dissolved 10 ml of dimethoxyethane and 10 ml of water. After the two solutions had been combined, the mixture was heated under reflux for 1 h. The two-phase system was cooled to room temperature and filtered under argon. The black residue was washed with a degassed acetone/water mixture (1:1) and dried under reduced pressure. Recrystallization from 30 ml of pyridine yielded black crystals, which were washed with acetone/water 1:1 and dried in vacuo.

Yield: 12.36 g brown crystals (12.03 mmol, 55 %).

IR (KBr): Figure A.7 on page 139.
$\tilde{\nu}$ (cm^{-1}) = 3451 br, 2958 s, 2926 m, 2867 m, 1595 s, 1483 s, 1446 m, 1416 s, 1373 m, 1359 m, 1227 s, 1151 w, 1074 w, 1038 m, 1011 w, 893 w, 787 w, 755 w, 695 m, 628 w, 603 m, 431 m.
Literature: R. Wu et al., *Inorg. Chem.* **1998**, *37*, 1913–1921.[219]

6.2.1.8 $[Fe_2CoO(piv)_6(pip)_3]$ (P8)

$[Co_2(OH_2)(piv)_4(Hpiv)_4]$ (**P1**, 5.07 g, 5.27 mmol) and $[Fe_3O(piv)_6(H_2O)_3]$piv (**P6**, 8.05 g, 8.51 mmol) were dissolved in 37 ml of piperidine and heated under reflux for 5 h. After cooling to 55 °C 122 ml of acetone were added and the solution was refluxed for 1 h. The mixture was allowed to cool to room temperature and after 24 h the crystals formed were filtered off, washed with acetone and dried in air. The crude product **P8** was recrystallized from acetone containing a few drops of piperidine.

Yield: 8.9 g brown crystals (8.49 mmol, 80.5 %).
IR (KBr): Figure A.8 on page 139.
$\tilde{\nu}$ (cm^{-1}) = 3441 (br), 2955 (m), 1628 (s), 1604 (s), 1482 (m), 1452 (w), 1412 (s), 1371 (m), 1227 (m), 1018 (w), 985 (w), 874 (m), 786 (w), 714 (w), 603 (m), 425 (m).
Literature: Variation of A. S. Batsanov et al., *Koordinats. Khim.* **1991**, *17*, 662–669.[220]

6.2.2 Ligands

6.2.2.1 Di-*tert*-butyl-1,2-benzoquinone (L1b)

To a suspension of 4.4 g (20 mmol) of 3,5-di-*tert*-butylcatechol in 10 ml of glacial acetic acid was added in small portions a solution of 2.8 g (40 mmol) of sodium nitrite in 10 ml of water. Large amounts of nitrous gases evolved and the mixture turned brown. The suspension was rigorously stirred for one hour at room temperature, then diluted with 60 ml of water. The brownish precipitate was filtered off, washed with water and dried in air. The crude product was already reasonably pure. Recrystallization from *n*-hexane afforded large red needles.

Yield: 4.3 g red needles (19.5 mmol, 98.6 %).

^{1}H-NMR (400 MHz, $CDCl_3$) Figure A.40 on page 150.

δ (ppm) = 6.95 (d, $J = 2.2$, 1 H, H_4), 6.23 (d, $J = 2.2$, 1 H, H_6), 1.29 (d, $J = 1.1$, 9 H, H_{10}), 1.24 (d, $J = 1.1$, 9 H, H_{14}).

IR (KBr): Figure A.9 on page 140.

$\tilde{\nu}$ (cm^{-1}) = 3426 (br), 3066 (w), 2958 (s), 2871 (m), 1657 (s), 1623 (m), 1566 (m), 1477 (m), 1371 (s), 1275 (m), 1245 (m), 1023 (w), 952 (w), 893 (m), 813 (w), 656 (w), 581 (w).

Literature: T. M. Khomenko et al., *Russ. J. Org. Chem.* **2006**, *42*, 1653–1661.[221]

6.2.2.2 4-*tert*-Butyl-2,6-bis(((2-hydroxyethyl)imino)methyl)phenol (H_3debup, L3)

4-*tert*-Butyl-2,6-diformylphenol (L2)

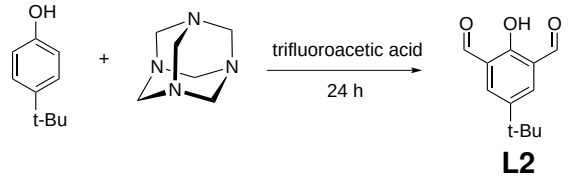

L2

Fig. 6.1: Synthesis of **L2**

4.66 g of 4-*tert*-butylphenol and 8.7 g of urotropine were dissolved in 55 ml of trifluoroacetic acid under argon atmosphere. The solution was heated under reflux for 24 h. After cooling to room temperature, the mixture was poured into 180 ml of 4 M hydrochloric acid and stirred for 10 min and the acid solution was extracted with dichloromethane (2 × 150 ml). The combined organic phases were washed with 4 M hydrochloric acid (2 × 200 ml), water (200 ml) and brine (200 ml). The organic phase was dried over sodium sulfate and purified by column chromatography (silica gel, chloroform, R_f 0.43).

Yield: 4.75 g yellow needles (23.0 mmol, 74.3 %).

^{1}H-NMR (400 MHz, $CDCl_3$) Figure A.41 on page 151.

δ (ppm) = 11.50 (s, 1 H, H_7), 10.50 (s, 2 H, H_8), 8.00 (s, 2 H, H_2), 1.38 (s, 9 H, H_{13}).

IR (KBr): Figure A.10 on page 140.

$\tilde{\nu}$ (cm^{-1}) = 3445 (br), 2963 (m), 2866 (m), 1659 (s), 1598 (s), 1469 (m), 1380 (m), 1316 (m), 1281 (m), 1226 (s), 1120 (w), 1033 (w), 981 (s), 827 (w), 756 (m), 735 (m), 616 (m), 507 (w).

Literature: L. F. Lindoy, *Synthesis* **1998**, *1998*, 1029–1032.[222]

4-*tert*-Butyl-2,6-bis(((2-hydroxyethyl)imino)methyl)phenol (H_3debup, L3)

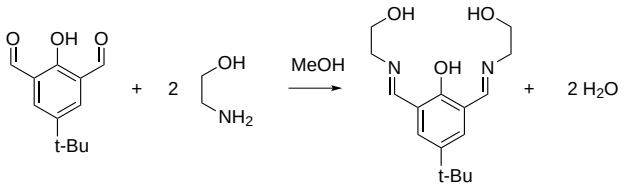

L2 **L3**

Fig. 6.2: Synthesis of **L3**

1.6 g (7.76 mmol) of 4-*tert*-butyl-2,6-diformylphenol (**L2**) and 0.95 g (15.5 mmol) of 2-aminoethanol were dissolved in 250 ml of methanol, stirred at room temperature for 12 h and heated under reflux for 1 h. The solvent was removed under reduced pressure. The crude solid **L3** was used without further purification.

Yield: 2.11 g orange solid (7.2 mmol, 92.8 %).

^{1}H-NMR (400 MHz, $CDCl_3$) Figure A.42 on page 151.

δ (ppm) = 8.60 (s, 2 H, H_{12}), 7.65 (s, 2 H, H_1), 3.95 (t, $J = 4.2$, 4 H, H_{18}), 3.79 (t, $J = 4.2$, 4 H, H_{16}), 1.34 (s, 9 H, H_8).

IR (KBr): Figure A.11 on page 140.

$\tilde{\nu}$ (cm^{-1}) = 3390 (br), 2954 (m), 1639 (s), 1527 (m), 1468 (m), 1385 (m), 1363 (m), 1260 (m), 1224 (m), 1126 (w), 1070 (m), 995 (w), 893 (w), 870 (w), 828 (w), 789 (w), 760 (w), 708 (w), 635 (w), 518 (w).

6.2.2.3 4-*tert*-Butyl-2,6-bis(((2-hydroxyphenyl)imino)methyl)phenol (H_3dabup, L4)

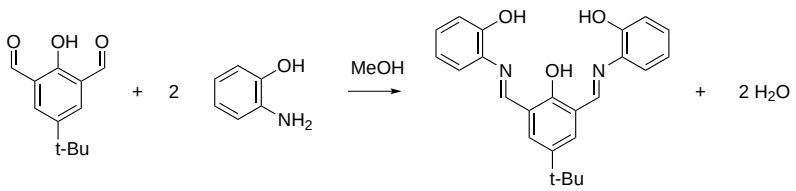

L2 **L4**

Fig. 6.3: Synthesis of **L4**

2.5 g (12.1 mmol) of 4-*tert*-butyl-2,6-diformylphenol (**L2**) and 2.65 g (24.2 mmol) of *o*-aminophenol were dissolved in 100 ml of dried methanol and heated under reflux

for 3 h. The solution was further stirred. After five days, the solvent was removed under reduced pressure. The residual solid was recrystallized from *n*-hexane.

Yield: 4.176 g red crystals (10.8 mmol, 88.7 %).
^{1}H-NMR (400 MHz, $CDCl_3$) Figure A.43 on page 152.
δ (ppm) = 9.04 (s, 2 H, H_8), 7.97 (s, 2 H, H_1), 7.31 (dd, 2 H, H_{21}), 7.25 (td, 2 H, H_{19}), 7.06 (dd, 2 H, H_{18}), 6.98 (td, 2 H, H_{20}), 6.86 to 6.65 (m, 1 H, H_7), 1.42 (s, 9 H, H_{27}).
IR (KBr): Figure A.12 on page 141.
$\tilde{\nu}$ (cm^{-1}) = 3425 (br), 3056 (m), 2957 (m), 1624 (s), 1587 (m), 1518 (s), 1462 (m), 1363 (m), 1334 (m), 1231 (s), 1152 (m), 1107 (m), 1036 (m), 928 (w), 881 (w), 808 (w), 747 (m), 572 (w), 499 (w).

6.2.2.4 *N*,*N*,*N*',*N*'-Tetra-2-picolyl-1,4-bis(2-aminoethyl)piperazine (tpbap, L7)

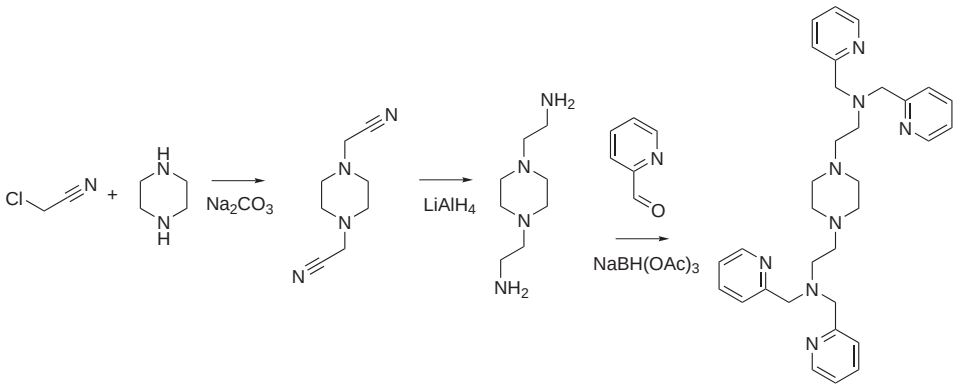

L5 **L6** **L7**

Fig. 6.4: Synthesis of **L7**

N,*N*'-Bis(cyanomethyl)piperazine (L5)

To a solution of 6.45 g (75 mmol) piperazine and 13.59 gram (180 mmol) chloroacetonitrile in 300 ml ethanol 31.8 g (300 mmol) sodium carbonate was added in small portions under stirring. The mixture was heated under reflux overnight. The hot solution was filtered and the remaining residue was thoroughly washed with hot ethanol. After the filtrate has been concentrated to 120 ml under reduced pressure the yellowish solvent was cooled to −18 °C. The product **L5** could be isolated by filtration.

Yield: 9.15 g colourless crystals (55.7 mmol, 74.3 %).

^{1}H-NMR (400 MHz, $CDCl_3$) Figure A.44 on page 152.
δ (ppm) = 3.57 (s, 4 H, H_1), 2.71 (s, 8 H, H_7).
^{13}C-NMR (100 MHz, $CDCl_3$) Figure A.45 on page 153.
δ (ppm) = 114.3 (s), 51.1 (s), 45.8 (s).
IR (KBr): Figure A.13 on page 141.
$\tilde{\nu}$ (cm^{-1}) = 3448 (br), 2963 (m), 2945 (m), 2915 (w), 2891 (m), 2824 (s), 2756 (m), 2711 (w), 2231 (w), 1456 (s), 1436 (m), 1379 (w), 1318 (s), 1296 (m), 1156 (s), 1134 (m), 1013 (s), 898 (w), 867 (s), 798 (m), 710 (w), 508 (w).
Literature: L. P. G. Wakelin et al., *J. Med. Chem.* **2003**, *46*, 5790–5802.[223]

N,*N*'-Bis(2-aminoethyl)piperazine (L6)

A solution of 2.5 g (15.2 mmol) *N*,*N*'-Bis(cyanomethyl)piperazine (**L5**) in 100 ml thf was dropped into a suspension of 2.66 g (70.0 mmol) lithium aluminium hydride in 100 ml thf. The mixture was heated under reflux for 4 h. Afterwards, the solution was cooled to 0 °C and 2.35 ml water was added, followed by 2.35 ml sodium hydroxide solution (15 %) and 7.05 ml water. The suspension was filtered and the residue was washed with a large amount of diethyl ether. The filtrate was dried over sodium sulfate and evaporated to dryness.

Yield: 1.58 g yellowish needles (9.17 mmol, 60.3 %).
^{1}H-NMR (400 MHz, $CDCl_3$) Figure A.46 on page 153.
δ (ppm) = 2.71 (t, $J = 6.3\,Hz$, 4 H, H_8), 2.41 (s, 4 H, H_1), 2.35 (t, $J = 6.3\,Hz$, 4 H, H_7), 1.47 (s, 4 H, H_9).
^{13}C-NMR (100 MHz, $CDCl_3$) Figure A.47 on page 154.
δ (ppm) = 61.14 (s, C_7), 53.24 (s, C_1), 38.78 (s, C_8).
IR (KBr): Figure A.14 on page 141.
$\tilde{\nu}$ (cm^{-1}) = 3385 (br), 2946 (s), 2828 (s), 1574 (s), 1487 (s), 1316 (s), 1156 (m), 1054 (w), 1006 (m), 819 (m), 778 (m), 605 (m), 419 (w).
Literature: R. Filosa et al., *Bioorg. Med. Chem.* **2009**, *17*, 13–24.[224]

N,*N*,*N*',*N*'-Tetra-2-picolyl-1,4-bis(2-aminoethyl)piperazine (L7)

To a solution of 1.0 g (5.8 mmol) *N*,*N*'-Bis(2-aminoethyl)piperazine (**L6**) in 150 ml dichloromethane 6.152 g (29.0 mmol)sodium triacetoxyborohydride was added in small portions. Under continuous stirring a solution of 2.611 g (24.4 mmol) 2-pyridine-

carboxaldehyde in 10 ml dichloromethane was added within 30 min. After the mixture had been stirred at room temperature for two days 50 ml saturated sodium hydrogen carbonate was added whereupon CO_2 evolved. The mixture was stirred for additional 30 min and extracted with dichloromethane and ethyl acetate. The organic phase was dried over sodium sulfate and evaporated to dryness. The crude product **L7** was purified by washing with acetone and dried in a vacuum.

Yield: 3.01 g yellowish powder (5.6 mmol, 97 %).
^{1}H-NMR (400 MHz, $CDCl_3$) Figure A.48 on page 154.
δ (ppm) = 8.57 to 8.44 (m, 4 H, H_{22}), 7.65 (td, 4 H, H_{24}), 7.52 (d, 4 H, H_{25}), 7.15 (ddd, 4 H, H_{23}), 3.85 (s, 8 H, H_{13}), 2.74 (t, 4 H, H_9) 2.67 to 2.22 (m, 1 H6, $H_{1,7}$).
^{13}C-NMR (100 MHz, $CDCl_3$) Figure A.49 on page 155.
δ (ppm) = 159.61 (s, C_{17}), 148.97 (s, C_{22}), 136.45 (s, C_{24}), 123.02 (s, C_{25}), 122.00 (s, C_{23}), 60.70 (s, C_{13}), 56.06 (s, C_7), 52.98 (s, C_9), 51.22 (s, C_1).
IR (KBr): Figure A.15 on page 142.
$\tilde{\nu}$ (cm^{-1}) = 3421 (br), 3057 (w), 3009 (w), 2939 (m), 2811 (m), 1589 (s), 1570 (m), 1471 (m), 1431 (s), 1363 (m), 1318 (m), 1301 (m), 1248 (m), 1145 (m), 1124 (m), 1051 (m), 1013 (m), 982 (m), 958 (w), 939 (w), 890 (w), 822 (w), 766 (s), 731 (w), 610 (w), 463 (w), 410 (w).

6.2.2.5 3,5-Bis(pyridine-2-yl)pyrazole (Hbpp, L9)

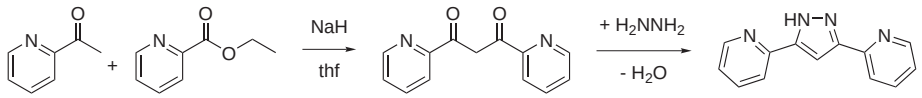

L8 **L9**

Fig. 6.5: Synthesis of **L9**

1,3-Bis(pyridine-2-yl)propane-1,3-dione (*o*-dppd, L8)

2-Acetylpyridine (5.0 g, 41 mmol) was dissolved in 200 ml of anhydrous tetrahydrofurane. Sodium hydride (60 % dispersion in mineral oil, 2.0 g, 50 mmol) was added carefully in small portions. Then, ethyl picolinate (6.24 g, 41 mmol) was added and the mixture was stirred at 60 °C. As the yellow solution thickened 50 ml of additional anhydrous thf were added. After 12 h the solvent was removed under reduced pressure and a 1:5 mixture of acetic acid and water was added to the remaining

solid. The residual solid was filtered and recrystallized from methanol and dried in a vacuum.

Yield: 7.939 g grey powder (35.1 mmol, 85 %).

^{1}H-NMR (400 MHz, $CDCl_3$) Figure A.50 on page 155.

δ (ppm) = 8.77 (d, 2 H), 8.63 (d, 0.5 H), 8.12 (d, 2 H), 7.95 to 8.08 (m, 4 H), 7.64 (t, 2.5 H), 4.85 (s, 0.5 H).

IR (KBr): Figure A.16 on page 142.

$\tilde{\nu}$ (cm^{-1}) = 3434 (br), 3135 (w), 3050 (w), 2924 (w), 1620 (s), 1563 (s), 1462 (s), 1426 (s), 1386 (m), 1324 (m), 1284 (m), 1068 (m), 993 (m), 845 (w), 788 (s), 740 (m), 705 (m), 612 (s), 501 (w), 458 (w).

Literature: P. C. Andrews et al., *Eur. J. Inorg. Chem.* **2009**, *2009*, 744–751.[225]

3,5-Bis(pyridine-2-yl)pyrazole (Hbpp, L9)

Hydrazine hydrate (0.750 g, 3.32 mmol) and *o*-dppd (**L8**, 0.750 g, 3.32 mmol) were dissolved in 50 ml of methanol and heated to 60 °C in a CEM laboratory microwave for 10 min (P = 150 W). The brown solution was cooled to 5 °C. After few hours Hbpp (**L9**) could be isolated by filtration as colorless needles.

Yield: 0.406 g colorless needles (1.8 mmol, 55 %).

^{1}H-NMR (400 MHz, $CDCl_3$) Figure A.51 on page 156.

δ (ppm) = 11.41 (s, 1 H, H_3), 8.65 (d, 2 H, $H_{9,16}$), 7.90 (d, 2 H, $H_{12,13}$), 7.78 (td, 2 H, $H_{11,14}$), 7.43 (s, 1 H, H_5), 7.27 (td, 2 H, $H_{10,15}$).

IR (KBr): Figure A.17 on page 142.

$\tilde{\nu}$ (cm^{-1}) = 3432 (br), 3143 (m), 3051 (m), 2925 (m), 2359 (m), 1595 (s), 1570 (m), 1509 (w), 1484 (m), 1448 (s), 1411 (m), 1320 (w), 1268 (w), 1227 (w), 1188 (m), 1050 (m), 1002 (m), 974 (w), 962 (w), 877 (w), 768 (s), 737 (m), 684 (w), 667 (w), 626 (m), 519 (w).

Literature: Variation of M. Ferles et al., *Collect. Czechoslov. Chem. Commun.* **1990**, *55*, 1228–1233.[226]

6.2.3 Complexes

6.2.3.1 $[Fe_2(H3,5\text{-dbcat})_2(3,5\text{-dbsq})_4]$ (C1)

0.95 g (1 mmol) of **P6** were dissolved in 30 ml of ethanol at room temperature. Under continuous stirring, a solution of 1.33 g (6 mmol) of 3,5-di-*tert*-butylcatechol in 30 ml of ethanol was added. The resulting deep blue solution was stirred at room temperature for one hour. After the insoluble material has been filtered of, the solution was kept at 20 °C for 24 h, after which violet crystals of complex **C1** precipitated.

Yield: 0.53 g dark violet crystals (0.37 mmol, 37 %).
IR (KBr): Figure A.18 on page 143.
$\tilde{\nu}$ (cm^{-1}) = 3492 (br), 2960 (s), 2907 (m), 2870 (m), 1579 (m), 1485 (s), 1490 (s), 1419 (m), 1362 (m), 1303 (m), 1246 (w), 1224 (w), 1091 (w), 1028 (w), 983 (m), 862 (w), 657 (w), 494 (m).
Elemental Analysis: Found: C, 69.29; H, 8.62. Calc. for $C_{84}H_{122}Fe_2O_{12}$ + H_2O: C, 69.41; H, 8.60 %.

6.2.3.2 $[Fe_2(3,5\text{-dbcat})_2(3,5\text{-dbsq})_2(py)_2]$ (C2)

0.95 g (1 mmol) of **P6** were dissolved in 30 ml of acetone at room temperature. Under stirring, a solution of 1.33 g (6 mmol) of 3,5-di-*tert*-butylcatechol in 30 ml of acetone was added. To the resulting deeply colored solution 237 mg (3 mmol) of pyridine were added and the reaction mixture was stirred at room temperature for four hours. After the insoluble material has been filtered off, the solution was kept at 20 °C for 24 h, after which brown crystals of complex **C2** precipitated.

Yield: 0.83 g brown crystals (0.72 mmol, 48 %).
IR (KBr): Figure A.19 on page 143.
$\tilde{\nu}$ (cm^{-1}) = 3086 (w), 2956 (s), 2904 (m), 2865 (m), 1714 (m), 1578 (m), 1490 (s), 1448 (s), 1410 (m), 1359 (m), 1308 (m), 1246 (s), 1154 (m), 984 (s), 910 (w), 860 (w), 827 (m), 750 (m), 682 (m), 654 (w), 580 (m), 549 (w), 491 (m).
Elemental Analysis: Found: C, 68.56; H, 7.85; N, 2.28. Calc. for $Fe_2C_{66}H_{90}O_8N_2$: C, 68.85; H, 7.89; N, 2.43 %.

6.2.3.3 $[Fe_4(OH)_2(3,5\text{-dbcat})_4(py)_2(piv_2)]$ (C3)

1.03 g (1 mmol) of **P7** were dissolved in 60 ml of acetone at room temperature. Under stirring, a solution of 1.33 g (6 mmol) of 3,5-di-*tert*-butylcatechol in 40 ml of acetone was added. The reaction mixture was stirred at room temperature for one hour. After the insoluble material has been filtered off, the solution was kept at 20 °C for 72 h, after which brown crystals of complex **C3** precipitated.

Yield: 0.94 g brown crystals (0.63 mmol, 42 %).
IR (KBr): Figure A.20 on page 143.
$\tilde{\nu}$ (cm^{-1}) = 3453 (br), 2957 (s), 2904 (m), 2867 (m), 1606 (m), 1578 (m), 1478 (s), 1447 (s), 1411 (m), 1385 (m), 1360 (m), 1278 (m), 1248 (m), 984 (s), 694 (w), 580 (w), 493 (w).
Elemental Analysis: Found: C, 60.83; H, 8.32; N, 2.11. Calc. for $C_{76}H_{110}Fe_4N_2O_{14}$: C, 60.89; H, 7.40; N, 1.87 %.

6.2.3.4 $[Co(3,5\text{-dbsq})(3,5\text{-dbcat})(4\text{-Mepip})_2]$ (C4)

237 mg (0.25 mmol) of $[Co_2(OH_2)(piv)_4(Hpiv)_4]$ (**P1**), 333 mg (1.5 mmol) of 3,5-di-*tert*-butylcatechol and 298 mg (3.0 mmol) of 4-methylpiperidine were dissolved in 15 ml acetonitrile and heated under reflux for one hour. The mixture was filtered to remove any insoluble residue. After one day, slow evaporation of the solvent yielded the crystalline complex **C4**, which was filtered off and washed with cold acetonitrile.

Yield: 249 mg dark blue crystals (0.36 mmol, 71.4 %).
IR (KBr): Figure A.21 on page 144.
$\tilde{\nu}$ (cm^{-1}) = 3567 (br), 2951 (s), 2869 (m), 2360 (w), 1573 (m), 1460 (m), 1415 (m), 1358 (m), 1278 (m), 1243 (m), 1199 (m), 1095 (m), 981 (m), 860 (m), 746 (w), 651 (m), 577 (w), 545 (w), 493 (w), 446 (w).
Elemental Analysis: Found: C, 68.59; H, 9.45; N, 4.48. Calc. for $C_{40}H_{66}CoN_2O_4$: C, 68.84; H, 9.53; N, 4.01 %.

6.2.3.5 $[Co(dbmpsq)(dbmpcat)(4\text{-Mepip})_2]$ (C5)

131 mg (0.125 mmol) of $[Co(piv)_2]_n$ (**P2**), 167 mg (0.75 mmol) of 3,5-di-*tert*-butylcatechol and 149 mg (1.5 mmol) of 4-methylpiperidine were dissolved in 15 ml of

acetonitrile and heated under reflux for one hour. Afterwards, the solution was filtered to remove any crystal nuclei. Slow evaporation of the solvent yielded **C5** after 24 h to 48 h.

Yield: 48 mg green plates (0.05 mmol, 43.0 %).
IR (KBr): Figure A.22 on page 144.
$\tilde{\nu}$ (cm^{-1}) = 3610 (br), 2952 (s), 2915 (s), 1615 (w), 1553 (m), 1509 (w), 1459 (m), 1260 (m), 1197 (m), 1112 (m), 1075 (m), 980 (m), 859 (m), 694 (w), 661 (w), 549 (w).
Elemental Analysis: Found: C, 68.78; H, 10.93; N, 5.86. Calc. for $C_{52}H_{88}CoN_4O_4 + H_2O$: C, 68.62; H, 9.97; N, 6.16 %.

6.2.3.6 (Hpip)[Co(tbcat)$_2$(pip)$_2$] (C6)

$[Co_2(OH_2)(piv)_4(Hpiv)_4]$ (**P1**, 237 mg, 0.25 mmol) and tetrabromocatechol (H_2tbcat, 319 mg. 0.75 mmol) were dissolved in 15 ml of acetonitrile. Under continuous stirring 128 mg of piperidine were added. The solution was heated under reflux for 30 min and subsequently filtered. The brown solution was slowly concentrated and after four days **C6** could be isolated by filtration as brown crystals.

Yield: 173 mg brown plates (0.149 mmol, 29.8 %).
IR (KBr): Figure A.23 on page 144.
$\tilde{\nu}$ (cm^{-1}) = 3443 (br), 2936 (w), 2854 (w), 1596 (w), 1432 (s), 1348 (w), 1263 (m), 1232 (m), 1085 (w), 1026 (w), 1004 (w), 930 (m), 876 (w), 772 (w), 743 (m), 632 (w), 571 (w).
Elemental Analysis: Found: C, 29.09; H, 3.01; N, 4.76. Calc. for $C_{27}H_{34}Br_8CoN_3O_4$ + MeCN: C, 28.93; H, 3.10; N, 4.65 %.

6.2.3.7 [Co$_3$(3,5-dbsq)$_2$(piv)$_4$(NEt$_3$)$_2$] (C7a)

0.131 g (0.5 mmol) of $[Co(piv)_2]_n$ (**P2**) were dissolved in 9 ml of acetonitrile[1] at room temperature. Under continuous stirring, a solution of 0.167 g (0.75 mmol) 3,5-di-*tert*-butylcatechol in 6 ml acetonitrile was added. The resulting dark solution was heated under reflux for ten minutes. After filtering off insoluble material, the solution was kept at 20 °C for 24 hours, after which dark green crystals of complex **C7a**

[1] Solvent purity and water content were found to be crucial in this synthesis. Best yields were obtained with purities higher than 99.8 %.

precipitated. The monoclinic antiperiplanar conformer **C7b** could be separated as a side product in rare cases and was solely identified by its crystal morphology.

Yield: 0.108 g dark green plates (0.09 mmol, 52.9 %).
IR (KBr): Figure A.24 on page 145.
$\tilde{\nu}$ (cm^{-1}) = 3434 (br), 2961 (s), 2866 (w), 1595 (s), 1481 (s), 1460 (m), 1412 (s), 1372 (m), 1227 (w), 1358 (m), 1096 (w), 1057 (w), 1028 (w), 987 (w), 892 (w), 867 (w), 787 (w), 740 (w), 610 (w), 582 (w), 427 (w).
Elemental Analysis: Found: C, 58.61; H, 8.91; N, 2.28. Calc. for $C_{60}H_{106}Co_3N_2O_{12}$: C, 58.86; H, 8.73; N, 2.29 %.

6.2.3.8 $[Co_4(3,5\text{-dbsq})_4(3,5\text{-dbcat})(piv)_2(Hpiv)_2]$ (C8)

$[Co_2(OH_2)(piv)_4(Hpiv)_4]$ (**P1**, 237 mg, 0.25 mmol) and 3,5-di-*tert*-butylcatechol (**L1a**, 139 mg. 0.625 mmol) were dissolved in 14 ml of acetonitrile under stirring. The dark solution was heated under reflux for 15 min. After the hot mixture was filtered, slow evaporation of the solvent was allowed. After 24 h dark green crystals of **C8** were separated by filtration.

Yield: 56 mg green plates (0.032 mmol, 25.7 %).
IR (KBr): Figure A.25 on page 145.
$\tilde{\nu}$ (cm^{-1}) = 3444 (br), 2957 (s), 2869 (m), 2362 (w), 1662 (m), 1579 (m), 1558 (m), 1482 (s), 1455 (s), 1413 (m), 1359 (s), 1330 (w), 1211 (m), 1096 (w), 1027 (w), 984 (m), 874 (w), 829 (w), 788 (w), 746 (w), 658 (w), 576 (w), 509 (w), 470 (w), 451 (w), 430 (w).
Elemental Analysis: Found: C, 60.74; H, 8.04. Calc. for $C_{90}H_{138}Co_4O_{18}$ + 2 H_2O: C, 60.73; H, 8.04 %.

6.2.3.9 $[Co_2(3,5\text{-dbsq})_2(pipycat)_2(pip)_2]$ (C9)

$[Co(piv)_2]_n$ (**P2**, 131 mg, 0.5 mmol) and 3,5-di-*tert*-butylcatechol (**L1a**, 167 mg, 0.75 mmol) were dissolved in 15 ml of acetonitrile under stirring. Piperidine (128 mg, 1.5 mmol) was added and the solution was heated under reflux for 30 min. The insoluble material was filtered off and the solution was slowly concentrated. After 48 h **C9** was isolated by filtration and washed with cold acetonitrile.

Yield: 69 mg dark blue plates (0.046 mmol, 18.5 %).

IR (KBr): Figure A.26 on page 145.
$\tilde{\nu}$ (cm^{-1}) = 2925 (s), 2856 (m), 1613 (w), 1550 (m), 1508 (w), 1451 (m), 1408 (m), 1388 (m), 1352 (m), 1257 (m), 1217 (m), 1106 (m), 1022 (m), 982 (m), 895 (m), 875 (m), 685 (m), 616 (w), 578 (m), 549 (m).
Elemental Analysis: Found: C, 67.35; H, 9.55; N, 6.62. Calc. for $C_{86}H_{126}Co_2N_6O_8$ + 1.5 MeCN + H_2O: C, 68.11; H, 8.51; N, 6.69 %.

6.2.3.10 $[Cu_6(3,5\text{-dbsq})_4(3,5\text{-dbcat})_2(piv)_4]$ (C10)

A solution of $[Cu_2(piv)_4(EtOH)_2]$ (**P3**, 156 mg, 0.25 mmol) and 3,5-di-*tert*-butylcatechol (**L1a**, 156 mg, 0.7 mmol) in 15 ml of acetone was heated under reflux for 30 min. The hot mixture was filtered and the filtrate was allowed to cool slowly. After 24 h the complex **C10** was separated by filtration and washed with cold acetone.

Yield: 32 mg black plates (0.015 mmol, 18.2 %).
IR (KBr): Figure A.27 on page 146.
$\tilde{\nu}$ (cm^{-1}) = 3452 (br), 2959 (s), 1575 (s), 1516 (m), 1453 (s), 1359 (m), 1299 (w), 1236 (m), 1094 (w), 1028 (w), 983 (w), 866 (w), 785 (w), 577 (w), 449 (w).
Elemental Analysis: Found: C, 59,17; H, 7,50. Calc. for $C_{104}H_{156}Cu_6O_{20}$: C, 59.27; H, 7.46 %.

6.2.3.11 $[Ni_4(3,5\text{-dbcat})_2(H3,5\text{-dbcat})_2(piv)_2(MeCN)_4]$ (C11)

$[Ni(piv)_2]_n$ (**P5**, 65 mg, 0.25 mmol), 3,5-di-*tert*-butylcatechol (**L1a**, 333 mg, 1.5 mmol) and triethylamine (177 mg, 1.75 mmol) were dissolved in 15 ml of acetonitrile and heated under reflux for 30 min. The solution was filtered and kept at room temperature for crystallization. After two weeks, **C11** was separated by filtration and washed with cold acetonitrile.

Yield: 54 mg green plates (0.043 mmol, 17.1 %).
IR (KBr): Figure A.28 on page 146.
$\tilde{\nu}$ (cm^{-1}) = 3422 (br), 2957 (s), 2870 (m), 1558 (s), 1481 (m), 1415 (s), 1361 (m), 1311 (m), 1277 (m), 1230 (m), 1112 (w), 1027 (w), 975 (s), 861 (w), 805 (m), 736 (w), 663 (m), 595 (m), 504 (w).
Elemental Analysis: Found: C, 59.39; H, 8.33; N, 3.27. Calc. for $C_{74}H_{112}N_4Ni_4O_{12}$: C, 59.87; H, 7.60; N, 3.77 %.

6.2.3.12 $(Hpip)_2[Co_2Fe_2(OH)(3,5\text{-}dbcat)_3(piv)_5(pip)]$ (C12)

$[Fe_2CoO(piv)_6(pip)_3]$ (**P8**, 262 mg, 0.25 mmol) was dissolved in 10 ml of acetone. A solution of 3,5-di-*tert*-butylcatechol (**L1a**, 167 mg, 0.75 mmol) in 5 ml of acetone was added to yield a dark mixture, which was heated under reflux for 30 min. The solution was filtered and allowed to slowly evaporate. After 24 h **C12** could be isolated by filtration and washed with cold acetone.

Yield: 51 mg brown blocks (0.03 mmol, 24.5 %).
IR (KBr): Figure A.29 on page 146.
$\tilde{\nu}$ (cm^{-1}) = 3444 (br), 2958 (m), 1628 (s), 1605 (s), 1480 (m), 1413 (s), 1368 (m), 1227 (m), 1019 (w), 985 (w), 874 (w), 713 (w), 603 (m), 425 (m).
Elemental Analysis: Found: C, 59.19; H, 11.00; N, 2.44. Calc. for $C_{82}H_{141}Co_2Fe_2N_3O_{17}$: C, 58.95; H, 8.51; N, 2.52 %.

6.2.3.13 $[Co_4(shi)_2(3,5\text{-}dbcat)(piv)_2(py)_5]$ (C13)

A solution of $[Co_2(OH_2)(piv)_4(Hpiv)_4]$ (**P1**, 237 mg, 0.25 mmol), salicylhydroxamic acid (H_3shi, 38 mg, 0.25 mmol), 3,5-di-*tert*-butyl-1,2-benzoquinone (3,5-dbbq, 55 mg. 0.25 mmol) and pyridine (79 mg, 1.0 mmol) in 15 ml acetonitrile was heated under reflux for 30 min. The brown mixture was filtered and the solvent was allowed to slowly evaporate. Complex **C13** was separated by filtration after 24 h and washed with cold acetonitrile.

Yield: 139 mg gold needles (0.103 mmol, 82.1 %).
IR (KBr): Figure A.30 on page 147.
$\tilde{\nu}$ (cm^{-1}) = 3431 (br), 2956 (m), 1584 (s), 1483 (m), 1448 (m), 1417 (m), 1390 (m), 1320 (m), 1261 (m), 1219 (m), 1155 (w), 1097 (w), 1069 (w), 978 (w), 941 (w), 758 (m), 694 (m), 605 (w), 433 (w).
Elemental Analysis: Found: C, 55.82; H, 5.33; N, 7.23. Calc. for $C_{63}H_{71}Co_4N_7O_{12}$: C, 55.88; H, 5.29; N, 7.24 %.

6.2.3.14 $[Co_2^{III}Co_7^{II}(shi)_4(piv)_8(Hpiv)_2(H_2O)_2(py)_4]$ (C14)

237 mg (0.25 mmol) of $[Co_2(OH_2)(piv)_4(Hpiv)_4]$, 38 mg (0.25 mmol) of salicylhydroxamic acid (H_3shi) and 28 mg (0.125 mmol) of 3,5-di-*tert*-butylcatechol were dissolved in 15 ml of acetonitrile. Under stirring, 49 mg (0.625 mmol) of pyridine were added.

The brown solution was heated under reflux for 30 min. Any insoluble residue was filtered off the mixture and the solvent was allowed to slowly evaporate. After four days, **C14** could be separated by filtration as brown crystals, whicht were washed with cold acetonitrile.

Yield: 57 mg brown blocks (0.023 mmol, 41.1 %).
IR (KBr): Figure A.31 on page 147.
$\tilde{\nu}$ (cm^{-1}) = 3428 (br), 2959 (m), 1601 (s), 1575 (s), 1533 (s), 1484 (s), 1447 (m), 1417 (s), 1360 (m), 1261 (m), 1227 (m), 1099 (w), 1070 (w), 1040 (w), 921 (w), 762 (m), 697 (m), 670 (w), 603 (w).
Elemental Analysis: Found: C, 47.21; H, 5.32; N, 4.61. Calc. for $C_{98}H_{132}Co_9N_8O_{34}$: C, 47.15; H, 5.33; N, 4.49 %.

6.2.3.15 $[Co_2^{III}Co^{II}(sal)_4(py)_4]$ (C15)

To a solution of 237 mg (0.25 mmol) of $[Co_2(OH_2)(piv)_4(Hpiv)_4]$, 77 mg (0.5 mmol) of salicylhydroxamic acid (H_3shi) and 165 mg (0.75 mmol) of 3,5-di-*tert*-butyl-1,2-benzoquinone (**L1b**) in 15 ml of acetonitrile 178 mg (2.25 mmol) of pyridine were added. The brown solution was heated under reflux for 30 min. The mixture was filtrated to remove insoluble impurities and kept at room temperature in a closed vial. After three months small crystals of the coordination network suitable for x-ray crystallography could be collected by filtration.

Yield: 33 mg brown crystals (0.032 mmol, 19.0 %).
IR (KBr): Figure A.32 on page 147.
$\tilde{\nu}$ (cm^{-1}) = 3420 (br), 3124 (w), 3071 (w), 1655 (s), 1600 (s), 1564 (s), 1526 (m), 1466 (s), 1381 (m), 1341 (m), 1255 (m), 1214 (w), 1143 (m), 1069 (w), 1037 (w), 891 (w), 757 (m), 696 (m), 598 (m), 484 (w).
Elemental Analysis: Found: C, 55.17; H, 3.26; N, 6.51. Calc. for $C_{48}H_{36}Co_3N_4O_{12}$ + 0.7 MeCN + 0.5 H_2O: C, 55.17; H, 3.66; N, 6.12 %.

6.2.3.16 $[Co_6(OH)_2(Hdebup)_2(piv)_8]$ (C16)

237 mg (0.25 mmol) of $[Co_2(OH_2)(piv)_4(Hpiv)_4]$ (**P1**) and 73 mg (0.25 mmol) of H_3debup (**L3**) were dissolved in 15 ml of acetone. The resulting brown solution was heated under reflux for 30 min and subsequently filtered. Slow evaporation of the solvent yielded **C16** as brown crystals, which were carefully washed with

cold acetonitrile. Addition of 3,5-di-*tert*-butylcatechol to the reaction mixture does not have an influence on the outcome and results in the formation of the same complex.

Yield: 32 mg brown crystals (0.018 mmol, 21.6 %).
IR (KBr): Figure A.33 on page 148.
$\tilde{\nu}$ (cm^{-1}) = 3553 (m), 3443 (br), 2957 (m), 2923 (m), 2865 (w), 1640 (m), 1604 (s), 1524 (m), 1483 (m), 1455 (m), 1417 (s), 1361 (m), 1288 (w), 1226 (m), 1045 (w), 975 (w), 887 (w), 786 (w), 691 (w), 619 (w), 575 (w), 414 (w).
Elemental Analysis: Found: C, 49.05; H, 6.71; N, 3.16. Calc. for $C_{72}H_{116}Co_6N_4O_{24}$: C, 48.71; H, 6.59; N, 3.16 %.

6.2.3.17 $(HNEt_3)_2[Co_6(CO_3)(dabup)_3(piv)_3]$ (C17)

237 mg of $[Co_2(OH_2)(piv)_4(Hpiv)_4]$, 97 mg (0.25 mmol) of H_3dabup (**L4**) and 76 mg (0.5 mmol) of triethylamine were dissolved in 15 ml of acetone. The mixture was heated under reflux for 30 min and subsequently filtered. After four days of slow evaporation of the solvent, small crystals of **C17** were separated be filtration and washed with cold acetone. The same reaction was also carried out with varied amounts of 3,5-di-*tert*-butylcatechol, which did not have an impact on the outcome.

Yield: 24 mg red-brown plates (0.015 mmol, 18.0 %).
IR (KBr): Figure A.34 on page 148.
$\tilde{\nu}$ (cm^{-1}) = 3444 (br), 2961 (m), 1707 (w), 1580 (s), 1479 (s), 1401 (m), 1360 (m), 1314 (m), 1224 (m), 1067 (w), 742 (m), 531 (m).
Elemental Analysis: Found: C, 56.15; H, 6.55; N, 4.85. Calc. for $C_{100}H_{122}Co_6N_8O_{15} + 6\,H_2O$: C, 56.18; H, 6.32; N, 5.24 %.

6.2.3.18 $[Co_4(OH)_2(dabup)(bobupimp)(piv)_3]$ (C18)

237 mg (0.25 mmol) of $[Co_2(OH_2)(piv)_4(Hpiv)_4]$, 97 mg (0.25 mmol) of H_3dabup (**L4**) and 110 mg (0.5 mmol) of 3,5-di-*tert*-butyl-1,2-benzoquinone were dissolved in 15 ml of acetonitrile. Under continuous stirring, 76 mg (0.75 mmol) of triethylamine were added and the mixture was heated under reflux for 30 min. The solution was filtered and kept in a closed vial. After six weeks, complex **C18** was isolated by filtration and washed with cold acetonitrile.

Yield: 28 mg brown crystals (0.021 mmol, 16.7 %).

IR (KBr): Figure A.35 on page 148.

$\tilde{\nu}$ (cm^{-1}) = 3414 (br), 2961 (m), 1689 (m), 1583 (s), 1479 (s), 1405 (m), 1362 (m), 1307 (m), 1248 (s), 1191 (m), 1152 (m), 1065 (w), 1030 (w), 984 (w), 837 (w), 741 (m), 654 (w), 553 (m), 453 (w).

Elemental Analysis: Found: C, 52.24; H, 7.02; N, 3.85. Calc. for $C_{73}H_{90}Co_4N_4O_{18}$ + 7 H_2O: C, 52.40; H, 6.26; N, 3.35 %.

6.2.3.19 $[Cu_4(3,5\text{-dbcat})_2(bobupimp)_2(acetone)_2]$ (C19)

$[Cu_2(piv)_4(EtOH)_2]$ (**P3**, 156 mg, 0.25 mmol), H_3dabup (**L4**, 97 mg, 0.25 mmol) and 3,5-di-*tert*-butylcatechol (111 mg, 0.5 mmol) were dissolved in 15 ml of acetone to yield a brown solution. Triethylamine (177 mg, 1.75 mmol) was added and the mixture was heated under reflux for 15 min. The solution was filtered and the filtrate was cooled down to room temperature. After three days, slow evaporation of the solvent resulted in brown crystals, which were filtered off and washed with cold acetone.

Yield: 64 mg brown rods (0.048 mmol, 38.4 %).

IR (KBr): Figure A.36 on page 149.

$\tilde{\nu}$ (cm^{-1}) = 3420 (br), 2959 (m), 2678 (w), 1484 (s), 1459 (m), 1420 (s), 1376 (m), 1360 (m), 1227 (m), 1196 (w), 1160 (w), 1092 (w), 1047 (w), 1008 (w), 898 (w), 789 (w), 737 (w), 619 (m), 531 (w), 445 (w).

6.2.3.20 $[Co_6(CO_3)(bpp)_3(H3,5\text{-dbcat})_4(piv)_3]$ (C20)

$[Co(piv)_2]_n$ (**P2**, 131 mg, 0.5 mmol), Hbpp (**L9**, 19 mg, 0.085 mmol) and 3,5-di-*tert*-butylcatechol (222 mg, 1.0 mmol) were dissolved in 10 ml of acetone and heated under reflux for 30 min. The solution was filtered and the solvent was allowed to evaporate slowly at room temperature. After 24 h the complex **C20** was collected by filtration and washed with cold acetone.

Yield: 48 mg red crystals (0.021 mmol, 25.4 %).

IR (KBr): Figure A.37 on page 149.

$\tilde{\nu}$ (cm^{-1}) = 3431 (br), 2960 (s), 2871 (m), 1727 (m), 1608 (m), 1510 (m), 1482 (s), 1462 (m), 1415 (s), 1364 (s), 1231 (m), 1144 (s), 1063 (m), 1030 (m), 981 (m), 903 (w), 772 (w), 611 (w).

6.2.3.21 $[Co_2(tpbap)(3,5\text{-}dbcat)_2](SO_4)$ (C21a)

56 mg (0.2 mmol) of $CoSO_4 \cdot 7\,H_2O$, 54 mg (0.1 mmol) of the ligand **L7** and 44 mg (0.2 mmol) of 3,5-di-*tert*-butylcatechol (3,5-dbcat) were mixed in 15 ml of methanol. After all reactants were dissolved 40 mg (0.4 mmol) of triethylamine were added. The solution was heated under reflux for an hour. After any insoluble residue was filtered off the green solution, the solvent was allowed to evaporate slowly. Complex **C21a** was separated by filtration and washed with cold methanol.

Yield: 83 mg of green plates (0.07 mmol, 69.7 %).
IR (KBr): Figure A.38 on page 149.
$\tilde{\nu}$ (cm^{-1}) = 3415 (br), 2952 (m), 1612 (m), 1555 (w), 1463 (m), 1441 (m), 1413 (m), 1359 (w), 1320 (w), 1281 (m), 1241 (m), 1120 (m), 979 (m), 826 (w), 769 (m), 620 (m).
Elemental Analysis: Found: C, 56.01; H, 7.75; N, 8.00; S, 2.63. Calc. for $C_{60}H_{80}Co_2N_8O_8S$ + 5.5 MeOH + 2 H_2O: C, 56.05; H, 7.61; N, 7.98; S, 2.28 %.

6.2.3.22 $[Co_2(tpbap)(3,5\text{-}dbcat)_2](ClO_4)_2$ (C21b)

In a procedure analog to the synthesis of **C21a** 73 mg (0.2 mmol) of $Co(ClO_4)_2 \cdot 6\,H_2O$, 54 mg (0.1 mmol) of the ligand **L7** and 44 mg (0.2 mmol) of $H_2$3,5-dbcat (**L1a**) were dissolved in 15 ml of ethanol. 40 mg (0.4 mmol) of triethylamine were added and the mixture was heated under reflux for an hour. The solution was filtered and allowed to evaporate slowly. After 24 h complex **C21b** precipitated as green crystals, which were filtrated and washed with cold ethanol.

Yield: 47 mg green plates (0.036 mmol, 36.3 %).
IR (KBr): Figure A.39 on page 150.
$\tilde{\nu}$ (cm^{-1}) = 3424 (br), 2952 (m), 1611 (m), 1555 (w), 1461 (m), 1440 (m), 1413 (m), 1359 (w), 1321 (w), 1281 (m), 1241 (m), 1204 (w), 1145 (m), 1118 (s), 1090 (s), 980 (m), 945 (w), 826 (w), 768 (m), 626 (m).
Elemental Analysis: Found: C, 54.59; H, 6.13; N, 8.45. Calc. for $C_{60}H_{80}Cl_2Co_2N_8O_{12}$ + 1.5 H_2O: C, 54.55; H, 6.33; N, 8.48 %.

Bibliography

[1] M. Kaku, Hyperspace: A Scientific Odyssey Through Parallel Universes, Time Warps, and the Tenth Dimension, Oxford University Press, **1995**.

[2] R. P. Feynman, The Character of Physical Law, Modern Library, **1994**.

[3] L. M. K. Vandersypen, M. Steffen, G. Breyta, C. S. Yannoni, M. H. Sherwood, I. L. Chuang, *Nature* **2001**, *414*, 883–887.

[4] S. Gulde, M. Riebe, G. P. T. Lancaster, C. Becher, J. Eschner, H. Häffner, F. Schmidt-Kaler, I. L. Chuang, R. Blatt, *Nature* **2003**, *421*, 48–50.

[5] G. Moore, *Proc. IEEE* **1998**, *86*, 82–85.

[6] M. Homeister, Quantum Computing Verstehen: Grundlagen - Anwendungen - Perspektiven, Springer-Verlag, **2008**.

[7] T. D. Ladd, F. Jelezko, R. Laflamme, Y. Nakamura, C. Monroe, J. L. OBrien, *Nature* **2010**, *464*, 45–53.

[8] D. Loss, D. P. DiVincenzo, *Phys. Rev. A* **1998**, *57*, 120–126.

[9] C. H. Bennett, D. P. DiVincenzo, *Nature* **2000**, *404*, 247–255.

[10] G. Aromí, D. Aguilà, P. Gamez, F. Luis, O. Roubeau, *Chem. Soc. Rev.* **2012**, *41*, 537–546.

[11] M. N. Leuenberger, D. Loss, *Nature* **2001**, *410*, 789–793.

[12] F. Troiani, A. Ghirri, M. Affronte, S. Carretta, P. Santini, G. Amoretti, S. Piligkos, G. Timco, R. E. P. Winpenny, *Phys. Rev. Lett.* **2005**, *94*, 207208.

[13] F. K. Larsen, E. J. L. McInnes, H. E. Mkami, J. Overgaard, S. Piligkos, G. Rajaraman, E. Rentschler, A. A. Smith, G. M. Smith, V. Boote, M. Jennings, G. A. Timco, R. E. P. Winpenny, *Angew. Chem.* **2003**, *115*, 105–109.

[14] G. A. Timco, E. J. L. McInnes, R. G. Pritchard, F. Tuna, R. E. P. Winpenny, *Angew. Chem. Int. Ed.* **2008**, *47*, 9681–9684.

[15] F. Meier, D. Loss, *Phys. Rev. B* **2001**, *64*, 224411.

[16] A. Ardavan, O. Rival, J. J. L. Morton, S. J. Blundell, A. M. Tyryshkin, G. A. Timco, R. E. P. Winpenny, *Phys. Rev. Lett.* **2007**, *98*, 057201.

[17] G. A. Timco, T. B. Faust, F. Tuna, R. E. P. Winpenny, *Chem. Soc. Rev.* **2011**, *40*, 3067–3075.

[18] G. A. Timco, S. Carretta, F. Troiani, F. Tuna, R. J. Pritchard, C. A. Muryn, E. J. L. McInnes, A. Ghirri, A. Candini, P. Santini, G. Amoretti, M. Affronte, R. E. P. Winpenny, *Nat. Nano.* **2009**, *4*, 173–178.

[19] T. B. Faust, V. Bellini, A. Candini, S. Carretta, G. Lorusso, D. R. Allan, L. Carthy, D. Collison, R. J. Docherty, J. Kenyon, J. Machin, E. J. L. McInnes, C. A. Muryn, H. Nowell, R. G. Pritchard, S. J. Teat, G. A. Timco, F. Tuna, G. F. S. Whitehead, W. Wernsdorfer, M. Affronte, R. E. P. Winpenny, *Chem. Eur. J.* **2011**, *17*, 14020–14030.

[20] T. B. Faust, F. Tuna, G. A. Timco, M. Affronte, V. Bellini, W. Wernsdorfer, R. E. P. Winpenny, *Dalton Trans.* **2012**, *41*, 13626–13631.

[21] G. F. S. Whitehead, F. Moro, G. A. Timco, W. Wernsdorfer, S. J. Teat, R. E. P. Winpenny, *Angew. Chem. Int. Ed.* **2013**, *52*, 9932–9935.

[22] V. I. Minkin, A. A. Starikova, A. G. Starikov, *Dalton Trans.* **2015**, *44*, 1982–1991.

[23] A. Dei, D. Gatteschi, C. Sangregorio, L. Sorace, *Acc. Chem. Res.* **2004**, *37*, 827–835.

[24] D. M. Adams, D. N. Hendrickson, *J. Am. Chem. Soc.* **1996**, *118*, 11515–11528.

[25] D. A. Shultz in *Magnetism: Molecules to Materials II*, (Eds.: J. S. Miller, Rcillon), Wiley-VCH Verlag GmbH & Co. KGaA, **2003**, pp. 281–306.

[26] Y. Garcia, V. Ksenofontov, P. Gütlich, *Hyperfine Interact.* **2002**, *139-140*, 543–551.

[27] N. S. Hush, A. T. Wong, G. B. Bacskay, J. R. Reimers, *J. Am. Chem. Soc.* **1990**, *112*, 4192–4197.

[28] A. Aviram, *Int. J. Quantum Chem.* **1992**, *42*, 1615–1624.

[29] O. Kahn, J. Kröber, C. Jay, *Adv. Mater.* **1992**, *4*, 718–728.

[30] A. Heckmann, C. Lambert, *Angew. Chem. Int. Ed.* **2012**, *51*, 326–392.

[31] J. Hankache, O. S. Wenger, *Chem. Rev.* **2011**, *111*, 5138–5178.

[32] M. Kaupp, M. Renz, M. Parthey, M. Stolte, F. Würthner, C. Lambert, *Phys. Chem. Chem. Phys.* **2011**, *13*, 16973–16986.

[33] V. Coropceanu, N. E. Gruhn, S. Barlow, C. Lambert, J. C. Durivage, T. G. Bill, G. Nöll, S. R. Marder, J.-L. Brédas, *J. Am. Chem. Soc.* **2004**, *126*, 2727–2731.

[34] P. Day, N. S. Hush, R. J. H. Clark, *Phil. Trans. R. Soc. A* **2008**, *366*, 5–14.

[35] C. M. Varma, *Rev. Mod. Phys.* **1976**, *48*, 219–238.

[36] N. Withers, *Nat. Chem.* **2010**, DOI 10.1038/nchem.959.

[37] J. P. Fackler in *Encyclopedia of Inorganic Chemistry*, John Wiley & Sons, Ltd, **2006**.

[38] J. Overgaard, E. Rentschler, G. A. Timco, F. K. Larsen, *ChemPhysChem* **2004**, *5*, 1755–1761.

[39] M. B. Robin, P. Day in *Advances in Inorganic Chemistry and Radiochemistry*, *Vol. 10*, (Ed.: H.J. Emeléus and A.G. Sharpe), Academic Press, **1967**, pp. 247–422.

[40] M. Parthey, M. Kaupp, *Chem. Soc. Rev.* **2014**, *43*, 5067–5088.

[41] Spin crossover in transition metal compounds, (Eds.: P. Gütlich, H. A. Goodwin), Springer, Berlin ; New York, **2004**.

[42] R. Boa, Theoretical Foundations of Molecular Magnetism, Elsevier, **1999**.

[43] P. Gütlich, A. Hauser, H. Spiering, *Angew. Chem. Int. Ed.* **1994**, *33*, 2024–2054.

[44] J. A. Real, A. B. Gaspar, M. C. Muñoz, *Dalton Trans.* **2005**, 2062–2079.

[45] P. Gütlich, A. Dei, *Angew. Chem.* **1997**, *109*, 2852–2855.

[46] C. G. Pierpont, S. Kitagawa in *Inorganic Chromotropism: Basic Concepts and Applications of Colored Materials*, (Ed.: Y. Fukuda), Springer, **2007**, pp. 116–142.

[47] A. C. Cope, A. C. Haven, F. L. Ramp, E. R. Trumbull, *J. Am. Chem. Soc.* **1952**, *74*, 4867–4871.

[48] R. M. Buchanan, C. G. Pierpont, *J. Am. Chem. Soc.* **1980**, *102*, 4951–4957.

[49] C. K. Jørgensen, *Coord. Chem. Rev.* **1966**, *1*, 164–178.

[50] W. Kaim, B. Schwederski, *Coord. Chem. Rev.* **2010**, *254*, 1580–1588.

[51] K. P. Butin, E. K. Beloglazkina, N. V. Zyk, *Russ. Chem. Rev.* **2005**, *74*, 531–553.

[52] M. M. Whittaker, J. W. Whittaker, *Biophys. J.* **1993**, *64*, 762–772.

[53] P. Chaudhuri, M. Hess, U. Flörke, K. Wieghardt, *Angew. Chem.* **1998**, *110*, 2340–2343.

[54] W. P. Griffith, *Transit. Metal Chem.* **1993**, *18*, 250–256.

[55] C. G. Pierpont, C. W. Lange, C. G. Pierpont, C. W. Lange in *Progress in Inorganic Chemistry*, 41, John Wiley & Sons, Inc., Hoboken, NJ, USA, **1994**, pp. 331–442.

[56] S. N. Brown, *Inorg. Chem.* **2012**, *51*, 1251–1260.

[57] D. Sato, Y. Shiota, G. Juhász, K. Yoshizawa, *J. Phys. Chem. A* **2010**, *114*, 12928–12935.

[58] A. Beni, C. Carbonera, A. Dei, J.-F. Létard, R. Righini, C. Sangregorio, L. Sorace, *J. Braz. Chem. Soc.* **2006**, *17*, 1522–1533.

[59] O. Sato, S. Hayami, Z.-z. Gu, K. Takahashi, R. Nakajima, A. Fujishima, *Chem. Phys. Lett.* **2002**, *355*, 169–174.

[60] O. Sato, S. Hayami, Z.-z. Gu, K. Takahashi, R. Nakajima, K. Seki, A. Fujishima, *J. Photochem. Photobiol. A* **2002**, *149*, 111–114.

[61] O. Sato, S. Hayami, Y. Einaga, Z.-Z. Gu, *Bull. Chem. Soc. Jpn.* **2003**, *76*, 443–470.

[62] C. Carbonera, A. Dei, C. Sangregorio, J.-F. Létard, *Chem. Phys. Lett.* **2004**, *396*, 198–201.

[63] P. L. Gentili, L. Bussotti, R. Righini, A. Beni, L. Bogani, A. Dei, *Chem. Phys.* **2005**, *314*, 9–17.

[64] O. Sato, A. Cui, R. Matsuda, J. Tao, S. Hayami, *Acc. Chem. Res.* **2007**, *40*, 361–369.

[65] O. Sato, J. Tao, Y.-Z. Zhang, *Angew. Chem. Int. Ed.* **2007**, *46*, 2152–2187.

[66] A. Beni, A. Dei, S. Laschi, M. Rizzitano, L. Sorace, *Chem. Eur. J.* **2008**, *14*, 1804–1813.

[67] P. Dapporto, A. Dei, G. Poneti, L. Sorace, *Chem. Eur. J.* **2008**, *14*, 10915–10918.

[68] P. Naumov, A. A. Belik, *Inorg. Chem. Commun.* **2008**, *11*, 465–469.

[69] G. Poneti, M. Mannini, L. Sorace, P. Sainctavit, M.-A. Arrio, A. Rogalev, F. Wilhelm, A. Dei, *ChemPhysChem* **2009**, *10*, 2090–2095.

[70] R. D. Schmidt, D. A. Shultz, J. D. Martin, P. D. Boyle, *J. Am. Chem. Soc.* **2010**, *132*, 6261–6273.

[71] R. D. Schmidt, D. A. Shultz, J. D. Martin, *Inorg. Chem.* **2010**, *49*, 3162–3168.

[72] B. Li, L.-Q. Chen, R.-J. Wei, J. Tao, R.-B. Huang, L.-S. Zheng, Z. Zheng, *Inorg. Chem.* **2011**, *50*, 424–426.

[73] L. Chen, R. Wei, J. Tao, R. Huang, L. Zheng, *Sci. China Chem.* **2012**, *55*, 1037–1041.

[74] J. Dai, S. Kanegawa, Z. Li, S. Kang, O. Sato, *Eur. J. Inorg. Chem.* **2013**, n/a–n/a.

[75] G. Poneti, M. Mannini, B. Cortigiani, L. Poggini, L. Sorace, E. Otero, P. Sainctavit, R. Sessoli, A. Dei, *Inorg. Chem.* **2013**, *52*, 11798–11805.

[76] A. Tashiro, S. Kanegawa, O. Sato, Y. Teki, *Polyhedron*, ICMM 2012 **2013**, *66*, 167–170.

[77] G. Poneti, L. Poggini, M. Mannini, B. Cortigiani, L. Sorace, E. Otero, P. Sainctavit, A. Magnani, R. Sessoli, A. Dei, *Chem. Sci.* **2015**, DOI 10.1039/C5SC00163C.

[78] J. D. Lipscomb, *Curr. Opin. Struc. Biol.* **2008**, *18*, 644–649.

[79] T. D. H. Bugg, *Tetrahedron* **2003**, *59*, 7075–7101.

[80] P. E. M. Siegbahn, T. Borowski, *Faraday Discuss.* **2010**, *148*, 109–117.

[81] M. Güell, P. E. M. Siegbahn, *J. Biol. Inorg. Chem.* **2007**, *12*, 1251–1264.

[82] C. Gerdemann, C. Eicken, B. Krebs, *Acc. Chem. Res.* **2002**, *35*, 183–191.

[83] C. Eicken, B. Krebs, J. C. Sacchettini, *Curr. Opin. Struc. Biol.* **1999**, *9*, 677–683.

[84] T. Klabunde, C. Eicken, J. C. Sacchettini, B. Krebs, *Nat. Struct. Mol. Biol.* **1998**, *5*, 1084–1090.

[85] E. I. Solomon, U. M. Sundaram, T. E. Machonkin, *Chem. Rev.* **1996**, *96*, 2563–2606.

[86] D. E. Wilcox, A. G. Porras, Y. T. Hwang, K. Lerch, M. E. Winkler, E. I. Solomon, *J. Am. Chem. Soc.* **1985**, *107*, 4015–4027.

[87] J. N. Hamann, M. Rolff, F. Tuczek, *Dalton Trans.* **2015**, *44*, 3251–3258.

[88] A. Bassan, T. Borowski, P. E. M. Siegbahn, *Dalton Trans.* **2004**, 3153–3162.

[89] J. Reim, B. Krebs, *J. Chem. Soc. Dalton Trans.* **1997**, 3793–3804.

[90] T. Tezgerevska, K. G. Alley, C. Boskovic, *Coord. Chem. Rev.* **2014**, *268*, 23–40.

[91] Y. Mulyana, G. Poneti, B. Moubaraki, K. S. Murray, B. F. Abrahams, L. Sorace, C. Boskovic, *Dalton Trans.* **2010**, *39*, 4757–4767.

[92] O.-S. Jung, D. H. Jo, Y.-A. Lee, B. J. Conklin, C. G. Pierpont, *Inorg. Chem.* **1997**, *36*, 19–24.

[93] A. Bencini, A. Caneschi, C. Carbonera, A. Dei, D. Gatteschi, R. Righini, C. Sangregorio, J. V. Slageren, *J. Mol. Struct.* **2003**, *656*, 141–154.

[94] A. Dei, L. Sorace, *Appl. Magn. Reson.* **2010**, *38*, 139–153.

[95] M. W. Lynch, D. N. Hendrickson, B. J. Fitzgerald, C. G. Pierpont, *J. Am. Chem. Soc.* **1981**, *103*, 3961–3963.

[96] M. W. Lynch, D. N. Hendrickson, B. J. Fitzgerald, C. G. Pierpont, *J. Am. Chem. Soc.* **1984**, *106*, 2041–2049.

[97] A. Caneschi, A. Dei, *Angew. Chem. Int. Ed.* **1998**, *37*, 3005–3007.

[98] D. M. Dooley, M. A. McGuirl, D. E. Brown, P. N. Turowski, W. S. Mclntire, P. F. Knowles, *Nature* **1991**, *349*, 262–264.

[99] G. Speier, Z. Tyeklár, P. Tóth, E. Speier, S. Tisza, A. Rockenbauer, A. M. Whalen, N. Alkire, C. G. Pierpont, *Inorg. Chem.* **2001**, *40*, 5653–5659.

[100] O. Rotthaus, F. Thomas, O. Jarjayes, C. Philouze, E. Saint-Aman, J.-L. Pierre, *Chem. Eur. J.* **2006**, *12*, 6953–6962.

[101] T. Glaser, M. Heidemeier, R. Fröhlich, P. Hildebrandt, E. Bothe, E. Bill, *Inorg. Chem.* **2005**, *44*, 5467–5482.

[102] A. Ghosh, T. Wondimagegn, E. Gonzalez, I. Halvorsen, *J. Inorg. Biochem.* **2000**, *78*, 79–82.

[103] C. W. Lange, C. G. Pierpont, *Inorg. Chim. Acta* **1997**, *263*, 219–224.

[104] H. Ohtsu, K. Tanaka, *Angew. Chem. Int. Ed.* **2004**, *43*, 6301–6303.

[105] N. Shaikh, S. Goswami, A. Panja, X.-Y. Wang, S. Gao, R. J. Butcher, P. Banerjee, *Inorg. Chem.* **2004**, *43*, 5908–5918.

[106] K. Nakano, S. Kawata, K. Yoneda, A. Fuyuhiro, T. Yagi, S. Nasu, S. Morimoto, S. Kaizaki, *Chem. Commun.* **2004**, 2892–2893.

[107] M. H. Klingele, B. Moubaraki, J. D. Cashion, K. S. Murray, S. Brooker, *Chem. Commun.* **2005**, 987–989.

[108] C. J. Schneider, J. D. Cashion, N. F. Chilton, C. Etrillard, M. Fuentealba, J. A. K. Howard, J.-F. Létard, C. Milsmann, B. Moubaraki, H. A. Sparkes, S. R. Batten, K. S. Murray, *Eur. J. Inorg. Chem.* **2013**, *2013*, 850–864.

[109] C. Boskovic in *Spin-Crossover Materials*, (Ed.: M. A. Halcrow), John Wiley & Sons Ltd, **2013**, pp. 203–224.

[110] O.-S. Jung, D. H. Jo, Y.-A. Lee, H. K. Chae, Y. S. Sohn, *Bull. Chem. Soc. Jpn.* **1996**, *69*, 2211–2214.

[111] S. Bin-Salamon, S. H. Brewer, E. C. Depperman, S. Franzen, J. W. Kampf, M. L. Kirk, R. K. Kumar, S. Lappi, K. Peariso, K. E. Preuss, D. A. Shultz, *Inorg. Chem.* **2006**, *45*, 4461–4467.

[112] M. P. Bubnov, N. A. Skorodumova, A. A. Zolotukhin, A. V. Arapova, E. V. Baranov, A. Stritt, A. Ünal, A. Grohmann, F. W. Heinemann, A. S. Bogomyakov, N. N. Smirnova, V. K. Cherkasov, G. A. Abakumov, *Z. anorg. allg. Chem.* **2014**, n/a–n/a.

[113] H. Liang, Y. M. Na, I. S. Chun, S. S. Kwon, Y.-A. Lee, O.-S. Jung, *Bull. Chem. Soc. Jpn.* **2007**, *80*, 916–921.

[114] N. G. R. Hearns, J. L. Korok, M. M. Paquette, K. E. Preuss, *Inorg. Chem.* **2006**, *45*, 8817–8819.

[115] A. Bencini, C. A. Daul, A. Dei, F. Mariotti, H. Lee, D. A. Shultz, L. Sorace, *Inorg. Chem.* **2001**, *40*, 1582–1590.

[116] Y. Suenaga, C. G. Pierpont, *Inorg. Chem.* **2005**, *44*, 6183–6191.

[117] A. Beni, A. Dei, D. A. Shultz, L. Sorace, *Chem. Phys. Lett.* **2006**, *428*, 400–404.

[118] K. G. Alley, G. Poneti, J. B. Aitken, R. K. Hocking, B. Moubaraki, K. S. Murray, B. F. Abrahams, H. H. Harris, L. Sorace, C. Boskovic, *Inorg. Chem.* **2012**, *51*, 3944–3946.

[119] K. G. Alley, G. Poneti, P. S. D. Robinson, A. Nafady, B. Moubaraki, J. B. Aitken, S. C. Drew, C. Ritchie, B. F. Abrahams, R. K. Hocking, K. S. Murray, A. M. Bond, H. H. Harris, L. Sorace, C. Boskovic, *J. Am. Chem. Soc.* **2013**, *135*, 8304–8323.

[120] B. Li, L.-Q. Chen, J. Tao, R.-B. Huang, L.-S. Zheng, *Inorg. Chem.* **2013**, *52*, 4136–4138.

[121] D. Schweinfurth, Y. Rechkemmer, S. Hohloch, N. Deibel, I. Peremykin, J. Fiedler, R. Marx, P. Neugebauer, J. van Slageren, B. Sarkar, *Chem. Eur. J.* **2014**, n/a–n/a.

[122] O.-S. Jung, C. G. Pierpont, *J. Am. Chem. Soc.* **1994**, *116*, 2229–2230.

[123] I. Imaz, D. Maspoch, C. Rodríguez-Blanco, J. M. Pérez-Falcón, J. Campo, D. Ruiz-Molina, *Angew. Chem. Int. Ed.* **2008**, *47*, 1857–1860.

[124] X.-Y. Chen, R.-J. Wei, L.-S. Zheng, J. Tao, *Inorg. Chem.* **2014**, DOI 10.1021/ic502471v.

[125] S. H. Bodnar, A. Caneschi, A. Dei, D. A. Shultz, L. Sorace, *Chem. Commun.* **2001**, 2150–2151.

[126] M. Affronte, A. Beni, A. Dei, L. Sorace, *Dalton Trans.* **2007**, 5253–5259.

[127] W.-Q. Cheng, G.-L. Li, R. Zhang, Z.-H. Ni, W.-F. Wang, O. Sato, *J. Mol. Struct.* **2015**, *1087*, 68–72.

[128] R. M. Buchanan, B. J. Fitzgerald, C. G. Pierpont, *Inorg. Chem.* **1979**, *18*, 3439–3444.

[129] M. Olmstead, P. Power, G. Speier, Z. Tyeklár, *Polyhedron* **1988**, *7*, 609–614.

[130] R. A. Reynolds, W. O. Yu, W. R. Dunham, D. Coucouvanis, *Inorg. Chem.* **1996**, *35*, 2721–2722.

[131] M. Diehl, Diploma Thesis, Universität Mainz, Mainz, **2012**.

[132] L. Horner, E. Geyer, *Chem. Ber.* **1965**, *98*, 2016–2045.

[133] A. G. Orpen, L. Brammer, F. H. Allen, O. Kennard, D. G. Watson, R. Taylor, *J. Chem. Soc. Dalton Trans.* **1989**, S1–S83.

[134] A. Panja, *RSC Adv.* **2013**, *3*, 4954–4963.

[135] G. I. Dzhardimalieva, A. D. Pomogailo, *Russ. Chem. Rev.* **2008**, *77*, 259–301.

[136] T. O. Denisova, F. M. Dolgushin, S. E. Nefedov, *Russ. Chem. Bull.* **2002**, *51*, 2310–2311.

[137] Y. Oka, K. Inoue, *Chem. Lett.* **2004**, *33*, 402–403.

[138] K. S. Gavrilenko, S. V. Punin, O. Cador, S. Golhen, L. Ouahab, V. V. Pavlishchuk, *J. Am. Chem. Soc.* **2005**, *127*, 12246–12253.

[139] M.-H. Zeng, X.-L. Feng, W.-X. Zhang, X.-M. Chen, *Dalton Trans.* **2006**, 5294.

[140] K. S. Gavrilenko, Y. L. Gal, O. Cador, S. Golhen, L. Ouahab, *Chem. Commun.* **2007**, 280–282.

[141] D.-X. Hu, P.-K. Chen, F. Luo, L. Xue, Y. Che, J.-M. Zheng, *Inorg. Chim. Acta* **2007**, *360*, 4077–4084.

[142] S. E. Nefedov, *Russ. Chem. Bull.* **2004**, *53*, 259–261.

[143] R. Chakrabarty, P. S. Mukherjee, P. J. Stang, *Chem Rev* **2011**, *111*, 6810–6918.

[144] B. J. Holliday, C. A. Mirkin, *Angew. Chem. Int. Ed.* **2001**, *40*, 2022–2043.

[145] F. A. Cotton, Z. Li, C. Y. Liu, C. A. Murillo, *Inorg. Chem.* **2007**, *46*, 9294–9302.

[146] R. A. Reynolds, D. Coucouvanis, *J. Am. Chem. Soc.* **1998**, *120*, 209–210.

[147] R. A. Reynolds, D. Coucouvanis, *Inorg. Chem.* **1998**, *37*, 170–171.

[148] H.-C. Chang, N. Nishida, S. Kitagawa, *Chem. Lett.* **2005**, *34*, 402–403.

[149] L. Feng, Z. Chen, M. Zeller, R. L. Luck, *Polyhedron*, Leovac Special Issue **2014**, *80*, 206–215.

[150] T. D. Keene, I. Zimmermann, A. Neels, O. Sereda, J. Hauser, S.-X. Liu, S. Decurtins, *Cryst. Growth. Des.* **2010**, *10*, 1854–1859.

[151] J. Yoshida, S.-i. Nishikiori, R. Kuroda, *Chem. Eur. J.* **2008**, *14*, 10570–10578.

[152] V. I. Ovcharenko, E. V. Gorelik, S. V. Fokin, G. V. Romanenko, V. N. Ikorskii, A. V. Krashilina, V. K. Cherkasov, G. A. Abakumov, *J. Am. Chem. Soc.* **2007**, *129*, 10512–10521.

[153] R. D. Harcourt, G. E. Martin, *J. Chem. Soc. Faraday Trans. 2* **1977**, *73*, 1–14.

[154] B. Weber, Koordinationschemie Grundlagen und aktuelle Trends, Springer Spektrum, Berlin, Heidelberg, **2014**.

[155] J. B. Goodenough, *Phys. Rev.* **1955**, *100*, 564–573.

[156] J. B. Goodenough, *J. Phys. Chem. Solids* **1958**, *6*, 287–297.

[157] S. Emori, M. Nakashima, W. Mori, *Bull. Chem. Soc. Jpn.* **2000**, *73*, 81–84.

[158] P. Happ, C. Plenk, E. Rentschler, *Coord. Chem. Rev.*, Progress in Magnetochemistry **2015**, *289290*, 238–260.

[159] M. S. Lah, V. L. Pecoraro, *J. Am. Chem. Soc.* **1989**, *111*, 7258–7259.

[160] M. S. Lah, B. R. Gibney, D. L. Tierney, J. E. Penner-Hahn, V. L. Pecoraro, *J. Am. Chem. Soc.* **1993**, *115*, 5857–5858.

[161] E. S. Koumousi, S. Mukherjee, C. M. Beavers, S. J. Teat, G. Christou, T. C. Stamatatos, *Chem. Commun.* **2011**, *47*, 11128–11130.

[162] M. S. Lah, M. L. Kirk, W. Hatfield, V. L. Pecoraro, *J. Chem. Soc. Chem. Commun.* **1989**, 1606–1608.

[163] V. L. Pecoraro, *Inorg. Chim. Acta* **1989**, *155*, 171–173.

[164] M. J. Hossain, H. Sakiyama, *Inorg. Chim. Acta* **2002**, *338*, 255–259.

[165] CO2 Now, CO2 Now, **2015**, `http://co2now.org/` (visited on Apr. 20, 2015).

[166] L. Wang, Y. Li, Y. Peng, Z. Liang, J. Yu, R. Xu, *Dalton Trans.* **2012**, *41*, 6242–6246.

[167] A. Graham, S. Meier, S. Parsons, R. E. P. Winpenny, *Chem. Commun.* **2000**, 811–812.

[168] G. J. T. Cooper, G. N. Newton, P. Kögerler, D.-L. Long, L. Engelhardt, M. Luban, L. Cronin, *Angew. Chem. Int. Ed.* **2007**, *46*, 1340–1344.

[169] T. C. W. Mak, P.-j. Li, C.-m. Zheng, K.-Y. Huang, *J. Chem. Soc. Chem. Commun.* **1986**, 1597–1598.

[170] M.-C. Suen, G.-W. Tseng, J.-D. Chen, T.-C. Keng, J.-C. Wang, *Chem. Commun.* **1999**, 1185–1186.

[171] M. J. Manos, A. D. Keramidas, J. D. Woollins, A. M. Z. Slawin, T. A. Kabanos, *J. Chem. Soc. Dalton Trans.* **2001**, 3419–3420.

[172] M.-L. Tong, M. Monfort, J. M. C. Juan, X.-M. Chen, X.-H. Bu, M. Ohba, S. Kitagawa, *Chem. Commun.* **2005**, 233–235.

[173] A. N. Georgopoulou, C. P. Raptopoulou, V. Psycharis, R. Ballesteros, B. Abarca, A. K. Boudalis, *Inorg. Chem.* **2009**, *48*, 3167–3176.

[174] A. Pons-Balagué, S. Piligkos, S. J. Teat, J. S. Costa, M. Shiddiq, S. Hill, G. R. Castro, P. Ferrer-Escorihuela, E. C. Sañudo, *Chem. Eur. J.* **2013**, *19*, 9064–9071.

[175] R. McLellan, J. Rezé, S. M. Taylor, R. D. McIntosh, E. K. Brechin, S. J. Dalgarno, *Chem. Commun.* **2014**, *50*, 2202–2204.

[176] P. Khakhlary, C. E. Anson, A. Mondal, A. K. Powell, J. B. Baruah, *Dalton Trans.* **2015**, *44*, 2964–2969.

[177] D. M. Adams, A. Dei, A. L. Rheingold, D. N. Hendrickson, *J. Am. Chem. Soc.* **1993**, *115*, 8221–8229.

[178] A. B. P. Lever, Inorganic Electronic Spectroscopy, Elsevier, Amsterdam, **1968**.

[179] M. Graf, G. Wolmershäuser, H. Kelm, S. Demeschko, F. Meyer, H.-J. Krüger, *Angew. Chem. Int. Ed.* **2010**, *49*, 950–953.

[180] S. Torelli, C. Belle, I. Gautier-Luneau, J. L. Pierre, E. Saint-Aman, J. M. Latour, L. Le Pape, D. Luneau, *Inorg. Chem.* **2000**, *39*, 3526–3536.

[181] S. Adhikari, A. Banerjee, S. Nandi, M. Fondo, J. Sanmartin-Matalobos, D. Das, *RSC Adv.* **2015**, *5*, 10987–10993.

[182] F. Zippel, F. Ahlers, R. Werner, W. Haase, H. F. Nolting, B. Krebs, *Inorg. Chem.* **1996**, *35*, 3409–3419.

[183] J. Ackermann, F. Meyer, E. Kaifer, H. Pritzkow, *Chem.-Eur. J.* **2002**, *8*, 247–258.

[184] A. Neves, L. M. Rossi, A. J. Bortoluzzi, B. Szpoganicz, C. Wiezbicki, E. Schwingel, W. Haase, S. Ostrovsky, *Inorg. Chem.* **2002**, *41*, 1788–1794.

[185] E. Monzani, G. Battaini, A. Perotti, L. Casella, M. Gullotti, L. Santagostini, G. Nardin, L. Randaccio, S. Geremia, P. Zanello, G. Opromolla, *Inorg. Chem.* **1999**, *38*, 5359–5369.

[186] R. Modak, Y. Sikdar, S. Mandal, S. Chatterjee, A. Bieko, J. Mroziski, S. Goswami, *Inorg. Chim. Acta* **2014**, *416*, 122–134.

[187] M. Maiti, D. Sadhukhan, S. Thakurta, E. Zangrando, G. Pilet, A. Bauzá, A. Frontera, B. Dede, S. Mitra, *Polyhedron* **2014**, *75*, 40–49.

[188] P. Seth, L. K. Das, M. G. B. Drew, A. Ghosh, *Eur. J. Inorg. Chem.* **2012**, *2012*, 2232–2242.

[189] A. Jana, N. Aliaga-Alcalde, E. Ruiz, S. Mohanta, *Inorg. Chem.* **2013**, *52*, 7732–7746.

[190] D. Dey, G. Kaur, A. Ranjani, L. Gayathri, P. Chakraborty, J. Adhikary, J. Pasan, D. Dhanasekaran, A. R. Choudhury, M. A. Akbarsha, N. Kole, B. Biswas, *Eur. J. Inorg. Chem.* **2014**, n/a–n/a.

[191] S. K. Dey, A. Mukherjee, *New J. Chem.* **2014**, DOI 10.1039/C4NJ00715H.

[192] M. Mitra, P. Raghavaiah, R. Ghosh, *New J. Chem.* **2014**, DOI 10.1039/C4NJ01587H.

[193] L. Michaelis, M. L. Menten, K. A. Johnson, R. S. Goody, *Biochem.* **2011**, *50*, 8264–8269.

[194] H. Lineweaver, D. Burk, *J. Am. Chem. Soc.* **1934**, *56*, 658–666.

[195] G. S. Eadie, *J. Biol. Chem.* **1942**, *146*, 85–93.

[196] B. H. J. Hofstee, *Nature* **1959**, *184*, 1296–1298.

[197] C. S. Hanes, *Biochem. J.* **1932**, *26*, 1406–1421.

[198] J. B. S. Haldane, *Nature* **1957**, *179*, 832–832.

[199] K. S. Banu, T. Chattopadhyay, A. Banerjee, S. Bhattacharya, E. Suresh, M. Nethaji, E. Zangrando, D. Das, *Inorg. Chem.* **2008**, *47*, 7083–7093.

[200] A. Banerjee, A. Guha, J. Adhikary, A. Khan, K. Manna, S. Dey, E. Zangrando, D. Das, *Polyhedron* **2013**, *60*, 102–109.

[201] A. Hazari, L. K. Das, R. M. Kadam, A. Bauzá, A. Frontera, A. Ghosh, *Dalton Trans.* **2015**, *44*, 3862–3876.

[202] S. Majumder, S. Mondal, P. Lemoine, S. Mohanta, *Dalton Trans.* **2013**, DOI 10.1039/C2DT32629A.

[203] L. Mandal, S. Sasmal, H. A. Sparkes, J. A. K. Howard, S. Mohanta, *Inorganica Chimica Acta* **2014**, *412*, 38–45.

[204] R. Modak, Y. Sikdar, S. Mandal, S. Goswami, *Inorg. Chem. Commun.* **2013**, *37*, 193–196.

[205] I. A. Koval, K. Selmeczi, C. Belle, C. Philouze, E. Saint-Aman, I. Gautier-Luneau, A. M. Schuitema, M. van Vliet, P. Gamez, O. Roubeau, M. Lüken, B. Krebs, M. Lutz, A. L. Spek, J.-L. Pierre, J. Reedijk, *Chem. Eur. J.* **2006**, *12*, 6138–6150.

[206] Bruker, APEX2 Software Suite, version 2.0, Madison, Wisconsin, USA, **2005**.

[207] A. Altomare, M. C. Burla, M. Camalli, G. L. Cascarano, C. Giacovazzo, A. Guagliardi, A. G. Moliterni, G. Polidori, R. Spagna, *J. Appl. Crystallogr.* **1999**, *32*, 115–119.

[208] M. C. Burla, M. Camalli, B. Carrozzini, G. L. Cascarano, C. Giacovazzo, G. Polidori, R. Spagna, *J. Appl. Crystallogr.* **2003**, *36*, 1103–1103.

[209] L. Palatinus, G. Chapuis, *J. Appl. Crystallogr.* **2007**, *40*, 786–790.

[210] G. M. Sheldrick, *Acta Crystallogr. Sect. A* **2008**, *64*, 112–122.

[211] O. V. Dolomanov, L. J. Bourhis, R. J. Gildea, J. A. K. Howard, H. Puschmann, *J. Appl. Crystallogr.* **2009**, *42*, 339–341.

[212] E. Bill, julX 1.41, **2008**, `http://www.mpibac.mpg.de/bac/logins/bill/julX_en.php`.

[213] N. F. Chilton, R. P. Anderson, L. D. Turner, A. Soncini, K. S. Murray, *J. Comput. Chem.* **2013**, *34*, 1164–1175.

[214] G. Aromí, A. S. Batsanov, P. Christian, M. Helliwell, A. Parkin, S. Parsons, A. A. Smith, G. A. Timco, R. E. P. Winpenny, *Chem. Eur. J.* **2003**, *9*, 5142–5161.

[215] T. O. Denisova, E. V. Amelchenkova, I. V. Pruss, Z. V. Dobrokhotova, O. P. Fialkovskii, S. E. Nefedov, *Russ. J. Inorg. Chem.* **2006**, *51*, 1020–1064.

[216] G. Chaboussant, R. Basler, H.-U. Güdel, S. Ochsenbein, A. Parkin, S. Parsons, G. Rajaraman, A. Sieber, A. A. Smith, G. A. Timco, R. E. P. Winpenny, *Dalton Trans.* **2004**, 2758.

[217] Z. V. Dobrokhotova, I. G. Fomina, M. A. Kiskin, A. A. Sidorov, V. M. Novotortsev, I. L. Eremenko, *Russ. Chem. Bull.* **2006**, *55*, 256–266.

[218] M. A. Kiskin, I. G. Fomina, A. A. Sidorov, G. G. Aleksandrov, O. Y. Proshenkina, Z. V. Dobrokhotova, V. N. Ikorskii, Y. G. Shvedenkov, V. M. Novotortsev, I. L. Eremenko, I. I. Moiseev, *Russ. Chem. Bull.* **2004**, *53*, 2508–2518.

[219] R. Wu, M. Poyraz, F. E. Sowrey, C. E. Anson, S. Wocadlo, A. K. Powell, U. A. Jayasooriya, R. D. Cannon, T. Nakamoto, M. Katada, H. Sano, *Inorg. Chem.* **1998**, *37*, 1913–1921.

[220] A. S. Batsanov, G. A. Timko, Y. T. Struchkov, N. V. Gerbeleu, K. M. Indrichan, *Koordinats. Khim.* **1991**, *17*, 662–669.

[221] T. M. Khomenko, O. V. Salomatina, S. Y. Kurbakova, I. V. Ilina, K. P. Volcho, N. I. Komarova, D. V. Korchagina, N. F. Salakhutdinov, A. G. Tolstikov, *Russ. J. Org. Chem.* **2006**, *42*, 1653–1661.

[222] L. F. Lindoy, *Synthesis* **1998**, *1998*, 1029–1032.

[223] L. P. G. Wakelin, X. Bu, A. Eleftheriou, A. Parmar, C. Hayek, B. W. Stewart, *J. Med. Chem.* **2003**, *46*, 5790–5802.

[224] R. Filosa, A. Peduto, S. D. Micco, P. d. Caprariis, M. Festa, A. Petrella, G. Capranico, G. Bifulco, *Bioorg. Med. Chem.* **2009**, *17*, 13–24.

[225] P. C. Andrews, G. B. Deacon, R. Frank, B. H. Fraser, P. C. Junk, J. G. MacLellan, M. Massi, B. Moubaraki, K. S. Murray, M. Silberstein, *Eur. J. Inorg. Chem.* **2009**, *2009*, 744–751.

[226] M. Ferles, R. Liboska, P. Trka, *Collect. Czechoslov. Chem. Commun.* **1990**, *55*, 1228–1233.

A

Spectra

A.1 Infrared Spectra

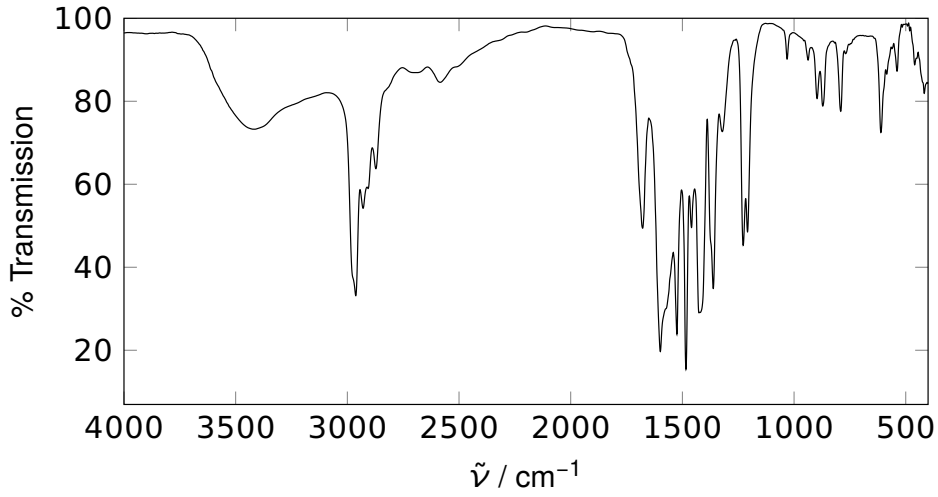

Fig. A.1: Infrared spectrum of **P1**

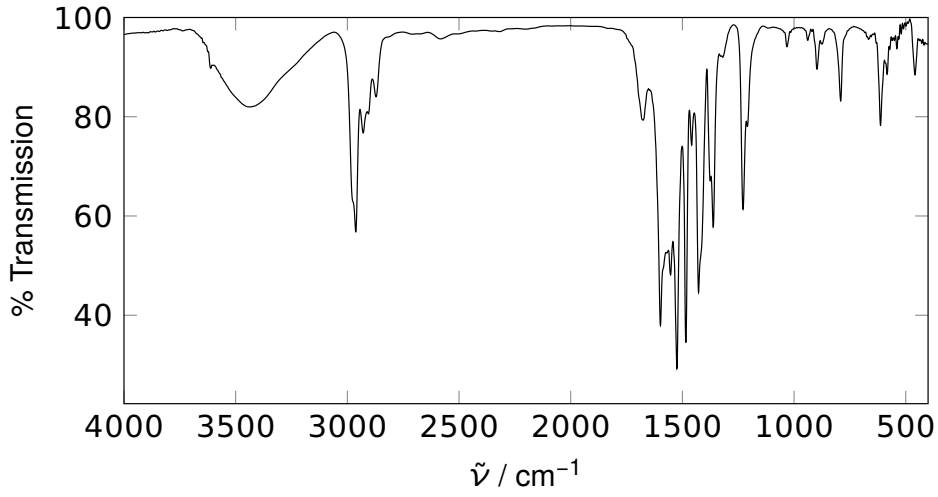

Fig. A.2: Infrared spectrum of **P2**

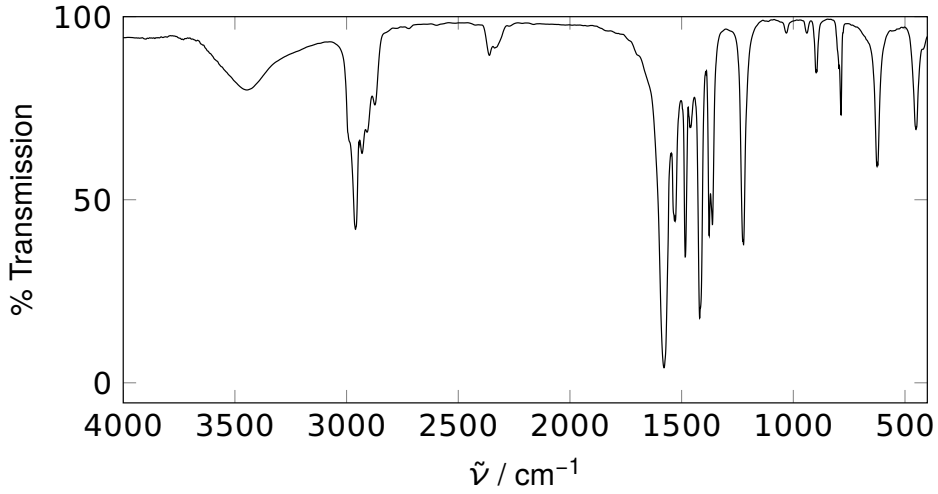

Fig. A.3: Infrared spectrum of **P3**

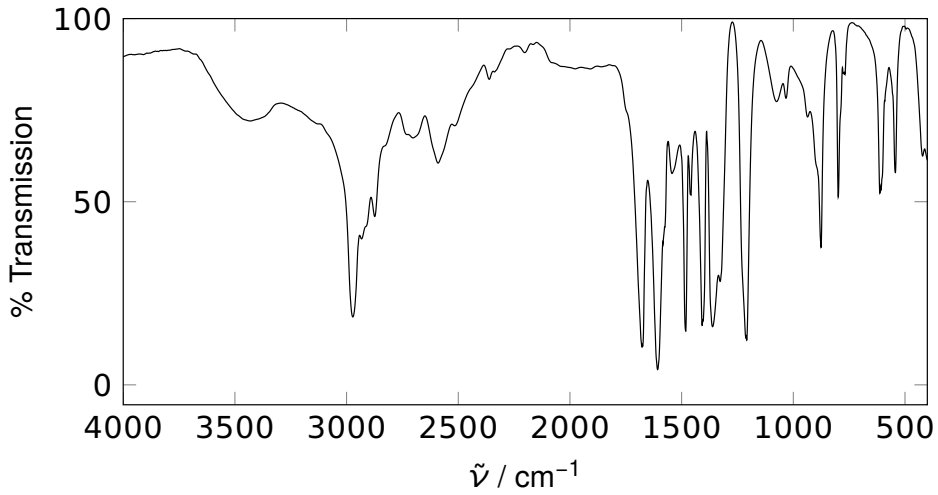

Fig. A.4: Infrared spectrum of **P4**

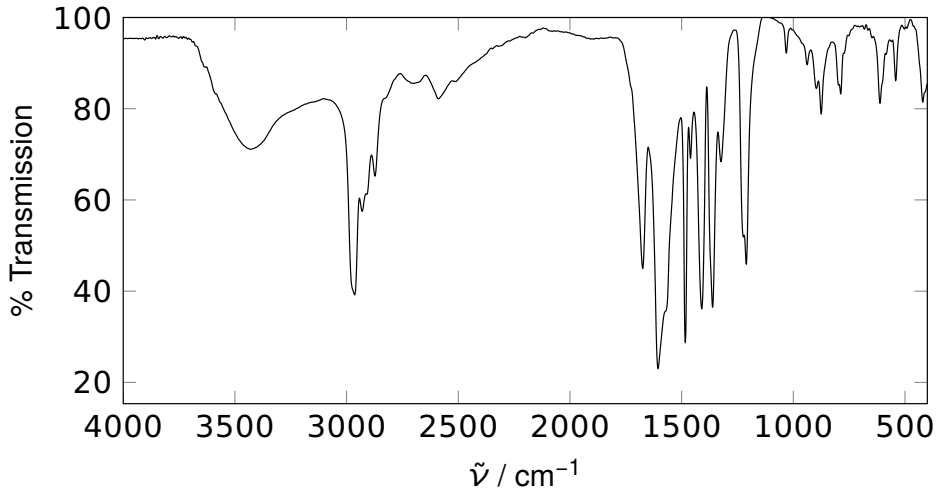

Fig. A.5: Infrared spectrum of **P5**

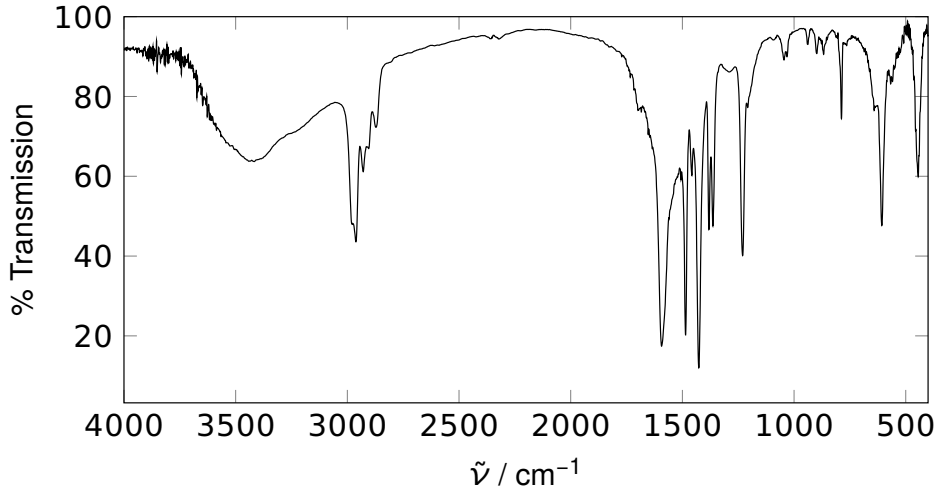

Fig. A.6: Infrared spectrum of **P6**

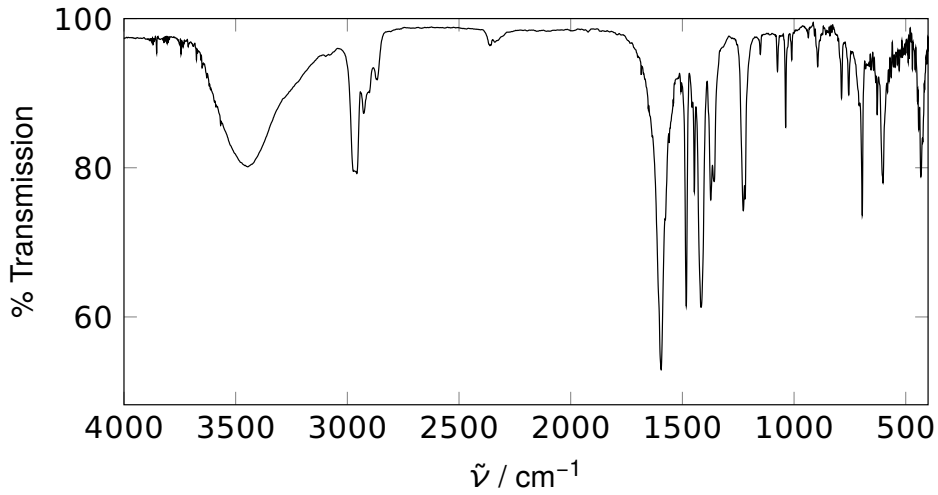

Fig. A.7: Infrared spectrum of **P7**

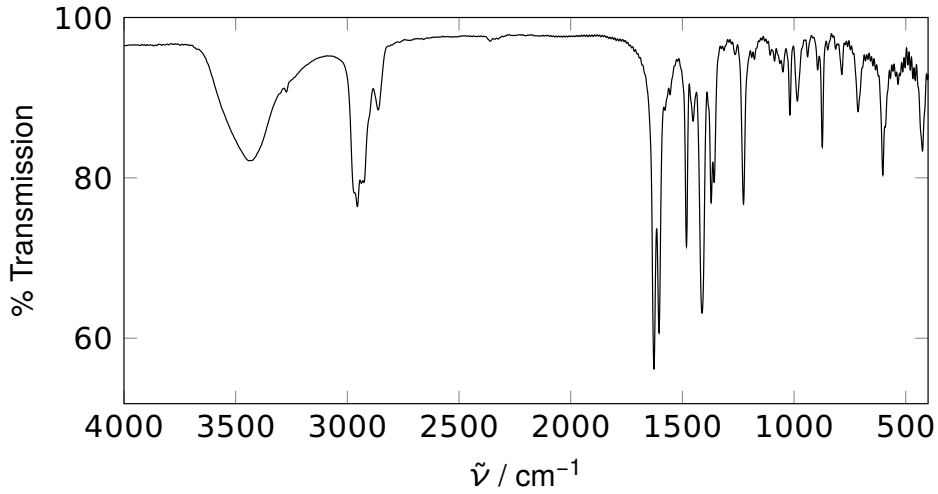

Fig. A.8: Infrared spectrum of **P8**

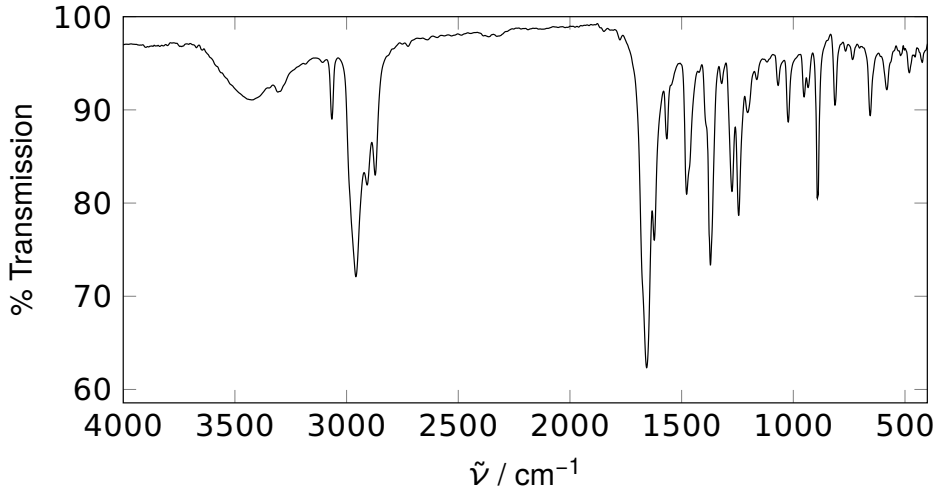

Fig. A.9: Infrared spectrum of **L1b**

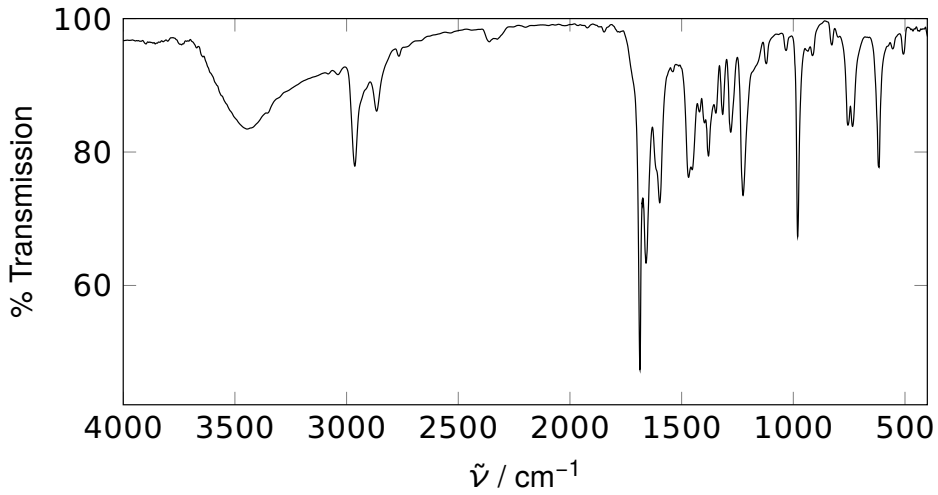

Fig. A.10: Infrared spectrum of **L2**

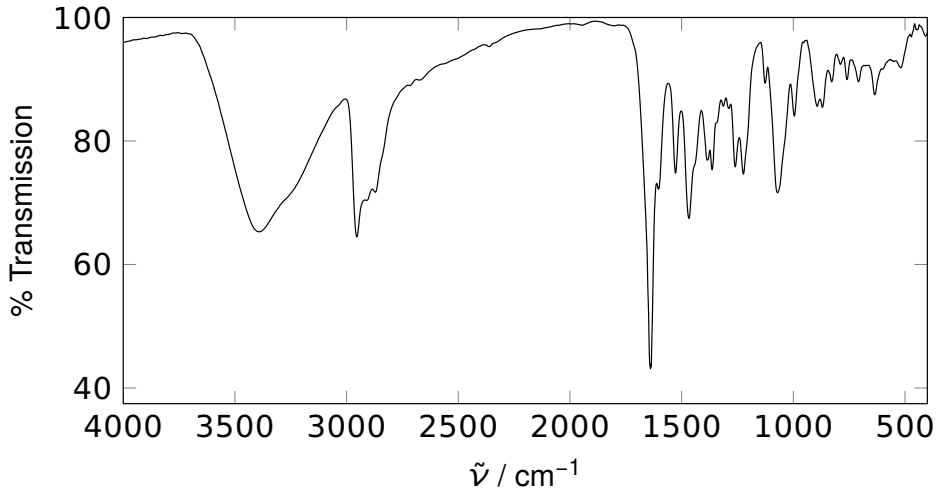

Fig. A.11: Infrared spectrum of **L3**

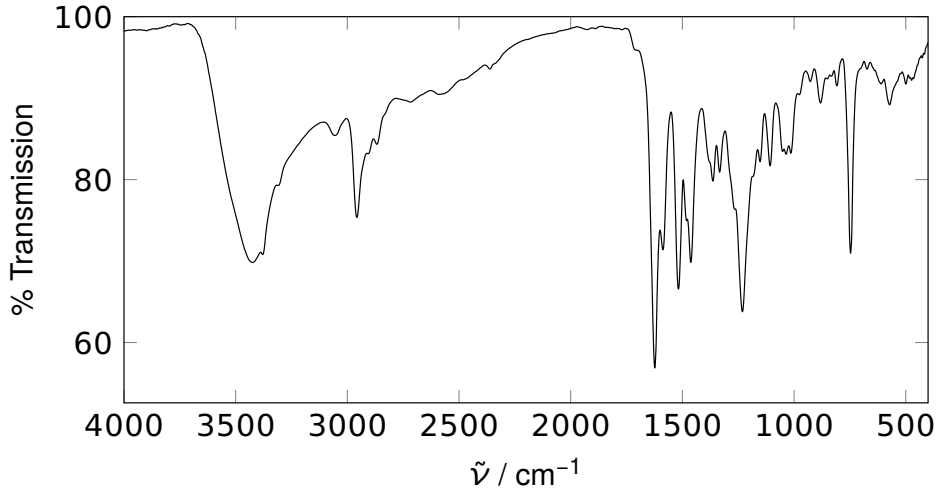

Fig. A.12: Infrared spectrum of **L4**

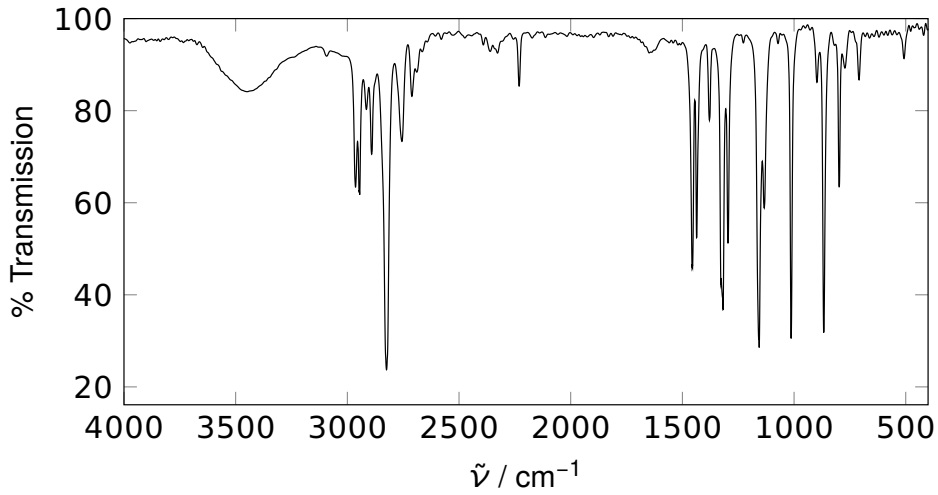

Fig. A.13: Infrared spectrum of **L5**

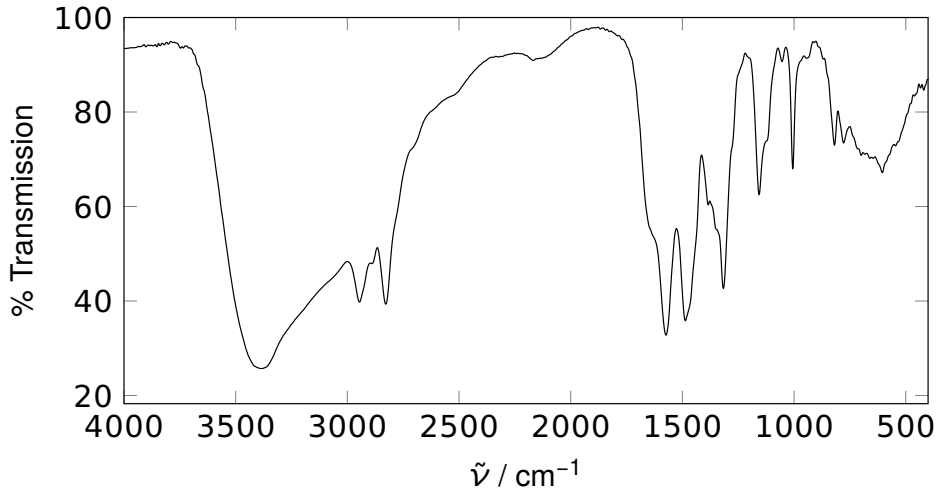

Fig. A.14: Infrared spectrum of **L6**

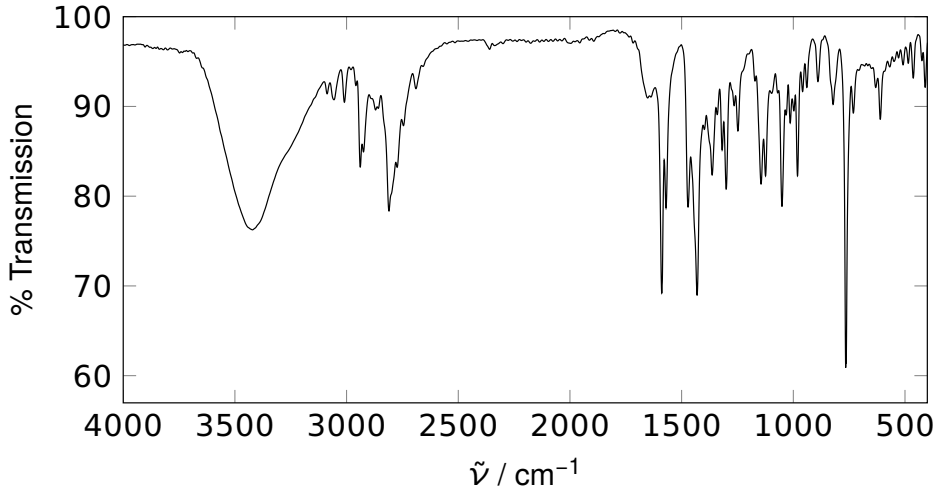

Fig. A.15: Infrared spectrum of **L7**

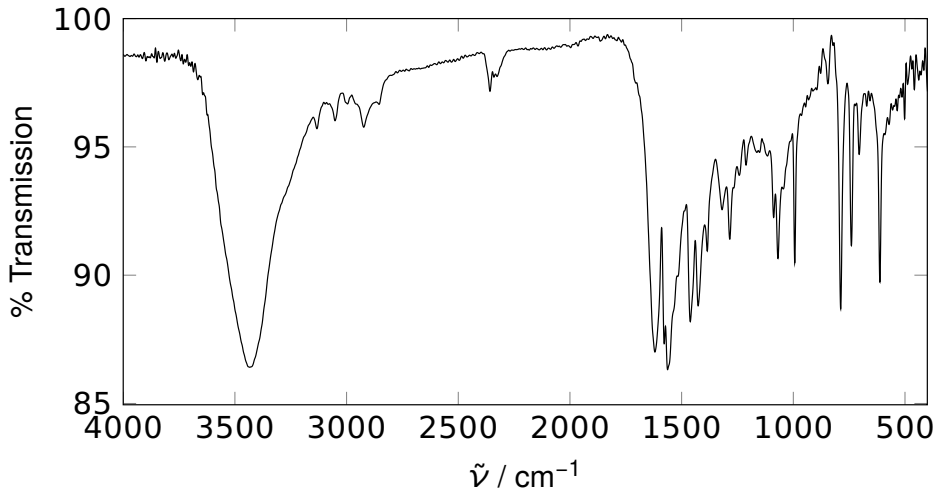

Fig. A.16: Infrared spectrum of **L8**

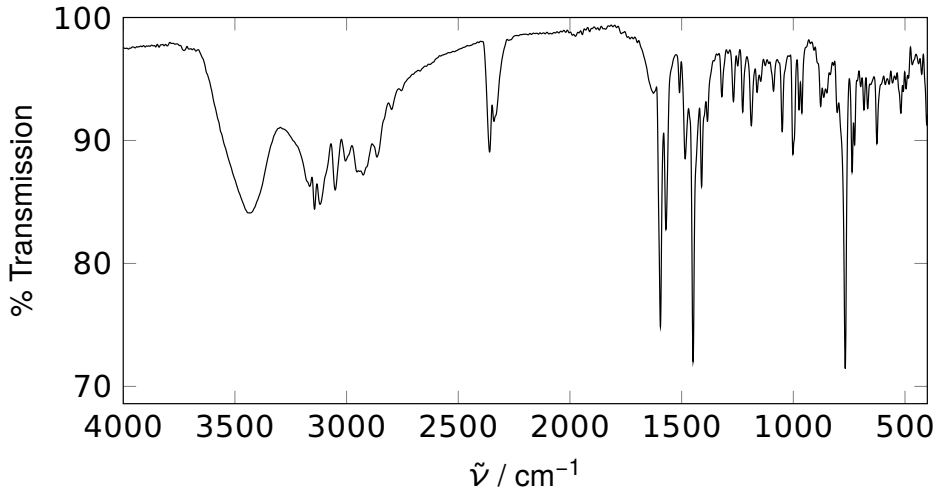

Fig. A.17: Infrared spectrum of **L9**

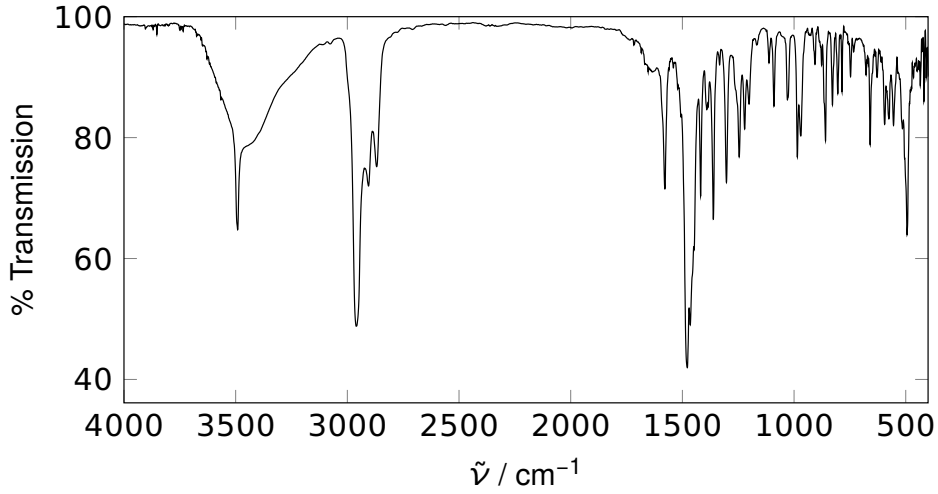

Fig. A.18: Infrared spectrum of **C1**

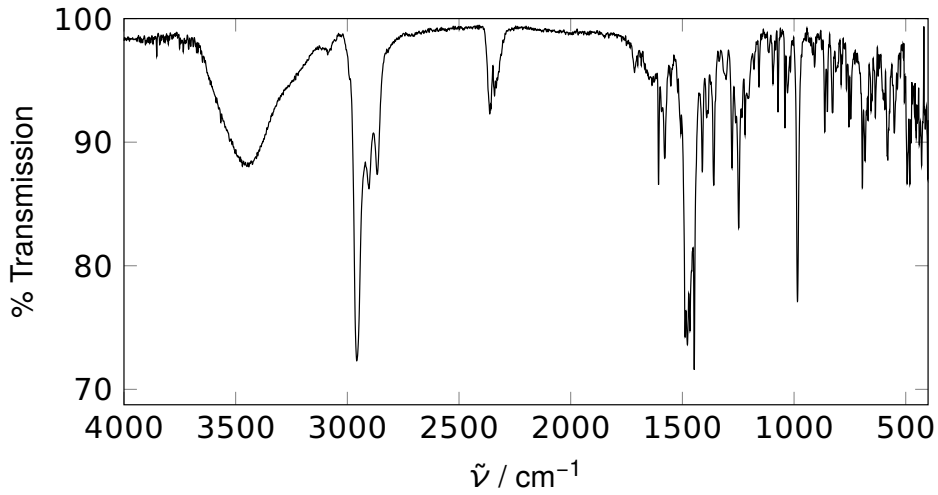

Fig. A.19: Infrared spectrum of **C2**

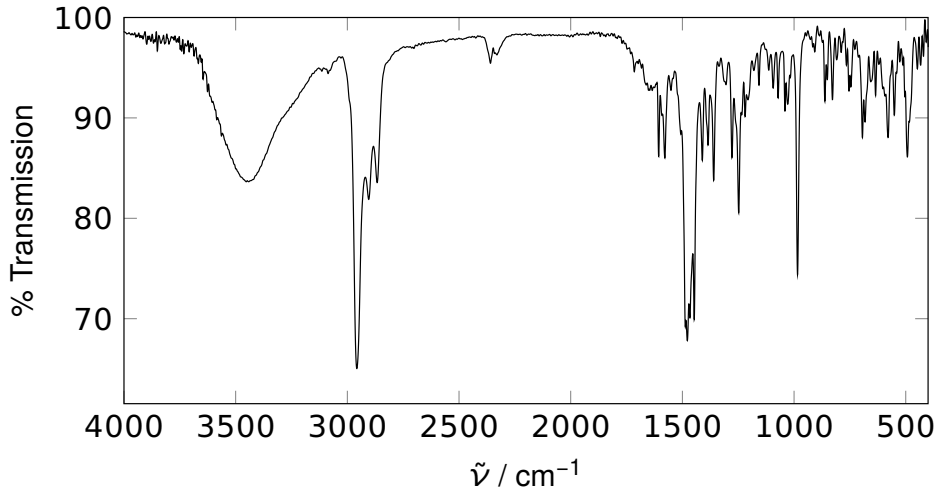

Fig. A.20: Infrared spectrum of **C3**

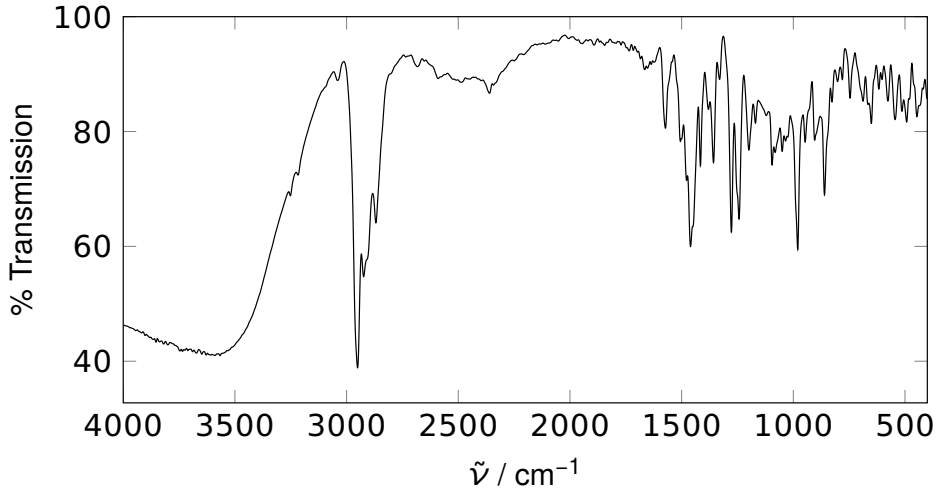

Fig. A.21: Infrared spectrum of **C4**

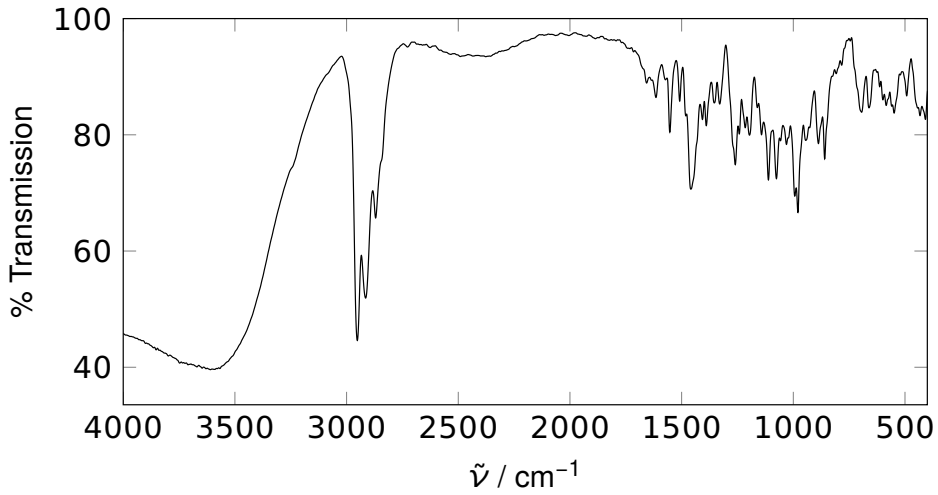

Fig. A.22: Infrared spectrum of **C5**

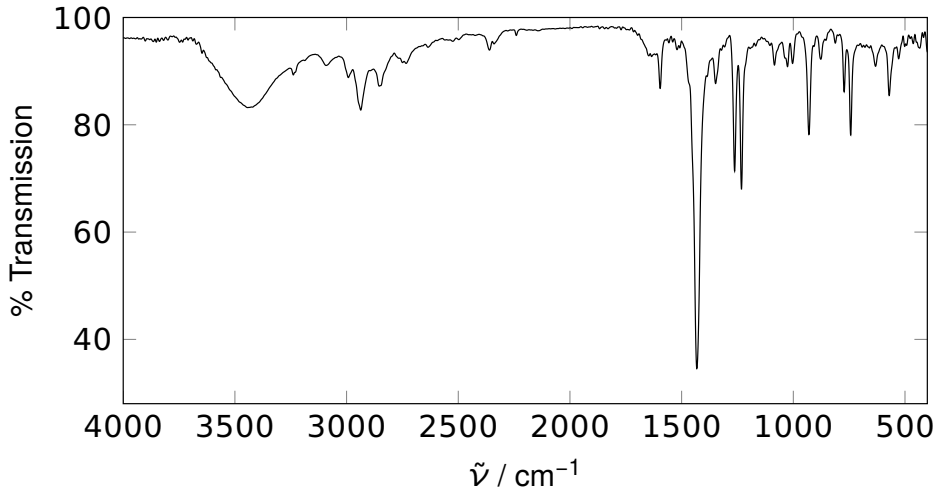

Fig. A.23: Infrared spectrum of **C6**

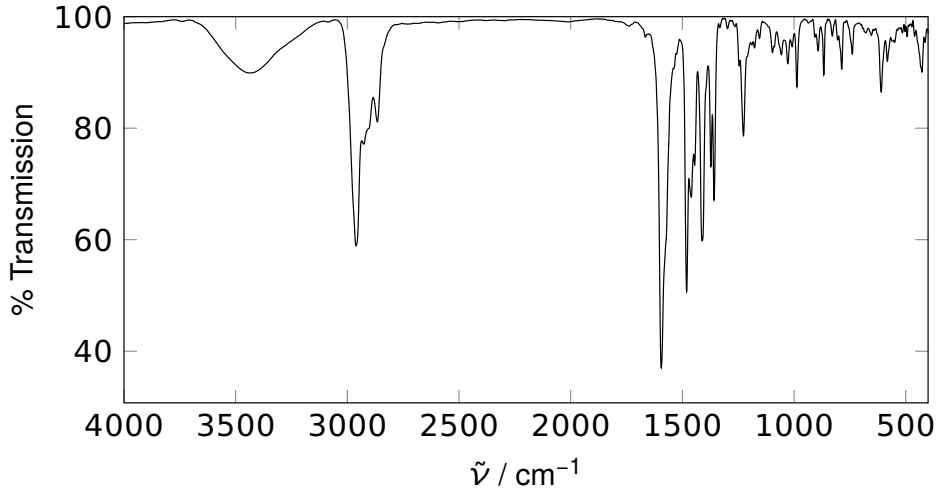

Fig. A.24: Infrared spectrum of **C7**

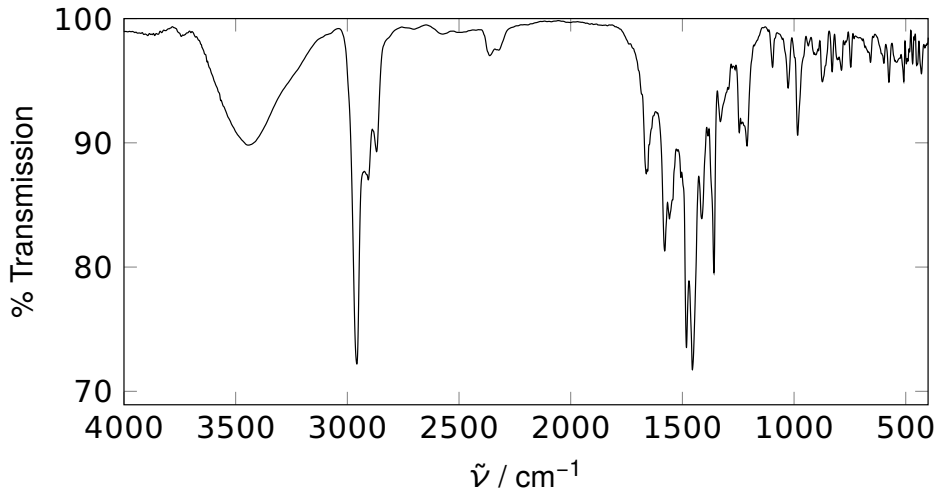

Fig. A.25: Infrared spectrum of **C8**

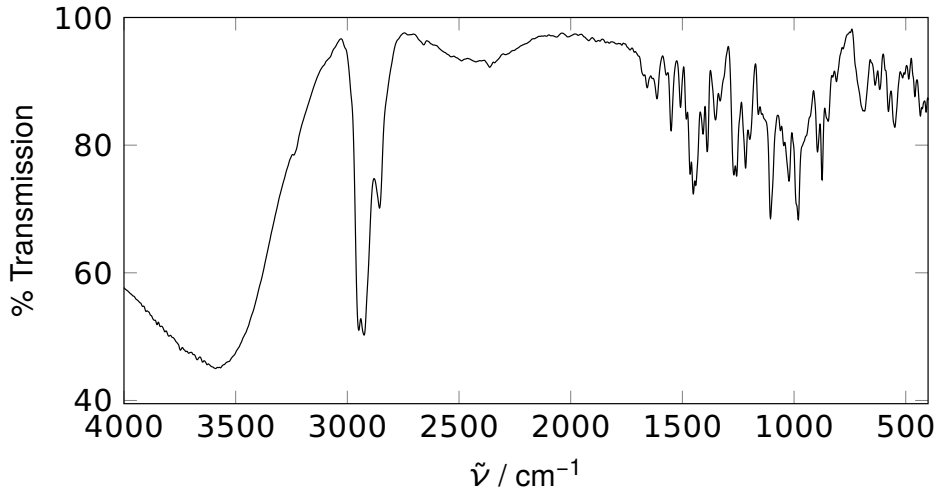

Fig. A.26: Infrared spectrum of **C9**

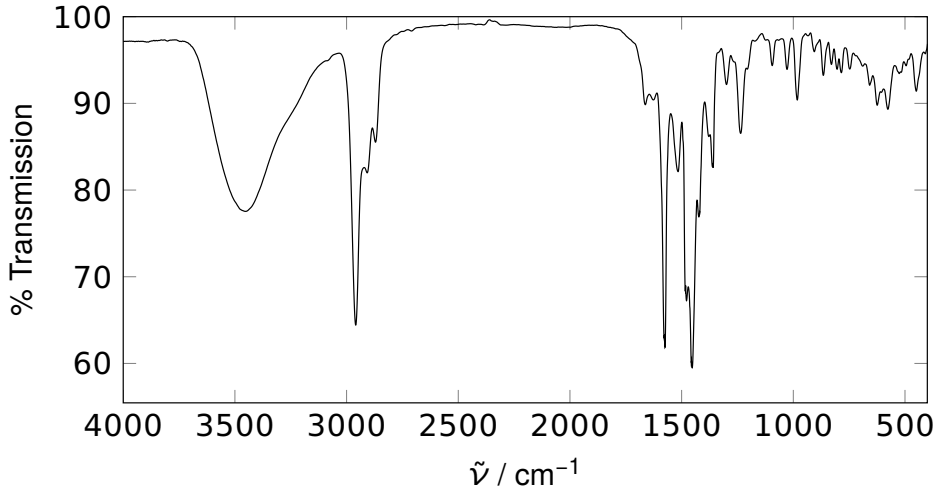

Fig. A.27: Infrared spectrum of **C10**

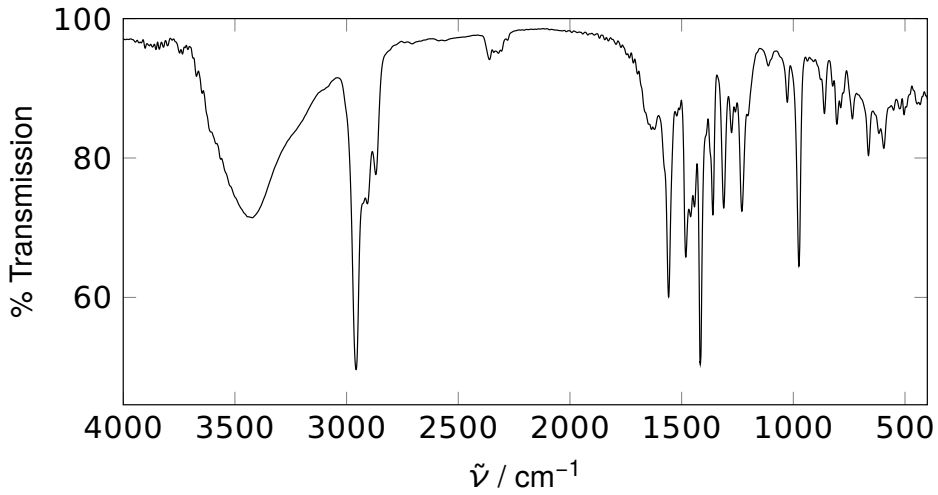

Fig. A.28: Infrared spectrum of **C11**

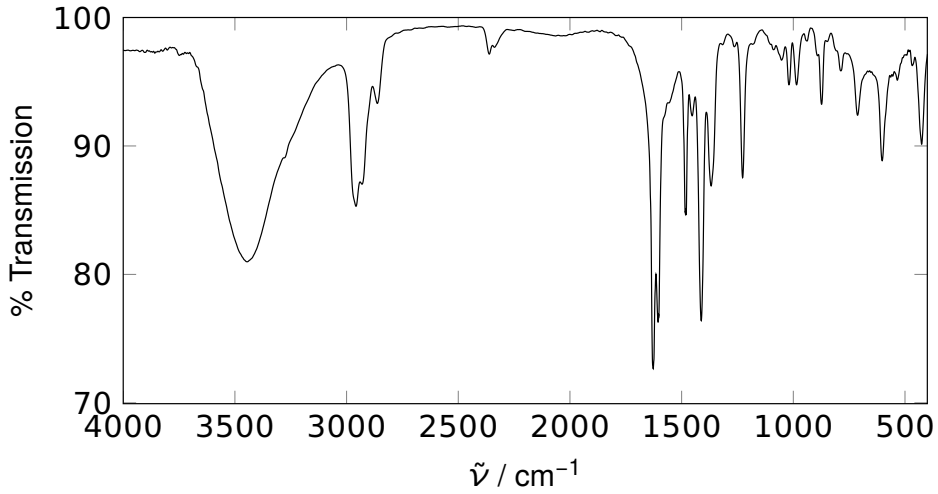

Fig. A.29: Infrared spectrum of **C12**

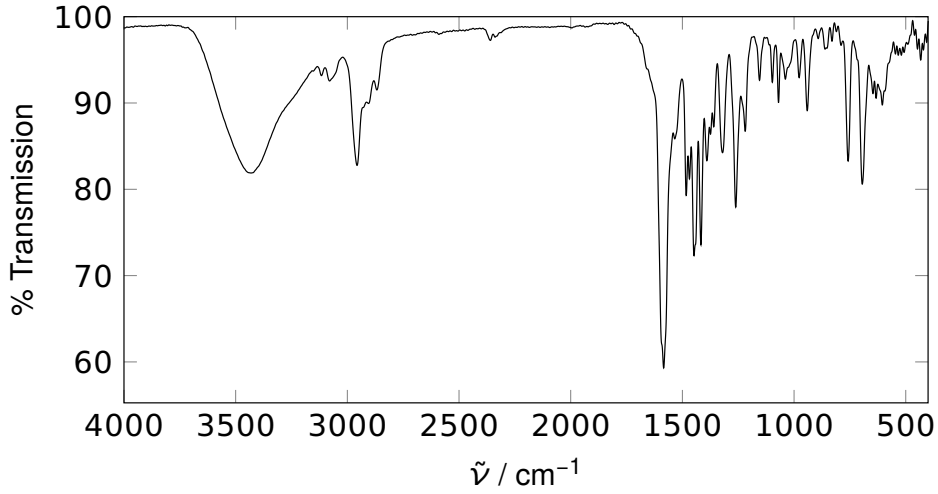

Fig. A.30: Infrared spectrum of **C13**

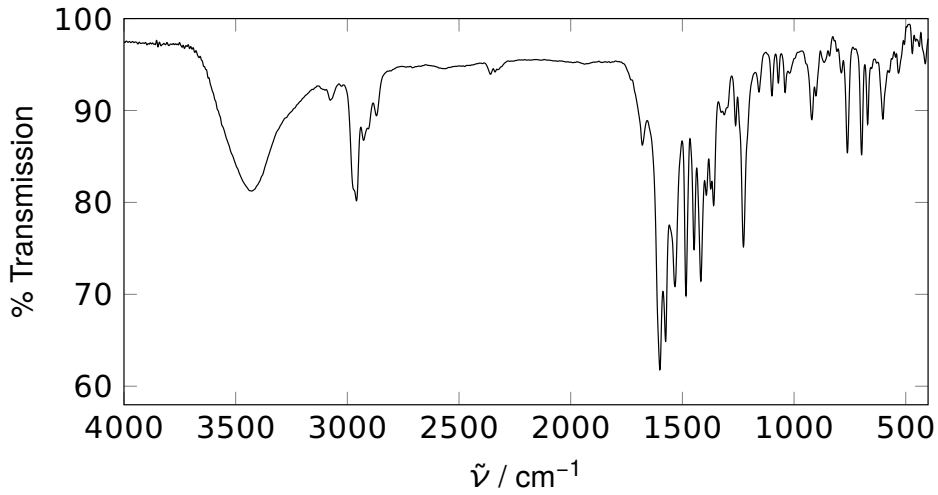

Fig. A.31: Infrared spectrum of **C14**

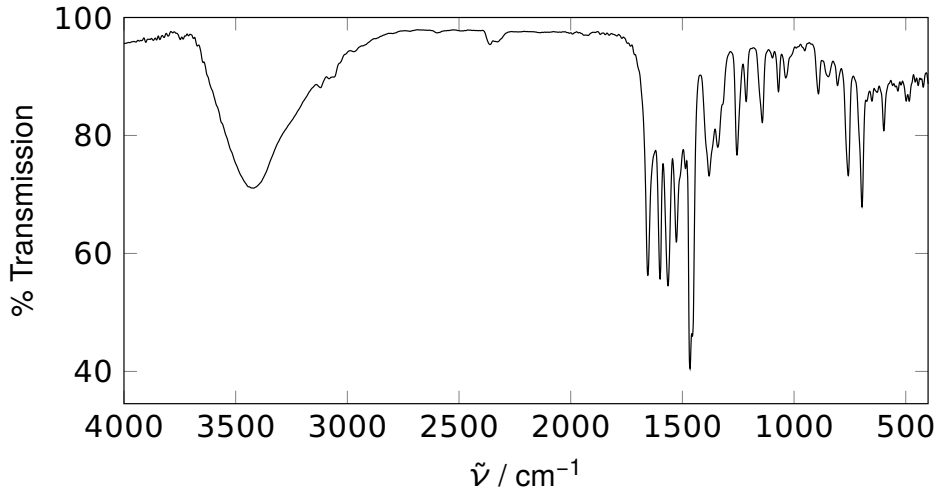

Fig. A.32: Infrared spectrum of **C15**

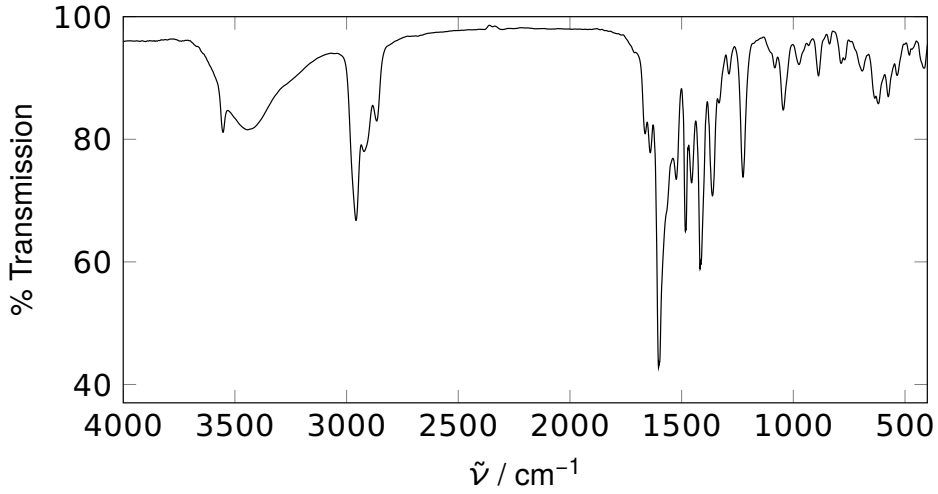

Fig. A.33: Infrared spectrum of **C16**

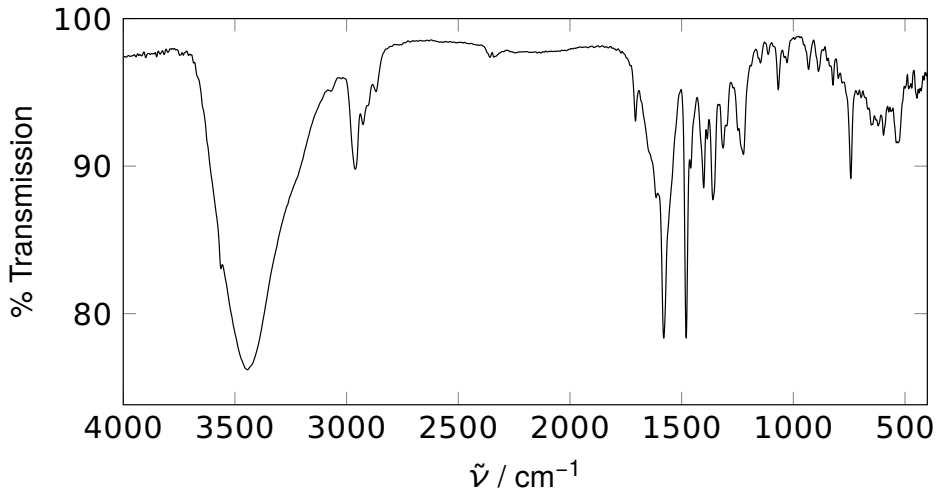

Fig. A.34: Infrared spectrum of **C17**

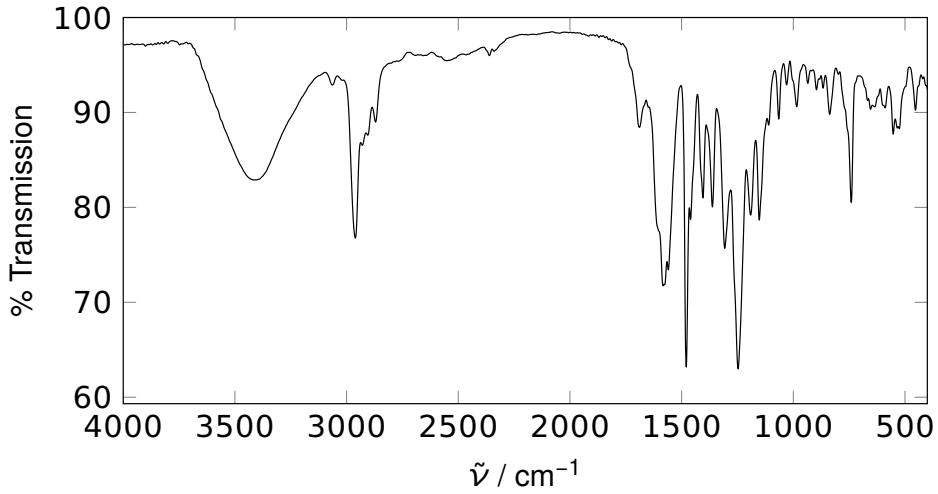

Fig. A.35: Infrared spectrum of **C18**

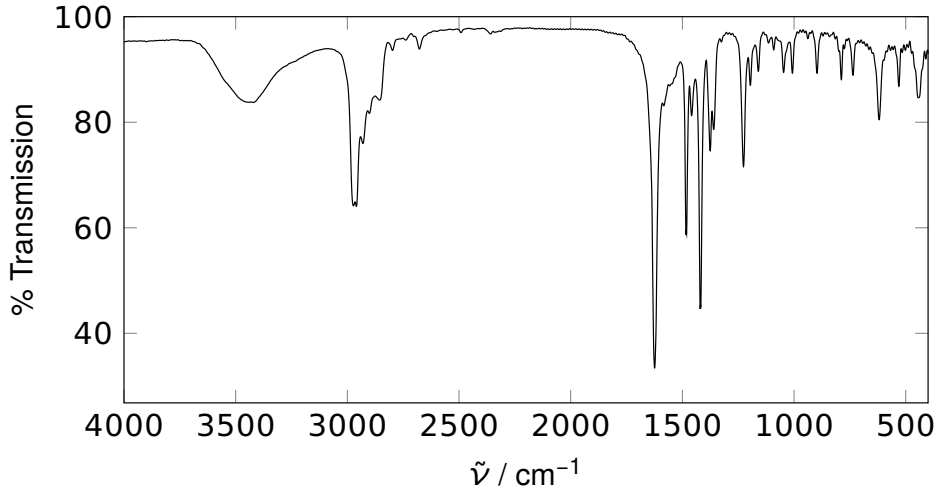

Fig. A.36: Infrared spectrum of **C19**

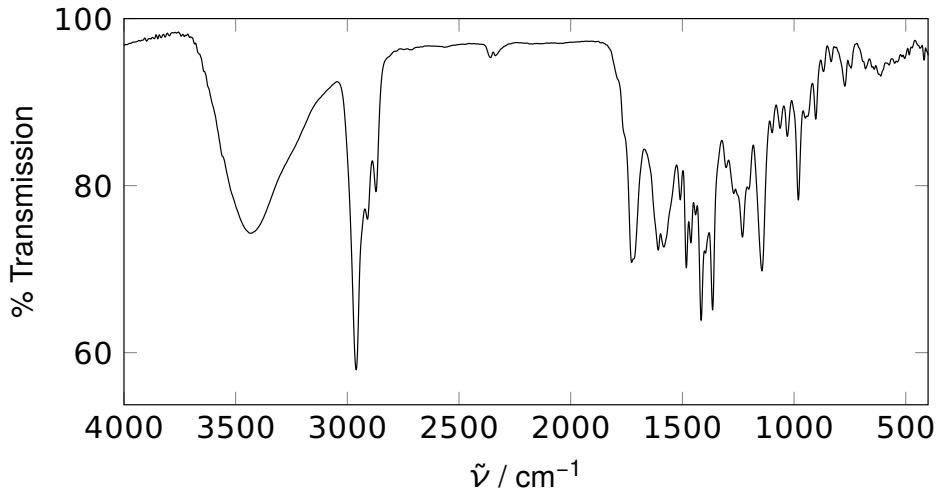

Fig. A.37: Infrared spectrum of **C20**

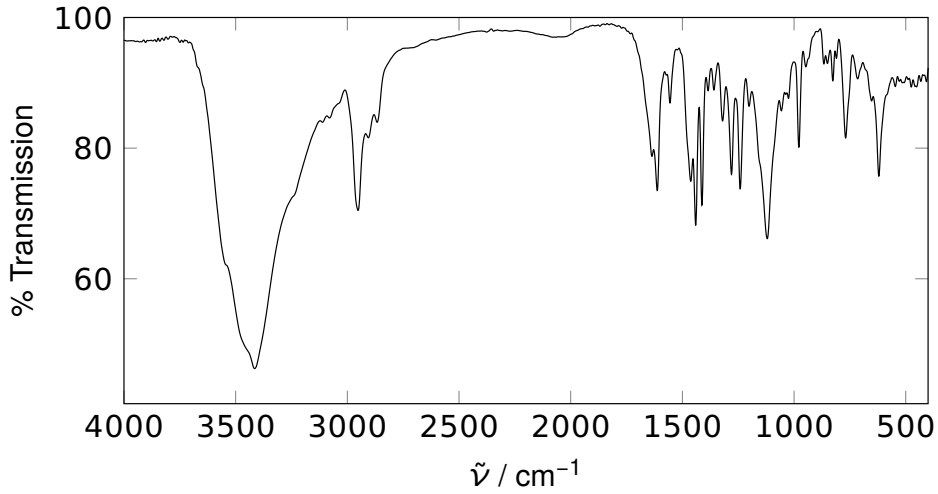

Fig. A.38: Infrared spectrum of **C21a**

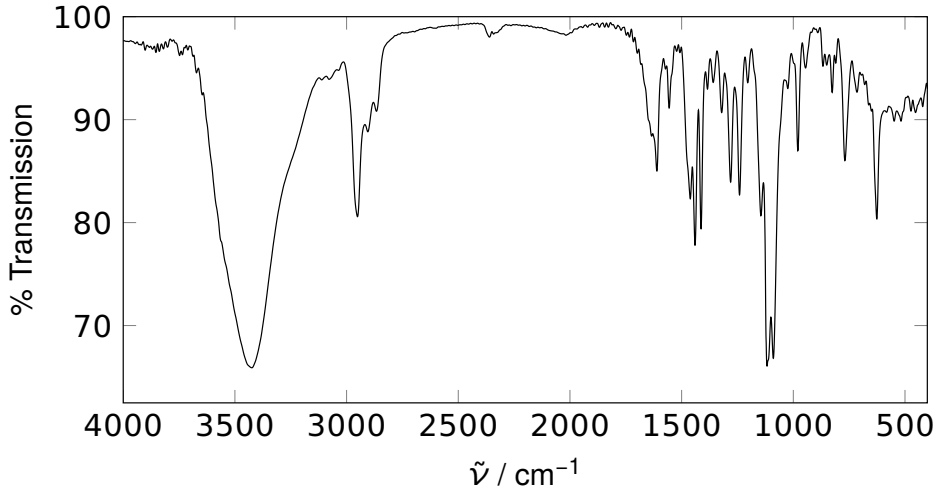

Fig. A.39: Infrared spectrum of **C21b**

A.2 NMR Spectra

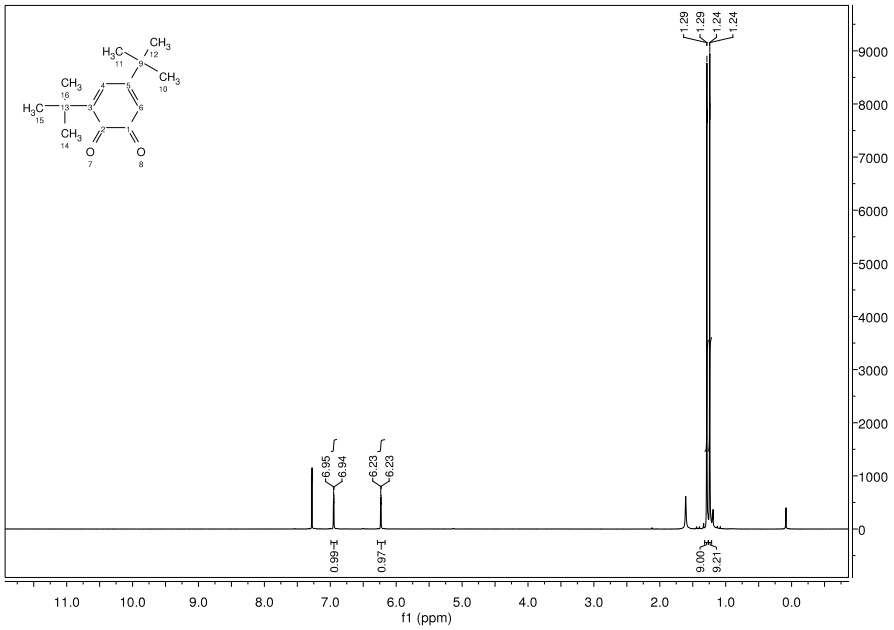

Fig. A.40: ^{1}H-NMR spectrum of **L1b**

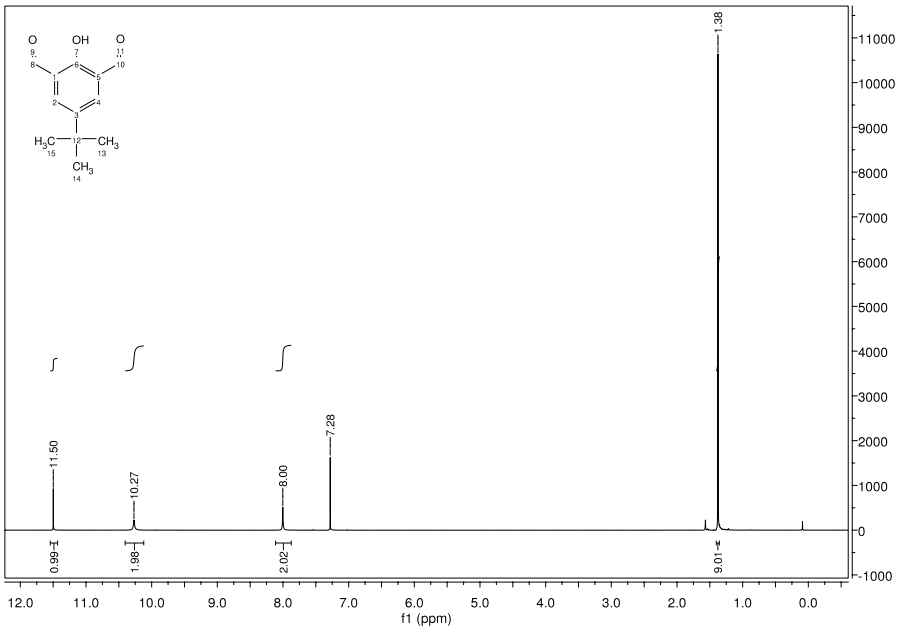

Fig. A.41: ^{1}H-NMR spectrum of **L2**

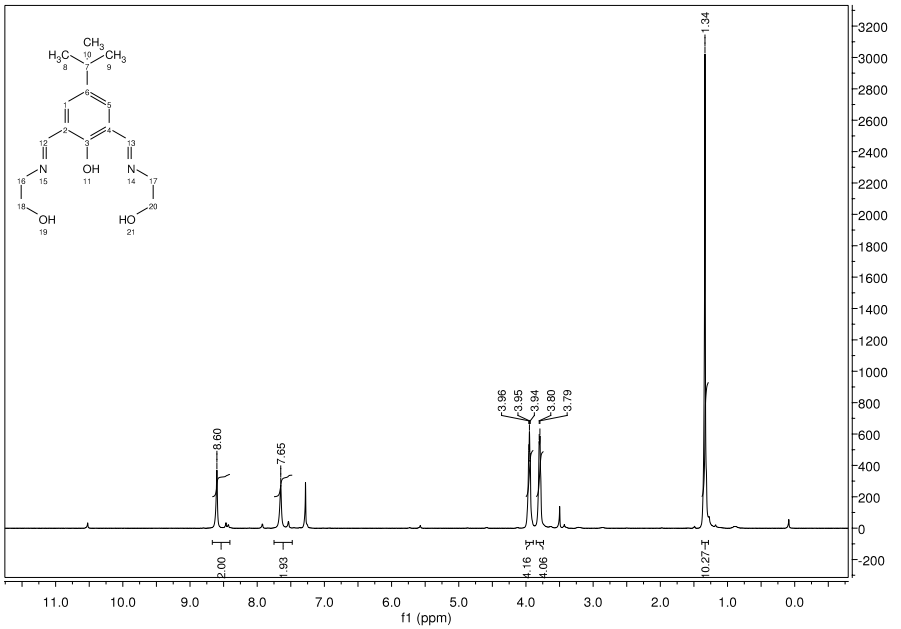

Fig. A.42: ^{1}H-NMR spectrum of **L3**

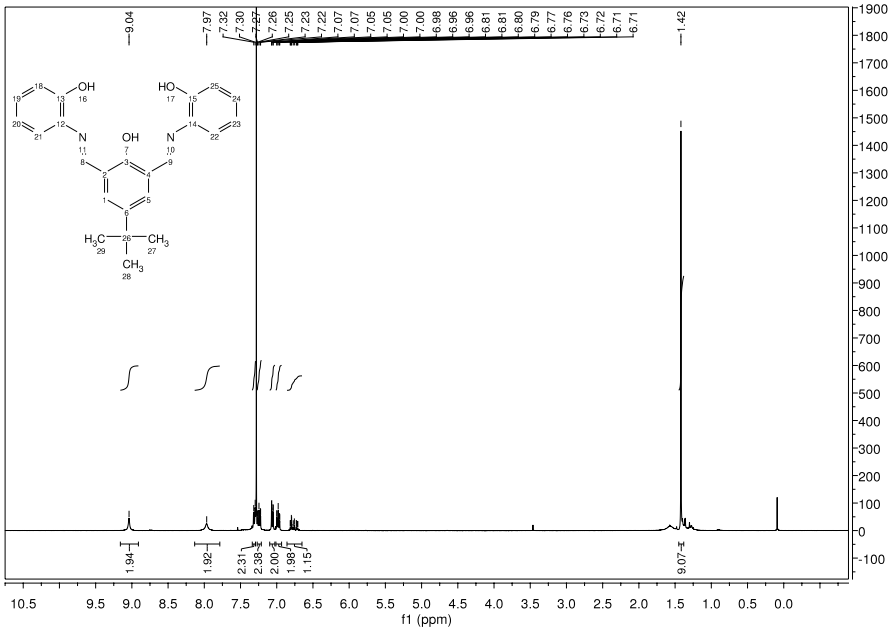

Fig. A.43: ^{1}H-NMR spectrum of **L4**

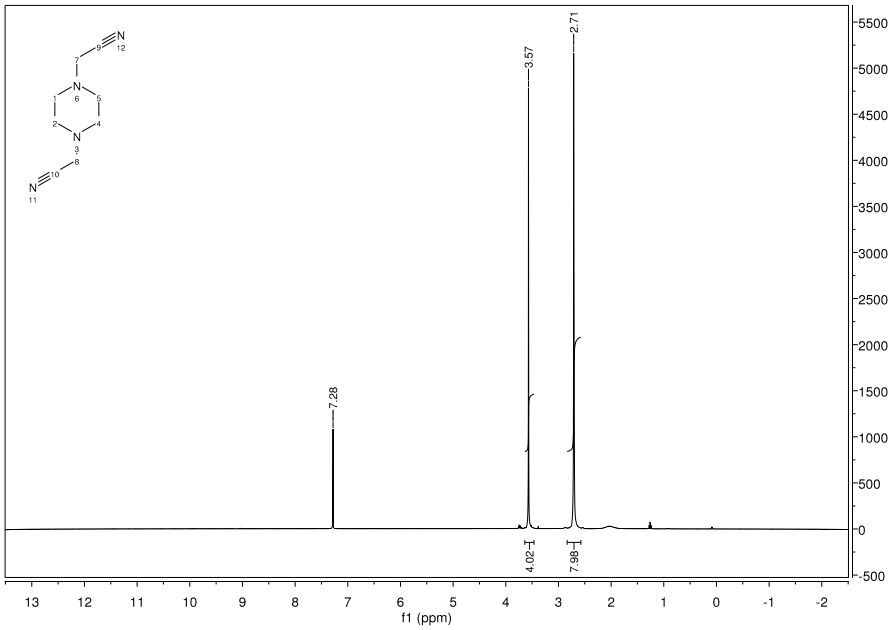

Fig. A.44: ^{1}H-NMR spectrum of **L5**

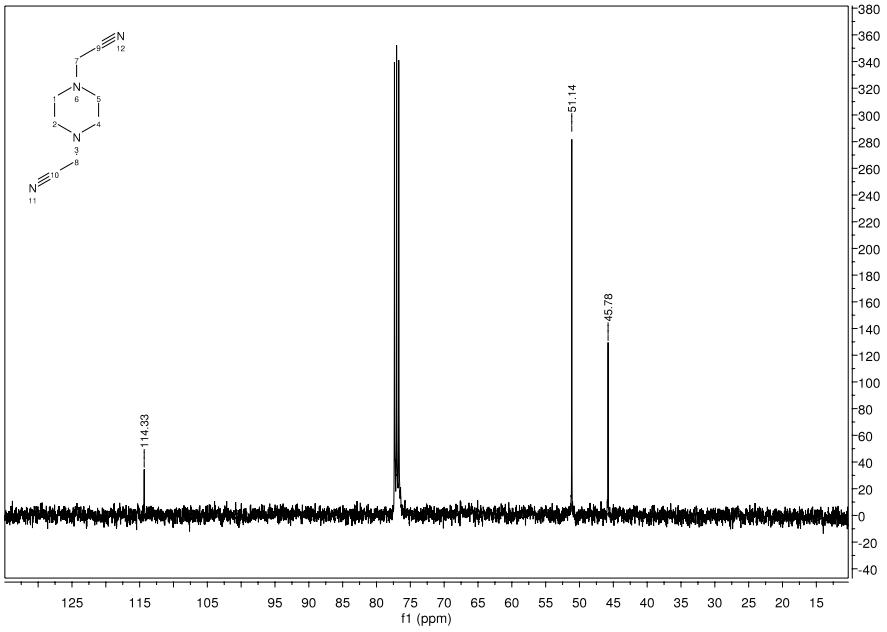

Fig. A.45: ^{13}C-NMR spectrum of **L5**

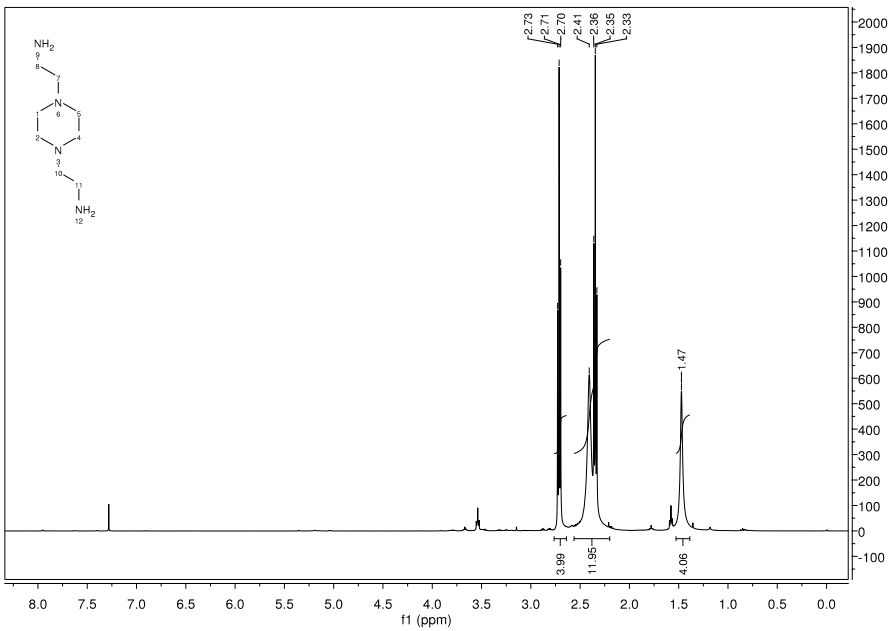

Fig. A.46: ^{1}H-NMR spectrum of **L6**

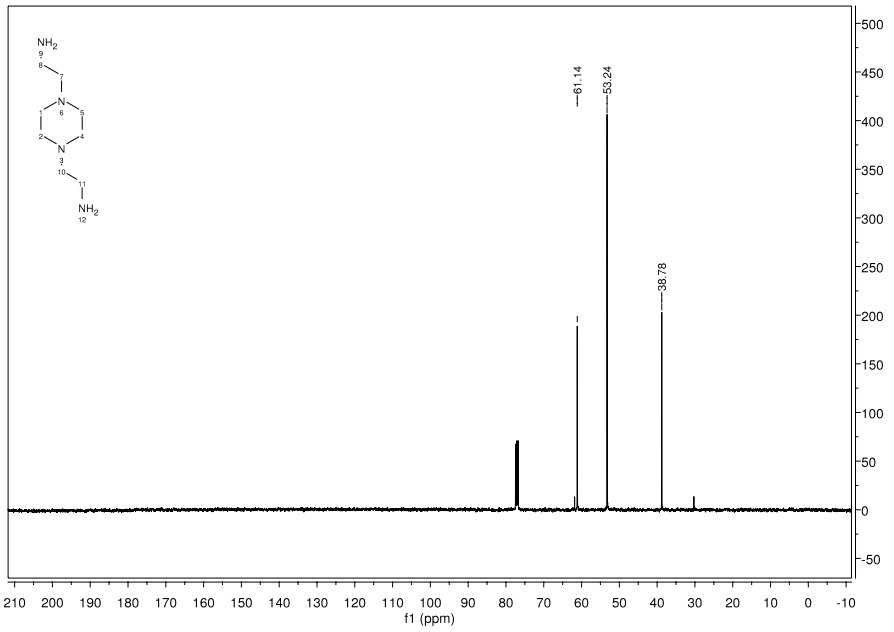

Fig. A.47: ^{13}C-NMR spectrum of **L6**

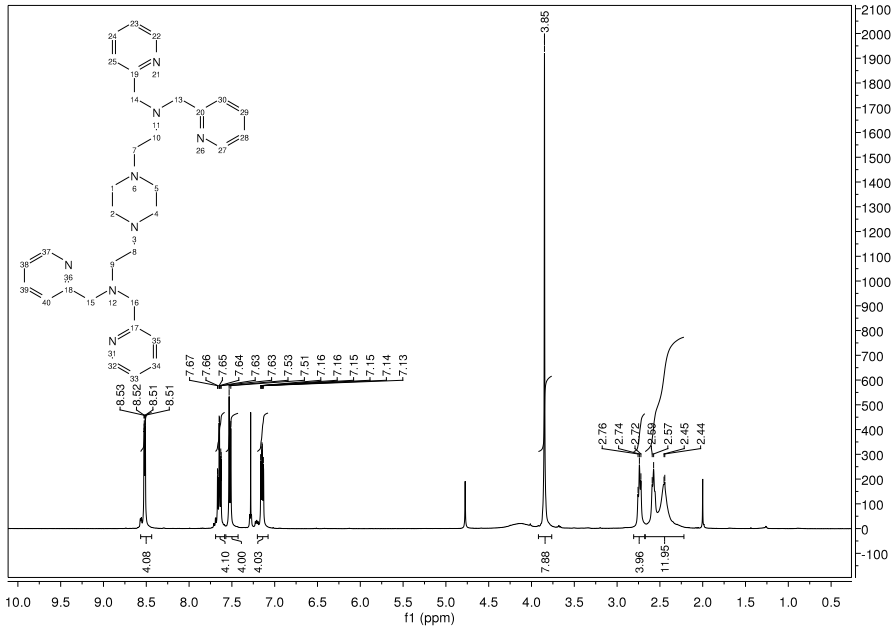

Fig. A.48: ^{1}H-NMR spectrum of **L7**

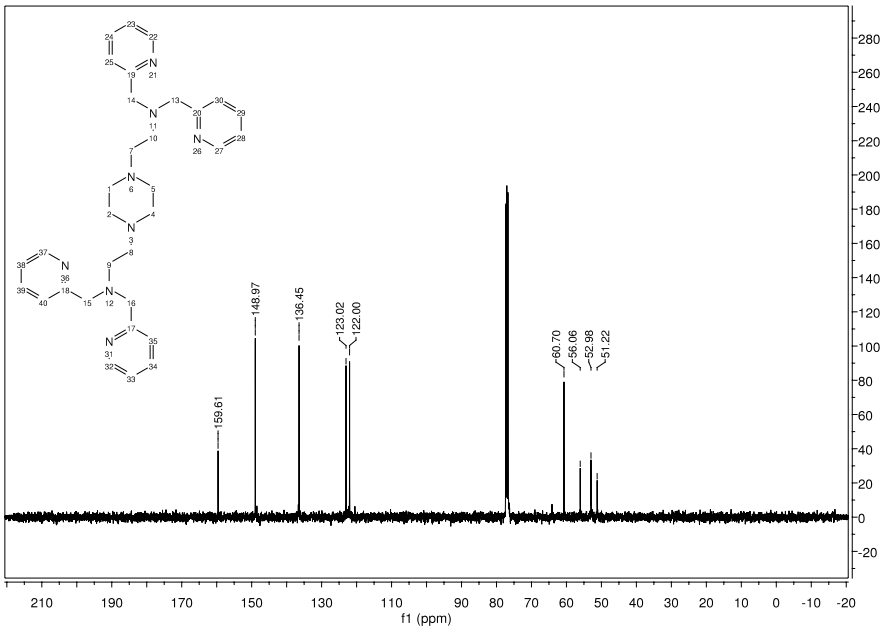

Fig. A.49: ^{13}C-NMR spectrum of **L7**

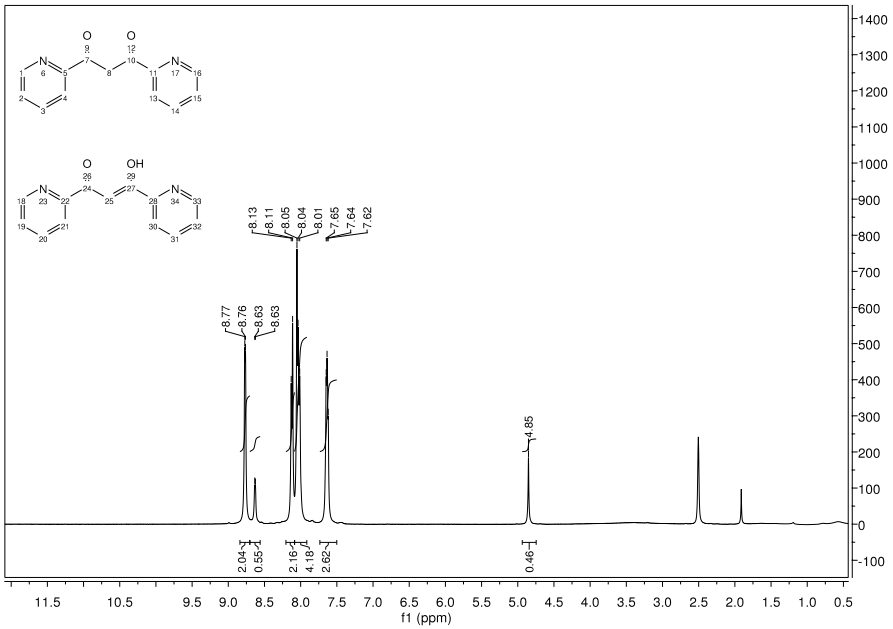

Fig. A.50: ^{1}H-NMR spectrum of **L8**

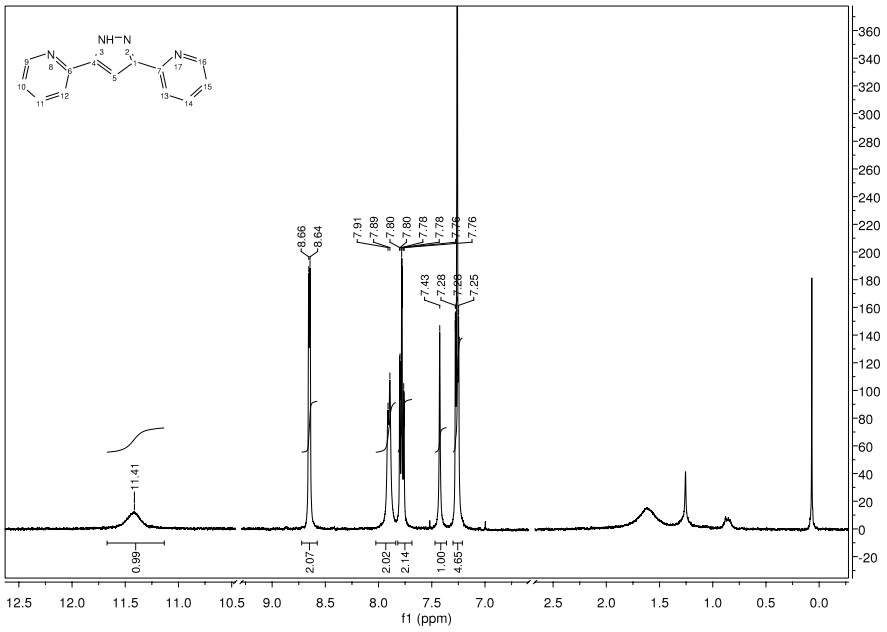

Fig. A.51: ^{1}H-NMR spectrum of **L9**

B Crystallographic Data

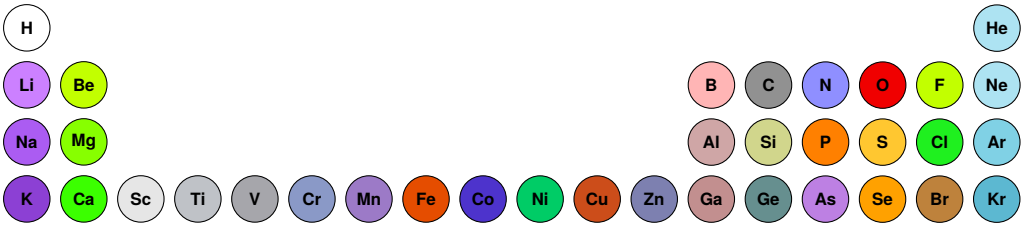

Fig. B.1: Color codes used for the representation of crystal structures

B.1 Measurement Parameters

Tab. B.1: Crystallographic data of **C4**, **C5** and **C6**

Identification code	**C4**	**C5**	**C6**
Empirical formula	$C_{40}H_{66}CoN_2O_4$	$C_{52}H_{88}CoN_4O_4$	$C_{29}H_{37}Br_8CoN_4O_4$
Formula weight/g mol^{-1}	697.87	892.19	1203.83
Temperature/K	173.15	173.15	173.15
Crystal system	orthorhombic	monoclinic	monoclinic
Space group	$Pca2_1$	$C2/c$	$P2_1$
a/Å	18.729(3)	20.209(7)	10.3888(2)
b/Å	10.738(2)	14.010(4)	17.3101(3)
c/Å	19.488(4)	23.383(7)	10.5887(2)
α/°	90	90	90
β/°	90	121.333(8)	99.6854(9)
γ/°	90	90	90
Volume/Å^3	3919.2(14)	5655(3)	1877.04(6)
Z	4	4	2
ρ_{calc}/(g cm^{-3})	1.183	1.048	2.130
μ/mm^{-1}	0.478	0.345	9.012
$F(000)$	1516.0	1948.0	1156.0
Crystal size/mm^3	0.15 × 0.13 × 0.05	0.17 × 0.1 × 0.02	0.19 × 0.12 × 0.03
Radiation	Mo$K\alpha$	Mo$K\alpha$	Mo$K\alpha$
2Θ range for data collection/°	3.794 to 49.812	3.63 to 56.152	3.978 to 66.554
Index ranges	$-22 \leq h \leq 20$ $-12 \leq k \leq 12$ $-12 \leq l \leq 23$	$-26 \leq h \leq 26$ $-18 \leq k \leq 18$ $-30 \leq l \leq 29$	$-15 \leq h \leq 16$ $-26 \leq k \leq 26$ $-16 \leq l \leq 15$
Reflections collected	14473	40709	54646
Independent reflections	5030	6835	14399
R_{int}	0.1705	0.1900	0.0673
R_{sigma}	0.2964	0.1888	0.0860
Data/restraints/parameters	5030/105/439	6835/89/331	14399/23/429
Goodness-of-fit on F^2	0.622	0.804	0.800
Final $R_1[I \geq 2\sigma(I)]$	0.0469	0.0612	0.0319
Final $wR_2[I \geq 2\sigma(I)]$	0.0666	0.1307	0.0496
Final R_1[all data]	0.1652	0.1618	0.0577
Final wR_2[all data]	0.0961	0.1557	0.0529

Tab. B.2: Crystallographic data of **C7a**, **C7b**, **C8**, **C9**, **C10** and **C11**

Identification code	**C7a**	**C7b**	**C8**	**C9**	**C10**	**C11**
Empirical formula	$C_{60}H_{106}Co_3N_2O_{12}$	$C_{60}H_{106}Co_3N_2O_{12}$	$C_{90}H_{138}Co_4O_{18}$	$C_{90}H_{132}Co_2N_8O_8$	$C_{104}H_{156}Cu_6O_{20}$	$C_{76}H_{115}N_5Ni_4O_{12}$
Formula weight/g mol^{-1}	1224.26	1224.25	1743.72	1571.89	2107.52	1525.56
Temperature/K	173.15	173.15	173.15	173.15	173.15	173.15
Crystal system	triclinic	monoclinic	monoclinic	triclinic	triclinic	triclinic
Space group	$P\bar{1}$	$P2_1/c$	$P2_1/c$	$P\bar{1}$	$P\bar{1}$	$P\bar{1}$
a/Å	11.17720(14)	13.5008(5)	24.5424(18)	11.119(3)	16.2012(6)	15.187(3)
b/Å	13.10042(16)	24.1414(9)	15.3073(11)	14.724(5)	16.3552(6)	15.675(3)
c/Å	23.7971(2)	10.9711(4)	29.163(2)	16.084(5)	24.9771(9)	19.938(4)
α/°	84.9849(9)	90	90	66.607(7)	72.5980(10)	102.955(5)
β/°	80.7041(9)	109.0460(10)	101.137(3)	88.815(7)	84.0730(10)	98.008(5)
γ/°	80.7263(11)	90	90	79.359(7)	66.6730(10)	116.843(5)
Volume/Å^3	3387.07(7)	3380.0(2)	10749.6(14)	2371.1(12)	5798.3(4)	3966.1(13)
Z	2	2	4	1	2	2
ρ_{calc}/(g cm^{-3})	1.200	1.203	1.077	1.101	1.207	1.276
μ/mm^{-1}	0.780	0.782	0.660	0.403	1.139	0.994
$F(000)$	1314.0	1314.0	3720.0	846.0	2228.0	1624.0
Crystal size/mm^3		0.32 × 0.32 × 0.25	0.39 × 0.27 × 0.08	0.24 × 0.2 × 0.08	0.19 × 0.12 × 0.04	0.13 × 0.1 × 0.05
Radiation	MoKα	MoKα	MoKα	MoKα	MoKα	MoKα
2Θ range for data collection/°	4.516 to 66.214	3.192 to 55.976	3.018 to 55.728	2.764 to 55.802	2.86 to 56.01	3.08 to 56.046
Index ranges	$-17 \leq h \leq 17$	$-17 \leq h \leq 17$	$-32 \leq h \leq 32$	$-14 \leq h \leq 14$	$-21 \leq h \leq 21$	$-19 \leq h \leq 20$
	$-20 \leq k \leq 20$	$-31 \leq k \leq 31$	$-20 \leq k \leq 17$	$-19 \leq k \leq 19$	$-21 \leq k \leq 21$	$-20 \leq k \leq 20$
	$-36 \leq l \leq 36$	$-14 \leq l \leq 14$	$-35 \leq l \leq 38$	$-21 \leq l \leq 21$	$-32 \leq l \leq 32$	$-26 \leq l \leq 18$
Reflections collected	209597	59665	108618	25280	84750	31358
Independent reflections	24624	8134	25507	11235	27941	18861
R_{int}	0.0389	0.0733	0.0951	0.1271	0.0811	0.1132
R_{sigma}	0.0250	0.0465	0.0901	0.2491	0.1320	0.2232
Data/restraints/parameters	24624/0/724	8134/230/430	25507/357/1121	11235/106/562	27941/93/1199	18861/138/914
Goodness-of-fit on F^2	1.040	1.011	1.010	0.728	0.818	0.964
Final $R_1[I \geq 2\sigma(I)]$	0.0515	0.0401	0.0537	0.0555	0.0435	0.0931
Final $wR_2[I \geq 2\sigma(I)]$	0.1212	0.0827	0.1139	0.0965	0.0978	0.2593
Final R_1[all data]	0.0629	0.0734	0.1126	0.1702	0.0837	0.1816
Final wR_2[all data]	0.1298	0.0949	0.1339	0.1196	0.1044	0.3045

Tab. B.3: Crystallographic data of **C12**, **C13**, **C14 C15**, **C16** and **C17**

Identification code	**C12**	**C13**	**C14**	**C15**	**C16**	**C17**
Empirical formula	$C_{85}H_{147}Co_2Fe_2N_3O_{18}$	$C_{71}H_{83}Co_4N_{11}O_{12}$	$C_{104}H_{141}Co_9N_{11}O_{34}$	$C_{48}H_{36}Co_3N_4O_{12}$	$C_{72}H_{118}Co_6N_4O_{24}$	$C_{106}H_{134}Co_6N_8O_{20}$
Formula weight/g mol^{-1}	1728.61	1518.20	2619.64	1037.60	1777.28	2193.78
Temperature/K	173.15	173.15	173.15	173.15	173.15	173.15
Crystal system	triclinic	monoclinic	triclinic	tetragonal	triclinic	orthorhombic
Space group	$P\bar{1}$	$P2_1/c$	$P\bar{1}$	$I4_1/a$	$P\bar{1}$	$Pbcn$
a/Å	15.462(5)	16.382(4)	15.2571(10)	17.960(2)	12.0944(14)	49.274(5)
b/Å	16.419(5)	24.924(6)	17.8012(12)	17.960	12.2121(14)	19.7548(15)
c/Å	18.503(5)	38.782(8)	26.2569(17)	13.6242(19)	14.2989(15)	22.9754(17)
α/°	87.949(5)	90	78.4068(16)	90	80.792(2)	90
β/°	89.623(5)	108.718(9)	77.4397(16)	90	89.138(2)	90
γ/°	86.903(5)	90	66.6606(15)	90	87.915(3)	90
Volume/Å^3	4687(2)	14997(6)	6338.4(7)	4394.5(12)	2083.2(4)	22364(3)
Z	2	8	2	4	1	8
ρ_{calc}/(g cm^{-3})	1.225	1.345	1.373	1.568	1.417	1.303
μ/mm^{-1}	0.713	0.934	1.221	1.190	1.239	0.936
$F(000)$	1856.0	6320.0	2714.0	2116.0	932.0	9184.0
Crystal size/mm^3	0.75 × 0.34 × 0.33	0.76 × 0.4 × 0.15	0.92 × 0.18 × 0.06	0.15 × 0.13 × 0.07	0.16 × 0.07 × 0.05	0.38 × 0.05 × 0.01
Radiation	MoKα	MoKα	MoKα	MoKα	MoKα	MoKα
2Θ range for data collection/°	3.428 to 56.63	1.634 to 56.19	3.126 to 55.968	3.752 to 55.772	4.08 to 56.122	1.652 to 56.04
Index ranges	$-20 \leq h \leq 20$ $-21 \leq k \leq 21$ $-24 \leq l \leq 24$	$-21 \leq h \leq 21$ $-32 \leq k \leq 32$ $-47 \leq l \leq 51$	$-20 \leq h \leq 20$ $-23 \leq k \leq 23$ $-34 \leq l \leq 34$	$-23 \leq h \leq 22$ $-23 \leq k \leq 19$ $-17 \leq l \leq 17$	$-15 \leq h \leq 15$ $-16 \leq k \leq 13$ $-18 \leq l \leq 18$	$-65 \leq h \leq 58$ $-25 \leq k \leq 26$ $-29 \leq l \leq 30$
Reflections collected	102305	189805	155772	16574	20829	167518
Independent reflections	23192	36567	30279	2609	10063	26942
R_{int}	0.0853	0.0741	0.1036	0.0699	0.0926	0.5798
R_{sigma}	0.0811	0.0758	0.0862	0.0458	0.1525	0.6767
Data/restraints/parameters	23192/319/1173	36567/138/1833	30279/253/1536	2609/0/153	10063/231/562	26942/258/1153
Goodness-of-fit on F^2	0.970	1.017	0.934	1.031	0.963	0.753
Final $R_1[I \geq 2\sigma(I)]$	0.0479	0.0977	0.0407	0.0499	0.0714	0.0821
Final $wR_2[I \geq 2\sigma(I)]$	0.1249	0.2878	0.0978	0.1233	0.1279	0.1778
Final R_1[all data]	0.0922	0.1352	0.0875	0.0909	0.1589	0.3360
Final wR_2[all data]	0.1404	0.3226	0.1109	0.1456	0.1564	0.2622

Tab. B.4: Crystallographic data of **C18**, **C19**, **C20 C21a** and **C21b**

Identification code	**C18**	**C19**	**C20**	**C21a**	**C21b**
Empirical formula	$C_{81}H_{102}Co_4N_8O_{18}$	$C_{91}H_{110}Cu_4N_4O_{15}$	$C_{111}H_{138}Co_6N_{12}O_{17}$	$C_{69}H_{116}Co_2N_8O_{17}S$	$C_{60}H_{80}Cl_2Co_2N_8O_{12}$
Formula weight/g mol^{-1}	1711.42	1753.98	2265.91	1479.61	1294.08
Temperature/K	173.15	173.15	173.15	173.15	173.15
Crystal system	triclinic	triclinic	monoclinic	monoclinic	triclinic
Space group	$P\bar{1}$	$P\bar{1}$	$P2_1/c$	$C2/c$	$P\bar{1}$
a/Å	13.4302(17)	13.4806(17)	15.3187(2)	26.051(3)	11.071(2)
b/Å	13.9487(18)	13.9286(17)	15.5354(2)	17.448(2)	11.3324(18)
c/Å	24.490(3)	14.2786(19)	51.3059(7)	17.215(2)	15.543(3)
α/°	94.527(4)	77.733(3)	90	90	107.932(6)
β/°	94.405(4)	62.104(3)	92.0822(9)	94.177(3)	97.683(7)
γ/°	104.223(3)	66.460(3)	90	90	94.644(7)
Volume/Å^3	4411.3(10)	2171.2(5)	12201.8(3)	7804.4(18)	1823.1(5)
Z	2	1	4	4	1
ρ_{calc}/(g cm^{-3})	1.288	1.341	1.233	1.259	1.179
μ/mm^{-1}	0.806	1.032	0.859	0.519	0.585
$F(000)$	1792.0	920.0	4744.0	3168.0	680.0
Crystal size/mm^3	0.19 × 0.16 × 0.02	1.33 × 0.23 × 0.06	0.2 × 0.1 × 0.06	0.46 × 0.34 × 0.3	0.19 × 0.15 × 0.02
Radiation	MoKα	MoKα	MoKα	MoKα	MoKα
2Θ range for data collection/°	1.676 to 51.058	3.19 to 55.77	1.588 to 55.806	2.812 to 55.73	3.744 to 56.07
Index ranges	$-16 \leq h \leq 16$ $-16 \leq k \leq 16$ $-29 \leq l \leq 19$	$-17 \leq h \leq 17$ $-18 \leq k \leq 18$ $-18 \leq l \leq 18$	$-19 \leq h \leq 20$ $-18 \leq k \leq 20$ $-61 \leq l \leq 67$	$-34 \leq h \leq 34$ $0 \leq k \leq 22$ $0 \leq l \leq 22$	$-13 \leq h \leq 14$ $-14 \leq k \leq 14$ $-20 \leq l \leq 20$
Reflections collected	38659	46447	108817	13257	18429
Independent reflections	16278	10263	29055	13257	8740
R_{int}	0.0808	0.0829	0.1204	?	0.1584
R_{sigma}	0.1199	0.0753	0.1761	0.1309	0.3032
Data/restraints/parameters	16278/153/1048	10263/177/582	29055/283/1397	13257/38/455	8740/79/379
Goodness-of-fit on F^2	0.962	0.911	0.819	1.041	0.941
Final $R_1[I \geq 2\sigma(I)]$	0.0574	0.0381	0.0499	0.0884	0.1072
Final $wR_2[I \geq 2\sigma(I)]$	0.1186	0.0860	0.0979	0.2066	0.2082
Final R_1[all data]	0.1249	0.0770	0.1365	0.1786	0.2736
Final wR_2[all data]	0.1437	0.0960	0.1188	0.2753	0.2692

B.2 Selected Bond Lengths

Tab. B.5: Selected bond lengths for **C4**

Atom	Atom	Length/Å	Atom	Atom	Length/Å
Co1	O1	1.901(9)	Co1	O4	1.884(9)
Co1	O2	1.905(9)	Co1	N1	1.969(9)
Co1	O3	1.885(9)	Co1	N2	1.978(9)
O1	C1	1.302(15)	O3	C15	1.348(15)
O2	C2	1.312(14)	O4	C16	1.362(14)
C1	C2	1.470(16)	C15	C16	1.423(16)
C2	C3	1.393(16)	C16	C17	1.404(15)
C3	C4	1.399(16)	C17	C18	1.407(16)
C4	C5	1.413(15)	C18	C19	1.391(15)
C5	C6	1.372(17)	C19	C20	1.388(17)
C6	C1	1.409(19)	C20	C15	1.369(19)

Tab. B.6: Selected bond lengths for **C5**

Atom	Atom	Length/Å	Atom	Atom	Length/Å
Co1	O1	1.885(2)	C2	C3	1.411(4)
Co1	O2	1.888(2)	C3	C4	1.387(4)
Co1	N2	1.977(3)	C4	C5	1.410(5)
O1	C1	1.328(4)	C5	C6	1.386(5)
O2	C2	1.330(3)	C6	C1	1.407(4)
C1	C2	1.430(4)			

Tab. B.7: Selected bond lengths for **C6**

Atom	Atom	Length/Å	Atom	Atom	Length/Å
Co1	N1	2.014(4)	Co1	O2	1.901(3)
Co1	N2	2.019(4)	Co1	O3	1.907(3)
Co1	O1	1.909(3)	Co1	O4	1.893(3)
O1	C1	1.333(5)	O3	C7	1.334(5)
O2	C2	1.318(5)	O4	C8	1.315(5)
C1	C2	1.445(6)	C7	C8	1.417(6)
C2	C3	1.385(6)	C8	C9	1.412(6)
C3	C4	1.413(6)	C9	C10	1.403(7)
C4	C5	1.396(6)	C10	C11	1.391(7)
C5	C6	1.394(6)	C11	C12	1.410(7)
C6	C1	1.397(6)	C12	C7	1.378(6)

Tab. B.8: Selected bond lengths for **C7a**

Atom	Atom	Length/Å	Atom	Atom	Length/Å
Co1	O1	2.1599	Co3	O3	2.1644
Co1	O2	1.9856	Co3	O4	1.9810
Co1	O5	1.9765	Co3	O9	1.9819
Co1	O7	1.9688	Co3	O11	1.9592
Co1	N1	2.2080	Co3	N2	2.1976
Co2	O1	2.1082	Co2	O8	2.0776
Co2	O3	2.1180	Co2	O10	2.0805
Co2	O6	2.0768	Co2	O12	2.0549
O1	C1	1.2877	O3	C15	1.2875
O2	C2	1.2884	O4	C16	1.2891
C1	C2	1.4616	C15	C16	1.4628
C2	C3	1.4410	C16	C17	1.4403
C3	C4	1.3737	C17	C18	1.3769
C4	C5	1.4414	C18	C19	1.4389
C5	C6	1.3736	C19	C20	1.3719
C6	C1	1.4190	C20	C15	1.4213

Tab. B.9: Selected bond lengths for **C7b**

Atom	Atom	Length/Å	Atom	Atom	Length/Å
Co1	O1	2.1691(15)	O1	C1	1.289(2)
Co1	O2	1.9755(15)	O2	C2	1.288(2)
Co1	O4	1.9674(16)	C1	C2	1.459(3)
Co1	O6	1.9662(15)	C2	C3	1.444(3)
Co1	N1	2.2322(19)	C3	C4	1.363(3)
Co2	O1	2.0989(14)	C4	C5	1.442(3)
Co2	O3	2.0768(16)	C5	C6	1.370(3)
Co2	O5	2.0849(16)	C6	C1	1.424(3)

Tab. B.10: Selected bond lengths for **C8**

Atom	Atom	Length/Å	Atom	Atom	Length/Å
Co1	O1	2.1100(18)	Co3	O5	2.0768(18)
Co1	O8	2.0198(19)	Co3	O7	2.2147(18)
Co1	O9	2.0972(17)	Co3	O8	2.0465(17)
Co1	O10	2.158(2)	Co3	O9	2.1874(19)
Co1	O11	2.1131(19)	Co3	O12	2.0405(19)
Co1	O15	2.0499(18)	Co3	O14	2.039(2)
Co2	O1	2.0599(17)	Co4	O3	2.091(2)
Co2	O2	2.0400(19)	Co4	O5	2.0800(19)
Co2	O3	2.0563(18)	Co4	O6	2.050(2)
Co2	O4	2.051(2)	Co4	O7	2.0655(17)
Co2	O7	2.0771(19)	Co4	O13	2.106(2)
Co2	O9	2.1414(18)	Co4	O17	2.069(2)
O1	C1	1.296(3)	O3	C15	1.310(3)
O2	C2	1.284(3)	O4	C16	1.286(3)
C1	C2	1.464(4)	C15	C16	1.457(4)
C2	C3	1.440(4)	C16	C17	1.447(4)
C3	C4	1.376(4)	C17	C18	1.369(4)
C4	C5	1.428(5)	C18	C19	1.428(5)
C5	C6	1.376(4)	C19	C20	1.381(4)
C6	C1	1.406(4)	C20	C15	1.404(4)
O5	C29	1.312(3)	O7	C43	1.389(3)
O6	C30	1.275(4)	O8	C44	1.366(3)
C29	C30	1.471(4)	C43	C44	1.415(4)
C30	C31	1.445(4)	C44	C45	1.412(4)
C31	C32	1.369(5)	C45	C46	1.402(4)
C32	C33	1.430(5)	C46	C47	1.395(4)
C33	C34	1.375(4)	C47	C48	1.396(4)
C34	C29	1.389(4)	C48	C43	1.367(4)
O9	C57	1.334(3)	C59	C60	1.376(4)
O10	C58	1.286(3)	C60	C61	1.441(4)
C57	C58	1.457(4)	C61	C62	1.372(4)
C58	C59	1.446(4)	C62	C57	1.381(4)

Tab. B.11: Selected bond lengths for **C9**. [1] : $1-x,-y,1-z$

Atom	Atom	Length/Å	Atom	Atom	Length/Å
Co1	O1	1.911(2)	Co1	O4	1.869(2)
Co1	O2	1.917(2)	Co1	N1[1]	1.942(3)
Co1	O3	1.868(2)	Co1	N3	1.991(3)
O1	C1	1.309(4)	O3	C15	1.348(4)
O2	C2	1.302(4)	O4	C16	1.352(4)
C1	C2	1.452(4)	C15	C16	1.415(4)
C2	C3	1.420(5)	C16	C17	1.408(4)
C3	C4	1.381(5)	C17	C18	1.398(5)
C4	C5	1.439(5)	C18	C19	1.403(5)
C5	C6	1.361(5)	C19	C20	1.425(4)
C6	C1	1.387(4)	C20	C15	1.394(4)

Tab. B.12: Selected bond lengths for **C10**. [1] : $1-x,-y,-z$

Atom	Atom	Length/Å	Atom	Atom	Length/Å
Cu1A	O1A	1.965(2)	Cu2A	O7A	1.955(2)
Cu1A	O2A	1.932(2)	Cu2A	O9A	1.932(2)
Cu1A	O3A	1.941(2)	Cu3A	O1A	2.265(2)
Cu1A	O4A	1.948(2)	Cu3A	O5A	1.996(2)
Cu2A	O3A	2.243(2)	Cu3A	O6A[1]	1.948(2)
Cu2A	O5A	2.006(2)	Cu3A	O8A[1]	1.931(2)
Cu2A	O6A[1]	1.948(2)	Cu3A	O10A[1]	1.951(2)
O1A	C1A	1.305(4)	O3A	C15A	1.307(3)
O2A	C2A	1.290(4)	O4A	C16A	1.288(4)
C1A	C2A	1.440(5)	C15A	C16A	1.445(5)
C2A	C3A	1.441(4)	C16A	C17A	1.446(4)
C3A	C4A	1.363(5)	C17A	C18A	1.366(5)
C4A	C5A	1.437(5)	C18A	C19A	1.435(5)
C5A	C6A	1.378(5)	C19A	C20A	1.376(4)
C6A	C1A	1.403(4)	C20A	C15A	1.402(4)
O5A	C29A	1.379(4)	C31A	C32A	1.395(5)
O6A	C30A	1.367(4)	C32A	C33A	1.403(4)
C29A	C30A	1.403(4)	C33A	C34A	1.385(4)
C30A	C31A	1.418(4)	C34A	C29A	1.393(5)

Tab. B.13: Selected bond lengths for **C11**

Atom	Atom	Length/Å	Atom	Atom	Length/Å
Ni1	O1	2.137(6)	Ni3	O3	2.086(6)
Ni1	O2	2.120(6)	Ni3	O7	2.118(5)
Ni1	O3	2.051(6)	Ni3	O8	2.090(6)
Ni1	O5	2.013(6)	Ni3	O9	2.075(6)
Ni1	O9	2.052(6)	Ni3	O11	2.020(6)
Ni1	N1	2.045(8)	Ni3	N3	2.054(7)
Ni2	O1	2.072(6)	Ni4	O1	2.078(6)
Ni2	O3	2.108(6)	Ni4	O7	2.064(6)
Ni2	O4	2.067(6)	Ni4	O9	2.129(6)
Ni2	O6	2.006(6)	Ni4	O10	2.047(6)
Ni2	O7	2.067(6)	Ni4	O12	1.997(6)
Ni2	N2	2.046(8)	Ni4	N4	2.077(8)
O1	C1	1.385(11)	O3	C15	1.376(10)
O2	C2	1.367(11)	O4	C16	1.397(10)
C1	C2	1.377(14)	C15	C16	1.416(12)
C2	C3	1.420(13)	C16	C17	1.367(12)
C3	C4	1.392(14)	C17	C18	1.393(13)
C4	C5	1.399(16)	C18	C19	1.381(14)
C5	C6	1.374(14)	C19	C20	1.409(12)
C6	C1	1.385(13)	C20	C15	1.388(11)
O7	C34	1.358(10)	O9	C48	1.360(9)
O8	C35	1.392(10)	O10	C49	1.386(10)
C34	C35	1.404(12)	C48	C49	1.414(12)
C35	C36	1.398(12)	C49	C50	1.412(12)
C36	C37	1.405(12)	C50	C51	1.375(13)
C37	C38	1.385(14)	C51	C52	1.396(13)
C38	C39	1.409(13)	C52	C53	1.389(12)
C39	C34	1.380(11)	C53	C48	1.388(12)

Tab. B.14: Selected bond lengths for **C12**

Atom	Atom	Length/Å	Atom	Atom	Length/Å
Fe1	O2	1.9113(17)	Co1	N1	2.155(2)
Fe1	O1	2.0790(18)	Co1	O9	2.1577(18)
Fe1	O4	1.9909(19)	Co1	O11	2.082(2)
Fe1	O3	2.0871(17)	Co1	O13	2.099(2)
Fe1	O7	2.0176(19)	Co1	O15	2.078(2)
Fe1	O5	2.0492(19)	Co1	O16	2.092(2)
Fe2	O3	2.0917(19)	Co2	O1	1.9947(17)
Fe2	O8	2.033(2)	Co2	O3	2.3664(19)
Fe2	O5	2.1288(18)	Co2	O9	1.9792(19)
Fe2	O6	1.920(2)	Co2	O10	2.006(2)
Fe2	O9	1.9938(18)	Co2	O12	1.9642(19)
Fe2	O14	1.956(2)			
O1	C1	1.368(3)	O3	C15	1.390(3)
O2	C2	1.331(3)	O4	C16	1.364(3)
C1	C2	1.419(4)	C15	C16	1.408(4)
C2	C3	1.412(3)	C16	C17	1.404(4)
C3	C4	1.392(4)	C17	C18	1.406(4)
C4	C5	1.401(4)	C18	C19	1.386(5)
C5	C6	1.400(4)	C19	C20	1.397(4)
C6	C1	1.372(4)	C20	C15	1.363(4)
O5	C29	1.370(3)	C31	C32	1.397(4)
O6	C30	1.349(3)	C32	C33	1.396(4)
C29	C30	1.415(4)	C33	C34	1.401(4)
C30	C31	1.392(4)	C34	C29	1.377(4)

Tab. B.15: Selected bond lengths for **C13**

Atom	Atom	Length/Å	Atom	Atom	Length/Å
Co1A	O1A	1.908(5)	Co2A	O4A	1.904(5)
Co1A	O2A	1.892(5)	Co2A	O5A	1.896(5)
Co1A	O3A	1.884(6)	Co2A	O6A	1.852(5)
Co1A	N1A	1.893(6)	Co2A	N2A	1.873(6)
Co1A	N3A	1.956(7)	Co2A	N5A	1.956(7)
Co1A	N4A	1.978(7)	Co2A	N6A	1.957(7)
Co3A	O1A	2.029(5)	Co4A	O7A	2.001(6)
Co3A	O5A	1.990(5)	Co4A	O8A	2.028(6)
Co3A	O8A	2.027(6)	Co4A	O10A	2.004(7)
Co3A	O9A	2.030(6)	Co4A	O12A	1.999(6)
Co3A	O11A	2.022(5)	Co4A	N7A	2.107(7)
O1A	C1A	1.377(9)	C3A	C4A	1.383(13)
O2A	C2A	1.345(10)	C4A	C5A	1.407(12)
C1A	C2A	1.398(11)	C5A	C6A	1.387(11)
C2A	C3A	1.422(11)	C6A	C1A	1.396(11)

Tab. B.16: Selected bond lengths for **C14**

Atom	Atom	Length/Å	Atom	Atom	Length/Å
Co1	O1	2.045(2)	Co2	O1	1.8877(19)
Co1	O6	2.1745(19)	Co2	O4	1.924(2)
Co1	O7	2.000(2)	Co2	O23	1.9640(19)
Co1	O18	2.043(2)	Co2	N1	1.898(2)
Co1	O23	2.1911(19)	Co2	N2	1.889(2)
Co1	O24	2.007(2)	Co2	N3	1.938(2)
Co3	O3	2.110(2)	Co4	O3	2.081(2)
Co3	O8	2.070(2)	Co4	O4	2.145(2)
Co3	O9	2.095(2)	Co4	O11	2.019(2)
Co3	O10	2.144(2)	Co4	O13	2.123(2)
Co3	O22	2.191(2)	Co4	O15	2.088(3)
Co3	O23	2.0710(19)	Co4	O22	2.104(2)
Co5	O2	2.029(2)	Co6	N6	1.901(2)
Co5	O3	2.1362(19)	Co6	N7	1.937(2)
Co5	O12	2.070(2)	Co6	O6	1.9679(19)
Co5	O14	2.020(2)	Co6	O18	1.890(2)
Co5	O17	2.248(3)	Co6	O21	1.925(2)
Co5	N4	2.120(3)	Co6	N5	1.896(2)
Co7	O5	2.2007(19)	Co8	O5	2.108(2)
Co7	O6	2.0586(19)	Co8	O20	2.0756(19)
Co7	O20	2.097(2)	Co8	O21	2.1378(19)
Co7	O25	2.078(2)	Co8	O28	2.132(2)
Co7	O26	2.102(2)	Co8	O30	2.011(2)
Co7	O27	2.146(2)	Co8	O32	2.119(2)
Co9	N8	2.118(3)	Co9	O29	2.042(2)
Co9	O19	2.027(2)	Co9	O31	2.064(2)
Co9	O20	2.1273(19)	Co9	O34	2.244(3)

Tab. B.17: Selected bond lengths for **C15**

Atom	Atom	Length/Å	Atom	Atom	Length/Å
Co1	O1	1.871(2)	Co2	O3	1.986(2)
Co1	O2	1.896(2)	Co1	N1	1.936(3)

Tab. B.18: Selected bond lengths for **C16**. ^{1} : $1-x, 1-y, -z$

Atom	Atom	Length/Å	Atom	Atom	Length/Å
Co1	O1	1.894(3)	Co2	O1	2.049(3)
Co1	O2	1.906(3)	Co2	O2	2.130(4)
Co1	O3	1.882(3)	Co2	O5	2.136(4)
Co1	O6	1.917(3)	Co2	O7	2.055(4)
Co1	O11	1.916(3)	Co2	O9	2.032(4)
Co1	N1	1.869(4)	Co2	N2	2.072(4)
Co3	O1	2.057(3)	Co3	O10	2.027(4)
Co3	O3^{1}	2.006(3)	Co3	O12^{1}	2.146(3)
Co3	O8	2.099(4)	Co3	O12	2.183(3)

Tab. B.19: Selected bond lengths for **C17**

Atom	Atom	Length/Å	Atom	Atom	Length/Å
Co1	N1	2.038(10)	Co2	N2	2.085(9)
Co1	O1	2.097(8)	Co2	O1	2.093(7)
Co1	O4	2.039(7)	Co2	O5	2.268(7)
Co1	O5	2.030(7)	Co2	O6	2.264(7)
Co1	O12	2.138(8)	Co2	O7	2.064(7)
Co1	O13	2.136(8)	Co2	O14	2.057(7)
Co3	N3	2.044(9)	Co4	N4	2.096(9)
Co3	O2	2.106(7)	Co4	O2	2.130(8)
Co3	O6	2.194(7)	Co4	O8	2.214(7)
Co3	O7	2.016(7)	Co4	O9	2.171(7)
Co3	O8	2.011(7)	Co4	O10	2.095(7)
Co3	O15	2.117(8)	Co4	O16	2.055(7)
Co5	N5	2.069(9)	Co6	N6	2.087(9)
Co5	O3	2.118(7)	Co6	O3	2.096(7)
Co5	O9	2.114(7)	Co6	O4	2.109(7)
Co5	O10	2.066(7)	Co6	O11	2.234(7)
Co5	O11	2.065(7)	Co6	O12	2.146(7)
Co5	O17	2.120(8)	Co6	O18	2.031(8)

Tab. B.20: Selected bond lengths for **C18**

Atom	Atom	Length/Å	Atom	Atom	Length/Å
Co1	O1	1.886(3)	Co2	O1	2.043(3)
Co1	O2	1.884(3)	Co2	O3	2.119(3)
Co1	O7	1.923(3)	Co2	O7	2.110(3)
Co1	O9	1.900(3)	Co2	O8	2.088(3)
Co1	O11	1.894(3)	Co2	O12	2.085(3)
Co1	N1	1.898(4)	Co2	N2	2.082(4)
Co3	O3	1.958(3)	Co4	O4	2.142(3)
Co3	O4	1.889(3)	Co4	O7	2.090(3)
Co3	O5	1.882(3)	Co4	O8	2.088(3)
Co3	O8	1.883(3)	Co4	O10	2.030(3)
Co3	O13	1.911(3)	Co4	O14	2.083(3)
Co3	N3	1.883(4)	Co4	N4	2.090(4)

Tab. B.21: Selected bond lengths for **C19**. ^{1} : $2-x,-y,1-z$

Atom	Atom	Length/Å	Atom	Atom	Length/Å
Cu1	O1	1.970(2)	Cu2	O1	1.970(2)
Cu1	O2	2.453(2)	Cu2	O2	1.926(2)
Cu1	O4	1.932(2)	Cu2	O4	1.957(2)
Cu1	O5	1.888(2)	Cu2	O4^{1}	2.412(2)
Cu1	N2	1.953(2)	Cu2	O6	2.675(3)
			Cu2	N1	1.937(2)
O4	C25	1.379(3)	C27	C28	1.395(4)
O5	C26	1.338(3)	C28	C29	1.397(4)
C25	C26	1.417(3)	C29	C30	1.403(4)
C26	C27	1.411(3)	C30	C25	1.369(3)

Tab. B.22: Selected bond lengths for **C20**

Atom	Atom	Length/Å	Atom	Atom	Length/Å
Co1	O1	2.053(2)	Co4	O3	2.070(2)
Co1	O4	2.014(3)	Co4	O4	2.012(3)
Co1	O12	1.983(3)	Co4	O17	1.973(3)
Co1	N1	2.184(3)	Co4	N7	1.996(4)
Co1	N2	1.999(3)	Co4	N8	2.183(4)
Co2	O2	2.135(2)	Co3	O2	2.134(2)
Co2	O6	2.061(2)	Co3	O8	2.046(2)
Co2	O8	2.053(2)	Co3	O10	2.088(2)
Co2	O14	2.110(2)	Co3	O15	2.101(2)
Co2	N3	2.102(3)	Co3	N5	2.152(3)
Co2	N4	2.145(3)	Co3	N6	2.093(3)
Co5	O1	2.063(2)	Co6	O3	2.072(2)
Co5	O6	1.982(2)	Co6	O10	1.970(2)
Co5	O13	2.035(3)	Co6	O16	2.018(3)
Co5	N9	2.123(3)	Co6	N11	2.094(3)
Co5	N10	2.085(3)	Co6	N12	2.129(3)
O4	C2	1.388(4)	O6	C16	1.364(4)
O5	C3	1.373(6)	O7	C17	1.369(4)
C2	C3	1.377(5)	C16	C17	1.414(5)
C3	C4	1.389(5)	C17	C18	1.394(5)
C4	C5	1.389(5)	C18	C19	1.407(4)
C5	C6	1.388(6)	C19	C20	1.384(5)
C6	C7	1.407(6)	C20	C21	1.397(5)
C7	C2	1.373(6)	C21	C16	1.378(5)
O8	C30	1.354(4)	O10	C44	1.375(4)
O9	C31	1.377(4)	O11	C45	1.369(4)
C30	C31	1.401(5)	C44	C45	1.401(5)
C31	C32	1.398(5)	C45	C46	1.396(5)
C32	C33	1.393(5)	C46	C47	1.396(5)
C33	C34	1.387(5)	C47	C48	1.391(5)
C34	C35	1.400(5)	C48	C49	1.396(5)
C35	C30	1.385(5)	C49	C44	1.383(5)

Tab. B.23: Selected bond lengths for **C21a**

Atom	Atom	Length/Å	Atom	Atom	Length/Å
Co1	O1	1.878(4)	Co1	N2	1.954(4)
Co1	O2	1.888(4)	Co1	N3	1.936(5)
Co1	N1	2.063(5)	Co1	N4	1.925(5)
O1	C1	1.349(7)	C3	C4	1.428(10)
O2	C2	1.369(7)	C4	C5	1.395(11)
C1	C2	1.395(9)	C5	C6	1.385(10)
C2	C3	1.394(9)	C6	C1	1.403(8)

Tab. B.24: Selected bond lengths for **C21b**

Atom	Atom	Length/Å	Atom	Atom	Length/Å
Co1	O1	1.892(6)	Co1	N2	1.940(6)
Co1	O2	1.884(5)	Co1	N3	1.956(6)
Co1	N1	2.056(5)	Co1	N4	1.908(7)
O1	C1	1.358(9)	C3	C4	1.391(12)
O2	C2	1.339(9)	C4	C5	1.386(13)
C1	C2	1.385(11)	C5	C6	1.402(13)
C2	C3	1.403(11)	C6	C1	1.432(12)

C